

Copyright
by
Rochan Raj Upadhyay
2006

The Dissertation Committee for Rochan Raj Upadhyay Certifies that this is the approved version of the following dissertation:

**SIMULATION OF POPULATION BALANCE EQUATIONS USING
QUADRATURE BASED MOMENT METHODS**

Committee:

Ofodike A. Ezekoye, Supervisor

Irene M. Gamba

John R. Howell

Robert D. Moser

Philip L. Varghese

**SIMULATION OF POPULATION BALANCE EQUATIONS USING
QUADRATURE BASED MOMENT METHODS**

by

Rochan Raj Upadhyay, B.Tech.; M.S.M.E.

Dissertation

Presented to the Faculty of the Graduate School of

The University of Texas at Austin

in Partial Fulfillment

of the Requirements

for the Degree of

Doctor of Philosophy

The University of Texas at Austin

December 2006

Acknowledgements

Firstly, I would like to thank Professor O. A. Ezekoye for his encouragement and assistance throughout my graduate study. It is very unlikely that I would be able to complete a task of this magnitude without his constant support. I would then like to thank my dissertation committee members for the time and effort they have spent on evaluating this dissertation. During my career as a graduate student I have tried to broaden my intellectual horizons by taking classes from a variety of departments other than mechanical engineering, particularly from the mathematics, physics and aerospace engineering departments. Hopefully any of the intellectual maturity that I have gained is reflected in this work. In any case, I am indebted to the all the professors whose classes I attended. I am grateful to Dr. Steve Biegalski for some research opportunities. I have also been involved in the teaching of the undergraduate heat transfer course for a couple of semesters. I would like to thank Professor Noel Clemens and Professor Robert Moser for giving me the opportunity. I would like to thank my friends (both from UT and elsewhere) for all the good times. In particular, I would like to thank Dr. Sean Jenkins for his help on numerous occasions. Last but not the least, a word of thanks goes to my parents who have provided support in difficult times.

SIMULATION OF POPULATION BALANCE EQUATIONS USING QUADRATURE BASED MOMENT METHODS

Publication No. _____

Rochan Raj Upadhyay, Ph.D.

The University of Texas at Austin, 2006

Supervisor: Ofodike A. Ezekoye

Population Balance Equations (PBE) are used for modeling a variety of particulate processes as well as various stochastic phenomena in science and engineering. However PBEs are difficult to solve because they describe the evolution of a probability density function (PDF) in high dimensional spaces. Due to their unique mathematical structure and properties, these equations require special solution techniques. Moment methods are a class of solution techniques that evolve only a few moments of the PDF. While moment methods are simpler, they are known to have closure problems, i.e. a finite set of moment equations do not fully describe the PDF or its evolution. The purpose of this dissertation is to investigate a closure scheme for the moment equations that is based on Gaussian quadrature. This approach, known as the Quadrature Method of Moments (QMOM), is very general as it does not require any a priori assumptions on the form of the PDF. In this study, I first evaluate the accuracy of the moment closure by

applying QMOM to solve some well known problems in aerosol science, such as particle nucleation and growth in well stirred reactors and size dependent transport of aerosol particles. I find that results obtained using QMOM compare favorably with results obtained using more expensive techniques. Moment methods are particularly suited for implementation in CFD codes. As an example of a model for smoke detectors, I use QMOM to simulate smoke entry and light scattering in a cylindrical cavity above a uniform flow. As further examples, I describe the use of QMOM in applications such as statistical uncertainty propagation and simulation of turbulent mixing and chemical reaction using the PDF transport equation. While moment methods are widely applicable, they have some limitations. I find that the solutions depend on the choice of moments and that there may not be a globally optimal set of moments. This becomes more problematic for solutions of multivariate PBEs using an extension called the Direct Quadrature Method of Moments (DQMOM). The insights from this work can lead to a greater appreciation of the benefits and limitations of moment methods for solving PBEs.

Table of Contents

List of Tables	xi
List of Figures	xii
Chapter 1: Introduction and Scope.	1
1.1 Overview of Population Balance equations.	1
1.2 Overview of computational approaches to solutions of PBEs.	3
1.3 Scope of the work.	6
1.3.1 Outline of the dissertation.....	7
Chapter 2: Population Balance Equations and the Quadrature Method of Moments.	9
2.1 The general population balance equation.	9
2.2 Examples of population balance equations used in this study.....	10
2.2.1 Aerosol dynamics.....	10
2.2.2 PDF transport equation.	13
2.3 Moment methods for the general population balance equation.	19
2.4 Concrete Examples of Moment equations.	21
2.4.1 Moment equation for the aerosol General Dynamic Equation. ...	21
2.4.2 Moment equations for the PDF transport equation.....	23
2.5 Closure of moment equations using numerical quadrature.....	24
2.6 Quadrature Method of Moments (QMOM).	25
2.6.1 Limitations of QMOM.....	33
(a) Extension to the multivariate case.....	33
(b) Awkward form for the transport terms in physical space.	34
2.7 The Direct Quadrature Method of Moments (DQMOM).	35
2.7.1 Computational issues regarding DQMOM.	37
2.7.2 Construction of a non-singular matrix.	39
2.8 Resolution of some issues in QMOM and DQMOM.	43
(i) Application of QMOM to univariate population balance equations arising from aerosol dynamics.	43

(ii) Application of DQMOM to multivariate population balance equations.	44
Chapter 3: Applications of QMOM and DQMOM to aerosol dynamics simulation.	45
3.1 Simulating particle formation and growth using the quadrature method of moments.	45
3.1.1 Introduction and motivation.	45
3.1.2. Particle formation and growth in a box.	47
3.1.3. Particle formation and growth in a nozzle.	51
3.1.4. Results and discussions.	54
Particle formation and growth in a box.	54
Particle formation and growth in a nozzle.	58
Evaluation of the one point quadrature approximation.	60
3.1.5. Conclusions.	65
3.2. Treatment of size dependant aerosol transport processes using QMOM/DQMOM.	66
3.2.1 Introduction and motivation.	66
3.2.2. Mathematical formulation and analytical solutions.	68
Case I: Simultaneous gravitational settling and diffusion.	70
Case II: Diffusion only.	71
Case III: Settling only.	71
3.2.3. Semi-analytical solutions for the moments.	71
Case I and II.	72
Case III.	75
3.2.4. The moment methods.	76
Quadrature method of moments (QMOM).	77
Direct quadrature method of moments (DQMOM).	78
3.2.5. QMOM vs. DQMOM.	79
3.2.6. Results and discussion.	80
Computation of the moments by integration of analytical solutions.	80
Effect of the choice of moments on the accuracy of the solution obtained using QMOM/DQMOM.	84

3.2.7. Conclusions.....	93
3.3. Example of QMOM coupled with CFD: Simulation of smoke entry and light scattering in a cylindrical cavity above a uniform flow.	94
3.3.1. Introduction and background.....	94
The two- parameter model for smoke detectors.	96
Motivations and scope of the present study.....	98
3.3.2. Flow and aerosol model.....	99
3.3.3. Light scattering model.	105
Extinction.....	107
Angular light scattering.....	110
3.3.4. Simulations and results.	113
Features of the flow field.	114
Smoke buildup within the detector.	116
Light scattering by smoke particles.	117
3.3.5 Detector response study.....	121
3.3.6. Conclusions.....	129
Chapter 4: Applications of QMOM and DQMOM to problems in uncertainty propagation and turbulent mixing and reaction.	131
4.1 Design Fire Evaluation Using the Quadrature Method of Moments.	132
4.1.1. Introduction and Background.	132
4.1.2. Mathematical representation of the propagation of uncertainty and the quadrature method of moments.....	136
4.1.3. Details of input variable distributions and fire models used....	139
Input fire heat release rate distribution.	139
Available Safe Egress Time (ASET) Model.....	142
Consolidated Fire and Smoke Transport (CFAST) Model.	143
4.1.4. Computational methods.	144
Monte Carlo Simulations.	144
Quadrature Method of Moments (QMOM).	145
GLD reconstruction of the CDF.	146
4.1.5. Results and Discussions.....	148
Comparison of ASET and CFAST results.....	148

Monte Carlo Simulation results for ASET and CFAST models.	149
QMOM results for ASET and CFAST models.....	153
4.1.6. Conclusions and further work.....	157
4.2. Simulation of the PDF transport equation for turbulent mixing and combustion using the Direct Quadrature Method of Moments.	158
4.2.1 Introduction and motivations.....	158
4.2.2 Derivation of the pdf transport equation for simulating a Partially Stirred Reactor.....	162
4.2.3 Application of the DQMOM.....	164
4.2.4 Chemistry Models.....	166
(a) One step chemistry mechanism.....	167
(b) Two-step chemistry mechanism.....	168
4.2.5 Computations and Discussion of Results.....	170
(a) Two stream mixing problem.....	171
(b) One step chemistry problem.....	174
(b) Two step chemistry problem.....	182
4.2.6 Conclusions.....	187
Chapter 5: Conclusions and further work.....	190
5.1 Summary of main results.....	190
5.2 Recommendations for future work.....	193
Appendix A.....	195
A.1. Obtaining the abscissas and weights for the quadrature formula.....	195
A.2. The product difference algorithm for getting elements of the tridiagonal matrix.....	200
Appendix B.....	201
B.1. Derivation of DQMOM equations for size dependent diffusion and transport.....	201
Bibliography.....	205
Vita	214

List of Tables

Table 2.1. Table showing the errors involved in computing the moment $M_{0.5}$ using $2N_Q+1$ integer moments for different numbers of quadrature points N_Q	30
Table 3.1.1. Non-dimensional terms used in equations 3.1.1 and 3.1.2.	51
Table 3.1.2. Non-dimensional terms used in equations 3.1.11 and 3.1.12.	54
Table 3.2.1. Comparison of the errors E_N and E_V of the QMOM/DQMOM solutions for different moment sequences and number of quadrature points for the case of diffusion only (Case II).....	91
Table 3.2.2. Comparison of the errors E_N and E_V of the QMOM/DQMOM solutions for different moment sequences and number of quadrature points for the case of settling only (Case III).....	92
Table 3.2.3. Comparison of the errors E_N and E_V of the QMOM/DQMOM solutions for different moment sequences and number of quadrature points for the case of simultaneous diffusion and settling (Case I).	92
Table 3.3.1. Summary of the boundary conditions used in the flow and aerosol dynamics simulation. (Boundaries are labeled in figure 3.3.2.)	101
Table 4.2.1. Summary of mixing and chemistry sub-models used in the computational problem for the partially stirred reactor.	170

List of Figures

Figure 2.1. Control volume in phase space used to derive the population balance equation.....	10
Figure 2.2. Schematic of various aerosol processes at the micro-scale.....	13
Figure 2.3. Schematic showing actual paths of the species and the path of notional (or conditional) particles in velocity composition space for a turbulent reacting flow.....	17
Figure 2.4. Integration of the function $v^{0.5}$ with respect to the lognormal density function using 2-point Gaussian quadrature.....	30
Figure 2.5. Schematic that shows the DQMOM procedure and the relation between QMOM and DQMOM.....	38
Figure 2.6. Example of the Graded Lexicographic (GLEX) Ordering for a set of trivariate moments. (Note that not all these moments can be used to create a non-singular Jacobian matrix A. Instead some moments need to be selectively discarded.)	43
Figure 3.1.1. Schematic diagram showing particle formation and growth in a nozzle.....	52
Figure 3.1.2. Variation of total number concentration with time for $R^* = 0.1$, comparison between exact, 1-point QMOM and lognormal calculations, box model with free molecular surface growth law and no coagulation.	56
Figure 3.1.3. Variation of the volume averaged particle diameter with time for $R^* = 0.1$, comparison between exact, 1-point. QMOM and lognormal calculations, box model with free molecular surface growth law and no coagulation.	57
Figure 3.1.4. Variation of total number concentration with time for $R^* = 0.1$ and $R^* = 1.0$, comparison of the lognormal, 1-point, 2-point and 3-point QMOM calculations, box model, with coagulation and combined surface growth laws.....	57
Figure 3.1.5. Variation of volume averaged particle diameter with time for $R^* = 0.1$ and $R^* = 1.0$, comparison of the lognormal, 1-point, 2-point and 3-point QMOM calculations, box model, with coagulation and combined surface growth laws.....	58
Figure 3.1.6. Variation of total number concentration with length along the nozzle, comparison of exact and 1-point QMOM calculations.....	59

Figure 3.1.7. Variation of number averaged diameter with length along the nozzle, comparison of exact and 1-point QMOM calculations.....	59
Figure 3.1.8. Variation in the error of 1-point quadrature calculation for area with polydispersity index for $R^* = 0.05$, $R^* = 0.1$ and $R^* = 1.0$	61
Figure 3.1.9. Polydispersity index and percentage error in total area, total number concentration and average diameter (1 st moment) between 1-point QMOM and exact calculations, box model with $R^* = 1.0$	63
Figure 3.1.10. Polydispersity index and percentage error in total area, total number concentration and average diameter (1 st moment) between 1-point QMOM and exact calculations, box model with $R^* = 10.0$	63
Figure 3.1.11. Polydispersity index and percentage error in total area and total number concentration between 1-point QMOM and exact calculations, problem of condensation in a nozzle.	65
Figure 3.2.1. Solutions for $M_0(x, t = 1)$ obtained from the numerical integration of the analytical solution (equation 6) with increasing number of quadrature points and choice of integer moment sequence for the case of combined diffusion and gravitational settling (Case I).....	82
Figure 3.2.2. Converged solutions of the numerical integrations for $M_0(x, t = 1)$ and $M_3(x, t = 1)$ using integer moment sequence and several fractional moment sequences. Case of combined diffusion and gravitational settling (Case I). Also shown is the solution using Monte Carlo integration that coincides with the solution obtained from fractional moments.....	83
Figure 3.2.3. Solutions for $M_0(x, t = 1)$ obtained from the numerical integration of the analytical solution (3.2.7) with increasing number of quadrature points and choice of integer moment sequence for the case of diffusion only (Case II).	83
Figure 3.2.4. Converged solutions for $M_0(x, t = 1)$ and $M_3(x, t = 1)$ using integer moment sequence and several fractional moment sequences. Case of diffusion only (Case	

II). Also shown is the solution from the Monte Carlo integration using 100,000 samples.	84
Figure 3.2.5. Comparison of the number fraction of aerosol deposited obtained from the analytical solution $N_a(t)$ and numerical solution $N_n(t)$ for the monodisperse case and for the three cases of combined diffusion and settling (Case I), diffusion only (Case II) and settling only (Case III).	88
Figure 3.2.6. Comparison of $N_a(t)$ (analytical solution) and $N_n(t)$ (solution from QMOM/DQMOM) for the polydisperse case. Effect of the choice of different moment sequences in the numerical solution is compared. Case of diffusion only (Case II).	88
Figure 3.2.7. Comparison of $N_a(t)$ and $N_n(t)$ for the polydisperse case. Effect of the choice of different moment sequences in the numerical solution is compared. Case of settling only (Case III).	89
Figure 3.2.8. Comparison of $N_a(t)$ and $N_n(t)$ for the polydisperse case. Effect of the choice of different moment sequences in the numerical solution is compared. Case of combined diffusion and gravitational settling (Case I).....	89
Figure 3.3.1. Schematic illustrating the first order, two parameter smoke detector model.	98
Figure 3.3.2. Geometry and computational grid. Flow direction is shown and the boundaries are labeled and referred to in Table 1.....	100
Figure 3.3.3. Schematic of the light scattering arrangement.	105
Figure 3.3.4 (a) X- and Z- velocity vector components at the plane of symmetry at $Y = 0.0$, (vector lengths are equal and do not show the magnitude). (b) Z- velocity component at the plane of symmetry at $Y = 0.0$	115
Figure 3.3.5. Plots of X-Y velocity vectors at the four different horizontal planes at $Z = 0.0\text{m}$, $Z = 0.025\text{m}$, $Z = 0.05\text{m}$ and $Z = 0.075\text{m}$. Z-velocity contours are also shown.	116
Figure 3.3.6. Variation of volume fraction with distance at the mid height of the cavity for various times. Volume fraction of the free stream is 10^{-9}	117
Figure 3.3.7. Variation of normalized intensity with distance at the mid height of the cavity for various times. Volume fraction of the free stream is 10^{-9}	119

Figure 3.3.8. Variation of scattered power at the circumference of the cavity with angle at mid-height for different times. Volume fraction of the free stream is 10^{-9}	120
Figure 3.3.9. Comparison of the angular scattering computed using 2-point, 3-point and 4-point quadrature approximations. Differences are too small for the three profiles to be distinguishable.	120
Figure 3.3.10. Log-log plot showing the variation of the detector activation time with velocity at the inlet. Comparison of the results obtained using the light scattering calculation (equation 3.3.18) and the detector response function (equation 3.3.19) for different choices of the threshold power, P'_{cr}	124
Figure 3.3.11. Log-log plot showing the variation of the detector activation time with smoke volume fraction at the inlet. Comparison of the results obtained using the light scattering calculation (equation 3.3.18) and the detector response function (equation 3.3.19) for different choices of the threshold power, P'_{cr}	124
Figure 3.3.12. Plot of the averaged and normalized volume fraction with time for different velocities to evaluate the mixing time scale parameter τ	126
Figure 3.3.13. Log-log plot showing the variation of the detector activation time (calculated using equation 3.3.18) with smoke volume fraction at the inlet, free stream velocity is 0.1m/s and 1m/s. Also shown are the best fits of the data to equation 3.3.21 obtained from the simple model (equation 3.3.3).	127
Figure 3.3.14. Plot of the activation time with logarithm of the volume fraction for different values of the geometric mean radius and the geometric standard deviation. The free stream velocity is 0.1 m/s.	128
Figure 4.1.1. Schematic illustrating the fire heat release rate (S) and the smoke layer height (Z) for a compartment fire.	134
Figure 4.1.2. Schematic of the propagation of statistical uncertainty problem as applied to a design fire application.	136
Figure 4.1.3. Schematic illustrating the sampling procedure used in the quadrature method of moments and the procedure for getting the CDF. Note that the schematic	

shows three quadrature points and three weights which would correspond to six known moments.....	139
Figure 4.1.4. Generalized beta probability density functions (PDFs) used for the fire heat release rates.....	141
Figure 4.1.5. Cumulative distribution functions (CDFs) corresponding to the PDFs in Figure 4.1.4.....	142
Figure 4.1.6. (Left) Compartment geometry for the ASET and CFAST (without window) models. (Right) Compartment geometry for the CFAST model with a window.....	144
Figure 4.1.7. Comparison of the ASET and CFAST model results for the smoke layer height with experimental data reported in Hurley (2003).....	148
Figure 4.1.9. CDFs corresponding to the PDFs in figure 4.1.8.	151
Figure 4.1.11. CDFs corresponding to the PDFs in figure 4.1.10.	152
Figure 4.1.12. PDFs of the smoke layer height at a critical time $t_{cr} = 120s$ obtained from Monte Carlo Simulations using the CFAST model with a horizontal vent (window) shown in figure 4.1.7. I, II, III, IV correspond to the different heat release rate PDFs in figure 4.1.4.....	152
Figure 4.1.13. CDFs corresponding to the PDFs in figure 4.1.12.	153
Figure 4.1.14. Study of the convergence of the skewness with increasing number of quadrature points. Results of using different moment sequences are shown.	155
Figure 4.1.15. Study of the convergence of the kurtosis with increasing number of quadrature points. Results of using different moment sequences are shown.	155
Figure 4.1.16. Reconstructed CDF using the Generalized Lambda Distribution (GLD) compared with CDF obtained from Monte Carlo simulations for the ASET model.....	156
Figure 4.1.17. Reconstructed CDF using the GLD compared with the CDF obtained from Monte Carlo Simulations using the CFAST model, with and without a window. The CDFs obtained using the ASET model is also shown. PDF I is used for the heat release rate PDF.	156
Figure 4.2.1. Schematic of a partially stirred reactor showing the fuel and oxidizer inlet and products outlet.....	164

Figure 4.2.2. Plot showing the mean and variance of the mixture fraction for the case of slower mixing, $\frac{\tau_{mix}}{\tau_{res}} = 1$. Convergence of Monte Carlo solutions can be seen.....	173
Figure 4.2.3. Plot showing the mean and variance of the mixture fraction for the case of faster mixing, $\frac{\tau_{mix}}{\tau_{res}} = 0.1$. Variances are lower due to faster mixing.	173
Figure 4.2.4 Scatter plot showing the distribution of mixture fraction (Z) and reaction progress variable (Y) at the stationary state. Dashed line shows the equilibrium state, circles slower mixing and triangles faster mixing.	175
Figure 4.2.5 Species means for the slower mixing case of $\tau_{res} = 0.1, \tau_{mix} = 0.1$. Only stationary state values are shown for the 3 point quadrature results.....	175
Figure 4.2.6 Species variances for the slower mixing case of $\tau_{res} = 0.1, \tau_{mix} = 0.1$. Only stationary state values are shown for the 3 point quadrature results.....	176
Figure 4.2.7 Species means for the faster mixing case of $\tau_{res} = 0.1, \tau_{mix} = 0.01$. Only stationary state values are shown for the 3 point quadrature results.....	176
Figure 4.2.8 Species variances for the faster mixing case of $\tau_{res} = 0.1, \tau_{mix} = 0.01$. Only stationary state values are shown for the 3 point quadrature results.....	177
Figure 4.2.9. Histogram that summarizes the total relative errors in the species means and variances. (ERR_1 and ERR_2 are as defined in the text. Z, Y Principal Dimension indicates that the mixture fraction (Z), reaction progress variable (Y) respectively are used as the principal dimension in SGLO.) Case of slower mixing $\tau_{res} = 0.1, \tau_{mix} = 0.1$	181
Figure 4.2.10. Same histogram as in figure 4.2.8 for the case of faster mixing ($\tau_{res} = 0.1, \tau_{mix} = 0.01$).	182
Figure 4.2.11. Scatter plot showing distribution of the mixture fraction and two reaction progress variables at the stationary state. Dash-dot lines correspond to equilibrium, unfilled triangles (Δ) the fast mixing case ($\tau_{res} = 0.1, \tau_{mix} = 0.01$) and filled circles the slow mixing case($\tau_{res} = 0.1, \tau_{mix} = 0.1$).	184

Figure 4.2.12. Species means for the faster mixing case of $\tau_{res} = 0.1, \tau_{mix} = 0.01$, 2 step chemistry model. Only stationary state values are shown for the 3 point quadrature results.	185
Figure 4.2.13. Species variances for the faster mixing case of $\tau_{res} = 0.1, \tau_{mix} = 0.01$, 2 step chemistry model. Only stationary state values are shown for the 3 point quadrature results.	185
Figure 4.2.14. Species means for the slower mixing case of $\tau_{res} = 0.1, \tau_{mix} = 0.1$, 2 step chemistry model. Only stationary state values are shown for the 3 point quadrature results.	186
Figure 4.2.15. Species variances for the slower mixing case of $\tau_{res} = 0.1, \tau_{mix} = 0.1$, 2 step chemistry model. Only stationary state values are shown for the 3 point quadrature results.	186
Figure 4.2.15. Histogram that summarizes the total relative errors in the species means and variances. (ERR_1 and ERR_2 are as defined in the text. Z, Y Principal Dimension indicates that the mixture fraction (Z), reaction progress variable (Y) respectively are used as the principal dimension in SGLO.) The two columns indicated as “Without Mean CO error” is the total relative error neglecting the mean CO mass fraction error. Case of slower mixing $\tau_{res} = 0.1, \tau_{mix} = 0.1$	187

Chapter 1: Introduction and Scope.

The subject matter of this dissertation involves the simulation of population balance equations using moment methods. Before delving into the technical details, I shall provide a brief introduction to population balance equations and some of the literature on this subject. I shall try to provide a context in which the contributions of the research work presented here can be evaluated. I briefly discuss the goals and motivations and the organization of the dissertation. In subsequent chapters the issues raised here will be dealt with in more detail.

1.1 OVERVIEW OF POPULATION BALANCE EQUATIONS.

Population balance modeling is a term used by chemical engineers studying particulate phenomena. The earliest example of a population balance equation (PBE) is the Boltzmann equation. The classical Boltzmann equation is an equation that describes the dynamics of a collection of molecules that move along rectilinear trajectories and collide as hard spheres. Furthermore, the Boltzmann equation was the first equation that dealt with the evolution of a probability density function (PDF). In the physics and mathematics literature this equation is called a kinetic equation. While I shall not discuss the many mathematical and physical subtleties of the Boltzmann equation, I remark that population balance equations are far more general than the Boltzmann equation. As an example, PBEs for aerosols generally deal with a collection of particles that are much larger than molecules and that undergo Brownian motion. Further when the particles collide, they may stick and they may also break apart if subjected to shear forces. These

equations are very useful for studying a variety of particulate processes involving aerosols, micro-emulsions, biological cells, bubbles, crystals, mists etc. Due to the universal nature of population balance modeling, the discussion of population balance equations appears in the textbooks across different disciplines. Randolph and Larson (1988) discuss its application to crystallization processes. Hidy and Brock (1970) and Friedlander (2000) discuss applications of the PBE to aerosol processes. For aerosols this equation is called the general dynamic equation (GDE). The text by Van Kampen (1992) explains the deep physical ideas behind these equations. Ramkrishna (2000) discusses some of the mathematical issues in the derivation of PBEs and also deals with some applications to chemical and biochemical processes. The mathematical literature is heavily dominated by the study of the Boltzmann equation (e.g. Cercignani (1990); Villani (2002)). While the general theory and numerical analysis of the closely related stochastic differential equations is available (Kloeden and Platen (1992), Carmona and Rozovskii (1998)), to the best of the author's knowledge, a systematic mathematical study of the population balance equation is not very widely known. In the opinion of this author, there is a far greater amount of literature that deals with the physical justification and derivations of the PBE than with the mathematical structure and properties of solutions.

Population balance equations essentially keep track of the dynamics and interactions of a population of particles. It will be seen in some applications that one can also deal with a population of abstract or notional particles whose presence or absence at a point in space denotes the occurrence or non-occurrence of an event. Hence the presence of a type of particle could indicate a particular event and the fraction of such

particles would indicate the probability of occurrence of the event at a particular point in space at an instant in time. In this work I shall deal with problems involving both real particles (such as aerosols) and notional particles (as used in simulations of turbulent combustion using PDF methods or for simulating the propagation of statistical uncertainty). The equations for both real and notional particles will be the same, only the modeling aspects and interpretation of the results will differ. As the PBE involves the solution of the evolution of either a univariate or multivariate PDF, its complexity is greater than other partial differential equations. As will be seen later, these equations are often defined in a higher dimensional space called a phase space. In the simplest example of aerosol particles, the phase space consists of the external coordinates, the physical space, and internal coordinates, such as the size (volume) of the particle. If the particle requires extra morphological or thermodynamic variables to describe its state, one would have to deal with multivariate PDFs. The importance of multivariate PDFs and the complexities of simulating Population Balance Equations involving multivariate PDFs have been discussed in numerous sources (e.g. Marchisio and Fox (2005)).

1.2 OVERVIEW OF COMPUTATIONAL APPROACHES TO SOLUTIONS OF PBEs.

Due to various applications of PBEs to different branches of science and engineering, the development of computationally efficient solutions to PBEs is very a important technological goal. Due to the integro-differential nature of PBEs and the high-dimensional domains, different solution techniques are used. Again due to the universal applications, researchers in different disciplines have developed different techniques. Different solution techniques enjoy different levels of popularity in different fields. For

instance, in aerosol science sectional methods are widely used. In this case the solution for the number density function is desired. The number density function defines the distribution of particles according to their volume or radius. In the sectional methods the volume-space is divided into different sections and equations are solved for the particles belonging to each discrete size bin (Gelbard et al. (1980)). MAEROS (Gelbard and Seinfeld (1980)) is a widely used code that implements the sectional method for solving the aerosol general dynamic equation. There is a widely held belief that sectional methods are computationally intractable for many emerging aerosol applications with the present computer hardware and software (Rosner et al. (2003)). This is especially true if the aerosol population is coupled to the flow field. For instance for large scale industrial production of nanoparticles, one needs to scale up of the synthesis techniques that chemists have devised in the laboratory. Industrial reactors normally involve complex turbulent flow fields and large spatial domains and one requires accurate and efficient simulation tools to study these processes. In these cases, it is expected that sectional methods will not be computationally feasible. Moment methods are generally regarded to be computationally tractable for these applications (McGraw and Wright (2003)). Moment methods reduce the complexity of population balance equations by simulating only the moments of the density functions. However, since a finite number of moments do not contain all the statistical information contained in the number density function, there are many applications where moment methods are not readily applicable. The method of moments with distribution reconstruction (e.g. Diemer and Olson (2002a; b)) is an approach that has been applied to problems where the details of the underlying distribution are desired. Another difficulty is that the moment equations are generally

unclosed and some moment closure hypothesis is necessary. The nature of the closure problem for chemical engineering applications was first recognized by Hulburt and Katz (1964). In recent years, several moment closure schemes have been developed. For instance, in the aerosol literature there is the Method of Moments with Interpolative Closure (MOMIC) pioneered by Frenklach (Frenklach and Harris (1987), Frenklach (2002)). There is the presumed lognormal method (Pratsinis (1988)) in which the form of the number density function is presumed to be lognormal. The evolution of the number density function is then completely determined by solving the evolution equations for three of its moments. The Quadrature Method of Moments (QMOM), (McGraw(1997)) and the Direct Quadrature Method of Moments (DQMOM) (Fox (2003)) are moment methods that use a computational closure scheme based on Gaussian integration. The investigation of the accuracy of these closure approximations is one of the major objectives of this dissertation and these methods will be discussed in greater detail in the next section. Additional literature on QMOM and DQMOM will also be discussed in the next section.

In turbulent mixing and combustion applications, the PDF transport equation is solved. This equation can be considered to be a population balance equation involving notional (or conditional) particles. The ideas behind this equation are discussed in Chapters 2 and 4. It is interesting to note that while moment methods and sectional methods are widely used in the aerosol community, researchers in turbulent combustion who use the PDF transport equation mainly use Monte Carlo methods for solution (Pope (1985)). It should be mentioned that turbulent combustion problems can be defined in a very high dimensional space and that Monte Carlo simulations may be the most natural

method for simulation. However, one can investigate the performance of moment methods in this high dimensional setting. There is very little work in the literature dealing with moment methods for the PDF transport equation. For very simple univariate problems, there is a presumed beta PDF method (Branley and Jones (2001)) that is analogous to the lognormal method discussed earlier. However the presumed PDF approach cannot be easily generalized to multivariate cases and can only be applied to limited applications. Various moment methods called conditional moment closure (CMC) methods are widely used for engineering calculations (Klimenko and Bilger (1999)). These methods normally use physical or empirical moment closure assumptions and have several limitations as discussed in Raman and Fox (2004).

1.3 SCOPE OF THE WORK.

The preceding discussion is meant to provide a quick overview of population balance equations and the literature dealing with its solution without discussing the physical and mathematical ideas. I wish to convey the fact that population balance modeling appears under different guises in different disciplines and each discipline has developed its own terminology and favorite computational solution techniques. The objective of this work is to investigate moment methods, in particular the Quadrature Method of Moments (QMOM) and the Direct Quadrature Method of Moments (DQMOM). The general question that I am interested in is can these methods overcome some of the limitations associated with moment methods and provide reasonably accurate solutions that can be used for engineering purposes. Some of the difficulties inherent in moment methods are inaccurate moment closure, unreasonable presumptions on the PDF

etc. Further, by considering applications from different disciplines, I wish to demonstrate the feasibility of using moment methods for a wide range of applications. While these are my primary goals, I will also consider the mathematical theory and computational requirements for implementing these methods. The theory should allow the reader to decide whether moment methods are the best suited for any particular application and also provide the finer details of implementation. The studies conducted in this work are expected to lead to a greater understanding of the potential benefits and limitations of moment methods for solving general population balance equations.

1.3.1 OUTLINE OF THE DISSERTATION

The remainder of the dissertation is organized as follows. In chapter two I present the population balance equations and briefly discuss the physical ideas leading to it. To emphasize the universality of the method, I do not confine myself to any particular application but instead develop the full population balance equation in all its generality. Then I shall examine concrete examples for applications in aerosol science and turbulent reacting flows. I develop the equation for the moments and discuss the Quadrature Method of Moments (QMOM) and the Direct Quadrature Method of Moments (DQMOM). I will present the mathematical theory for the univariate QMOM and I will discuss the difficulties in extending this theory to the multivariate case. I will then discuss a computational method for simulating general multivariate PBEs using the DQMOM. I will present an algorithm for ordering the moments of a multivariate PDF that can be used in DQMOM to evolve a set of moments. I raise several important issues in the solution of QMOM and DQMOM equations which I will discuss in more detail in

chapters 3 and 4. In chapter 3, applications of QMOM and DQMOM to univariate population balance equations will be presented. Applications are drawn from problems in aerosol science. I consider classic problems such as the simulation of nucleation, surface growth and agglomeration in well stirred reactors and nozzles. To investigate the coupling of population balance models with CFD codes, I will consider the simulation of the smoke entry and light scattering in a smoke detector. I also study problems involving size dependent aerosol diffusion and settling. These problems are meant to be a computational validation of QMOM and DQMOM for univariate population balance equations. Hence I compare solutions obtained using moment methods with other solution techniques. Results of these validation studies provide useful guidelines on practical application of QMOM/DQMOM. In chapter 4, I discuss problems other than aerosols for which population balance concepts can be used. I consider the problem of propagation of statistical uncertainty that can be used in design problems involving uncertainty in some design parameters. I study an application to fire safety design. I also look at the problem of turbulent mixing and combustion in a partially stirred reactor. In this example, I test the theory of multivariate DQMOM that is discussed in chapter 2. Again I look at the accuracy of the DQMOM solutions by comparing with solutions obtained using Monte Carlo simulations. In chapter 5, I summarize the main findings and propose directions for future investigations.

Chapter 2: Population Balance Equations and the Quadrature Method of Moments.

2.1 THE GENERAL POPULATION BALANCE EQUATION.

The population balance equation is essentially the mathematical statement of the law of conservation of particles in phase space (Randolph and Larsson (1988)). The $D+3$ dimensional phase space consists of external and internal coordinates, namely the three dimensions of space (x_1, x_2, x_3) and D generalized coordinates $(\xi_1, \xi_2, \dots, \xi_D)$. It is useful to distinguish between these two coordinates both from the physical and mathematical points of view due to the different boundary conditions used. The population of particles is characterized by a number density function, $n(\xi_1, \xi_2, \dots, \xi_D; x_1, x_2, x_3, t)$ defined over the internal variables at each point in physical space and time. For instance, for the case of spherical aerosol particles only one internal coordinate, say its radius, r , is necessary to characterize each particle. Then to describe the aerosol population completely, one would need a solution for $n(r; x_1, x_2, x_3, t)$. Applying the law of conservation of particles one can show that the number density n evolves in phase space as follows (Ramkrishna (2000)):

$$\frac{Dn}{Dt} = \frac{\partial n}{\partial t} + \frac{\partial U_i n}{\partial x_i} + \frac{\partial G_i n}{\partial \xi_i} = B - D. \quad 2.1$$

Figure 2.1 shows the schematic. U_i is the velocity of each particle in the direction x_i . G_i is the generalized convection velocity in the direction of each internal coordinate ξ_i . B and D are the birth and death terms. These terms account for the discontinuous changes in the state of the particles due to random collision or breakage events. These

stochastic processes are usually modeled as Poisson processes (Feller (1967)) and involve integrals over the internal coordinates. Hence these terms are responsible for the integro-differential nature of these equations. Even though the birth and death terms represent stochastic processes, the equation for the evolution of the number density function is deterministic.

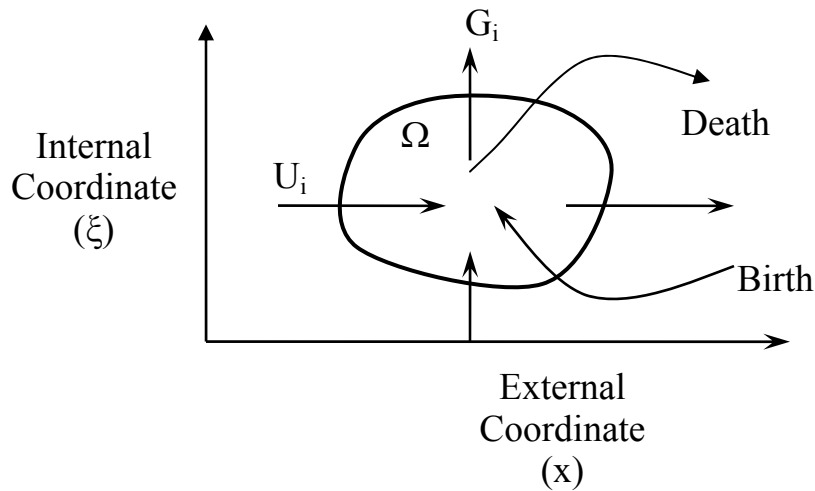


Figure 2.1. Control volume in phase space used to derive the population balance equation.

2.2 EXAMPLES OF POPULATION BALANCE EQUATIONS USED IN THIS STUDY.

To orient the reader, I now show specific examples of population balance equations that I have used in this study.

2.2.1 Aerosol dynamics.

In the context of aerosol dynamics, the population balance equation is usually referred to as the general dynamic equation (GDE). For most aerosol applications, each aerosol particle is uniquely characterized by its volume (v) or radius (r). The population

balance equation is then written for the number density function $n(v; x_1, x_2, x_3, t)$. From equation 2.1, using $\xi_1 = v$ and $\xi_i = 0, i = 2, 3, 4, \dots$ one gets

$$\frac{Dn}{Dt} = \frac{\partial n}{\partial t} + \frac{\partial U_i n}{\partial x_i} + \frac{\partial G_1 n}{\partial v} = \frac{\partial}{\partial x_i} \left(D \frac{\partial n}{\partial x_i} \right) + B - D, \quad 2.2$$

where U_i is the resultant particle velocity in the direction x_i . This velocity is the resultant of the fluid velocity $U_{f,i}$, gravitational settling velocity $C_{s,i}$, the thermophoretic velocity $C_{T,i}$ and other migration velocities. There is also a stochastic component of the particle velocity due to Brownian motion. The transport due to the fluctuating velocity is modeled using the gradient diffusion model and gives rise to the first term on the right hand side. Specific expressions for the particle diffusivity, D , settling velocity C_s and thermophoretic velocity C_T are provided in Friedlander (2000). These terms usually depend on the volume of the particle as will be shown later. G_1 is the convection velocity in volume space. It models the surface growth of particles due to condensation of supersaturated vapor on its surface. It may also account for the evaporation of particles or other processes that cause continuous changes in the volume of the particle. The birth and death terms account for the aggregation processes in which particles of two different sizes randomly collide and stick to each other giving birth to a new particle:

$$B - D = \frac{1}{2} \int_0^v \beta(\tilde{v}, v - \tilde{v}) n(\tilde{v}) n(v - \tilde{v}) d\tilde{v} - \int_0^\infty \beta(v, \tilde{v}) n(v) n(\tilde{v}) d\tilde{v}. \quad 2.3$$

The first term represents the ‘‘birth’’ of a particle of volume v . Such an event can occur when particles of volumes \tilde{v} and $v - \tilde{v}$ collide. $\beta(\tilde{v}, v - \tilde{v})$ is the aggregation kernel and

gives the rate of aggregation of two randomly chosen particles of volumes \tilde{v} and $v - \tilde{v}$. In the mathematical terminology of Poisson-Markov processes, β is also referred to as a transition probability. The second term represents the “death” of a particle of volume v . Such an event occurs when the particle of volume v randomly collides and sticks to any other particle in the population. Other birth and death processes are possible in systems that allow particle breakage. The complete GDE can then be written as:

$$\frac{\partial n}{\partial t} + \frac{\partial U_{f_i} n}{\partial x_i} + \frac{\partial C_{s_i} n}{\partial x_i} + \frac{\partial C_{T_i} n}{\partial x_i} + \frac{\partial G_1 n}{\partial v} = \frac{\partial}{\partial x_i} \left(D \frac{\partial n}{\partial x_i} \right) + \frac{1}{2} \int_0^v \beta(\tilde{v}, v - \tilde{v}) n(\tilde{v}) n(v - \tilde{v}) d\tilde{v} - \int_0^\infty \beta(v, \tilde{v}) n(v) n(\tilde{v}) d\tilde{v}. \quad 2.4$$

The left hand side represents the time rate of change of the aerosol population, convection by the fluid, transport in phase space (external and internal coordinates) due to gravitational settling, thermophoresis and surface growth respectively. The right hand side represents the change of the aerosol number density due to diffusion (Brownian motion) and the aggregation processes. A schematic of the various aerosol processes that cause changes in the number density is shown in figure 2.2. The GDE for aerosols does not account for the inertial forces acting on a particle which cause acceleration of the particle. In the population balance approach, the particle velocities can be considered to be additional internal coordinates and the inertial forces on the particles cause changes in the number density in velocity space. In the physics literature, these processes are called Rayleigh processes (Van Kampen (1992)). Such effects need to be considered when modeling aerosol impaction but are relatively unimportant for small sized particles for which inertial effects are negligible. Alternatively, one may interpret the GDE as

representing aerosol dynamics in which the particle velocity relaxation time is much faster than other time scales and therefore the particle velocity is always the velocity of the fluid or the steady terminal velocity (in case of settling). In this study, I do not consider problems involving inertial effects.

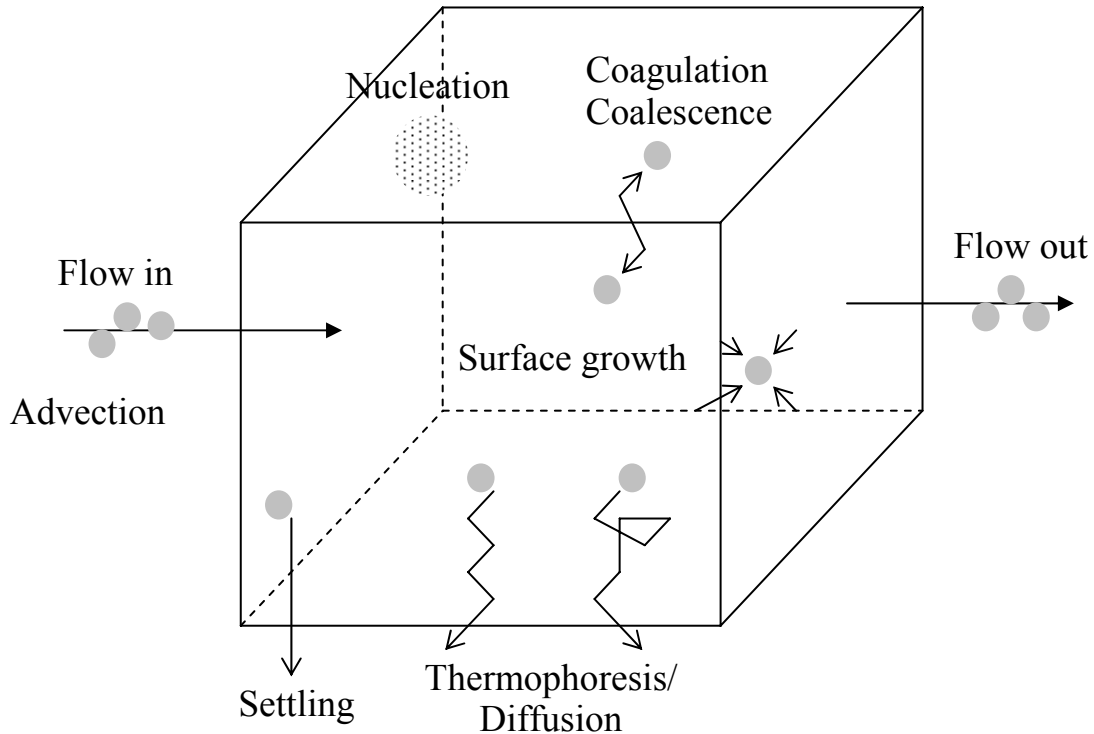


Figure 2.2. Schematic of various aerosol processes at the micro-scale.

2.2.2 PDF transport equation.

The PDF transport equation uses different mathematical ideas in its derivation and is more abstract than the GDE. The problem I am generally interested in is to predict the time evolution of various chemical species in a turbulent flow field. In this problem, the stochasticity arises due to the following reasons. Consider the evolution of a single

species concentration in a turbulent flow field. Figure 2.3 shows how the species concentration may evolve in velocity-composition state space $(\vec{V}, \vec{\psi})$ due to chemical reaction and turbulent transport. There are fluctuations in the species concentrations down to the Kolmogorov scales because the species are transported in a turbulent flow field. Furthermore, due to the chaotic nature of the turbulent flow field, the trajectory in the state space can be completely different for different evolutions from the same initial conditions. In stochastic theory, the species concentrations are random fields (Adler (1981)). The reason for the non-uniqueness of trajectories can also be seen from the following equations describing the velocity and species evolution (Fox (2003)):

$$\frac{DU_i}{Dt} = \frac{\partial U_i}{\partial t} + U_j \frac{\partial U_i}{\partial x_j} = \nu \frac{\partial^2 U_i}{\partial x_j \partial x_j} - \frac{1}{\rho} \frac{\partial p}{\partial x_i} + g_i, \quad 2.5$$

$$\frac{D\phi_i}{Dt} = \frac{\partial \phi_i}{\partial t} + U_j \frac{\partial \phi_i}{\partial x_j} = \Gamma_i \frac{\partial^2 \phi_i}{\partial x_j \partial x_j} + S_i(\vec{\phi}). \quad 2.6$$

Equation 2.5 describing the evolution of the velocity fields is the familiar Navier-Stokes equations for incompressible flow (Panton (2005)). In equation 2.6, ϕ_i is the mass fraction or concentration of the i th species. The terms on the left hand side represent the transport due to the turbulent flow field. The first term on the right hand side is due to molecular diffusion and the second is due to the chemical reaction. $S_i(\vec{\phi})$ is called the chemical source term. Since ϕ_i , U_j and all derivatives of ϕ_i are random fields, the dynamics given by equations 2.5 and 2.6 cannot be completely determined from the information contained in the state space $(\vec{V}, \vec{\psi})$ that provides single-point statistics of ϕ_i and U_j . This is due to the presence of the molecular diffusion and pressure gradient

terms which involve derivatives of the velocity and species fields. All derivatives require two-point statistics that is not contained in the space $(\vec{V}, \vec{\psi})$. One can include the derivatives of ϕ_i in the state space but the equations that define the evolution of these terms would contain other derivatives that are not in the state space. The lack of statistical closure in these equations is well known (Pope (1985)). Due to these reasons, it is customary to define notional particles (Pope (1985)) or conditional particles (Baldyga and Bourne (1999)) in the velocity-composition space. These particles have deterministic trajectories whose evolution is governed by the conditionally expected values of the other random fields. For instance, the population balance equation for notional particles in the velocity-composition state space is as follows (Pope (1985)):

$$\frac{\partial f_{\vec{U}, \vec{\phi}}}{\partial t} + V_i \frac{\partial f_{\vec{U}, \vec{\phi}}}{\partial x_i} + \frac{\partial}{\partial V_i} \left(\langle A_i | \vec{V}, \vec{\psi} \rangle f_{\vec{U}, \vec{\phi}} \right) + \frac{\partial}{\partial \psi_i} \left(\langle \Theta_i | \vec{V}, \vec{\psi} \rangle f_{\vec{U}, \vec{\phi}} \right) = 0. \quad 2.7$$

$f_{\vec{U}, \vec{\phi}}(\vec{V}, \vec{\psi}; \vec{x}, t)$ is the 1-point joint velocity composition PDF. In the literature it is customary to denote the random fields by \vec{U} and $\vec{\phi}$. \vec{U} and $\vec{\phi}$ contain the full multi-point, multi-time statistics of the velocity and scalar fields while their single point realization is denoted by \vec{V} and $\vec{\psi}$. Also the conditional expectations are determined from equations 2.5 and 2.6 as:

$$\begin{aligned} \langle A_i | \vec{V}, \vec{\psi} \rangle &= \left\langle v \frac{\partial^2 U_i}{\partial x_j \partial x_j} - \frac{1}{\rho} \frac{\partial p}{\partial x_i} + g_i \middle| \vec{V}, \vec{\psi} \right\rangle \\ \langle \Theta_i | \vec{V}, \vec{\psi} \rangle &= \left\langle \Gamma_i \frac{\partial^2 \phi_i}{\partial x_j \partial x_j} + S_i(\vec{\phi}) \middle| \vec{V}, \vec{\psi} \right\rangle \end{aligned} \quad 2.8$$

One can see that A_i and Θ_i in equation 2.8 denote the terms appearing on the right hand side of equations 2.5 and 2.6 respectively. For instance, A_i can be interpreted as the acceleration of the fluid. For this reason, the conditional expectation involving A_i is also called the conditional acceleration. In principle, it is possible to compute the conditional expectations in equation 2.7. One can employ DNS simulations to obtain the full multipoint statistics of the velocity fields and species profiles and then extract the conditional expectations (Fox (2003)). In that case one would have to deal with the unresolved mathematical issues concerning the existence, uniqueness and regularity of the Navier-Stokes equations (Frisch (1995)). However attempts have been made to estimate the conditional expectations for Large Eddy Simulations of turbulence as reported in Langford and Moser (1999). In the combustion literature, various models have been used for the conditional expectations. All models involve stochastic processes that mimic the evolution of the conditional particles in velocity-composition space. These models require inputs from experimental measurements of different statistical quantities in turbulent reacting flows. Details behind some of the models used for the conditional expectations are outlined in the review article by Pope (1985).

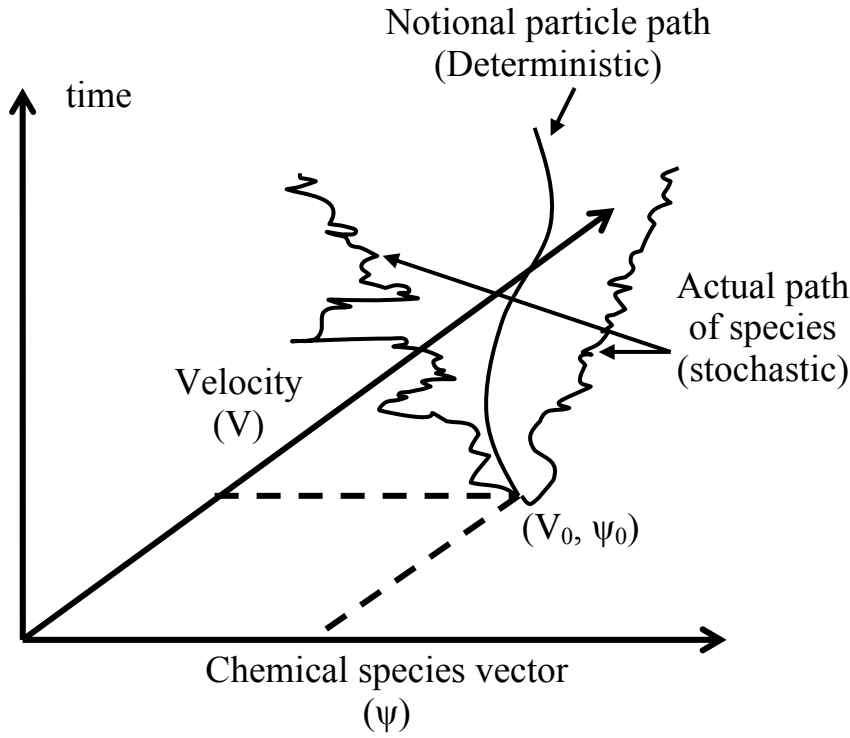


Figure 2.3. Schematic showing actual paths of the species and the path of notional (or conditional) particles in velocity composition space for a turbulent reacting flow.

In this work, I shall deal with the joint scalar PDF transport equations. This equation is obtained by integrating over the velocity space to obtain the marginal PDF, $f_{\bar{\psi}}(\bar{\psi}; \bar{x}, t)$, called the joint scalar PDF. The equation for the evolution of $f_{\bar{\psi}}(\bar{\psi}; \bar{x}, t)$ is as follows (Fox (2003)):

$$\frac{\partial f_{\bar{\psi}}}{\partial t} + \langle U_i \rangle \frac{\partial f_{\bar{\psi}}}{\partial x_i} = \frac{\partial}{\partial x_i} \left[\Gamma_T \frac{\partial}{\partial x_i} f_{\bar{\psi}} \right] - \frac{\partial}{\partial \psi_i} \left[\left\langle \Gamma_i \frac{\partial^2 \phi_i}{\partial x_j \partial x_j} \middle| \bar{\psi} \right\rangle f_{\bar{\psi}} \right] - \frac{\partial}{\partial \psi_i} [S_i(\bar{\psi}) f_{\bar{\psi}}]. \quad 2.9$$

In equation 2.9, the second term on the left hand side represents the transport of the scalar due to the mean flow field $\langle U_i \rangle$. The first term in the right hand side represents transport

due to turbulent velocity fluctuations that is modeled as a gradient diffusion process with turbulent diffusivity Γ_T . The second term represents molecular diffusion which is modeled as the convection in $\vec{\psi}$ space due to the conditional expectation term. As mentioned earlier, the conditional expectation term needs to be modeled. The type of population balance equation that results depends on the model used for this term. A widely used model is the Interaction by Exchange with the Mean (IEM) described in Dopazo (1975). This is a deterministic mixing model which states that particles relax to the mean composition at a certain rate determined by a mixing time τ_{mix} :

$$\left\langle \Gamma_i \frac{\partial^2 \phi_i}{\partial x_j \partial x_j} \middle| \vec{\psi} \right\rangle = \left(\frac{\langle \phi_i \rangle - \psi_i}{\tau_{mix}} \right). \quad 2.10$$

The PBE resulting from this model is a simple transport equation without the integral birth and death terms. Other models for the conditional expectation also exist. A popular model is the Coalescence-Dispersion model (C-D) model first described in Curl (1963). In this model the transport in composition space is modeled as a Poisson jump process which consists of random interactions between the notional particles. The PBE obtained from this model consists of birth and death terms that involve integrals (e.g. Pope (1985)). A Fokker Planck model can also be used for the transport term. In this case the PBE will contain a diffusion term in $\vec{\psi}$ space. Details of this model can be found in Fox (2003). In this study I shall not investigate the C-D and Fokker-Planck models. While modeling of conditional expectations is the most important aspect of PDF transport methods in reacting flows (Fox (2003)), I shall only be concerned with the solution of the equations using known models. The last term on the right hand side of 2.8 represents the

chemical reactions. Since the chemical source term involves only the single-point statistical information that is provided by the single point joint scalar PDF $f_{\bar{\phi}}(\bar{\psi}; \bar{x}, t)$, closure models are not required for this term.

Despite the different physical and mathematical ideas used for derivation of the PDF transport equation, the resulting form is identical to Population Balance Equations. While some of the concepts presented here can aid the reader in understanding the physics behind PDF transport methods used in turbulent reacting flows, the discussion is not meant to be a rigorous introduction to the subject. Further details can be found in Pope (1985), Baldyga and Bourne (1999) and Fox (2003).

2.3 MOMENT METHODS FOR THE GENERAL POPULATION BALANCE EQUATION.

The solution to the general population balance equation defined in section 2.1 involves several difficulties. These difficulties are due to the high dimensional nature and the integro-differential structure of the equations. The moment methods aim to simplify PBEs using certain averages called the moments of the density function. By the use of moments, one can convert the PBE into partial differential equations in three dimensional space. Furthermore, the form of the resulting equations is compatible with commercial PDE solvers that have been widely used in engineering.

The moments of a general multivariate PDF, $n(\xi_1, \xi_2, \dots, \xi_D)$, defined over D internal coordinates, $\xi_i; i = 1..D$, is defined as follows:

$$M_{l_1, l_2, \dots, l_d} = \int_{\Omega} \xi_1^{l_1} \xi_2^{l_2} \dots \xi_D^{l_D} n(\xi_1, \xi_2, \dots, \xi_D) d\xi_1 d\xi_2 \dots d\xi_D. \quad 2.11$$

Ω is the domain in the D -dimensional space over which the PDF is defined. Each moment is indexed by a D -tuple of numbers $\{l\} = (l_1, l_2, \dots, l_D)$ and is a scalar quantity that depends only on the spatial and temporal variables. In the method of moments, one first derives equations for the evolution of the moments. Let us consider the abstract PBE given in equation 2.1. To get the evolution equation for the moment indexed by $\{l\} = (l_1, l_2, \dots, l_D)$, I multiply equation 2.1 by $\xi_1^{l_1} \xi_2^{l_2} \dots \xi_D^{l_D}$ and integrate over the domain Ω :

$$\begin{aligned} \frac{\partial M_{\{l\}}}{\partial t} + \frac{\partial \int_{\Omega} \prod_{k=1}^D \xi_k^{l_k} U_i(\vec{\xi}; \vec{x}, t) n(\vec{\xi}; \vec{x}, t) d\vec{\xi}}{\partial x_i} - \sum_{i=1}^D \int_{\Omega} l_i G_i(\vec{\xi}; \vec{x}, t) \xi_i^{l_i-1} \prod_{\substack{k=1 \\ k \neq i}}^D \xi_k^{l_k} n(\vec{\xi}; \vec{x}, t) d\vec{\xi} \\ + \sum_{i=1}^D I_{\{l\}}(\xi_i) \Big|_{\partial\Omega_i} = \int_{\Omega} \left(\prod_{k=1}^D \xi_k^{l_k} \right) (B(\vec{\xi}; \vec{x}, t) - D(\vec{\xi}; \vec{x}, t)) d\vec{\xi}. \end{aligned} \quad 2.12$$

In the above equation, the third term in the left hand side represents the term involving the convection in internal coordinates. The fourth term accounts for the source terms on boundaries of the internal coordinates. Specifically, it is given by:

$$\sum_{i=1}^D I_{\{l\}}(\xi_i) \Big|_{\partial\Omega} = \left[\xi_i^{l_i} \int_{\Omega_{\xi_i}} \left(\prod_{\substack{k=1 \\ k \neq i}}^D \xi_k^{l_k} \right) G_i(\vec{\xi}; \vec{x}, t) n(\vec{\xi}; \vec{x}, t) d\vec{\xi} \right]_{\partial\Omega}. \quad 2.13$$

$\partial\Omega$ is the boundary of the domain Ω . The third and fourth terms are obtained using integration by parts on the $\frac{\partial G_i n}{\partial \xi_i}$ term in equation 2.1. For the general PBE, the source terms in the boundary appear as boundary conditions over the internal coordinates and are not explicitly present in the equation. However, for the moment equations, which

involves integration over the domain of the internal coordinates, the boundary growth terms explicitly appear in the equations.

At this point, the presentation of the moment equation is very abstract. It is still possible to observe that while the dimensions have been reduced to the three spatial variables by integrating over all internal coordinates, the equation is still integro-differential. All moment methods must prescribe some techniques for evaluating the integrals over the (unknown) number density function $n(\vec{\xi}; \vec{x}, t)$. In subsequent sections, I shall discuss the quadrature method of moments that enable the evaluation of these integrals. Now I consider specific concrete examples of the moment equations for the aerosol General Dynamic Equation and the PDF transport equation defined earlier.

2.4 CONCRETE EXAMPLES OF MOMENT EQUATIONS.

To orient the reader, I consider concrete examples of the moment equations for the aerosol General Dynamic Equation (GDE) and the PDF transport equation defined earlier.

2.4.1 Moment equation for the aerosol General Dynamic Equation.

In this case, the number density depends only on the volume, v , of the particle. The k -th moment is defined as:

$$M_k(\vec{x}, t) = \int_0^{\infty} v^k n(v; \vec{x}, t) dv. \quad 2.14$$

The moments provide important information about the aerosol population. Integral moments (i.e. where k in equation 2.14 is an integer) such as M_0 and M_1 give the total number of particles and the total volume respectively. Fractional moments M_k where k

is a fraction are also used. For instance the moment $M_{2/3}$ is proportional to the total surface area of the aerosol particle population. The moment equation is obtained by multiplying equation 2.4 by the volume variable v and integrating over the range of v :

$$\begin{aligned} \frac{\partial M_k}{\partial t} + \frac{\partial}{\partial x_i} \int_0^\infty [U_{f_i}(v; \vec{x}, t) + C_{S_i}(v) + C_{T_i}(v)] v^k n(v; \vec{x}, t) dv \\ - k \int_0^\infty v^{k-1} G(v) n(v; \vec{x}, t) dv + I(v = v_c) v_c^m \\ = \frac{\partial}{\partial x_i} \int_0^\infty D(v) \frac{\partial n(v; \vec{x}, t)}{\partial x_i} v^k dv + \frac{1}{2} \int_0^\infty \int_0^\infty [(u+v)^k - u^k - v^k] \beta(u, v) n(u; \vec{x}, t) n(v; \vec{x}, t) dudv \end{aligned} \quad .2.15$$

Equation 2.15 is just a special case of equation 2.12 with $D = 1$, $\xi_1 = v$ and $\xi_i = 0; i = 2..D$. The domain Ω is $[0, \infty]$. The second term on the left hand side represents the advection in physical space due to fluid velocity, particle settling velocity and thermophoretic velocity respectively. The third term represents the particle surface growth due to condensation or evaporation. The fourth term is a source term that accounts for the appearance of new particles of critical volume v_c by nucleation from the gas phase. It can be considered to be a growth term at the boundary of v -space since v_c is the smallest possible particle size. $I(v = v_c)$ is the nucleation rate that gives the rate at which new particles of critical size v_c form from the supersaturated gas phase. Details of the derivation of $I(v = v_c)$ for aerosols can be found in Friedlander (2000). The first term on the right hand side models the diffusion due to Brownian motion while the second term models coagulation. To write coagulation in this form requires the

assumption that the coagulation kernel $\beta(u, v)$ is symmetric (Williams and Loyalka (1991)). This assumption is valid for most kernels used for Brownian, gravitational, laminar shear and turbulent coagulation. Equation 2.15 cannot be solved without a procedure that can enable the evaluation of the integrals over the unknown number density function $n(v; \bar{x}, t)$. Details of how these expressions can be written in terms of the moments are discussed later.

2.4.2 Moment equations for the PDF transport equation.

In general, the PDF transport equation deals with the evolution of a multivariate PDF. Therefore one has to deal with the general moment equation outlined in section 2.3. Let $f_\phi(\vec{\psi}; \bar{x}, t)$ be the joint scalar PDF of D chemical species denoted by $\vec{\psi} = (\psi_1, \psi_2, \dots, \psi_D)$. As mentioned earlier multivariate moments are characterized by a D -tuple of numbers $\{l\} = (l_1, l_2, \dots, l_D)$:

$$M_{\{l\}}(\bar{x}, t) = \int_{\Omega} \psi_1^{l_1} \psi_2^{l_2} \dots \psi_D^{l_D} n(\vec{\psi}; \bar{x}, t) d\psi_1 d\psi_2 \dots d\psi_D. \quad 2.16$$

In this case I have taken $\xi_i = \psi_i; i = 1..D$. The domain, Ω , is the allowable space of species concentrations (i.e. where the constraint of element conservation is satisfied) (Fox(2003)). If the ψ_i s are the species mass fractions then $\Omega \subset [0,1]^D$. Multivariate moments carry a lot of useful statistical information about the system. For the case $D = 2$, some of the useful moments are as follows.

First order moments; $M_{(1,0)}, M_{(0,1)}$: Mean of species ψ_1 and species ψ_2 respectively.

Second order moments; $M_{(2,0)}$, $M_{(0,2)}$, $M_{(1,1)}$: These moments are related to the variance of ψ_1 , variance of ψ_2 and covariance between ψ_1 , ψ_2 respectively.

Other higher order moments may also be essential in describing the system.

The moment equations for the PDF transport equation described in equation 2.9 are:

$$\begin{aligned} \frac{\partial M_{\{l\}}}{\partial t} + \langle U_i \rangle \frac{\partial M_{\{l\}}}{\partial x_i} &= \frac{\partial}{\partial x_i} \left[\Gamma_T \frac{\partial}{\partial x_i} M_{\{l\}} \right] \\ - \sum_{i=1}^D \int_{\Omega} l_i \left[\frac{(\langle \psi_i \rangle - \psi_i)}{\tau_{mix}} + S_i(\vec{\psi}) \right] &\psi_i^{l_i-1} \left(\prod_{\substack{k=1 \\ k \neq i}}^D \psi_k^{l_k} \right) f_{\phi}(\vec{\psi}; \vec{x}, t) d\vec{\psi}. \end{aligned} \quad 2.17$$

The IEM model defined in equation 2.10 has been used to model the molecular mixing term. The second term on the right hand side involves both the molecular mixing term (modeled by the IEM) and the chemical source term. The chemical source term cannot be written in terms of the moments $M_{\{l\}}$ and therefore a moment closure scheme needs to be prescribed. The success of moment methods depends on the accuracy with which the chemical source term can be represented. However at the level of the PDF transport equation, the chemical source term appears in closed form (Pope (1985)) since it depends only on the one-point statistics described by $f_{\phi}(\vec{\psi}; \vec{x}, t)$.

2.5 CLOSURE OF MOMENT EQUATIONS USING NUMERICAL QUADRATURE.

In general, the equations for the moments are unclosed. This can be seen in the examples of moment equations given in the previous section. For the moment equations describing aerosol dynamics (equation 2.15), the closure issues arise due to volume dependent aerosol velocity, diffusion, surface growth terms, and coagulation. The

solution of the moment equations involves the determination of the space time evolution of a selected set of moments. The number density function is unknown and hence integrals over the unknown density function must be approximated in terms of the moments that are being solved. The closure issues in the PDF transport equation are also the same. Closure problems arise because the information contained in a PDF cannot be obtained from a finite set of moments. Population balance equations generally describe the dynamics of a probability density function (PDF) and in most cases the dynamics depends on the complete information contained in the PDF. Mathematically, the closure problem arises due to specific functional forms of the integrands in equation 2.15 that prevent writing the integrals in terms of known moments. One of the major objectives of this dissertation is to investigate the moment closure using quadrature based moment methods. These methods develop numerical integration formulae based on Gaussian quadrature to evaluate the unclosed integrals. The principal techniques are called the Quadrature Method of Moments (McGraw (1997)) and the Direct Quadrature Method of Moments (Fox (2003)). I shall first discuss the theory of QMOM and then explain some of the difficulties and limitations of QMOM. Then I shall discuss DQMOM and also consider some of the limitations. For both methods, I shall explain the computational issues that need to be investigated. These investigations are reported in chapters 3 and 4.

2.6 QUADRATURE METHOD OF MOMENTS (QMOM).

The Quadrature Method of Moments was first proposed by McGraw (1997) for the modeling of condensation in clouds. In recent years a number of papers have appeared in the literature dealing with the application of QMOM to all aspects of aerosol

dynamics. I refer the reader to Terry, McGraw and Rangel (2001), Upadhyay and Ezekoye (2003, 2005, 2006), Marchisio et al. (2003), Marchisio, Vigil and Fox (2003a, 2003b), McGraw and Wright (2003).

In QMOM, the moment equations are closed by using the Gaussian quadrature technique to evaluate unclosed integrals. The task is to evaluate integrals as accurately as possible when the number density function is unknown but a certain number of its moments are known.

Gaussian quadrature is a very old and established method for integrating a function. It is remarkable that the integration is extremely accurate with only a few quadrature points (Lanczos (1956)). Gaussian integration involves weighted integration of a function. For instance, let us take one of the unclosed terms appearing in the moment equation for the aerosol GDE:

$$\bar{I} = \int_0^{\infty} v^{k-1} G(v) n(v) dv. \quad 2.18$$

Here $v^{k-1}G(v)$ is the function to be integrated with respect to an unknown weight function $n(v)$. In the univariate case, a number (say N_Q) of points are chosen in the interval (here $[0, \infty]$) and the function (here $v^{k-1}G(v)$) is evaluated at the N_Q points known as the quadrature points. An interpolating polynomial of order N_Q-1 is passed through the discrete values of the function evaluated at the quadrature points. The integration scheme is then called N_Q -point Gaussian quadrature or simply N_Q -point quadrature. The fundamental theorem of Gaussian quadrature states that the quadrature points correspond to the roots of a polynomial that is orthogonal with respect to the

weight function $n(v)$ (Lanczos (1956)). Given a certain number of these quadrature points, Gaussian quadrature assures that the error in evaluating the integral would be the minimum. Standard Gaussian quadrature deals with integrals where the weight is of a known form (Press et. al. (1992)) and the orthogonal polynomials tend to be of a known type. In my case, the weight function is unknown but a certain number of its moments are known. The theory of Gaussian quadrature with unknown weight function and the derivation of orthogonal polynomials is provided in Appendix A. The problem then reduces to determination of the quadrature points and weights from which one can compute the integral using the following quadrature formula.

$$\hat{I} \approx \sum_{i=1}^{N_Q} \hat{v}_i^{k-1} G(\hat{v}_i) W_i \quad 2.19$$

In the above formula \hat{v}_i are the quadrature points and W_i are called the quadrature weights. By the theory of Gaussian quadrature, the N_Q -point quadrature formula is exact for all polynomials up to degree $2N_Q-1$.

The quadrature points are obtained as roots of orthogonal polynomials as outlined in Appendix A. The weights W_i are the weighted integrals of the Lagrange interpolating polynomials P_i passing through the quadrature points:

$$P_i(v) = \frac{\prod_{\substack{j=1 \\ j \neq i}}^{N_Q} (v - \hat{v}_j)}{\prod_{\substack{j=1 \\ j \neq i}}^{N_Q} (\hat{v}_i - \hat{v}_j)}, \quad 2.20$$

and

$$W_i = \int_0^{\infty} P_i(v)n(v)dv = a_0 M_{N_Q-1} + a_1 M_{N_Q-2} + \dots + a_{N_Q-1} M_0. \quad 2.21$$

where $(a_0, a_1, \dots, a_{N_Q-1})$ are the coefficients that depend only on $2N_Q$ moments of $n(v)$.

Both the N_Q quadrature points and weights are functions of only the $2N_Q$ moments of $n(v)$ and therefore the quadrature formula can be constructed from the moments of $n(v)$ alone. The method of computing the quadrature points and weights by finding roots of polynomials is convenient only for 1-, 2- or 3- point quadrature. This is due to the availability of formulae that give the roots of linear, quadratic and cubic polynomials. For higher order quadrature schemes, it is more convenient to use an alternative procedure described by Gordon (1968). This is because the numerical problem of finding roots of higher-order polynomials is “notoriously ill-conditioned” (Gordon (1968)). In this method the quadrature points and weights are the eigenvalues and eigenvectors of a tri-diagonal matrix. The Product-Difference algorithm presented in Gordon (1968) and also in Appendix A can be used to construct the elements of the tri-diagonal matrix. Computationally efficient algorithms exist for the computation of eigenvalues and eigenvectors of a tri-diagonal matrix (e.g. the GAUCOF subroutine in Press et al. (1992)).

I now take a simple example to illustrate the technique. Let us try to evaluate an unclosed integral $M_{0.5} = \int_0^{\infty} v^{0.5} n(v)dv$ when only the four moments M_0, M_1, M_2 and M_4

are known. Figure 2.4 is a graphical representation of the Gaussian integration scheme. In this example, the two quadrature points ($N_Q = 2$) are calculated from the four given

moments using the technique described in Appendix A. The function to be integrated, $v^{0.5}$, is approximated using a linear function (a polynomial of order N_Q-1). Figure 2.4 shows that while the linear approximation of $v^{0.5}$ is not good in a global sense, the approximation is fairly accurate in a localized region where the weight function $n(v)$ peaks. An intuitive idea behind the quadrature based integration is to determine the discrete points in regions where the weight or measure is concentrated and then attempt to approximate the function accurately in those local regions. In Table 2.1, I present the error in the integration and I see that the integration is fairly accurate with a very small number (2 or 3) of quadrature points.

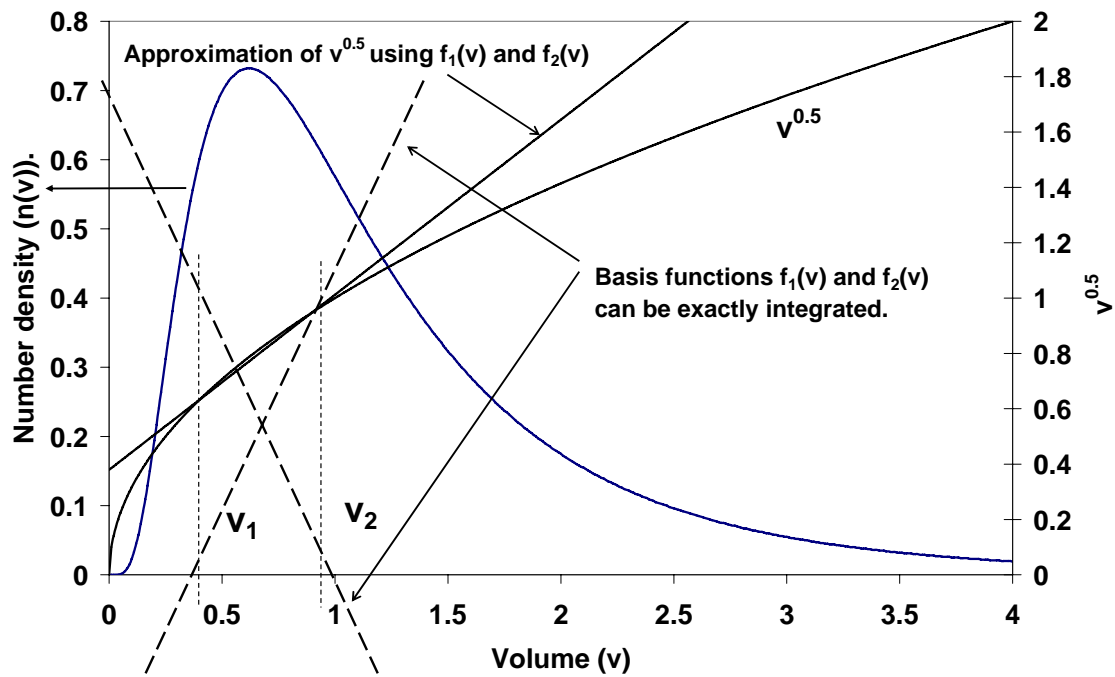


Figure 2.4. Integration of the function $v^{0.5}$ with respect to the lognormal density function using 2-point Gaussian quadrature.

No. of quadrature Points (N_Q)	$M_{0.5}$ Integration	Approximating Function	% Error
1	1.0420	Constant	2.1
2	1.0229	Linear	0.21
3	1.0213	Quadratic	0.06
Exact	1.0207		

Table 2.1. Table showing the errors involved in computing the moment $M_{0.5}$ using $2N_Q+1$ integer moments for different numbers of quadrature points N_Q .

By using the Gaussian quadrature formula, a closed set of moment equations can be obtained. For the moment equation for the aerosol GDE, the closed set of moment equations are:

$$\begin{aligned} \frac{\partial M_k}{\partial t} + \frac{\partial}{\partial x_i} \sum_{n=1}^{N_Q} [U_{fi}(\hat{v}_n; \bar{x}, t) + C_{Si}(\hat{v}_n) + C_{Ti}(\hat{v}_n)] \hat{v}_n^k W_n - k \sum_{n=1}^{N_Q} \hat{v}_n^{k-1} G(\hat{v}_n) + I(v = v_c) v_c^m \\ = D \frac{\partial^2 M_k}{\partial x_i^2} + \frac{1}{2} \sum_{m=1}^{N_Q} \sum_{n=1}^{N_Q} [(\hat{v}_m + \hat{v}_n)^k - \hat{v}_m^k - \hat{v}_n^k] \beta(\hat{v}_m, \hat{v}_n) W_m W_n. \end{aligned} \quad 2.22$$

Equation 2.22 must be solved for a set of $2N_Q$ moments such as $\{M_0, M_1, \dots, M_{2N_Q-1}\}$. Then equation 2.22 represents a set of coupled nonlinear partial differential equations. The quadrature points and weights depend on the moments alone and they are the same for each integral; summation in equation 2.22. They can be evaluated from the moment set at time t , to get the moments at time $t + \Delta t$. The solution to these equations will be discussed in subsequent chapters. The solution is subject to some constraints in the moments. From the theory of moments, (Wall (1948)), the moments always have to satisfy the following determinant conditions:

$$\begin{aligned} M_0 = 1, \\ \left| \begin{array}{c} M_0 M_1 \dots M_{P-1} \\ M_1 M_2 \dots M_P \\ \vdots \\ M_{P-1} M_P \dots M_{2P-2} \end{array} \right| > 0, \end{aligned} \quad 2.23$$

$$\left| \begin{array}{c} M_1 M_2 \dots M_P \\ M_2 M_3 \dots M_{P+1} \\ \vdots \\ M_P M_{P+1} \dots M_{2P-1} \end{array} \right| > 0. \quad 2.24$$

where P is the number of quadrature points used and the moments are normalized so that $M_0 = 1$.

Condition (2.23) is the requirement that the size distribution is strictly positive while condition (2.24) is the requirement that the size distribution be defined for positive values only. Moment methods involving approximate closure suffer sometimes in that these conditions can be violated. This is a serious problem because if these conditions fail even once during the computations the method will fail. It is hard to determine if conditions (2.23) and (2.24) are satisfied at each instant during the computations. For problems involving combined nucleation, surface growth and coagulation, it is difficult to maintain conditions (2.23) and (2.24) for 2-point and 3-point quadrature calculations. For a problem in which particles of a single critical size form by nucleation, only the 1-point quadrature can be used to start the simulations. This is because for the 2-point and 3-point calculations, the size distribution must be at least bi- and tri-disperse respectively. In other pathological cases, it is easier to first calculate the roots and check if they are real, positive and distinct. If they are, then the above conditions are automatically satisfied. If not the roots must be recalculated using a smaller number of moments, that is the order of the quadrature method must be reduced. This method works because for one point quadrature the condition reduces to $M_0, M_1 > 0$. This is easy to satisfy for almost any physical problem. Using this artifice does not seem to have a major effect on the accuracy of the method. From my experience, higher order quadrature methods fail when the size distribution is narrow and for these problems lower order quadrature methods are sufficiently accurate.

2.6.1 Limitations of QMOM.

(a) *Extension to the multivariate case.*

Apart from the need to satisfy constraints on the moments, QMOM suffers from a number of drawbacks. A major limitation of QMOM is the difficulty in extending it to the multivariate case. Some attempts have been made in extending QMOM as reported in Wright et al. (2001), Rosner and Pykkonen (2002) and Yoon and McGraw (2004a; 2004b). The last work describes a technique called the PCA-QMOM in which principal component analysis is used to determine the principal axes along which the quadrature points and weights can be assigned using the univariate quadrature theory. All the above methods use ad hoc assumptions to circumvent the difficulty of finding suitable cubature formulae in higher dimensions. The mathematical issues regarding this problem are discussed in Dunkl and Xu (2001) and Xu (1994). In complete analogy to the univariate (one-dimensional) case, the cubature points are the common roots of a set of multivariate polynomials. A cubature formula in D -dimensions, analogous to equation 2.19 would be:

$$I = \sum_{k=1}^{N_Q} f(\hat{x}_k) W_k, \quad 2.25$$

where the k -th quadrature point \hat{x}_k is now a point in D dimensions. For 2.25 to be a Gaussian cubature formula (i.e. to be exact for all multivariate polynomials of total degree $2n-1$), requires $N_Q = \frac{(n-1+D)!}{(n-1)!D!}$ distinct quadrature points \hat{x}_k . Xu (1994)

mentions that one can very rarely find a Gaussian cubature formula in the multivariate case. One must therefore look for less optimal cubature formulae. There are lots of difficulties if one attempts to generalize the procedure outlined in Appendix A for the

one-dimensional case. For example, the three term relation for the successive orthogonal multivariate polynomials will involve matrices. In the D -dimensional case, the quadrature points and weights will be the joint eigenvalues and eigenvectors of a set of D block tri-diagonal matrices (Xu (1994)). The construction of these block tri-diagonal matrices would require a number of matrix operations that can be quite complex. The author is not aware of any algorithm analogous to the Product-Difference algorithm that can create the block tri-diagonal matrices from the multivariate moments. A thorough discussion of multivariate cubature using linear algebraic techniques can be found in Dunkl and Xu (2001). A challenge remains in developing a computationally efficient algorithm for implementing some of the ideas explained in Dunkl and Xu (2001).

(b) Awkward form for the transport terms in physical space.

From the computational point of view, a practical difficulty arises in the case of the transport terms in physical space. For example, for the moment evolution equations (equation 2.22), the flux in physical space (second term in the left hand side) is a flux of the quadrature sum. In practice, one would like to solve the moment equations using some CFD solver which solves convection diffusion equations of the form

$$\frac{\partial M_k}{\partial t} + \frac{\partial}{\partial x_i} U_i M_k = \dots, \text{ i.e. the convective flux should involve the same evolved moment}$$

M_k . Since the quadrature sum depends on a set of moments, it is not possible to write the equation in the above form for QMOM. This practical difficulty can be avoided using the Direct Quadrature Method of Moments that will be discussed next.

2.7 THE DIRECT QUADRATURE METHOD OF MOMENTS (DQMOM).

As noted earlier, two of the difficulties associated with QMOM are the inability to easily extend it to multivariate problems and the practical difficulty in implementing it on commercial CFD codes. DQMOM is an extension of QMOM. Some of the ideas behind DQMOM can be found in Piskunov and Golubev (2002) and Piskunov et al. (2002). The JMT method proposed in McGraw and Wright (2003) is very similar to DQMOM. However a self-contained theory and an algorithm for computational implementation is provided by Fox and coworkers (Fox (2003), Fan et al. (2004) and Marchisio and Fox (2005)).

In order to demonstrate the applicability to a general multivariate problem, I present the implementation of DQMOM to the case of the PDF transport equation. In DQMOM, a coarse grained representation of the underlying probability density function is defined as:

$$f_\phi(\vec{\psi}, \vec{x}, t) = \sum_{n=1}^{N_\phi} W_n(\vec{x}, t) \prod_{k=1}^D \delta(\psi_k - \hat{\psi}_{k,n}(\vec{x}, t)). \quad 2.26$$

Here $W_n(\vec{x}, t)$ is the n -th quadrature weight, $\hat{\psi}_{k,n}(\vec{x}, t)$ is the n -th quadrature point for the k -th internal variable, $\delta(\psi_k - \hat{\psi}_{k,n}(\vec{x}, t))$ is the Dirac delta function centered at $\hat{\psi}_{k,n}(\vec{x}, t)$.

A representation of the underlying PDF in this form ensures that a finite number of moments are exactly reproduced. Unlike in QMOM, evolution equations are solved for the quadrature weights $W_n(\vec{x}, t)$ and the product of quadrature weights and points $S_{k,n}(\vec{x}, t) = W_n(\vec{x}, t) \hat{\psi}_{k,n}(\vec{x}, t)$. These equations can be obtained by substituting equation 2.26 into the PDF transport equation (equation 2.9). This procedure is detailed in Fox

(2003) and involves using properties of the Dirac Delta function. While this is a valid approach, an alternative method of deriving the equations without using generalized functions, would be to directly use the moment equations. The multivariate moments are:

$$M_{\{l\}} = \sum_{n=1}^{N_Q} W_n(\vec{x}, t) \prod_{k=1}^D \hat{\psi}_k^{l_k}(\vec{x}, t). \quad 2.27$$

In equation 2.27, $\{l\} = \{l_1, l_2, \dots, l_D\}$ denotes a D -tuple of numbers that index a multivariate moment. Substitution of this form into the moment equation (equation 2.17) and algebraic manipulations yields the following set of linear equations:

$$\begin{aligned} \sum_{n=1}^{N_Q} \left[\left(1 - \sum_{k=1}^D l_k \right) \prod_{k=1}^d \hat{\psi}_{k,n}^{l_k} \right] a_n + \sum_{n=1}^{N_Q} \sum_{m=1}^D \left[\frac{\partial}{\partial \hat{\psi}_{m,n}} \left(\prod_{k=1}^d \hat{\psi}_{k,n}^{l_k} \right) \right] b_{m,n} \\ = \sum_{n=1}^{N_Q} \sum_{m=1}^D \sum_{o=1}^D \frac{\partial^2}{\partial \hat{\psi}_{m,n} \partial \hat{\psi}_{o,n}} \left(\prod_{k=1}^D \hat{\psi}_{k,n}^{l_k} \right) W_n \Gamma \left[\frac{\partial \hat{\psi}_{m,n}}{\partial x_i} \frac{\partial \hat{\psi}_{o,n}}{\partial x_i} \right]. \end{aligned} \quad 2.28$$

The above set of equations can be written in a matrix form:

$$A\alpha = \beta. \quad 2.29$$

A is an $N_Q(D+1) \times N_Q(D+1)$ matrix. Each row is indexed by a D -tuple $\{l\}$:

$$A_{\{l\}} = \left[\underbrace{\left(1 - \sum_{k=1}^D l_k \right) \prod_{k=1}^d \hat{\psi}_{k,n}^{l_k}; n=1, \dots, N_Q}_{(N_Q)cols} ; \underbrace{\frac{\partial}{\partial \hat{\psi}_{m,n}} \left(\prod_{k=1}^d \hat{\psi}_{k,n}^{l_k} \right); n=1, \dots, N_Q, m=1, \dots, D}_{(N_Q \times d)cols} \right]. \quad 2.30$$

Hence each row is determined by a moment $M_{\{l\}}$ and to construct A requires a set of $N_Q(D+1)$ moments. For this example, β consists of the $N_Q(D+1)$ terms defined in the right hand side of equation 2.28. The vector α of length $N_Q(D+1)$ consists of the

source terms $(a_n; n = 1, \dots, N_\rho; b_{m,n}; n = 1, \dots, N_\rho; m = 1, \dots, D)$. These terms are the source terms for the following equations for $W_n(\vec{x}, t)$ and $S_{m,n}(\vec{x}, t)$:

$$\begin{aligned} \frac{\partial W_n}{\partial t} + \langle U_i \rangle \frac{\partial W_n}{\partial x_i} - \frac{\partial}{\partial x_i} \Gamma \frac{\partial W_n}{\partial x_i} &= a_n; n = 1, \dots, N_\rho \\ \frac{\partial S_{m,n}}{\partial t} + \langle U_i \rangle \frac{\partial S_{m,n}}{\partial x_i} - \frac{\partial}{\partial x_i} \Gamma \frac{\partial S_{m,n}}{\partial x_i} &= b_{m,n}^*; n = 1, \dots, N_\rho; m = 1, \dots, D \end{aligned} \quad , \quad 2.31$$

with $b_{m,n}^* = b_{m,n} - \left[\frac{(\langle \psi_m \rangle - \hat{\psi}_{m,n})}{\tau_{mix}} + S(\hat{\psi}_n) \right] W_n$. Equation 2.31 is a system of convection-

diffusion equations with source terms obtained by solving the system of linear equations defined in equations 2.28 or 2.29. The source terms a_n and $b_{m,n}$ are extra terms needed to ensure that the evolution of the quadrature points and weights is consistent with the evolution of the chosen set of $N_\rho(D+1)$ moments. The solution of 2.31 with suitable initial and boundary conditions provides the space-time dependent moments of the joint scalar PDF. A schematic that summarizes the DQMOM technique is outlined in Figure 2.5.

2.7.1 Computational issues regarding DQMOM.

From the previous section, I see that the DQMOM method involves the solution of convection-diffusion-reaction equations for a set of scalars. These equations can be easily implemented in any Computational Fluid Dynamics (CFD) code. To get the reaction source terms requires the solution of a system of $N_\rho(D+1)$ linear equations. For instance for a 3-D unsteady problem, one would have to solve the matrix equation at each grid point for each time step. This would be a computationally expensive procedure

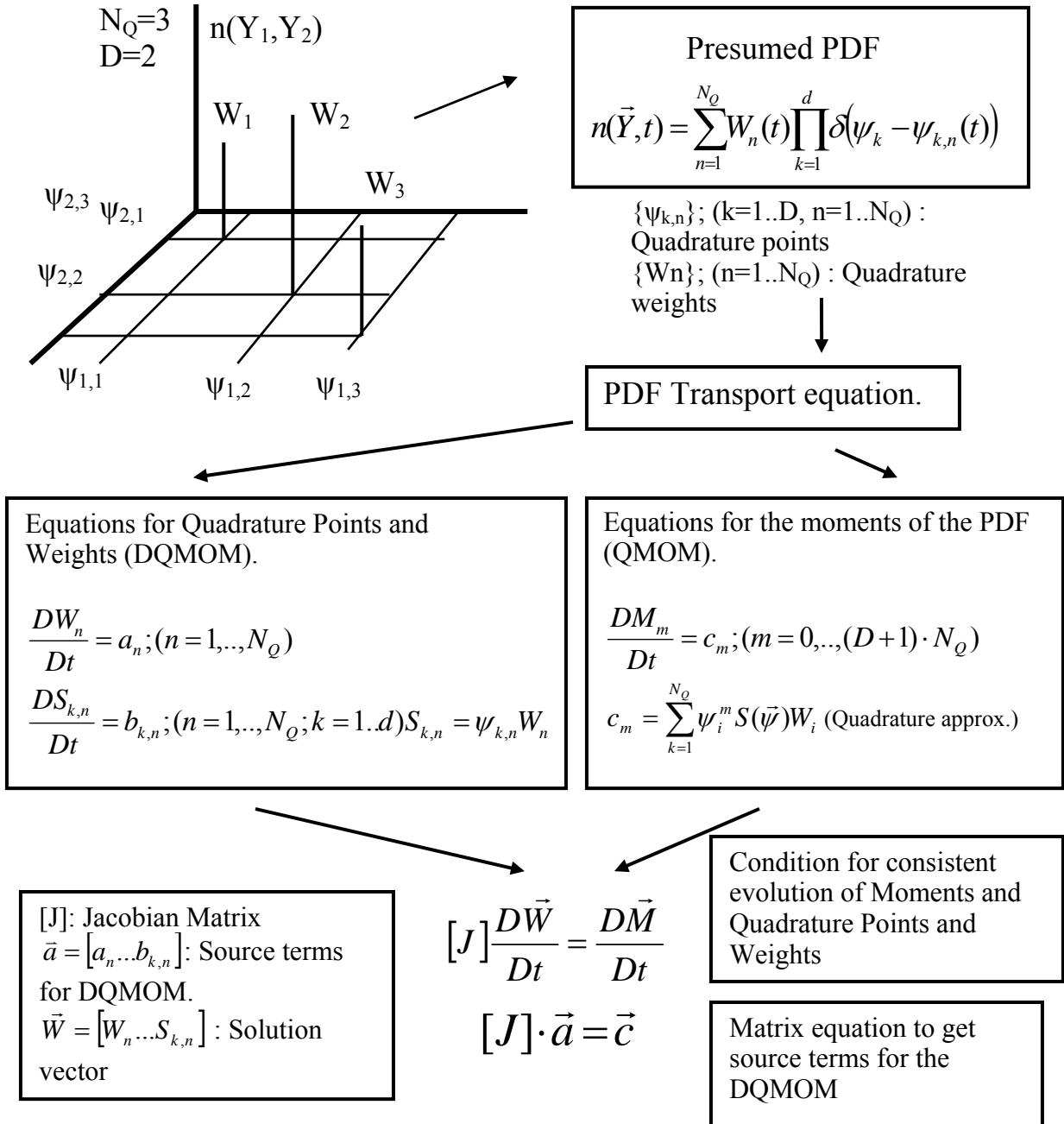


Figure 2.5. Schematic that shows the DQMOM procedure and the relation between QMOM and DQMOM.

if either N_Q or D is large and therefore this method appears to be best suited for low dimensional problems (small D) and where a small number of quadrature points (small N_Q) is sufficient for getting accurate results. A difficult problem arises due to the singularity of the matrix A defined in equation 2.29. It is well known that this matrix can be singular for some choices of moments. For instance, Fox (2003) gives the example of a bivariate problem ($D = 2$) with $N_Q = 2$ quadrature points. In this case the most natural choice of moments $M_{00}, M_{01}, M_{10}, M_{11}, M_{02}, M_{20}$, (i.e. the zeroth, first and second order moments) would give rise to a singular matrix A . Thus for these problems it is not possible to evolve this set of moments and if the particular application requires all these moments, then the number of quadrature points needs to be increased. In the following section, I shall discuss an algorithm that can construct a non-singular matrix A .

A practical advantage of DQMOM over QMOM is the expression for the flux and diffusion terms that makes it compatible with CFD solvers. In the example of the PDF transport equation, the convective and diffusive flux terms do not depend on the internal coordinates. In section 3, I shall discuss an aerosol problem of size dependent settling and diffusion that can be conveniently implemented using DQMOM.

2.7.2 Construction of a non-singular matrix.

In this section I describe an algorithm that may be used to construct the non-singular matrix A defined in equation 2.29. The matrix A can be interpreted as a Jacobian matrix that relates the changes in the quadrature points and weights to the changes in the moments:

$$\frac{D\vec{W}}{Dt} = [A]^{-1} \frac{D\vec{M}_{\{l\}}}{Dt}, \quad 2.32$$

where $\vec{W} = (W_1, \dots, W_{N_Q}, S_{1,1}, \dots, S_{D, N_Q})$, $\vec{M}_{\{l\}} = (M_{\{l\}1}, \dots, M_{\{l\}N_Q(D+1)})$ and each row of the matrix A defined in equation 2.29 is constructed from a moment $M_{\{l\}}$ indexed by a D -tuple $\{l\} = \{l_1, l_2, \dots, l_D\}$. Hence a specification of a set of moments is equivalent to the specification of a set of D -tuple of integers. The problem then is to choose a set of $N_Q(D+1)$ moments that can be used to obtain the $N_Q(D+1)$ rows of the matrix A with the restriction that the matrix be invertible.

Upadhyay and Ezekoye (2006) have demonstrated that the choice of moments may be dependent on the problem and that there may not be a universally optimal moment set. Hence to impose some order in the sequence of moments and at the same time to discard the moments that give rise to a singular matrix, I propose the method of Selective Graded Lexicographic Ordering (SGLO).

The graded lexicographic order is an ordering scheme for multivariate polynomials. It is clear that ordering a set of multivariate moments is equivalent to ordering a set of D -tuple of integers. Since any finite set of real numbers can be mapped to a set of integers, this method is valid for both integer and fractional moments. In this context I want to order multivariate moments of the form $M_{\{l\}} = M_{l_1, l_2, \dots, l_d}$. The definition of graded lexicographic order (GLEX) is as follows (e.g. Dunkl and Xu (2001)). Let

$l = (l_1, l_2, \dots, l_D)$ and $l^* = (l_1^*, l_2^*, \dots, l_D^*)$ be two D -tuples with $|l| = \sum_{i=1}^D l_i$. The moment M_l

precedes M_{l^*} in the ordering ($M_l \succ_{glex} M_{l^*}$) if (i) $|l| < |l^*|$ or (ii) in case $|l| = |l^*|$ then the

first non zero entry in the difference $l - l^*$ is positive. As an example take the three multivariate moments indexed by $M_{\{l\}} = M_{0,0,0}$, $M_{\{l^*\}} = M_{1,0,0}$ and $M_{\{l^{**}\}} = M_{0,1,0}$. Then by (i), $M_{\{l\}} \succ_{\text{glex}} M_{\{l^*\}}, M_{\{l^{**}\}}$ since $|l| < |l^*| = |l^{**}|$ and by (ii) $M_{\{l^*\}} \succ_{\text{glex}} M_{\{l^{**}\}}$ since $|l^*| = |l^{**}|$ but the first non-zero element in $l^* - l^{**} = (1,0,0) - (0,1,0) = (1,-1,0)$ is positive. So the GLEX ordering is $[M_{\{l\}}, M_{\{l^*\}}, M_{\{l^{**}\}}] = [M_{0,0,0}, M_{1,0,0}, M_{0,1,0}]$. This type of ordering ensures that the 0th order moment is tracked before all the 1st order moments. And all 1st order moments are tracked before the 2nd order moments (which provide information on pair correlations) and so on. However a strict ordering using this scheme is not possible because some moments cause the resulting matrix to be singular. Hence a selective ordering is necessary. In practice a set of D -tuples (ordered according to GLEX) is generated; then, as the matrix A is built up row by row, a singular value decomposition of the matrix is performed. If the condition number of the matrix becomes very large then the current row associated with a particular D -tuple is discarded and the next D -tuple in the order is chosen. This procedure, which I have called Selective Graded Lexicographic Ordering (SGLO), ensures that the matrix A in (1.7) is non-singular. As an example let us take the case $N_Q = 2, D = 3$ (tri-variate problem with two quadrature points). In this case, $N_Q \times (D + 1) = 8$ moments are required for the DQMOM. The set of eight valid moments obtained using SGLO is given by M_{m_1, m_2, m_3} with $(m_1, m_2, m_3) = (0,0,0), (1,0,0), (0,1,0), (0,0,1), (2,0,0), (1,1,0), (3,0,0)$. Note that it is not possible to track some of the second order moments such as $(0,1,1), (1,0,1), (0,0,2)$ etc. as inclusion of these moments would cause the Jacobian matrix A to be singular. If some of the moments carry essential

information for a particular application then they can be selected and the remaining moments can be ordered using SGLO. A graphical illustration of the Graded Lexicographic ordering method is shown in Figure 2.6. The ordering I have discussed is not the only possible ordering. However, it has several features that may be of use in moment methods. In most applications, the lower order moments may carry essential information and need to be tracked before higher order moments. This is ensured using GLEX ordering. Another feature is that it is possible to order the variables in terms of their importance in a problem. For example, in Figure 2.6, let us take the three coordinates to be associated with the variables (ψ_1, ψ_2, ψ_3) . Further let us suppose that ψ_1 is the principal variable, i.e. the most important variable for a particular application and for which one requires the most detailed statistics. Then GLEX ordering will ensure that a larger number of the higher order moments of ψ_1 are selected. While SGLO provides a systematic method of selecting valid moments and has many desirable features, I make no claim that it is a universally acceptable scheme. As we shall see, the optimal choice of moments does depend on the problem and may require trial and error to discover.

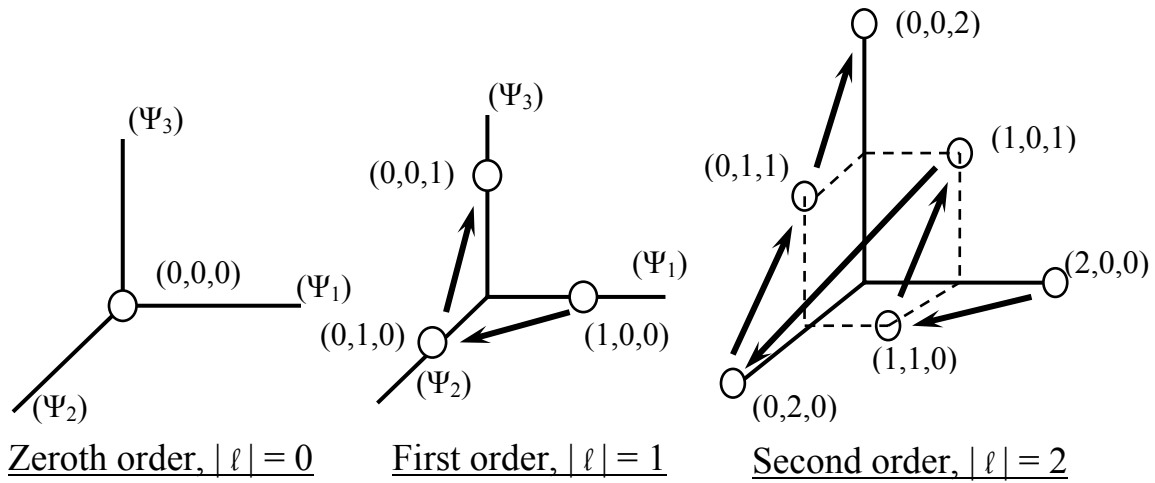


Figure 2.6. Example of the Graded Lexicographic (GLEX) Ordering for a set of trivariate moments. (Note that not all these moments can be used to create a non-singular Jacobian matrix A . Instead some moments need to be selectively discarded.)

2.8 RESOLUTION OF SOME ISSUES IN QMOM AND DQMOM.

After presenting the theory behind population balance equations, moment methods and QMOM/DQMOM techniques to solve the moment equations, I discuss the issues that I shall investigate in further detail. The resolution of some of these problematic issues is the major scientific contribution of this work.

(i) Application of QMOM to univariate population balance equations arising from aerosol dynamics.

In chapter 3, I apply the QMOM for a number of problems arising in aerosol science. In particular I shall investigate the use of QMOM in problems involving aerosol nucleation and surface growth. In this class of problems, one has an aerosol population that grows from a single-sized nucleated particle. In this method one does not have a well defined initial number density function to initiate the simulations. I shall discuss the

feasibility of adaptively changing the number of quadrature points during a simulation. Another important issue in aerosol dynamics is the simulation of size dependent aerosol transport. The transport of aerosol particles by settling and diffusion depends on the radius of each particle and hence each particle in the aerosol population is transported at different rates. This can lead to difficulties in the numerical solution due to dispersive fluxes. The QMOM equations involve awkward terms for the flux of particles in physical space. I shall demonstrate that DQMOM avoids these practical difficulties. By looking at a simple problem in which analytical solutions are available, I shall show that solutions depend on the set of moments that are chosen.

I then discuss the coupling of population balance equations to CFD codes. This is important from a technological point of view because population balance models need to be used to model aerosol dynamics in the presence of complex fluid flows in devices with complex geometries. I take the example of a simplified smoke detector model and simulate the smoke entry and light scattering processes. These examples are meant to illustrate the numerous practical problems that can be solved by using the theoretical concepts discussed in this chapter.

(ii) Application of DQMOM to multivariate population balance equations.

As discussed in this section, there are a number of unresolved issues in the implementation of DQMOM to multivariate population balance equations. In chapter 4, I shall investigate the application of DQMOM to a Partially Stirred Reactor. I shall determine the accuracy of the DQMOM solutions by comparing results with results obtained using Direct Monte Carlo simulations. In particular, I shall investigate the feasibility of the SGLO method for selection of moments and then try to provide some heuristic guidelines on the optimal choice of moments for reacting flow simulations.

Chapter 3: Applications of QMOM and DQMOM to aerosol dynamics simulation.

Having described the theory behind population balances and moment methods for its solution, I now turn to some of the applications. In this chapter, I present solutions of the population balance equation for aerosols (known in the literature as the aerosol general dynamic equation (GDE)). I first consider a well known computational problem in aerosol science of nucleation, surface growth and coagulation in a perfectly stirred reactor (Upadhyay and Ezekoye (2003)). I then look at a problem involving size dependent gravitational settling and diffusion of particles between infinite parallel plates (Upadhyay and Ezekoye (2005b)). One of the objectives of considering these theoretical problems is to validate the quadrature method of moments (QMOM) and compare its cost and accuracy with respect to other solution techniques. Finally as an engineering application, I present a simulation of smoke entry and light scattering in a photoelectric smoke detector (Upadhyay and Ezekoye (2005a)).

3.1 SIMULATING PARTICLE FORMATION AND GROWTH USING THE QUADRATURE METHOD OF MOMENTS.

3.1.1 Introduction and motivation.

Particles for many industrial applications are increasingly generated in the gas phase in aerosol reactors. There is then a need for obtaining a better understanding of the reactor parameters influencing generation of aerosol materials from the gas phase, especially the early stages of particle formation which involves nucleation and condensation of a low vapor pressure species. To study a complex process like particle formation and growth and to predict strategies for production of monodisperse particles

requires more than just intuition and trial and error. This is especially so because the final powder characteristics are sensitive to reactor conditions and processes occurring in extremely short time scales. Accurate mathematical models describing different phenomena that occur in widely different time scales are necessary. As mentioned in chapter 2, the aerosol general dynamic equation is a very general model for simulating a variety of aerosol processes. There are numerous techniques for solving the GDE. In this section I consider the quadrature method of moments (QMOM) for solution. As discussed earlier, QMOM is a technique for solving the moment equations of the GDE without presuming a standard size distribution function and is applicable for a very large class of surface growth laws and coagulation kernels.

The main focus in this section will be clarification of the applicability of reduced quadrature points in modeling multi-physics aerosol evolution. I examine two classical analyses of aerosol formation process using the quadrature method of moments. The first is the formation and growth of aerosols in an isothermal, constant pressure, constant reaction rate, spatially homogeneous batch reactor. Friedlander (1983) derived an exact solution involving only the moments of the size distribution. The assumptions made were that the nucleation phenomena can be modeled using the classical theory of nucleation, surface condensational growth occurs in the free molecular regime and that coagulation can be neglected. These assumptions help in closing the moment equations because the diffusion growth law in the free molecular regime is independent of the radius. Pratsinis (1988) further studied this problem, solving the moment equations using the lognormal model for the aerosol size distribution function. This enables investigation of growth laws that are more complex, for example ones in which a transition occurs from the free

molecular to the continuum transport regime. Most importantly, coagulation can be studied to see how it affects the size distribution of the particles. Pratsinis (1988) was able to show that the simple lognormal approximation gave the correct trends for various useful reactor performance indices like the total number concentration of particles, their volume averaged diameters, the polydispersity index (a measure of the width of the distribution) etc. The QMOM is suitable for solving this problem without the assumption of lognormality and hence is expected to be more useful in the general case where the size distribution is not well known. The second problem of condensation in a nozzle is essentially a more complicated version of the first. The modeling of the formation and growth of aerosol particles here is slightly more involved than in the previous case because of the non-uniform temperature and pressure, sensitive dependence of thermodynamic parameters on the temperature and pressure, effects of the geometry of the nozzle and coupling of aerosol processes with the gas dynamics. Turner et al. (1988) developed a set of ordinary differential equations for modeling the aerosol dynamics coupled to the gas dynamics. The assumptions made are similar to the first problem where coagulation was neglected and surface growth was assumed to occur by the free molecular diffusion process. I also solve this problem using QMOM and discuss the various issues involved.

3.1.2. Particle formation and growth in a box.

This problem concerns the formation and growth of aerosol particles in a constant temperature, constant pressure and spatially homogeneous batch reactor. Due to the complete absence of transport phenomena, this model is also called a zero-dimensional

model. A chemical reaction occurring at a constant rate creates supersaturation and new particles are formed by homogeneous nucleation. Friedlander (1983) has derived an exact solution for the moments for the case where the classical theory of nucleation is valid and where surface growth occurs in the free molecular regime. Pratsinis (1988) developed a less restrictive model assuming a lognormal profile for the size distribution. With this assumption more general surface growth laws can be used, such as one which models a transition from the free molecular regime to the continuum, and coagulation can also be included. I shall solve the same problem using the quadrature method of moments which obviates the need for assuming a specific form for the size distribution.

I take the radius instead of the volume as the internal coordinate. In this case, this is more convenient because the surface growth law depends on the area of the particle which being proportional to the radius squared is naturally expressed as the second moment. For an isothermal, spatially homogeneous reactor with quiescent fluid and no diffusion of particles and after suitable non-dimensionalization, the QMOM equations reduce to the following:

$$\begin{aligned}
 dM_m^* / d\theta - m \sum_{i=1}^{N_Q} \hat{r}_i^{*m-1} G^*(\hat{r}_i^*) W_i^* + I^*(r = r_c^*) k^{*m/3} = \\
 1/2 \sum_{i=1}^{N_Q} \sum_{j=1}^{N_Q} [(\hat{r}_i^{*3} + \hat{r}_j^{*3})^{m/3} - \hat{r}_i^{*m} - \hat{r}_j^{*m}] \beta^*(\hat{r}_i^*, \hat{r}_j^*) W_i^* W_j^* . \\
 m = 0, 1, \dots, 2N_Q - 1
 \end{aligned} \tag{3.1.1}$$

The nomenclature and non-dimensionalization scheme is the same as in Pratsinis (1988) and given in Table 3.1.1. The equation for the condensable species is

$$dS / d\theta = R^* - I^* k^* - \sum_{i=1}^{N_Q} \tau(\tilde{G}^*(\hat{r}_i^*) / v_1) W_i^* \tag{3.1.2}$$

The growth laws in radius space for the free molecular and continuum regimes are the following.

Free molecular:

$$G_{FM} = dr / dt = v_1 n_s (S - 1) (k_b T / 2\pi m_1)^{1/2}. \quad 3.1.3$$

Continuum:

$$G_C(r) = dr / dt = D_1 v_1 n_s (S - 1) / r. \quad 3.1.4$$

For the combined growth law the following interpolation formula is used.

$$G(r) = \frac{G_{FM} G_C(r)}{G_{FM} + G_C(r)} \quad 3.1.5$$

In the above equations and in what follows, v_1 is the volume, m_1 is the mass and D_1 the diffusivity of the monomer. S is the saturation ratio.

For the monomer equation the surface growth laws need to specify the number of monomers added and these are related to the volumetric growth rate.

Free molecular:

$$\tilde{G}_{FM}(r) = 4\pi r^2 G_{FM} / v_1 \quad 3.1.6$$

Continuum:

$$\tilde{G}_C(r) = 4\pi r^2 G_C(r) / v_1$$

And for the problem of combined growth laws, the interpolating formula of the form given in equation 3.1.5 is used with $\tilde{G}_{FM}(r)$ and $\tilde{G}_C(r)$. The coagulation kernels are of the following type:

Free molecular:

$$\beta_{FM}(v, \bar{v}) = (3/4\pi)^{1/6} (6k_b T v_1 / m_1)^{1/2} (1/v + 1/\bar{v})^{1/2} (v^{1/3} + \bar{v}^{1/3})^2; \quad 3.1.7$$

Continuum:

$$\beta_C(v, \bar{v}) = 2k_B T / 3\mu (Cu(v)/v^{1/3} + Cu(\bar{v})/\bar{v}^{1/3})(v^{1/3} + \bar{v}^{1/3}); \quad 3.1.8$$

where $Cu(v)$ is the Cunningham slip factor given by

$$Cu(v) = 1 + 1.25(\lambda / r(v)) \quad 3.1.9$$

Again for the combined coagulation problem the same interpolating formula (3.1.5) is used. The rate of nucleation is assumed to be given by the classical theory of nucleation.

That expression is given in Friedlander (2000).

$$I(r = r_c) = 2 \left[\frac{p_1}{(2\pi m_1 k_b T)^{1/2}} \right] (n_1 v_1^{2/3}) \left[\frac{\sigma v_1^{2/3}}{k_B T} \right]^{1/2} \exp \left[\frac{-16\pi\sigma^3 v_1^2}{3(k_b T)^3 (\ln S)^2} \right] \quad 3.1.10$$

For the sake of comparison, the conditions necessary for the applicability of this equation are assumed to hold. In equations 3.1.2 to 3.1.10, v_1 , m_1 , n_1 , D_1 pertain to the volume mass, number density and diffusivity of the monomer (condensable species). n_s is the number concentration of the monomer at saturation. λ is the mean free path of the gas, σ is the surface energy of the solid particle and k_B is the Boltzmann constant.

The formula in equation 3.1.5 to model the growth law over the entire range of Knudsen numbers has been shown to be very nearly the same as using Fuch's interpolation formula that is more generally used (Pratsinis, 1988). It reduces to the free molecular and continuum growth laws at large and small Knudsen numbers respectively. The same formula is used to get a combined coagulation kernel from the free molecular

(equation 3.1.7) and continuum Brownian kernels (equation 3.1.8) to be consistent with Pratsinis (1988).

Symbol	Meaning
$\tau = [n_s s_1 (k_b T / 2\pi m_1)^{1/2}]^{-1}$	Characteristic time scale for particle growth
$\theta = t / \tau$	Time
$M_m^* = M_m / n_1 r_1^m$	m th moment
$r^* = r / r_1$	Size
$I^*(r_c^*) = I(r_c^*) / (n_s / \tau)$	Nucleation rate
$G^*(r^*) = G(r) / (r_1 / \tau)$	Surface growth rate
$k^* = v / v_c$	Number of nuclei in critical sized cluster of volume v_c
$k^{*m/3} = r / r_c$	Number of nuclei in critical sized cluster of radius r_c
$w^* = n / n_s$	Size distribution
$\beta^* = \beta n_s \tau$	Coagulation rate
$S = n_1 / n_s$	Saturation ratio
$R^* = R / (n_s / \tau)$	Rate of gas to particle production reaction

Table 3.1.1. Non-dimensional terms used in equations 3.1.1 and 3.1.2.

3.1.3. Particle formation and growth in a nozzle.

Particles can also be formed by expanding a gas in a nozzle. Figure 3.1.1 shows a schematic of the process. The unsaturated vapor in a reservoir is transported by a carrier gas to the nozzle entrance. The expansion that takes place in the nozzle reduces the temperature and hence the saturation vapor pressure decreases rapidly. This leads to supersaturation of the vapor and a burst of nucleation at a fixed location. If the flow rate, concentration of the precursor and the nozzle area ratio are carefully chosen, a burst of nucleation occurs near the nozzle exit. After passing through the nozzle the condensed drops are allowed to solidify and grow by surface addition in a straight section. The vapor expansion method is a good strategy for production of monodisperse particles. However

in this chapter dealing with the validation of QMOM, I shall only be concerned with a solution to a simplified problem.

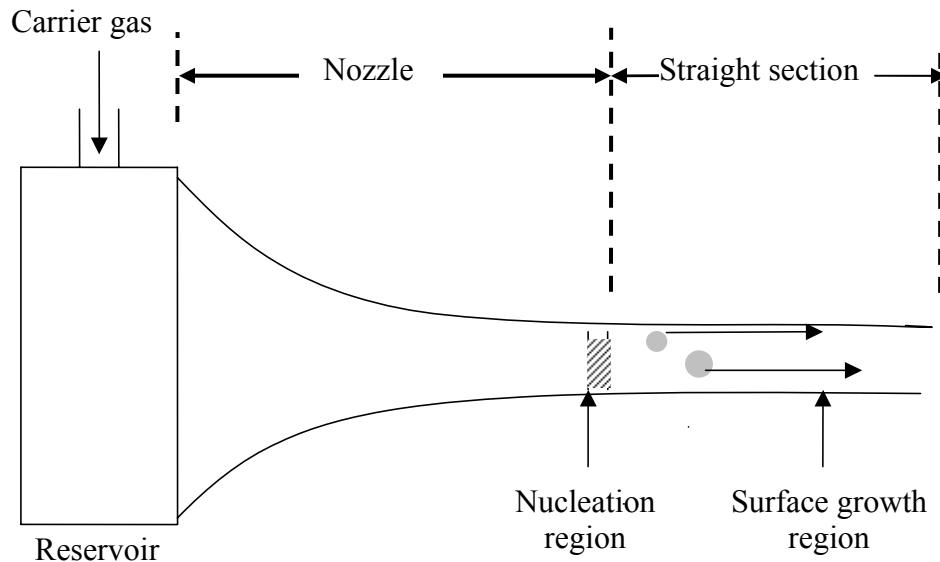


Figure 3.1.1. Schematic diagram showing particle formation and growth in a nozzle.

Condensation in a nozzle is similar to the batch reactor model considered except that the temperature, pressure and volume change with location along the nozzle. Turner et al. (1988) developed a set of equations for modeling the aerosol nucleation and surface growth in the free molecular regime. This problem is a more complicated version of the box model (Pratsinis (1988)) in that the thermodynamic state variables depend on location along the nozzle and the gas dynamics is coupled to the aerosol dynamics. Here, I will solve exactly the same problem as in Turner et al. (1988) using QMOM. The set of equations for the gas dynamics and the thermodynamic properties is given in Turner et al.

(1988). The GDE for the aerosol dynamics with the quadrature approximation is the following.

$$\begin{aligned}
U^* dM_m^* / dx^* - m \sum_{i=1}^{N_Q} \hat{r}_i^{*m-1} I^*(\hat{r}_i^*) W_i^* - I^* k^{*m/3} = \\
1/2 \sum_{i=1}^{N_Q} \sum_{j=1}^{N_Q} [(\hat{r}_i^{*3} + \hat{r}_j^{*3})^{m/3} - \hat{r}_i^{*m} - \hat{r}_j^{*m}] \beta^*(\hat{r}_i^*, \hat{r}_j^*) W_i^* W_j^* \\
+ [U^* (1/\alpha) d\alpha / dx^* (Ma^2 (1-g) + \gamma Ma^2) d] M_m^* \\
- [U^* (-Q^* + \Delta^* + \mu^*) (1-g) d] M_m^* \\
m = 0, 1, \dots, 2N_Q - 1
\end{aligned} \tag{3.1.11}$$

The equation for the conservation of the monomer (condensable molecule) is

$$\begin{aligned}
U^* dn_1^* / dx^* + I^* k^* + A^* V^* (n_1^* - n_{1s}^*) = \\
[U^* (1/\alpha) d\alpha / dx^* (Ma^2 (1-g) + \gamma Ma^2) D] n_1^* \\
+ [U^* (-Q^* + \Delta^* + \mu^*) (1-g) d] n_1^*
\end{aligned} \tag{3.1.12}$$

The nucleation and growth term and the coagulation kernels have the same form as equations 3.1.3 to 3.1.10 given earlier. For this problem I use only the free molecular growth law and nucleation and neglect coagulation. A simple finite difference method is used to solve equations 3.1.11 and 3.1.12. Again the results of the solution to this problem using the QMOM are given in the next section.

Symbol	Meaning
$x^* = n_{10} s_1 x$	Length along the nozzle
$U^* = U / (k_b T_0 / 2\pi m_1)^{1/2}$	Gas velocity
$M_m^* = M_m / n_{10} r_1^m$	m^{th} moment
$r^* = r / r_1$	Particle size
$I^*(r_c^*) = I(r_c^*) / n_{10}^2 s_1 (k_b T_0 / 2\pi m_1)^{1/2}$	Nucleation rate
$I^*(r^*) = I(r) / n_{10} r_1 s_1 (k_b T_0 / 2\pi m_1)^{1/2}$	Growth rate
$\beta^* = \beta / s_1 (k_b T_0 / 2\pi m_1)^{1/2}$	Coagulation kernel
α	Nozzle cross sectional area
Ma	Mach number

g	Mass fraction in the condensed phase
γ	Ratio of the heat capacities
$d = [(1 - Ma^2)(1 - g) - \gamma Ma^2 g]^{-1}$	Term appearing in equation for gas expansion
Q^*	Rate of heat generation due to condensation
Δ^*	Rate of mass loss of gas phase due to condensation
μ^*	Rate of change of average gas molecular weight due to condensation
$n_1^* = n_1 / n_{10}$	Monomer concentration normalized by concentration in the reservoir n_{10}
$n_{1s}^* = n_1 / n_{1s}$	Monomer concentration at saturation

Table 3.1.2. Non-dimensional terms used in equations 3.1.11 and 3.1.12.

3.1.4. Results and discussions.

Particle formation and growth in a box.

The objective is to compare results obtained using QMOM with the exact and lognormal calculations. Figure 3.1.2 shows the variation in total number concentration with the non-dimensional residence time for the case where coagulation is neglected and the growth law is the diffusion limited free molecular growth law. The results using the QMOM are compared with those in Pratsinis (1988). For this problem, the moment equations can be closed exactly for the 2- point and 3- point quadrature calculations and hence these match the exact solution. The 1-point quadrature calculation requires a quadrature approximation for computing the area and hence it is only approximate. The 1-point approximation slightly overpredicts the total number concentration while the lognormal calculation underpredicts it. Figure 3.1.3 shows the comparison of the volume-averaged diameters for the same problem. Again while the 2-point and higher quadrature schemes are exact, the one point computation gives a slightly better approximation than

the lognormal. This is a considerable advantage since the 1-point calculation is computationally more efficient and easier to implement than the lognormal calculation. This is because the 1-point scheme requires the tracking of just two moments whereas the lognormal method requires the tracking of three moments along with the evaluation of integrals. Figure 3.1.4 shows the variation in number concentration with time for two different reaction rates, $R^* = 0.1$ and $R^* = 1.0$, for the combined growth law and with coagulation. In this case the growth law is taken to be the harmonic mean of the diffusion limited growth laws for free molecular and continuum regimes (equation 3.1.5). Then the functional form for this law is $a/(b + cr)$, which cannot be closed exactly. For the coagulation kernel I again use the harmonic mean of the two kernels as in Pratsinis (1988). For both reaction rates, there is very little difference between the 2- and 3-point quadrature calculations. This is presumably due to the fact that the size distribution never gets to be very wide due to the weaker effect of coagulation in this problem. As in the previous case, the 1-point quadrature solution is a more accurate approximation than the lognormal approximation. Considering the 2- and 3- point calculations to be accurate, one can see that the accuracy of the lognormal and 1-point schemes gets better as the reaction rate increases. When the reaction rate increases, the size distribution becomes narrower and fewer moments are required to describe the aerosol dynamics. The errors associated with an assumed size distribution also begin to decrease. Figure 3.1.5 shows comparison of the volume-averaged diameter for the same problem as in figure 3.1.4. The trends shown by the three calculations are the same as that shown in figure 3.1.3. Although for figures 3.1.4 and 3.1.5 one cannot say which of the calculations are exact, it

seems reasonable to again conclude that the 3-point calculations are the most accurate. 2-point results are very close to the 3-point that indicates the fast convergence. The accuracy improves very slightly on increasing the number of quadrature points.

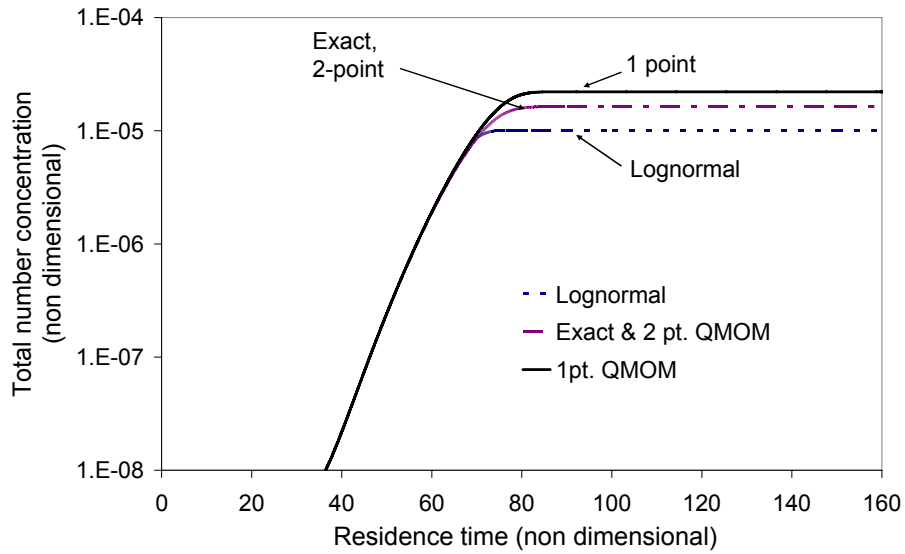


Figure 3.1.2. Variation of total number concentration with time for $R^* = 0.1$, comparison between exact, 1-point QMOM and lognormal calculations, box model with free molecular surface growth law and no coagulation.

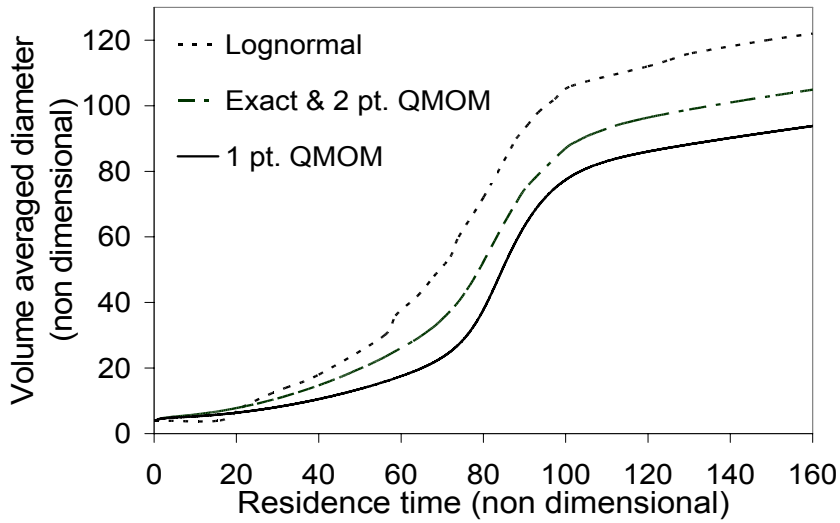


Figure 3.1.3. Variation of the volume averaged particle diameter with time for $R^* = 0.1$, comparison between exact, 1-point. QMOM and lognormal calculations, box model with free molecular surface growth law and no coagulation.

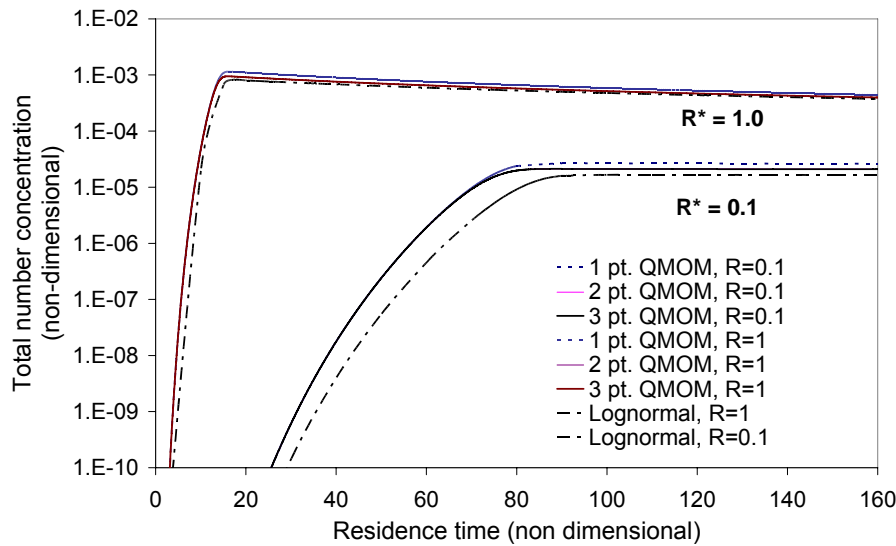


Figure 3.1.4. Variation of total number concentration with time for $R^* = 0.1$ and $R^* = 1.0$, comparison of the lognormal, 1-point, 2-point and 3-point QMOM calculations, box model, with coagulation and combined surface growth laws.

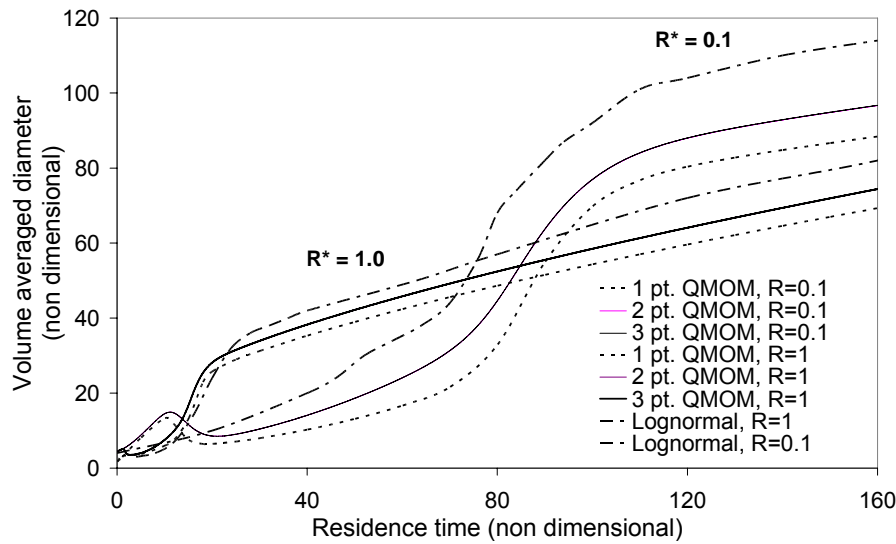


Figure 3.1.5. Variation of volume averaged particle diameter with time for $R^* = 0.1$ and $R^* = 1.0$, comparison of the lognormal, 1-point, 2-point and 3-point QMOM calculations, box model, with coagulation and combined surface growth laws.

Particle formation and growth in a nozzle.

This problem is interesting in that there is a very sharp burst of nucleation followed by surface growth. The two phenomena are separated. Figure 3.1.6 shows the variation in total number concentration with distance along the nozzle for the exact calculations from Turner *et al.* (1988) and the 1-point quadrature approximation. Figure 3.1.7 shows the comparison for the number averaged diameter (defined as M_1^* / M_0^*). The 2-point and higher calculations are exact in this case due to assumptions listed earlier.

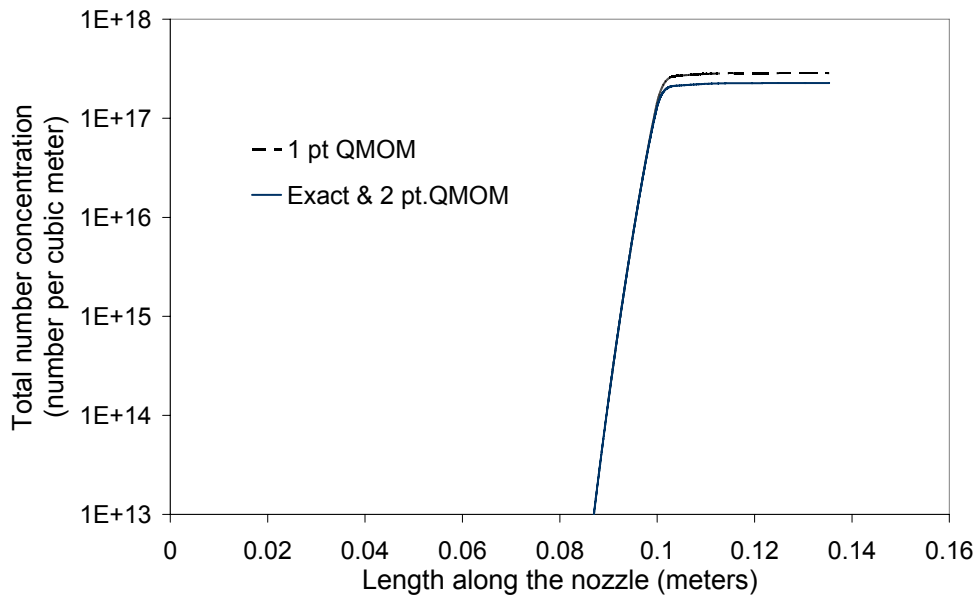


Figure 3.1.6. Variation of total number concentration with length along the nozzle, comparison of exact and 1-point QMOM calculations.

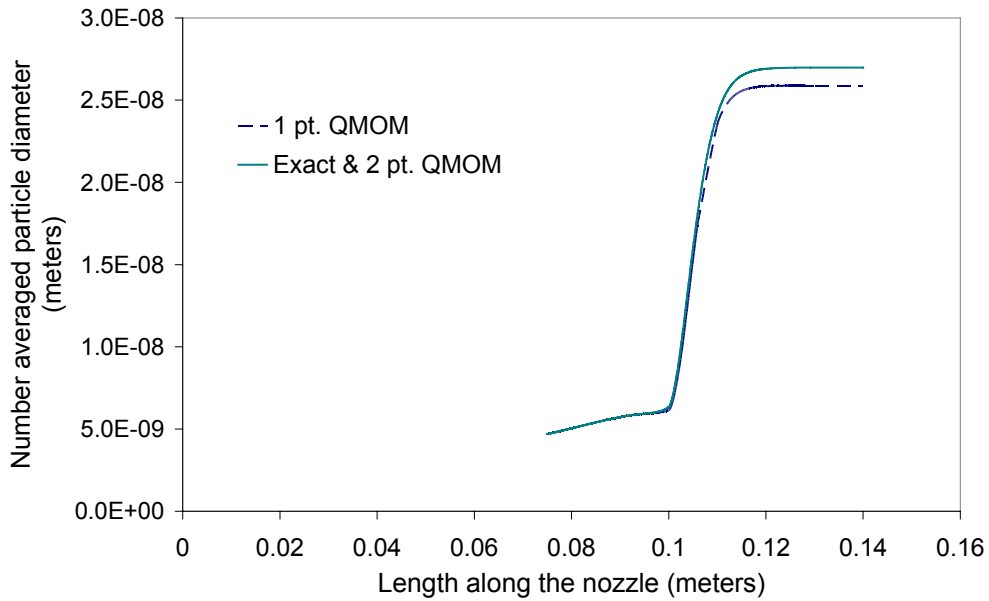


Figure 3.1.7. Variation of number averaged diameter with length along the nozzle, comparison of exact and 1-point QMOM calculations.

Evaluation of the one point quadrature approximation.

There are various reasons for using the 1-point quadrature calculation as discussed in section 2.6 (page 32). In figure 3.1.8, I examine the error in calculating the area using the 1-point approximation as a function of the polydispersity index. The polydispersity index or the coefficient of variation is a measure of the width of the size distribution function (Randolph & Larson (1988)). It is defined as $W = (M_2M_0 - M_1^2)^{1/2} / M_1$. It is seen from figure 3.1.8 that all the graphs for different reaction rates merge into one graph showing that the error in the area approximation is a function of the polydispersity index alone and independent of the reaction rate. This suggests that a useful way of deciding when to switch between various order quadrature calculations can be based on the magnitude of the polydispersity index. However this can be done only for 2-point and higher schemes since in the 1-point method, it is not possible to evaluate M_2 to be used in the definition of the polydispersity index. The polydispersity index is calculated using the 2-point scheme to evaluate its effect on the error due to the 1-point calculation. The percentage error is computed from the difference between 1-point and 2-point quadrature results.

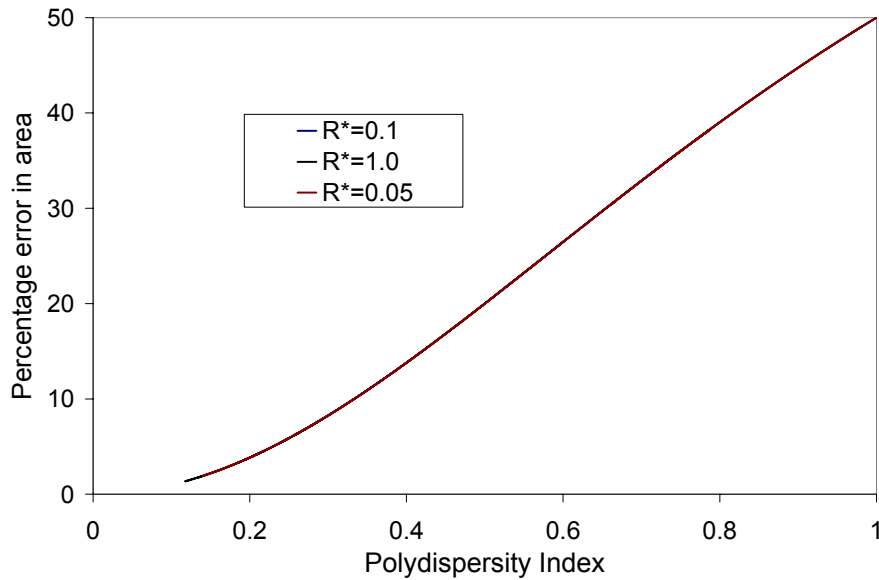


Figure 3.1.8. Variation in the error of 1-point quadrature calculation for area with polydispersity index for $R^* = 0.05$, $R^* = 0.1$ and $R^* = 1.0$.

In the problem of aerosol growth in a box, the inaccuracy in the area calculation leads to an inaccuracy in the saturation ratio because the saturation ratio is governed by the competition between the rate at which new particles are created by homogeneous nucleation and the rate at which the surface area of existing particles scavenge the condensable species. Homogeneous nucleation determines the total number concentration, and since the rate of nucleation depends sensitively on the saturation ratio, the error in the area computation leads to a large error in the total number calculation. But when the nucleation rate is much larger than the rate of surface growth, the variation in total number concentration is virtually independent of the surface area and hence errors in its calculation due to 1-point approximation are not significant. When the total area becomes large enough, the scavenging of the monomers by the existing particles leads to

a reduction in the saturation ratio. Hence in this case errors in the area calculation do matter in the final result. However, if the polydispersity index remains relatively small, the error is smaller, and tolerable accuracy can be obtained. This is illustrated in figure 3.1.9 and figure 3.1.10. Interestingly, as the reaction rate is increased from $R^* = 0.1$ to $R^* = 10.0$, corresponding to a faster nucleation rate, there is a sharp decrease in the polydispersity index. The associated result is that the error in the area calculation drops for the high reaction rate because the polydispersity index is lower; this is consistent with figure 3.1.8 which showed that the error in area grows more slowly when the polydispersity index is low. The error in the computation for the number concentration drops from approximately 35% to 15%. The 1-point computation also gets more accurate as the reaction rate gets higher. Figure 3.1.11 shows the same comparison for the problem of condensation in a nozzle. In the previous two cases the condensable species were generated by a steady chemical reaction. In the nozzle problem there is a much higher saturation ratio, leading to a burst of nucleation followed by a near immediate cessation of nucleation, and rapid surface growth. This suggests that nucleation and surface growth phenomena are separated. This can be seen by the much narrower peak and the sharper drop in the polydispersity index in figure 3.1.11. This figure also shows the variation in the error in the number calculation and average radius.

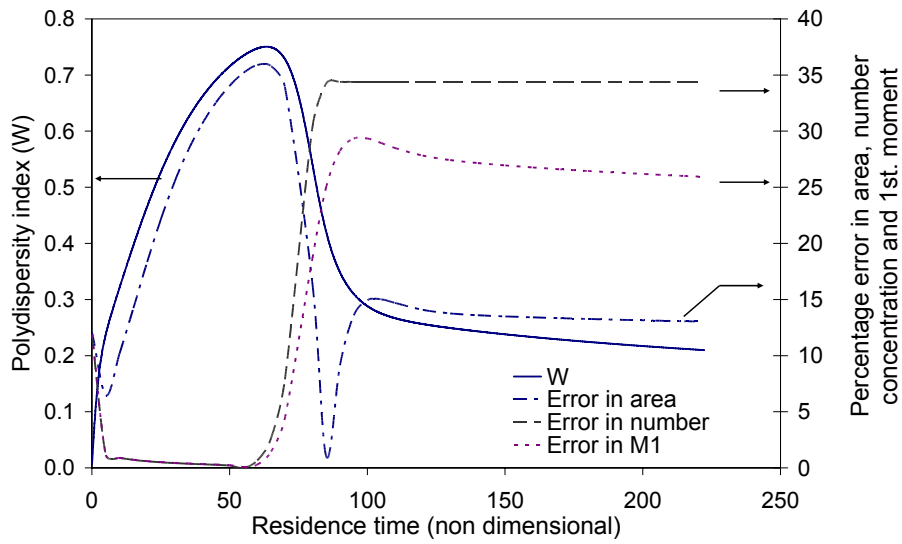


Figure 3.1.9. Polydispersity index and percentage error in total area, total number concentration and average diameter (1st moment) between 1-point QMOM and exact calculations, box model with $R^* = 1.0$.

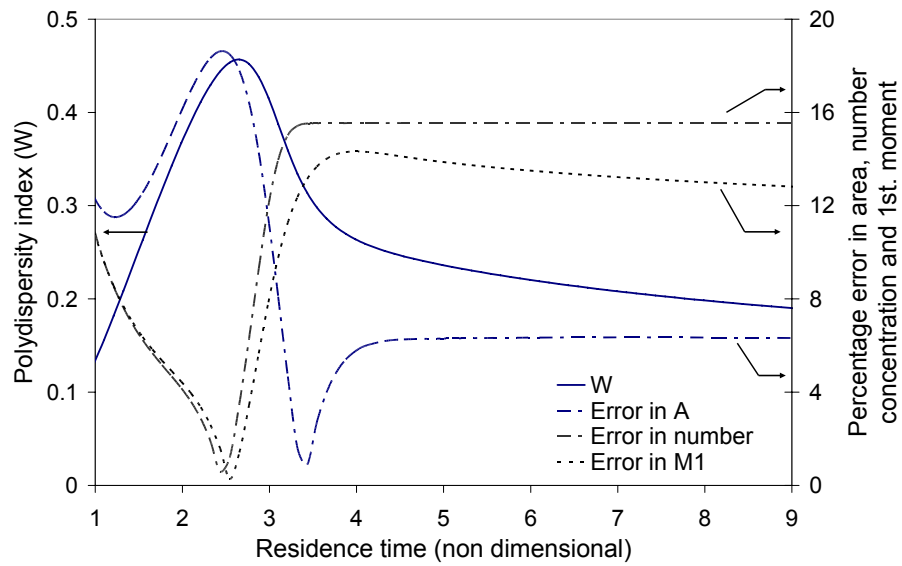


Figure 3.1.10. Polydispersity index and percentage error in total area, total number concentration and average diameter (1st moment) between 1-point QMOM and exact calculations, box model with $R^* = 10.0$.

In this case both the polydispersity and the error in the area calculation are large initially and although the error in area drops as fast as the polydispersity index, it is still sufficiently large to cause a slight error in the determination of the saturation ratio. Small differences in the saturation ratio can cause a large change in the final number concentration because of the very sensitive dependence of the rate of nucleation on the saturation ratio.

This suggests a useful strategy for solving problems of this sort where the size distribution evolves “out of nothing”. In higher order quadrature methods there appears to be a need to specify an initial size distribution function. This does not appear to be a restriction for the 1-point method. When the first particles of a critical sized radius appear, the size-distribution is strictly monodisperse and the 1-point quadrature approximation can be implemented. Thus, I recommend that at the beginning of a process when the polydispersity index is zero and beginning to increase, the 1-point approximation should be used. In practice, there are physical scenarios where these requirements can be relaxed. For example, if the coagulation rate is sufficiently large relative to the nucleation rate, or if the nucleation process results directly in a polydisperse distribution, it may be feasible to begin with a higher order approximation. For nucleation resulting in an effectively monodisperse distribution, errors in a one point approximation in the calculation of the area and other coagulation terms do not affect the result for the number concentration calculation because the rate of nucleation is many times larger than surface growth and coagulation rates. When the polydispersity begins to increase and the rate of surface growth gets comparable to the rate of homogeneous nucleation, then I suggest that the calculations be continued with two or more quadrature

points, thus improving the accuracy in the crucial stages when the total surface area is important in quenching homogeneous nucleation.

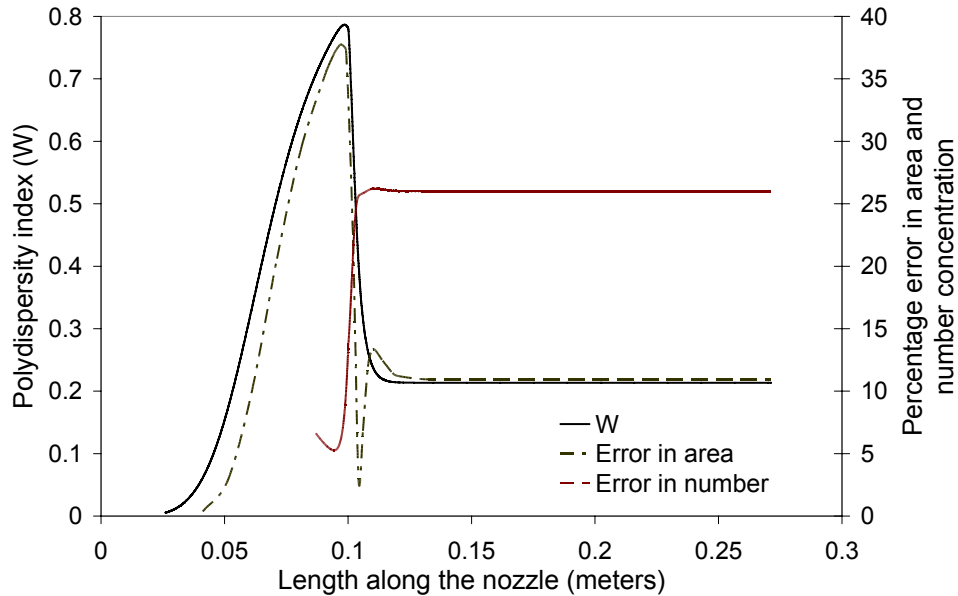


Figure 3.1.11. Polydispersity index and percentage error in total area and total number concentration between 1-point QMOM and exact calculations, problem of condensation in a nozzle.

3.1.5. Conclusions.

In this section I have examined the suitability of applying the quadrature method of moments (QMOM) to the solution of problems in aerosol dynamics in which nucleation, surface growth and coagulation occur simultaneously. I have reworked three typical problems and compared the results with results obtained using the QMOM. The benefits of using QMOM are that it can handle more complex problems involving complicated growth and coagulation processes, can easily be incorporated into other fluid dynamic or combustion calculations and can be used for any form of the size distribution

function. This is expected to be a significant advantage in modeling processes where nothing is known about the size distribution.

The 1-point quadrature is the simplest type of moment calculation in which only the first two moments need to be calculated. In the problems I considered, the 1-point calculations predicted the qualitative trends and gave quantitative results of accuracy comparable with the calculation which assumed a lognormal size distribution. 2-point quadrature, which is only slightly more complicated, gives very accurate results. As expected, the error in the 1-point quadrature approximations goes down as size distribution becomes narrower. In many cases where the size distribution evolves due to nucleation, surface growth and coagulation, it is desirable to start the computations without assuming any initial size distribution. This can be done by starting with 1-point and subsequently increasing the number of quadrature points. In this manner, the best features of 1-point and higher quadrature calculations can be utilized.

3.2. TREATMENT OF SIZE DEPENDENT AEROSOL TRANSPORT PROCESSES USING QMOM/DQMOM.

3.2.1 Introduction and motivation.

In the previous section, I discussed the applicability of QMOM to aerosol processes involving nucleation, surface growth and coagulation. While QMOM appears to be a promising tool for those problems and a number of other aerosol applications described in the references outlined in section 2.6, it is necessary to increase their applicability to a wider range of problems. Aerosol transport by gravitational settling and diffusion can be important in a number of natural phenomena and industrial applications such as filtration, sampling, deposition on the small airways of the lungs etc. The

diffusion of aerosols differs from the diffusion of molecules in that the diffusion coefficient depends on the size of the particle as shown by Einstein (1905). Further in the convective transport by gravitational settling, the settling velocity also depends on the size of the particle as has been described by Fuchs (1964). In fact for any other aerosol transport mechanism such as electrophoresis or thermophoresis, different sized particles move with different velocities leading to dispersive flux and diffusion problems. The implementation of size dependent transport phenomena in moment methods can lead to numerical difficulties. In a recent study, Settumba and Garrick (2004) have identified some problems associated with the implementation of size dependent diffusion in moment methods with closure based on the presumed lognormal density. The case of size dependent convection (flux) has been treated previously by Fan et al. (2004). To my knowledge an evaluation of QMOM or DQMOM for problems involving size dependent diffusion has not been carried out.

In this section, I focus on the numerical issues related to the use of QMOM and DQMOM for simulation of aerosol settling and diffusion with size dependent coefficients. I take a simplified problem of aerosol settling and diffusion between infinite parallel plates. This is a problem for which analytical solutions for the number density function can be obtained and the moments can be obtained by integration over the number density. When the moment equations are considered, it is seen that using even the simplest expressions for the diffusion coefficient and settling velocities leads to moment closure problems. I use QMOM and DQMOM for closure of the moment equations. For the problem considered in this study, moment methods may not be the most appropriate choice for the solution. However, the simplified nature of the problem and the availability

of analytical solutions can be used to clarify the nature of the solutions of the moment equations. I discuss the relation between the QMOM and DQMOM approaches for solution of the moment equations. These two methods lead to different interpretations and techniques for the solution of the moment equations but the solution is exactly the same. Furthermore, I find that solutions for the moments depend on the initial choice of moments and that it is possible to improve the accuracy with an optimal choice of moments.

3.2.2. Mathematical formulation and analytical solutions.

In this study I consider the diffusion and gravitational settling of particles contained within infinite horizontal plates. The governing differential equation is a Fokker-Planck equation of the type

$$\frac{\partial n(r; x, t)}{\partial t} = \frac{\partial}{\partial x} D(r) \frac{\partial n(r; x, t)}{\partial x} + \frac{\partial}{\partial x} C_s(r) n(r; x, t). \quad 3.2.1$$

Equation 3.2.1 is a part of the general dynamic equation for aerosols (Friedlander (2000)) in which the coagulation, surface growth and nucleation etc. have been neglected. Here the aerosol population is described by its radius, r . $n(r; x, t)$ is the aerosol number density function that depends on space and time. The diffusion coefficient $D(r)$ and the gravitational settling velocity $C_s(r)$ depend on the radius, r , of the particle and are given by:

$$D(r) = \frac{kT}{6\pi\mu r}, \quad 3.2.2$$

$$C_s(r) = \frac{4\rho_p g r^2}{18\mu} \left(1 - \frac{\rho_{air}}{\rho_p} \right). \quad 3.2.3$$

In writing equations 3.2.2 and 3.2.3 I have neglected the slip correction which becomes important when the particle size approaches the mean free path of the gas. However this omission is not a serious restriction. In the analysis that follows, the effect of slip can be easily included as long as the settling velocity and diffusion coefficients do not depend on space and time. Forms of equation 3.2.1 have been studied by various researchers within the context of deposition of particles in the airways of the lungs. Davies (1949), Wang et al. (1968) and Goldberg et al. (1978) derived solutions of 3.2.1 with the assumption of constant diffusion and settling velocities (no size dependence).

I now define the following non-dimensional quantities:

$$\tilde{x} = \frac{x}{L}; \quad \tilde{n} = \frac{n}{N_0}; \quad \tilde{t} = \frac{t}{t_{ch}}; \quad \tilde{D}(r) = \frac{D(r)}{D(\bar{r}_0)}; \quad \tilde{C}_s(r) = \frac{C_s(r)}{C_s(\bar{r}_0)}.$$

t_{ch} is the characteristic time scale defined as $t_{ch} = \frac{L}{C_s(\bar{r}_0)}$ when $C_s(\bar{r}_0) \neq 0$ and

$t_{ch} = \frac{L^2}{D(\bar{r}_0)}$ when $C_s(\bar{r}_0) = 0$. $C_s(\bar{r}_0)$ and $D(\bar{r}_0)$ are the settling velocity and diffusion

coefficient evaluated at the geometric mean radius \bar{r}_0 of the initial distribution.

In terms of the non-dimensional quantities, equation 3.2.1 can be written as:

$$\frac{\partial \tilde{n}(r; \tilde{x}, \tilde{t})}{\partial \tilde{t}} = \frac{1}{Pe} \frac{\partial}{\partial \tilde{x}} \tilde{D}(r) \frac{\partial \tilde{n}(r; \tilde{x}, \tilde{t})}{\partial \tilde{x}} + \frac{\partial}{\partial \tilde{x}} \tilde{C}_s(r) \tilde{n}(r; \tilde{x}, \tilde{t}), \quad 3.2.4$$

where $Pe = \frac{C_s(\bar{r}_0)L}{D(\bar{r}_0)}$ is a non-dimensional parameter, the Peclet number, that compares

the effect of settling to diffusion. If $Pe \gg 1$, then the problem is settling dominated

whereas if $Pe \ll 1$ implies that the problem is diffusion dominated. By definition Pe

depends on the height of the chamber as well as the mean of the initial aerosol size distribution.

To solve equation 3.2.4, initial conditions and boundary conditions are required. I assume that the initial condition is a lognormal distribution that is uniform in space. The walls are taken to be perfect sinks for the particles:

$$\begin{aligned}\tilde{n}(r; \tilde{x}, 0) &= n_{LN}(\bar{r}_0, \sigma_g) \quad (0 < \tilde{x} < 1); \\ \tilde{n}(r; \tilde{x}, \tilde{t}) &= 0 \quad \tilde{x} = 0, 1.\end{aligned}\tag{3.2.5}$$

Case I: Simultaneous gravitational settling and diffusion.

The solution to equation 3.2.4 with the boundary conditions 3.2.5 can be obtained using separation of variables. The tildes have been dropped and all quantities are dimensionless:

$$\begin{aligned}n(r; x, t) &= n(r; x, 0) \sum_{j=1}^{\infty} \left\{ \frac{8\pi j D(r)^2}{(Pe^2 C_s(r)^2 + 4\pi^2 j^2 D(r)^2)} \left(1 - (-1)^j \exp\left(\frac{Pe C_s(r)}{2D(r)}\right) \right) \right. \\ &\quad \left. \exp\left(-\lambda_j^2 t - \frac{Pe C_s(r) x}{2D(r)}\right) \sin(j\pi x) \right\}.\end{aligned}\tag{3.2.6}$$

$$\lambda_j^2 = \frac{D(r)}{Pe} \left(j^2 \pi^2 + \frac{Pe^2 C_s(r)^2}{4D(r)^2} \right)$$

The solution is identical to the constant diffusivity case since in this problem there are no interactions between the particles and the particles of a fixed radius settle and diffuse independently of all the other particles. The solution 3.2.6 is similar to the solutions obtained by Wang et al. (1968) and Davies (1969) with the exception that I have retained the radius dependence of $D(r)$ and $C_s(r)$. Now I look at the limiting cases.

Case II: Diffusion only.

For the case of diffusion only, $C_s(r)$ is equal to zero and the $1/Pe$ term in equation 3.2.4 does not appear, as a different scaling is used for the characteristic time. In this case the following solution can be obtained using separation of variables:

$$n(r; x, t) = n(r; x, 0) \sum_{j=1}^{\infty} \left\{ \frac{2}{j\pi} (1 - (-1)^j) \exp(-\lambda_j^2 t) \sin(j\pi x) \right\} \quad 3.2.7$$
$$\lambda_j^2 = D(r)(j^2\pi^2)$$

Case III: Settling only.

The solution for the case of pure settling is obtained using the method of characteristics.

For settling only, equation 3.2.4 becomes:

$$\frac{\partial n(r; x, t)}{\partial t} = \frac{\partial}{\partial x} C_s(r) n(r; x, t). \quad 3.2.8$$

The solution to equation 3.2.8 is given by:

$$n(r; x, t) = n_0(x + C_s(r)t) \quad \text{if } x + C_s(r)t < 1,$$
$$n(r; x, t) = 0 \quad \text{if } x + C_s(r)t \geq 1. \quad 3.2.9$$

3.2.3. Semi-analytical solutions for the moments.

My objective in this section to obtain accurate solutions for the moments by integrating the analytical solutions 3.2.6, 3.2.7 and 3.2.9 using numerical quadrature. These moments will be used as benchmark solutions for comparison with moments obtained from the solution of the moment evolution equations using QMOM / DQMOM.

For cases I and II considered above, the moments can be obtained by integrating the solutions 3.2.6 or 3.2.7. It is seen that to get the k^{th} moment involves the integration of a function of the form $g(r; x, t) = r^k f(r; x, t)$ over the initial lognormal number density function $n(r; x, 0)$, i.e.,

$$M_k(x, t) = \int_0^\infty r^k n(r; x, t) dr = \int_0^\infty r^k f(r; x, t) n(r; x, 0) dr. \quad 3.2.10$$

Here $f(r; x, t)$ is a finite sum that approximates the infinite series in 3.2.6 or 3.2.7. Each term of the series expression depends on the particle radius r through the r -dependence of $C_s(r)$ and $D(r)$. To evaluate this integral I make use of the method suggested by Wilck (2001) for accurate integration of functions over the lognormal distribution. In this case since the weight function (lognormal density) and hence all its moments are known, a Gaussian quadrature formula of arbitrarily high order can be developed.

The quadrature formula for evaluating equation 3.2.10 is then given by

$$M_k(x, t) \approx \sum_{i=1}^{N_Q} (\hat{r}_i)^k f(\hat{r}_i) W_i \quad 3.2.11$$

where \hat{r}_i is the quadrature point and W_i is the quadrature weight. N_Q is the number of quadrature points and $2N_Q$ moments are required to determine N_Q quadrature points.

Due to the complicated dependence on r of the integrand, it is necessary to check the convergence of the quadrature sum. I now put forward a strategy for checking the convergence of quadrature approximations to the integral for all three cases.

Case I and II.

To obtain the moments as a function of space and time one needs to evaluate an integral of the form 3.2.10. From equation 3.2.6, one sees that the r dependence of the integrand is extremely complicated and one needs a large number of quadrature points for accurate evaluation of the integral. In my example, $f(r; x, t)$ needs to be integrated over a lognormal distribution using the quadrature formula (3.2.11). A sequence of moments of the lognormal density needs to be used to obtain the quadrature points and weights. The moments of the lognormal distribution are given by (e.g. Williams and Loyalka (1991))

$$M_{k, LN} = M_{0, LN} \exp\left(k \ln(r_g) + \frac{k^2 (\ln(\sigma_g))^2}{2}\right) \quad 3.2.12$$

In the above formula k can be taken to be an integer or fraction. When the integer moment sequence $M_k, k = 0, 1, 2, 3, \dots, 2N_Q - 1$ is chosen the quadrature approximation 3.2.11 becomes exact for all integrands that are polynomials up to order $2N_Q - 1$. When a fractional moment sequence, say $M_{k/3}, k = 0, 1, 2, 3, \dots, 6N_Q - 3$ is specified, then at the cost of specifying three times more moments, one also gets exact results for all integrands

that are polynomials up to order $2N_Q - 1$ or power laws of the form $\sum_{k=0}^{6N_Q-3} a_k r^{k/3}$. By

choosing fractional moment sequences of lower orders, it is possible to get the exact integral for a larger class of functions. Another interpretation is that by choosing a larger number of fractional moments, the underlying number density function (in this case the lognormal density), is represented more accurately. Due to the complicated form of the function $f(r; x, t)$ to be integrated, a-priori it is not evident which is the best moment

sequence. Therefore to check the convergence of the quadrature sum, it is necessary to check that the quadrature sum is independent of the number of quadrature points and also independent of the choice of moment sequences of smaller and smaller fractions.

The choice of fractional moment sequences to obtain a quadrature formula has been discussed by McGraw and Wright (2003) in the context of the quadrature method of moments (QMOM). The same principle is used for integration over the lognormal or any other distribution. Since the quadrature points are roots of an orthogonal polynomial obtained from the moments, a change of variables is required and the fractional moments of the original distribution is transformed into the integer moments of a new distribution. For example, suppose I specify a fractional moment sequence of the original lognormal distribution, $n_{LN}(r)$, as $M_{k/3}, k = 0,1,2,3...6N_Q - 3$.

$$M_{k/3} = \int_0^{\infty} r^{k/3} n_{LN}(r) dr \quad 3.2.13$$

A new variable s is defined by the mapping $s = r^{1/3}$. The density $m(s)$, in terms of the transformed variable s , is related to the original density $n_{LN}(r)$ by the coordinate transformation rule

$$m(s)ds = n_{LN}(r)dr \quad 3.2.14$$

By writing 3.2.13 in terms of the new variable s and using 3.2.14, one gets

$$M_{k/3} = \tilde{M}_k = \int_0^{\infty} (s^3)^{k/3} m(s)ds = \int_0^{\infty} s^k m(s)ds \quad 3.2.15$$

It can be seen that one does not need the expression for $m(s)$ since one knows its moments in terms of the moments of the original distribution. The fractional moment sequence $\{M_{k/3}\}$ in r is converted to an integer moment sequence $\{\tilde{M}_k\}$ in s . Now the

quadrature points and weights can be obtained using $\{\tilde{M}_k\}$. The quadrature approximation of the integral 3.2.11 in terms of the variable s is given by

$$M_k(x, t) \approx \sum_{i=1}^{N_Q} (\hat{s}_i^3)^k f(\hat{s}_i^3) W_i \quad 3.2.16$$

Where $M_k(x, t)$ are the moments of the analytical solution for the number density 3.2.6 or 3.2.7.

Case III.

In the case of pure settling a different strategy must be employed to obtain the moments. One needs to calculate the moments of the number density given in equation 3.2.9. When the initial number density is a lognormal, the solution is a truncated lognormal density where the radius of truncation depends on space and time. From equation 3.2.3 one sees that $C_s(r) = C_{s0} r^2$ where C_{s0} is a constant independent of r that

is given by $C_{s0} = \frac{4\rho_p g}{18\mu} \left(1 - \frac{\rho_{air}}{\rho_p}\right)$. The moment solution to 3.2.9 is given by

$$M_k(x, t) = \int_0^{r < \left(\frac{1-x}{C_{s0}t}\right)^{1/2}} r^k n_{LN}(r; x, t) dr \quad 3.2.17$$

The lognormal density function with the radius normalized such that $\ln(r_g)$ is zero is given by

$$n_{LN}(r; x, t) dr = \frac{1}{\sqrt{2\pi}(\ln \sigma_g)r} \exp\left(\frac{-(\ln r)^2}{2(\ln \sigma_g)^2}\right) dr \quad 3.2.18$$

The lognormal density is a normal density in $\ln(r)$ so using $r^k = \exp(k \ln r)$ in 3.2.18 and after some algebra one gets

$$M_k(x, t) = \exp\left(\frac{k^2}{2}(\ln \sigma_g)^2\right) \int_0^{\left(\frac{1-x}{C_{s0}t}\right)^{1/2}} \frac{1}{\sqrt{2\pi}(\ln \sigma_g)r} \exp\left[-\frac{(\ln(r) - k(\ln \sigma_g))^2}{2(\ln \sigma_g)^2}\right] dr \quad 3.2.20$$

The expression integrand is another lognormal density function with the same geometric standard deviation but shifted in r . Hence the solution for the moments is given by the cumulative distribution function (CDF) of the shifted lognormal distribution (e.g. Weisstein (1999)).

$$M_k(x, t) = \exp\left(\frac{k^2}{2}(\ln \sigma_g)^2\right) \cdot CDF\left(\left(\frac{1-x}{C_{s0}t}\right)^{1/2}\right) \quad 3.2.21$$

where $CDF(x)$ is the CDF of the shifted lognormal distribution given by

$$CDF(x) = \frac{1}{2} \left[1 + \operatorname{erf}\left(\frac{\ln x - k(\ln \sigma_g)^2}{\sqrt{2} \ln \sigma_g}\right) \right] \quad 3.2.22$$

3.2.4. The moment methods.

In this section I discuss alternative methods to obtain the moments by solving the moment transport equations corresponding to equation 3.2.4. In the previous section analytical solutions for the number density are obtained and moments can be obtained up to arbitrary accuracy by numerical integration using fixed quadrature points and weights. In moment methods a system of differential equations are solved for a sequence of moments and it becomes inefficient to track a very large number of moments. Therefore a truncated sequence of moments need to be used and the transport equations for the moments cannot be closed. I will use QMOM and DQMOM to solve the moment

equations. These methods use a smaller number of quadrature points and weights that change in time and space.

Quadrature method of moments (QMOM).

The equation for the moments M_k can be obtained by multiplying equation 3.2.4 by r^k and integrating over the entire range of radii:

$$\frac{\partial M_k(x,t)}{\partial t} = \frac{1}{Pe} \frac{\partial^2}{\partial x^2} \int_0^\infty r^k D(r) n(r; x, t) dr + \frac{\partial}{\partial x} \int_0^\infty r^k C_s(r) n(r; x, t) . \quad 3.2.23$$

Equation 3.2.23 suffers from the ‘closure problem’. For $D(r)$ and $C_s(r)$ given by equations 3.2.2 and 3.2.3, it is not possible to represent the integrals directly in terms of the set of moments M_k ($0 \leq k \leq 2N_Q - 1$) that are being solved. As discussed in section 2.6, in QMOM, the closure is accomplished by Gaussian quadrature. The QMOM representation of equation 3.2.23 is given by

$$\frac{\partial M_k(x,t)}{\partial t} = \frac{1}{Pe} \frac{\partial^2}{\partial x^2} \sum_{j=1}^{N_Q} (\hat{r}_j)^k D(\hat{r}_j) W_j + \frac{\partial}{\partial x} \sum_{j=1}^{N_Q} (\hat{r}_j)^k C_s(\hat{r}_j) W_j , \quad 3.2.24$$

where \hat{r}_j and W_j are the quadrature points and weights respectively and they only depend on the moments M_k . The initial and boundary conditions are given by:

$$M_k(x,0) = M_{(LN)k} \quad (0 < x < 1)$$

$$M_k(x,t) = 0 \quad x = 0,1$$

where $M_{(LN)k}$ are the k^{th} moments of the initial lognormal distribution.

Direct quadrature method of moments (DQMOM).

The general theory of DQMOM is already discussed in section 2.7. The DQMOM formulation for the solution of the Fokker Planck equation in 3.2.1 is given in greater detail in Appendix B. One sees that transport equations have to be solved for the quadrature weights, W_i , and quadrature point-weight products, $S_i = W_i \hat{r}_i$.

$$\frac{\partial W_i}{\partial t} - \frac{\partial C_s(\hat{r}_i)W_i}{\partial x} - \frac{\partial}{\partial x} D(\hat{r}_i) \frac{\partial}{\partial x} W_i = a_i \quad (i = 1..N_Q) \quad 3.2.25$$

$$\frac{\partial S_i}{\partial t} - \frac{\partial C_s(\hat{r}_i)S_i}{\partial x} - \frac{\partial}{\partial x} D(\hat{r}_i) \frac{\partial}{\partial x} S_i = b_i \quad (i = 1..N_Q) \quad 3.2.26$$

a_i and b_i are source terms that are necessary in order to force a sequence of $2N_Q - 1$ moments to evolve correctly. In general a_i and b_i are obtained by solving a system of linear equations as shown in Appendix B. The initial and boundary conditions are given by:

$$W_i(x,0) = W_{i,LN} \quad (0 < x < 1), i = 1..N_Q \quad 3.2.27$$

$$S_i(x,t) = S_{i,LN} = W_{i,LN} \hat{r}_{i,LN} \quad (0 < x < 1), i = 1..N_Q \quad 3.2.28$$

$$W_i(0,t) = W_i(1,t) = S_i(0,t) = S_i(1,t) = 0 \quad 3.2.29$$

$\hat{r}_{i,LN}, W_{i,LN}$ are the i^{th} quadrature point and weight for the initial lognormal distribution.

In general, if the diffusion coefficient is size dependent then the source terms a_i, b_i in equations 3.2.25 and 3.2.26 are complicated non-linear functions of W_i, S_i and their gradients. Equations 3.2.25 and 3.2.26 are then a set of coupled non-linear partial differential equations. It must be noted that in general the source terms contain expressions due to coagulation, breakage etc. which are again coupled and non-linear. In

the problem that I have considered in this study, the initial number density is specified as being uniform throughout space and hence $\frac{\partial \hat{r}_i}{\partial x} = 0$. For this case the source terms a_i and b_i are identically zero and the equations and boundary conditions for S_i and W_i are identical. The equations 3.2.26 and 3.2.27 become linear and uncoupled, but the size dependence of the velocity and diffusivity remain in the equations.

3.2.5. QMOM vs. DQMOM.

The QMOM formulation of the problem is given by equation 3.2.24 and the DQMOM formulation is given by equations 3.2.25 and 3.2.26. For univariate population balance equations, these two methods give identical solutions (Marchisio and Fox (2005)) but the methodology and the interpretation of the problem is different.

In terms of implementation in existing CFD codes, I see that the DQMOM formulation given in equations 3.2.25 and 3.2.26 is more convenient. The equations resemble transport equations for scalars and the coupling appears in the source terms. Most commercial CFD codes have been designed to handle the transport equations in the form of equations 3.2.25 and 3.2.26. In contrast, the flux and diffusion terms in the QMOM formulation involve integrals or quadrature sums. Another important difference between the two methods is in the choice of moment sequences. In the DQMOM formulation as given in Fox (2003) or in Appendix B, any moment sequence can be chosen as long as the matrices involved do not become singular. As mentioned earlier, in QMOM, a three term recurrence relation between consecutive orthogonal polynomials is used to compute the quadrature points and therefore an ordered moment sequence is

required. Further any ordered moment sequence such as $[0,1/k,2/k,3/k,\dots]$ has to be transformed to an integer moment sequence after a change in variables.

3.2.6. Results and discussion.

Computation of the moments by integration of analytical solutions.

As shown in section 3.2.3, one can obtain solutions for the moments by numerical integration of the number density function. These solutions will be used to benchmark the solutions for the moments obtained using QMOM and DQMOM. Due to the complicated form of equation 3.2.11, it is necessary to check for the convergence of the quadrature approximation of the integral. For the case of simultaneous gravitational settling and diffusion (Case I), the expression to be integrated is 3.2.6. Figure 3.2.1 shows the results of the quadrature approximations (3.2.11) (using large N_Q) for computing M_0 . It is seen that a large number of quadrature points are needed before the solution converges. For instance, the difference between successive approximations becomes small only when 20 or more quadrature points are used. The solutions are assumed to “converge” when the maximum difference between successive approximations becomes very small. However the converged solution for M_0 , obtained using an integer moment sequence for calculating the quadrature points and weights, may not be the correct solution. As discussed in section 3.2.3, better accuracy can be obtained by the use of fractional lower order moments. Figure 3.2.2 shows the converged results for M_0 and M_3 for choices of an integer moment sequence M_k and fractional moment sequences $M_{k/2}, M_{k/3}, M_{k/4}$. The graphs in figure 3.2.2 show that the converged solution obtained using integer moment sequences is different from that obtained using fractional moment sequences.

For each of the moment sequences, 100 quadrature points (200 moments) are used to compute M_0 and M_3 . However, for each moment sequence, the solutions get very close to each other after 20 or more quadrature points as shown in figure 3.2.1 for the integer moment sequence. The solutions obtained using $M_{k/2}, M_{k/3}, M_{k/4}$ are all close together. For reasons outlined earlier, the converged solution obtained with the use of fractional moment sequences is considered to be the correct analytical solution for the moments. As an independent validation, the integration is also carried out using the Monte Carlo scheme that is not based on quadrature. Figure 3.2.2 also shows that the results obtained using Monte Carlo integration with 10,000 samples coincide with the solution using fractional moments. For diffusion only (Case II), the integrand is obtained from equation 3.2.7. Inspection of equation 3.2.7 shows that the expression is greatly simplified compared to the combined settling and diffusion case (equation 3.2.6), in particular the exponential terms involving $C_s(r)$ drop out. Figure 3.2.3 shows the convergence of the quadrature approximation using integer moment sequences. As compared to Case I, fewer moments are required to attain convergence. In this case the difference between the successive approximations becomes small when only 5 quadrature points are used. Figure 3.2.4 shows the effect of choice of different moment sequences. In contrast to figure 3.2.2 for Case I, the solutions obtained using different moment sequences are almost the same. For this case the Monte Carlo integration also converges to the solution obtained from quadrature. Surprisingly, compared to Case I a larger number of samples are needed for the Monte Carlo results to converge. For instance in figure 3.2.4 I show the results using 100,000 samples and these results still show some statistical

fluctuations. This is a puzzling effect as DQMOM results showed better convergence for this case.

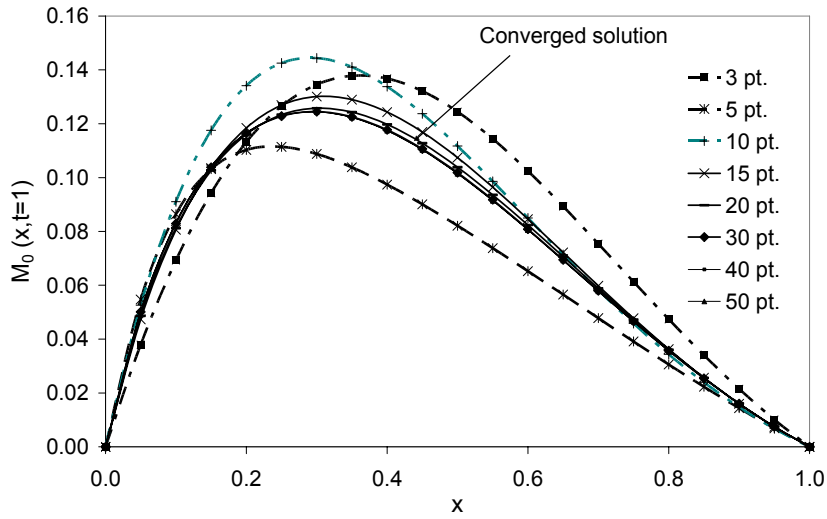


Figure 3.2.1. Solutions for $M_0(x, t=1)$ obtained from the numerical integration of the analytical solution (equation 6) with increasing number of quadrature points and choice of integer moment sequence for the case of combined diffusion and gravitational settling (Case I).

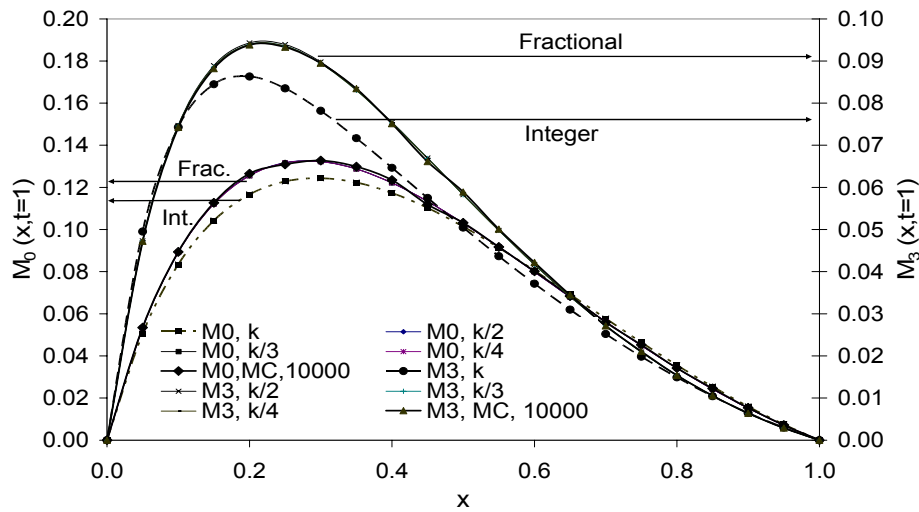


Figure 3.2.2. Converged solutions of the numerical integrations for $M_0(x, t = 1)$ and $M_3(x, t = 1)$ using integer moment sequence and several fractional moment sequences. Case of combined diffusion and gravitational settling (Case I). Also shown is the solution using Monte Carlo integration that coincides with the solution obtained from fractional moments.

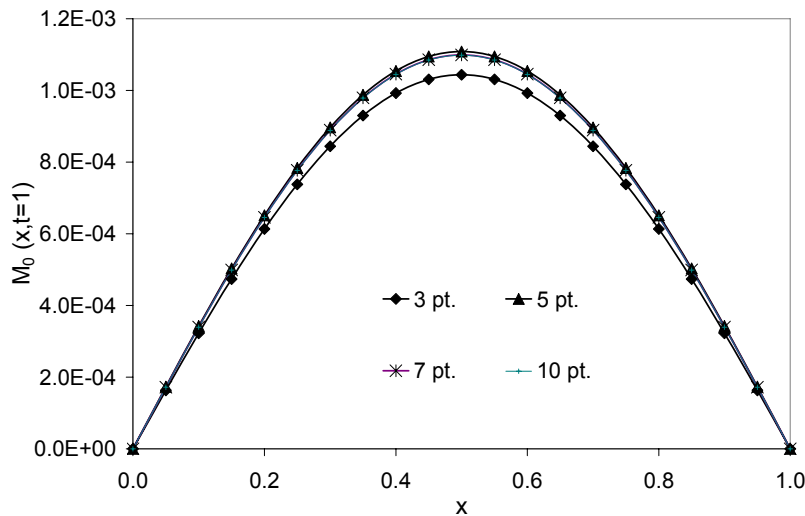


Figure 3.2.3. Solutions for $M_0(x, t = 1)$ obtained from the numerical integration of the analytical solution (3.2.7) with increasing number of quadrature points and choice of integer moment sequence for the case of diffusion only (Case II).

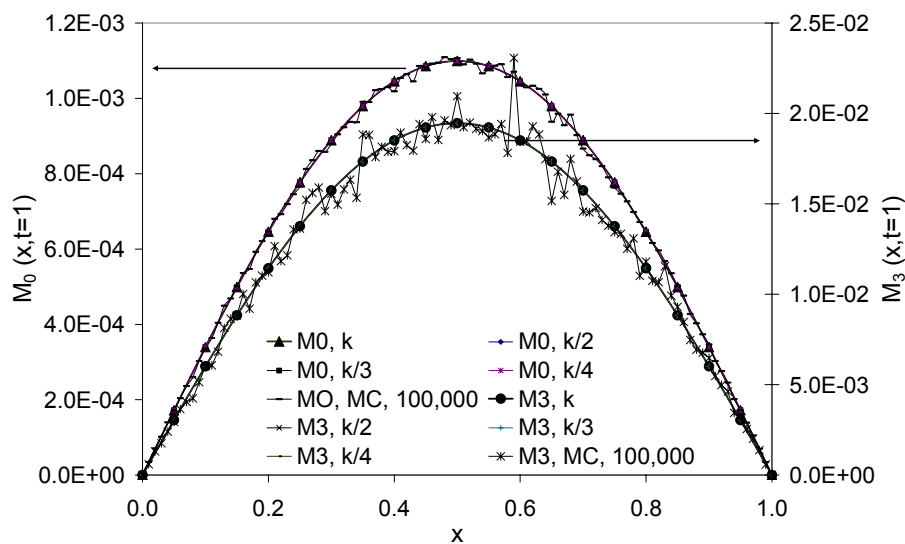


Figure 3.2.4. Converged solutions for $M_0(x, t=1)$ and $M_3(x, t=1)$ using integer moment sequence and several fractional moment sequences. Case of diffusion only (Case II). Also shown is the solution from the Monte Carlo integration using 100,000 samples.

Effect of the choice of moments on the accuracy of the solution obtained using QMOM/DQMOM.

When the moments are evaluated by integration of the analytical solution for the number density, one sees that as many as forty moments (for twenty quadrature points) may be needed. Further, the solutions obtained using integer moments or fractional moments may be different. In practice, for most aerosol computations it is not necessary to obtain extreme accuracy in the numerical solutions. However, while working with a fixed number of moments, it may be desirable to choose the optimum set of moments that gives the greatest accuracy. In this section, I compare numerical solutions of the moment equations with the benchmark solutions obtained by integrating analytical expressions for the number density. The results presented in this section are for the moment methods

discussed in section 3.2.4. Unlike in the previous section, here the quadrature points and weights are evolved in space and time and a maximum of only five quadrature points are used.

For numerical solutions of the moment equations, I choose to solve the DQMOM form of the equations given by equations 3.2.25 and 3.2.26. As discussed in section 3.2.4, for the problem considered, the source terms a_i, b_i in equations 3.2.25 and 3.2.26 are zero and the quadrature points \hat{r}_i do not change with time. The equations are effectively uncoupled and linear. Equations 3.2.25 and 3.2.26 are a set of linear transport equations in one dimension. The finite control volume method (Patankar (1980)) is used. An explicit scheme is used for the time marching with very small time steps to avoid instability.

The objective of the study is to evaluate errors due to closure of the moment equations. A suitable quantity that is useful and whose error can be compared is the fraction of the number $N(t)$ or volume $V(t)$ of aerosol deposited. These are defined by:

$$N(t) = 1 - \frac{\int_0^1 M_0(x,t) dx}{\int_0^1 M_0(x,0) dx}, \quad 3.2.30$$

$$V(t) = 1 - \frac{\int_0^1 M_3(x,t) dx}{\int_0^1 M_3(x,0) dx}. \quad 3.2.31$$

Two different methods are used to compute $N(t)$ and $V(t)$. First, the moments for each x_i, t_i are obtained by integration of analytical solutions using the methods described in

the previous section. For the case of settling only, the solution is given directly by the formula 3.2.20. The analytical values $N(t_i)_a$ and $V(t_i)_a$ are obtained by numerical integration of the moments over the spatial domain $[0,1]$ and using equations 3.2.30 and 3.2.31. Then numerical solutions are computed for the same discrete set of points x_i, t_i . If $N(t_i)_n$ and $V(t_i)_n$ denote the numerical solutions to equations 3.2.30 and 3.2.31, then the time integrated or cumulative error is defined as:

$$E_N = \int_0^T |N(t)_a - N(t)_n| dt \approx \sum_{i=1}^I |N(t_i)_a - N(t_i)_n| \Delta t_i, \quad 3.2.32$$

$$E_V = \int_0^T |V(t)_a - V(t)_n| dt \approx \sum_{i=1}^I |V(t_i)_a - V(t_i)_n| \Delta t_i, \quad 3.2.33$$

where the analytical solutions are evaluated at time intervals of $\Delta t_i = 10^{-3}$. The numerical solutions are computed using much smaller time steps of $\Delta t_i = 10^{-6}$ but in computing E_N and E_V the numerical solutions are sampled at the same times t_i as the analytical solutions.

It is necessary to ensure that numerical errors in the DQMOM solutions remain small and that for the monodisperse case the two solutions are very close to each other. Figure 3.2.5 shows the comparison of $N(t)_a$ and $N(t)_n$ for the monodisperse case. In this case there are no closure problems and the two solutions are very close together for all three cases. The maximum absolute difference is of the order of 10^{-3} for Cases I and II while there is no difference for Case III. For the polydisperse case, the numerical solutions all use three quadrature points but with different initial moment sequences. The

sequence M_{3k} means that initially the moments $M_0, M_3, M_6, M_9, M_{12}, M_{15}$ are used to evaluate the quadrature points and weights. Figure 3.2.6, figure 3.2.7 and figure 3.2.8 show the comparison of $N(t_i)_a$ and $N(t_i)_n$ for the case of pure diffusion (Case II), pure settling (Case III) and combined settling and diffusion (Case I) respectively. Figure 3.2.6 shows that the solutions obtained using different moment sequences are very close, the maximum absolute error is around 0.05 for the M_{3k} sequence. For the integer and fractional moment sequences, it is smaller than 0.005. In figure 3.2.7, I compare the solution obtained with the choice of different moment sequences with the analytical solution. The solution obtained with the M_{3k} sequence shows that by $t=1$, all the particles are deposited. In this case higher moments are used to calculate the quadrature points and weights and therefore the quadrature points are larger. As mentioned previously, the larger quadrature points correspond to bigger particles that settle faster.

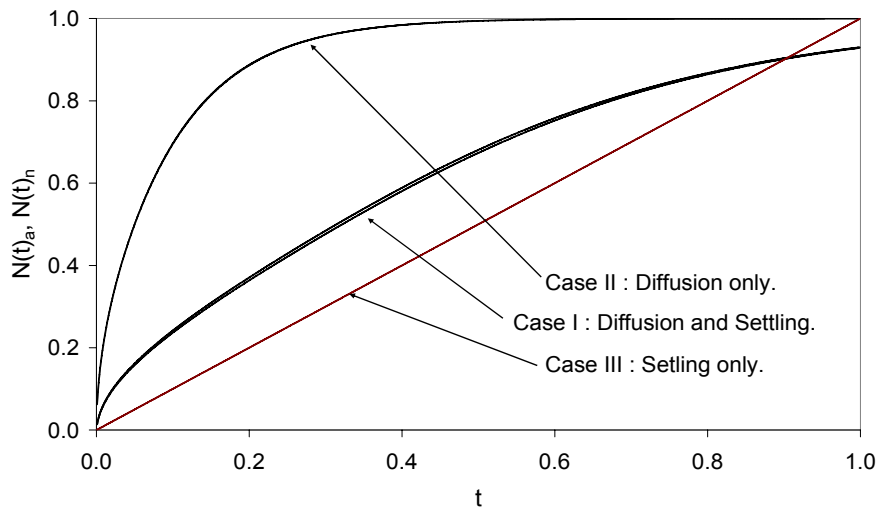


Figure 3.2.5. Comparison of the number fraction of aerosol deposited obtained from the analytical solution $N_a(t)$ and numerical solution $N_n(t)$ for the monodisperse case and for the three cases of combined diffusion and settling (Case I), diffusion only (Case II) and settling only (Case III).

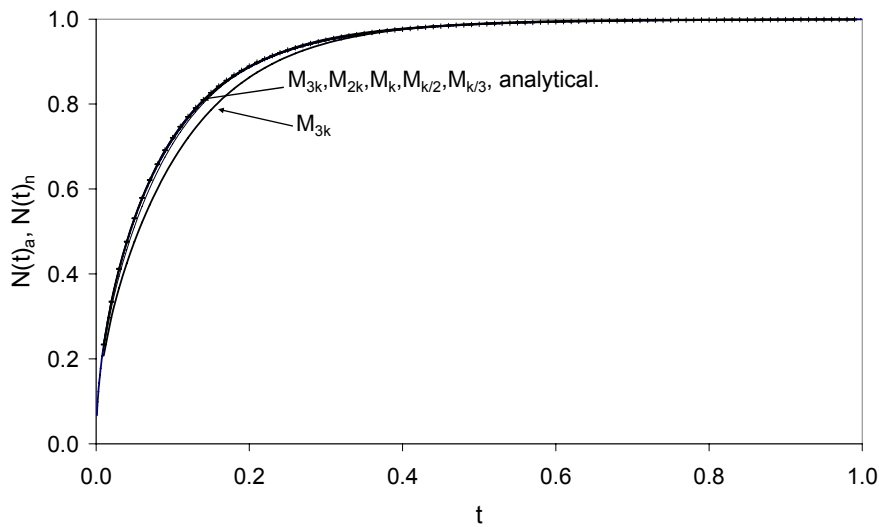


Figure 3.2.6. Comparison of $N_a(t)$ (analytical solution) and $N_n(t)$ (solution from QMOM/DQMOM) for the polydisperse case. Effect of the choice of different moment sequences in the numerical solution is compared. Case of diffusion only (Case II).

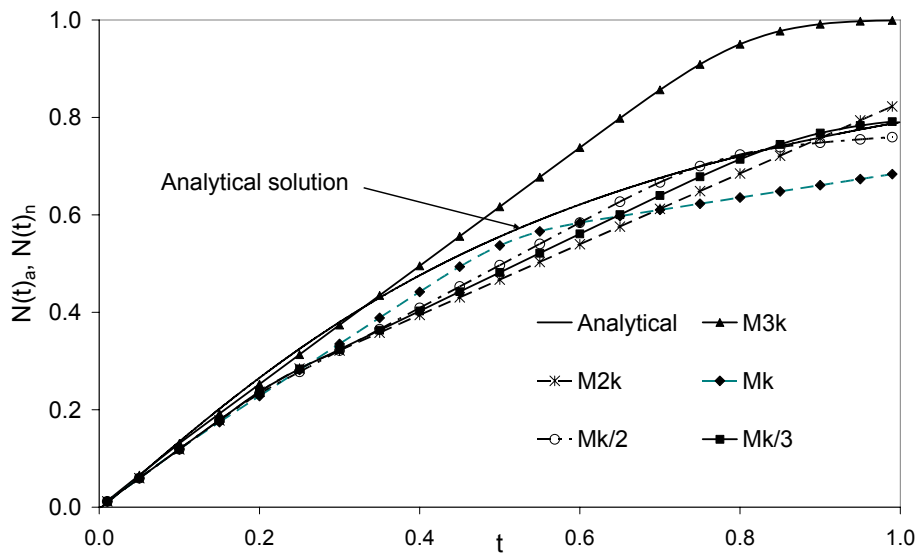


Figure 3.2.7. Comparison of $N_a(t)$ and $N_n(t)$ for the polydisperse case. Effect of the choice of different moment sequences in the numerical solution is compared. Case of settling only (Case III).

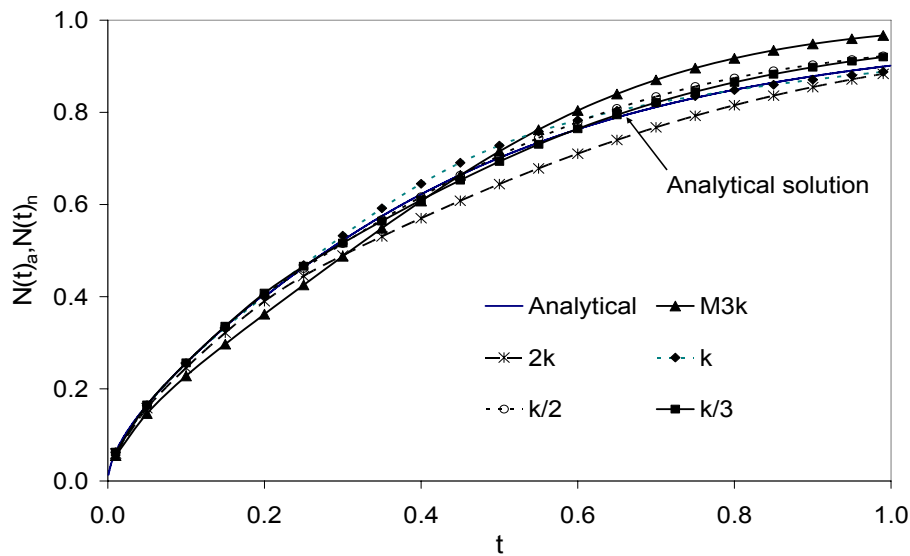


Figure 3.2.8. Comparison of $N_a(t)$ and $N_n(t)$ for the polydisperse case. Effect of the choice of different moment sequences in the numerical solution is compared. Case of combined diffusion and gravitational settling (Case I).

Looking at the solution obtained using the integer moment sequence M_k and the fractional moment sequences $M_{k/2}$ and $M_{k/3}$, I see that the M_k solution is better for the time interval $t \sim 0.2 - 0.6$ but for $t > 0.6$ the $M_{k/2}$ and $M_{k/3}$ solutions get better. At longer times the large particles will have settled and only the smaller particles are left. Then I see that solutions obtained using fractional moments are more accurate. For the solution obtained using the M_{2k} sequence, $N(t_i)_n$ is initially small but starts to increase faster than the solutions obtained using M_k , $M_{k/2}$ and $M_{k/3}$. In figure 3.2.8, the combined effect of settling and diffusion is considered. In this case, the solutions obtained using different moment sequences are again slightly different, but the variations are smaller than for pure settling.

The preceding results show that solutions depend on the initial choice of moments to describe the population. Further solutions obtained using a particular moment sequence may be more accurate for some time interval while it may be less accurate for other times. In Tables 3.2.1, 3.2.2 and 3.3.3, I look at the total error E_N and E_V defined in equations 3.3.32 and 3.3.33. Table 3.2.1 shows the results for Case II (diffusion). I see that errors for both M_0 and M_3 are smaller when the moment sequences M_k , $M_{k/2}$ and $M_{k/3}$ are chosen. The time integrated error is highest when the M_{3k} sequence is chosen. The proper choice of moment sequence appears to be more significant factor in the reduction of error than the number of quadrature points used. For instance, in all cases I do not get much reduction in the error when the number of quadrature points is increased. The same trends are seen in Table 3.2.2 and Table 3.2.3 for Case III (pure settling) and

Case I (simultaneous settling and diffusion) respectively. The errors are largest for the Case III. An interesting observation is that the choice of M_{3k} moment sequence leads to a larger error for the problems considered. The M_{3k} sequence is analogous to choice of the volume to describe the particle state. Results obtained in this work seem to indicate that for aerosol problems involving settling and diffusion, the particle radius is a better choice for the internal variable.

Moment Sequence	1 pt. ($\times 10^{-3}$)		3 pt. ($\times 10^{-3}$)		4 pt. ($\times 10^{-3}$)		5 pt. ($\times 10^{-3}$)	
	E_N	E_V	E_N	E_V	E_N	E_V	E_N	E_V
$3m$			10.6	13.4	10.5	13.0	10.4	12.9
$2m$			2.7	2.1	2.3	1.5	2.1	1.3
m	0.84	0.84	0.8	0.9	0.8	0.8	0.8	0.8
$m/2$			0.9	1.4	0.8	0.8	0.8	0.8
$m/3$			0.9	3.0	0.8	0.8	0.8	0.8

Table 3.2.1. Comparison of the errors E_N and E_V of the QMOM/DQMOM solutions for different moment sequences and number of quadrature points for the case of diffusion only (Case II).

Moment Sequence	1 pt. ($\times 10^{-3}$)		3 pt. ($\times 10^{-3}$)		4 pt. ($\times 10^{-3}$)		5 pt. ($\times 10^{-3}$)	
	E_N	E_V	E_N	E_V	E_N	E_V	E_N	E_V
$3m$			96.9	112.4	95.4	111.5	95.1	111.3
$2m$			47.6	62.1	51.5	56.9	54.1	54.4
m	0	0	48.8	34.3	34.9	35.6	36.4	37.9
$m/2$			30.3	40.5	51.6	40.4	47.1	33.4
$m/3$			36.2	41.6	53.0	36.5	40.2	32.7

Table 3.2.2. Comparison of the errors E_N and E_V of the QMOM/DQMOM solutions for different moment sequences and number of quadrature points for the case of settling only (Case III).

Moment Sequence	1 pt. ($\times 10^{-3}$)		3 pt. ($\times 10^{-3}$)		4 pt. ($\times 10^{-3}$)		5 pt. ($\times 10^{-3}$)	
	E_N	E_V	E_N	E_V	E_N	E_V	E_N	E_V
$3m$			40.7	65.4	40	64.6	39.9	64.4
$2m$			32.9	33.0	31.7	27.9	30.7	25.6
m	5.3	5.3	10.7	19.8	10.3	11.8	6.2	9.2
$m/2$			11.7	15.5	6.3	11.4	5.0	7.63
$m/3$			8.7	16.7	7.3	10.6	5.5	7.3

Table 3.2.3. Comparison of the errors E_N and E_V of the QMOM/DQMOM solutions for different moment sequences and number of quadrature points for the case of simultaneous diffusion and settling (Case I).

3.2.7. Conclusions.

In this section I examined the problem of aerosol settling and diffusion in which the settling velocity and diffusion coefficient depends on the size of the particle. I took a simple problem for which analytical solutions for the number density exists. The moment solutions can be obtained using numerical integration of the number density. I then compared these moments with the solutions obtained from the moment equations. The moment methods that I focussed on are the quadrature method of moments (QMOM) and the direct quadrature method of moments (DQMOM). Both methods use Gaussian quadrature for moment closure and give identical solutions but the implementation is different. The efficacy of these methods for treatment of size dependent aerosol transport processes had not been previously considered.

For the simplified problem considered in this study, it becomes possible to focus on the error in the closure of the moment equations. I investigated the nature of the solutions of the moment equations by taking different moment sequences of the initial number density and evaluating the number and volume fraction of aerosol deposited. Due to the unclosed form of the moment equations, the solutions depended on the initial choice of moment sequences. I also found that the error introduced by an improper choice of moment sequence may be more significant than the error due to choice of low order quadrature schemes. While it would be helpful if there were a rigorous procedure for determining the best moment sequence for any aerosol problem, it is unlikely that there is a globally optimal moment sequence. Different moment sequences give more weight to the larger particles or to the smaller sized particles. For instance at some stages of the evolution, the larger sized particles may influence the dynamics while for other stages,

the dynamics of the smaller particles may be more important. Then different moment sequences may be appropriate for different stages of the aerosol dynamics. This suggests that locally adaptive quadrature approximations could be developed to minimise the global error of the solutions. Investigation of these issues could lead to a better understanding of moment methods for various problems in aerosol science.

3.3. EXAMPLE OF QMOM COUPLED WITH CFD: SIMULATION OF SMOKE ENTRY AND LIGHT SCATTERING IN A CYLINDRICAL CAVITY ABOVE A UNIFORM FLOW.

After discussing the application of QMOM and DQMOM to some well known theoretical problems in aerosol science, I turn to an example illustrating an engineering application. In this section, I use computational fluid dynamics (CFD) and aerosol dynamics modeling to investigate the buildup of smoke and light scattering in a cylindrical cavity geometry, considered to be an idealized representation of a photoelectric smoke detector. CFD coupled with the quadrature method of moments (QMOM) is used for simulation of aerosol dynamics. The Rayleigh-Debye-Gans-Polydisperse-Fractal-Aggregate (RDG-PFA) theory (Sorensen (2001)) is used for calculation of smoke extinction and angular light scattering. The major objective of the study is more to illustrate the application of a powerful tool for analyzing aerosol dynamics in practical devices than to investigate smoke detector physics.

3.3.1. Introduction and background.

Smoke detectors have been credited as being the single most influential technology in reducing the number of fire deaths over the past 30 years. The accurate detection of a fire often means the difference between safe egress and potentially life threatening conditions for people caught in structure fires. Consequently, during the

simulation of a fire scenario, the accurate prediction of the response of smoke detectors is crucial. Due to the scale and complexity of a fire event, methods for detector activation prediction have mostly relied on empirical techniques. A widely used method is the temperature correlation and the response time index (RTI) method (Heskestad and Delichatsios (1977a; 1977b), Benjamin et. al. (1979)). The temperature correlation method is based on the reasoning that heat generation and transport from a burning material to a sensing location is analogous to the smoke generation and transport from the fire to the sensor and therefore the temperature and smoke concentration must be correlated. The response is predicted using the RTI which is a measure of the sensitivity of the detector to temperature changes. Generally a temperature rise of 13°C above the ambient is used as the criterion for detector activation. The shortcomings of this approach have been discussed by Bukowski and Averill (1998). For effective detection of a fire one needs to accurately determine the total time associated with the ignition and growth of the fire, transit of the smoke or other combustion byproducts to a detector and the detector activation time. Simplified physical arguments have been used to derive correlations for the time scales associated with all of the above phenomena. A summary of these correlations is presented by Newman (1987). In particular, an empirical correlation for the detector response time based on a detector response function is given in Mulholland and Liu (1981). The correlation is developed for a particular smoke detector model. One of the objectives of this study is to compare detector response times obtained using this correlation with direct simulations. More detailed treatment like Computational Fluid Dynamics (CFD) can provide a more accurate prediction of fire detection times (Ierardi and Barnett (2003)). However detailed models involving the

coupled flow field and aerosol dynamics effects are only recently being considered (e.g. Snegirev et al. (2001)).

The two- parameter model for smoke detectors.

For an understanding of activation for a particular type of detector it is appropriate to focus on the smoke/aerosol properties (concentration, size distribution, index of refraction etc.) in the vicinity of the detector. The most widely used model for smoke detector activation assumes that activation is dependent only on the smoke concentration within the sensing chamber/volume inside the smoke detector housing. The sensing chamber/volume smoke concentration is modeled as a first order system that is coupled to an external smoke concentration with a time lag (e.g. Cleary et al. (2000)). A schematic of this model is shown in figure 3.3.1.

$$\frac{dC_s}{dt} = \frac{1}{\tau} (C_{s\infty}(t - t_e) - C_s(t)); t \geq t_e \quad 3.3.1$$

In equation 3.3.1 $C_s(t)$ is the smoke mass concentration inside the sensing chamber at time t and $C_{s\infty}$ is the smoke concentration external to the detector housing at an earlier time $t - t_e$. There are two time parameters t_e and τ in equation 3.3.1. The parameter t_e denotes the time lag that is associated with the entry and penetration of the smoke into the sensing chamber of the detector. Depending on the detector design, smoke has to be transported through an external detector housing consisting of filters, baffles and other obstacles used to block stray light (in the case of photoelectric detectors) from entering the sensing chamber. A model suggested by Heskestad (1975) is to use a plug flow model over an equivalent length scale, L_e . The entry time is given by:

$$t_e = \frac{L_e}{U_e}. \quad 3.3.2$$

The second time constant τ gives the mixing time or the time scale required for smoke concentration to reach the threshold for detector activation. Both these parameters depend on the geometry as well as the size distribution of the smoke and local convection velocity through the detector. If I assume that the external smoke concentration is constant then equation 3.3.1 can be integrated to give

$$\frac{C_s(t)}{C_{s\infty}} = 1 - \exp\left(\frac{-(t-t_e)}{\tau}\right) \quad t \geq t_e, \quad 3.3.3$$

$$\frac{C_s(t)}{C_{s\infty}} = 0 \quad t < t_e.$$

It may be possible to scale the mixing time parameter, τ , with the inlet velocity as

$$\tau = \frac{L_{mix}}{U_e}, \quad 3.3.4$$

where L_{mix} is a characteristic mixing length scale. One of objectives of this work is to test this hypothesis and determine L_{mix} using equation 3.3.4.

Another quantity of interest in detection is the extinction coefficient and it is usually assumed that the extinction coefficient is proportional to the concentration. Experimental characterization of smoke detectors involves the determination of the two time parameters (t_e and τ) or the length scale L_{mix} and threshold concentration $C_{sr}(t_r)$ by assuming a fit of the form 3.3.2 or 3.3.4 from which t_e and τ can be calculated (e.g. Bjorkman et al. (2002); Cleary et al. (2000)).

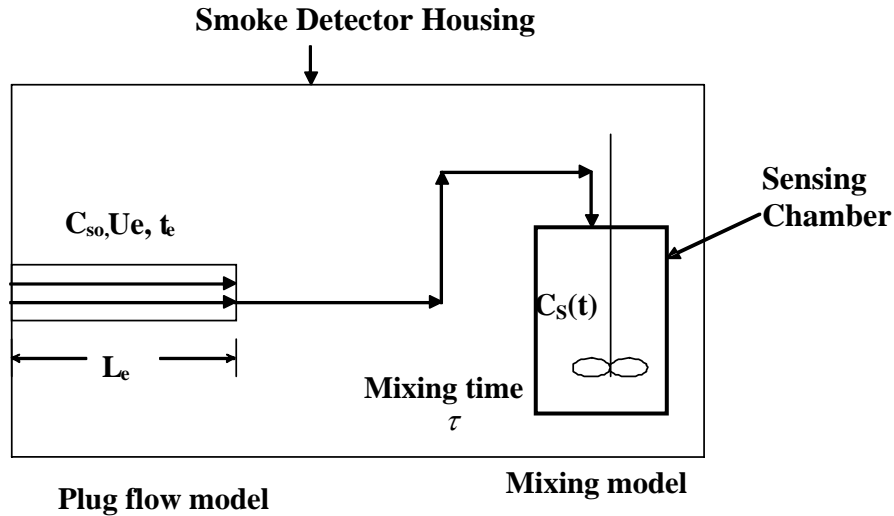


Figure 3.3.1. Schematic illustrating the first order, two parameter smoke detector model.

Motivations and scope of the present study.

In spite of the numerous experimental studies to characterize smoke detectors, the theoretical study of these processes remains a difficult task. This is due to the fact that smoke detector geometries as well as the physics associated with the detection process are complicated. Nevertheless, due to differences in design and the practical difficulties in experimentally characterizing each brand, a theoretical analysis of detector response involving first principles is clearly necessary. Due to advances in CFD and aerosol dynamics modeling, it is gradually becoming feasible to study smoke entry and build up as well as predicting detector response theoretically. Once a standardized methodology is available manufacturers can evaluate different designs without the need for expensive testing.

In this study, I focus on some basic phenomena that are important in most detectors of the photoelectric type. I perform a CFD study coupled with aerosol dynamics of the smoke accumulation in the sensing chamber. Due to the extreme variations in design, I ignore the time constant associated with smoke entry, t_e , and instead focus on the mixing process (i.e. the time scale τ). This allows us to focus on a simplified geometry that ignores the complications of the smoke entry process. The smoke entry problem is basically a CFD problem for which simulation tools exist. However, the detection process involves electromagnetic scattering for which specialized models need to be used. I therefore present calculations for the extinction coefficient and the angular distribution of light scattering from fractal agglomerates. Although I have chosen a simplified geometry, the purpose is to illustrate analytical methods that can be adapted to a wide range of detector designs.

3.3.2. Flow and aerosol model.

In this section I briefly describe the CFD model and the aerosol equations. A simplified geometry is used to model the smoke detector system (cf. figure 3.3.2). The computational grid shown in figure 3.3.2 is generated using the software Gambit 2.1. Hexahedral meshes are used for both the cavity and the external domain. The flow solver is capable of creating the grid interface between the two domains.

Unlike typical smoke detectors that consist of an external housing enclosing a smaller sensing chamber, I effectively consider a detector whose internal cavity is comprised entirely of the sensing chamber. For simplicity only one half of the detector is considered as the inflow and detector geometry are both symmetric with respect to the

vertical plane. The main flow is set up along the x -axis (from $-x$ to $+x$). The internal cavity has a radius of 7.5 cm and a height of 10cm. A LED light source and a photodiode

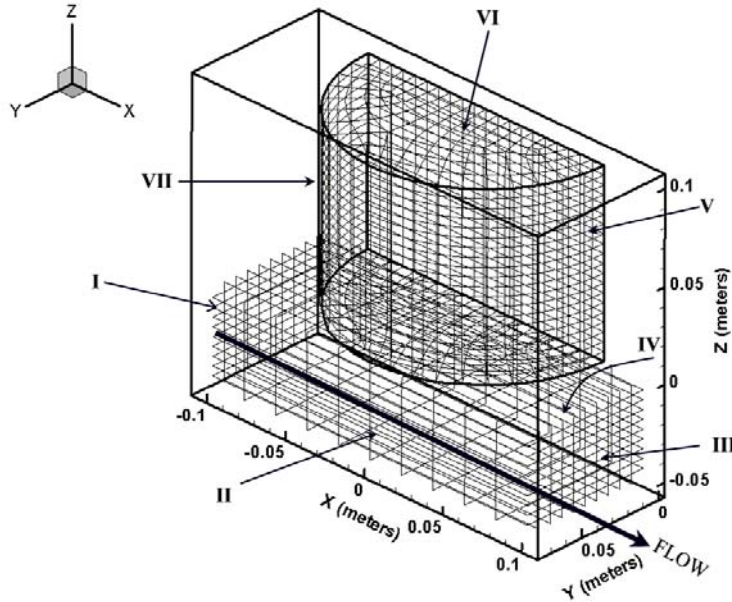


Figure 3.3.2. Geometry and computational grid. Flow direction is shown and the boundaries are labeled and referred to in Table 1.

Boundary	Flow Boundary Condition	Aerosol Boundary Condition
I	Fixed Inlet Velocity	Fixed inlet moments (lognormal distribution).
II	Symmetry	Symmetry
III	Constant pressure (Atmospheric pressure)	Zero gradients for the moments in flow direction $\vec{V} \cdot \nabla M_m = 0, m = 0,1,2,3;$
IV	Wall (no slip)	Perfectly absorbing wall $M_m = 0, m = 0,1,2,3$
V	Symmetry	Symmetry
VI	Wall (no slip)	Perfectly absorbing wall $M_m = 0, m = 0,1,2,3$
VII	Wall (no slip)	Perfectly absorbing wall $M_m = 0, m = 0,1,2,3$

Table 3.3.1. Summary of the boundary conditions used in the flow and aerosol dynamics simulation. (Boundaries are labeled in figure 3.3.2.)

are assumed to be placed at an elevation of 5cm (mid-height) within the cavity. The details of the scattering arrangement are given in the next section. Below the cavity, an external flow is simulated in a computational volume that is 20 cm in length, 7.5 cm in width and 4 cm in depth. As mentioned earlier I only consider the flow field at the location of the sensing chamber. The primary flow field induces a secondary recirculating flow within the cavity where the smoke detection takes place. This secondary flow is responsible for transport of the smoke to the location of the LED beam. The light scattered by the particles that are present in the path of the LED beam (i.e. the scattering volume at location s') is detected by a photodiode that is assumed to be placed at the polar angle, ϕ , on the cavity circumference (cf. figure 3.3.3). The internal flow within the smoke detector is simulated using a commercial CFD package (Fluent 6.1). The CFD solver has been benchmarked to solve the mass and momentum equations. The aerosol dynamics associated with the problem is considered next.

A user defined function has been included to solve the aerosol general dynamic equation (GDE). The GDE is discussed in section 2.2.1 (equation 2.4). The form of the GDE that I use in this study is:

$$\frac{\partial n(r_v)}{\partial t} + \frac{\partial}{\partial x_i} U_{f,i} n(r_v) + \frac{\partial}{\partial x_i} C_{s,i}(r_v) n(r_v) = \frac{\partial}{\partial x_i} D(r_v) \frac{\partial n(r_v)}{\partial x_i} + 1/2 \int_0^r \beta \left(\tilde{r}_v, (r_v^3 - \tilde{r}_v^3)^{\frac{1}{3}} \right) n(\tilde{r}_v) n((r_v^3 - \tilde{r}_v^3)^{\frac{1}{3}}) d\tilde{r}_v - \int_0^\infty \beta(r_v, \tilde{r}_v) n(r_v) n(\tilde{r}_v) d\tilde{r}_v, \quad 3.3.5$$

where the state of the particle (fractal aggregate) is assumed to be defined by its volume equivalent radius r_v . Comparison of equation 2.4 with equation 3.3.5 shows that I have neglected the surface growth terms that model nucleation and condensation as these phenomena are not important in smoke detector physics. The second term on the left hand side gives the convective transport of the smoke by the fluid flow. The flow field is obtained from the CFD solver. The term describes gravitational settling with terminal settling velocity $C_{S,i}(r_v)$. The first term on the right hand side gives the diffusion of the aerosol and the second term models the coagulation. For the problem under consideration, the effects of gravitational settling, diffusion and coagulation were found to be negligible. These aerosol evolution processes are important in the smoke generation and transport phases and ultimately determine the aerosol size distribution at the point of detector entry. The GDE is solved using a Quadrature Method of Moments (QMOM) formulation discussed in section 2.6. In QMOM the moment equations can be approximately closed once the integrals involving $n(r_v, t)$ are evaluated using quadrature sums. The QMOM equations corresponding to equation 3.3.5 are

$$\begin{aligned} \frac{\partial M_m}{\partial t} + \frac{\partial}{\partial x_i} U_{f,i} M_m + \frac{\partial}{\partial x_i} C_{S,i} M_m &= \frac{\partial}{\partial x_i} \left(D \frac{\partial M_m}{\partial x_i} \right) \\ + 1/2 \sum_{k=1}^{N_Q} \sum_{l=1}^{N_Q} [(\hat{r}_{v,k}^3 + \hat{r}_{v,l}^3)^{\frac{m}{3}} - \hat{r}_{v,k}^m - \hat{r}_{v,l}^m] \beta(\hat{r}_{v,k}, \hat{r}_{v,l}) W_k W_l, & \quad 3.3.6 \\ m = 0, 1, 2, 3, \dots & \end{aligned}$$

where $\hat{r}_{v,k}$ are the quadrature points and W_i are the quadrature weights. In this work, size dependence of diffusivity is not considered. An equivalent diffusivity evaluated for the average size of the particles is used. The effective diffusivity and settling velocity,

neglecting the slip correction, is given by $D = \frac{k_B T}{6\pi\mu\bar{r}_v}$ and $U_t = \frac{4\rho g\bar{r}_v^2}{18\mu}$ respectively. For

the size of the particles considered, the settling velocities are found to be much smaller than the smallest flow velocities encountered in the problem and thus gravitational settling is neglected. For instance, for the typical particle sizes considered in this work, the diffusivity is of the order of 10^{-11} m²/s, and the settling velocity is of the order of 10^{-5} to 10^{-6} m/s. Taking the radius of the cavity as a characteristic length scale, the

characteristic time scales for diffusion, $\tau_{diff} \sim \frac{R^2}{D}$ is of the order of 10^8 seconds. The

characteristic time for settling is approximately $\tau_{settling} \sim \frac{R}{U_t} \sim 10^4$ seconds. Both these

time scales are much larger than the maximum flow convective time scale,

$\tau_{flow} \sim \frac{R}{U} \sim 10^2$, considered in this study. The continuum Brownian kernel for fractal

aggregates is used. β for collision of two particles of volume v_i and v_j is given by

$\beta = \frac{2k_B T}{3\mu} \left(v_i^{1/D_f} + v_j^{1/D_f} \right) \left(v_i^{-1/D_f} + v_j^{-1/D_f} \right)$. Taking an average value of β , the

characteristic coagulation time is given by $\tau_{coag} \sim \frac{6\mu}{8k_B T \bar{v} M_0}$. Here M_0 is the first

moment and \bar{v} is the average volume of the aggregates. Calculations show that τ_{coag} is

much greater than any other time scale. As mentioned earlier surface growth and

nucleation effects are not considered. For the smoke detector problem considered in this

work only convective effects are dominant and the aerosol computations are very much

simplified.

As discussed earlier, the quadrature method of moments (QMOM) is an increasingly popular method for solving aerosol dynamics problems. This is because unlike other moment methods, there are no assumptions or restrictions on the form of the size distribution function. A further use of the QMOM is that other quantities of interest like the extinction coefficient and the intensity of scattered light can be approximated directly from the moments, M_m , that are obtained from solution of equations 3.3.6. For this particular problem, the coagulation, diffusion, and sedimentation terms are negligible, and the full capabilities of QMOM are not utilized. QMOM nevertheless appears to be a very useful tool for more sophisticated studies of smoke detectors. The number of quadrature points N_Q to be used in equation 3.3.6 is determined by the required accuracy of the quadrature sum in approximating the integral. The number of quadrature points must also be chosen such that other smoke properties that are approximated by quadrature sums are accurate. In this problem, the size distribution always remains lognormal due to negligible effects of diffusion and coagulation. A lognormal distribution can be completely specified using three moments. The smoke extinction coefficient and the angular intensity involve integration over the lognormal distribution and both are found to be accurately evaluated using two quadrature points. Therefore, in this study the two-point quadrature scheme ($N_Q = 2$) is used and the four moments M_0, M_1, M_2, M_3 are tracked.

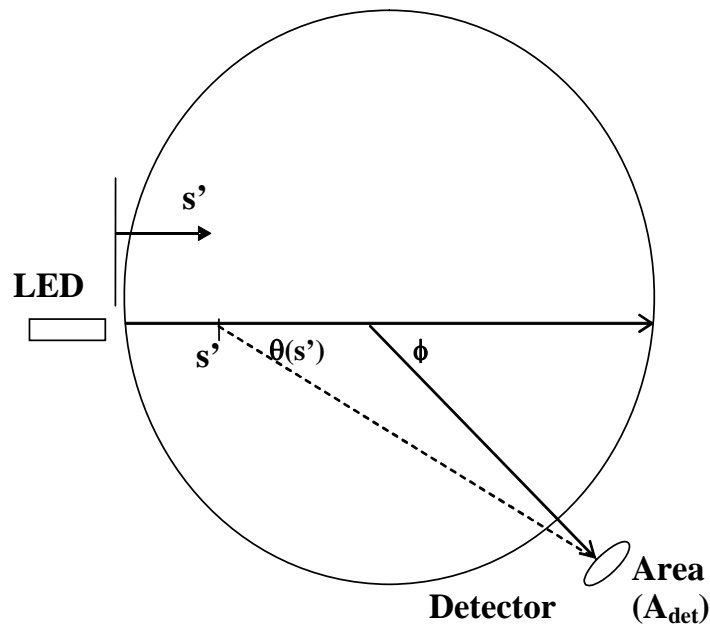


Figure 3.3.3. Schematic of the light scattering arrangement.

3.3.3. Light scattering model.

The photoelectric detector works on the light scattering principle. A light source, typically a light emitting diode, emits a beam towards a light stop. An alarm activation detector, typically at some angle, ϕ , to the beam in the scattering plane, measures light scattering to determine the presence of smoke particles. The geometry to be considered for the scattering model is shown in figure 3.3.3. The scattering arrangement is similar to that used in experimental studies of a photoelectric detector (e.g. Weinert et al. (2003)). A light beam from a LED source is shone across the chamber. If particles are present in the

chamber, they scatter light. The light scattered by the particles is incident on detectors placed on the periphery of the cavity. For this analysis I take an LED beam incident in a horizontal plane at the mid-height of the cylindrical cavity and calculate the angular scattering distribution along the outer circumference.

Light scattering from irregular particles is a complicated phenomenon. A complete characterization of the light scattered from soot or smoke requires the solution of Maxwell's equations. Due to the complexity of these equations, they have only been carried out for some basic shapes. However a simplification exists for computation of light scattering due to soot produced from flaming fires. In this case, it has been shown that the structure of soot aggregates is fractal (e.g. Sorensen et al. (1992)). It has also been shown that for these aggregates, the Rayleigh-Debye-Gans approximation is applicable (see for example Farias et al. (1995), Sorensen (2001)). The Rayleigh-Debye-Gans-Polydisperse-Fractal-Aggregates (RDG-PFA) approach considerably simplifies computations of the absorption and extinction properties of soot agglomerates as shown below. It must be mentioned that this approximation is valid only for soot produced from typical flaming fires. For smoke generated from smoldering combustion or other nuisance aerosols, this approximation is not valid as can be seen from the degree of polarization measurements presented in Loepfe et al. (1997) and Weinert et al. (2003). Computations using the more complicated Mie theory have only recently being carried out (Sorensen and Fischbach (2000)). In the following I briefly develop the equations for the absorption and scattering coefficients for fractal aggregates and present a methodology for computation of angular light scattering.

Extinction.

First the incident intensity along the LED light beam needs to be established. The general theory uses the total absorption and scattering cross sections. A soot cluster consists of a number of spherical primary particles distributed in a fractal cluster. The primary particles are assumed to be Rayleigh absorbers and scatterers. The total absorption cross section for an aggregate is the sum of the absorption cross sections of the Rayleigh particles (Nelson (1989)).

$$\sigma_{abs} = 4\pi Nka^3 E(m) \quad 3.3.7$$

In this equation N is the number of primary particles per aggregate, a is the primary particle radius and m is the complex index of refraction for soot. In this work, m is taken to be $1.54 + 0.48i$. This value is reported in Koylu and Faeth (1996) for soot generated by turbulent diffusion flames of hydrocarbon fuels. It is also mentioned that the refractive index is relatively independent of the type of fuel in the visible and infrared spectrum. The factor for absorption $E(m) = \text{Im}((m^2 - 1)/(m^2 + 2))$ and $k = 2\pi/\lambda$ where λ is the wavelength of the incident radiation. The differential scattering cross section is not simply the sum of the scattering cross sections of the individual Rayleigh particles because one has to consider the interference of light scattered by the individual primary particles. These effects are modeled by the use of a structure factor which contains the information about the spatial arrangement of the primary particles within the cluster. It is a function of the scattering wave vector, q ($q = \frac{4\pi}{\lambda} \sin \theta/2$) and a characteristic size of

the cluster usually taken to be the radius of gyration, R_g . The differential scattering cross section for incident unpolarized light is then written as (Sorensen (1997))

$$\frac{d\sigma_{scat}}{\partial\Omega} = N^2 k^4 a^6 F(m) \left(\frac{1 + \cos^2 \theta}{2} \right) S(qR_g) \quad 3.3.8$$

$$S(qR_g) = \left(1 + \left(\frac{2}{3D_f} \right) q^2 R_g^2 \right)^{\frac{-D_f}{2}} \quad 3.3.9$$

where $S(qR_g)$ is the structure factor, D_f is the fractal dimension of the aggregate. Various forms of the structure factor have been proposed in the literature. However they are not too different and for the sake of simplicity, the Fischer-Burford form (equation 3.3.9) is used in this study. The differential scattering cross section multiplied by the incident intensity gives the fraction of the total power scattered in a particular solid angle and hence is an important quantity in the study of angular light scattering. The total scattering cross section can be found by integrating over all solid angles. Details of the integration can be found in Sorensen (1997).

$$\sigma_{scat} = \int_0^{2\pi} \frac{d\sigma_{scat}}{d\Omega} d\theta \int_0^\pi \sin^3 \varphi d\varphi = \frac{8\pi}{3} N^2 k^4 a^6 F(m) G(kR_g) \quad 3.3.10$$

where

$$G(kR_g) = \left[1 + \left(\frac{4}{3D_f} \right) k^2 R_g^2 \right]^{\frac{-D_f}{2}} \quad 3.3.11$$

The differential scattering cross section depends on θ . The integration in equation 3.3.10 is non-trivial because the expression for the structure factor, which has a θ dependence, is usually complicated. To carry out this integration, the relatively simpler Guinier form

$(S(q) = 1 - \frac{q^2 R_g^2}{3})$ of the structure factor that is valid for small qR_g is used. The result is then modified to get an expression, $G(kR_g)$, that is valid for the entire range of qR_g . This approach is similar to the one used by Dobbins and Megaridis (1991) with the slight difference that my computation involves unpolarized incident light. Expressions 3.3.7 and 3.3.8 have been obtained for a cluster of a particular size. For a polydisperse population of aggregates, the expressions need to be integrated over the entire size distribution. The size dependencies are contained in N and R_g . In my calculations I have chosen the volume equivalent radius as the size parameter. The volume of the fractal cluster can thus be obtained and from it the two quantities, N and R_g :

$$N = \frac{v}{v_p} = \left(\frac{r_v}{a}\right)^3; v_p = (4/3)\pi a^3, \quad 3.3.12$$

$$R_g = a \left(\frac{N}{k_f}\right)^{\frac{1}{D_f}}. \quad 3.3.13$$

The values of the fractal prefactor ($k_f = 2.44$) and fractal dimension ($D_f = 1.8$) are taken from Koylu and Faeth (1994). The extinction for the entire population is determined by integrating over the size distribution. A particularly nice feature of the quadrature method of moments is that integrals over the size distribution can be easily and accurately approximated by quadrature sums. The value for the local population averaged extinction coefficient is then evaluated as

$$\bar{K}_{ext} = \int_0^{\infty} (\sigma_{scat}(r_v) + \sigma_{abs}(r_v)) n(r_v) dr_v = \sum_{i=1}^{N_Q} (\sigma_{scat}(\hat{r}_{v,i}) + \sigma_{abs}(\hat{r}_{v,i})) W_i \quad 3.3.14$$

Once the total absorption and scattering cross sections and the extinction coefficient have been determined, the intensity along the path length of the light beam can be easily found using an application of the Beer Lambert law.

$$I(s) = I_0 \exp\left(-\int_0^s \overline{K}_{ext}(s') ds'\right) \quad 3.3.15$$

I_0 is the incident intensity at $s = 0$. Computational results show that extinction is negligible for detector activation studies and attenuation along the LED beam can be ignored.

Angular light scattering.

I can finally calculate the angular variation of the scattered light intensity. Refer to the geometry for the light scattering shown in figure 3.3.3. In my analysis, the scattering plane is a horizontal plane at the mid-height of the cylindrical cavity. A source of incoherent, monochromatic light of wavelength, λ , equal to 632nm (usually a Light Emitting Diode (LED)) is placed at one location at the circumference such that the beam is along a diameter. The diameter of the LED beam is assumed to be equal to the width of a computational cell (i.e. 5mm). In practice there could be a divergence of the beam from the LED. In such a case the scattering volume becomes a conical region and light scattering computations must be carried out over all the cells lying in the scattering volume. In this study, the LED beam is assumed to be collimated.

A survey of different smoke detector designs revealed that there is a wide variation in the beam divergence as well as the wavelength of the LED. In most cases the beam divergence is small (around 10°-15°). Further, as most of the scattering into the

detector comes from the scattering volume close to the LED beam, the usually small angular divergence is ignored in this study. The beam diameter of 5mm is chosen by measuring the width of the aperture for a particular smoke detector model. The wavelength of 632 nm is characteristic of a red LED and also corresponds to the standard He-Ne lasers used by various researchers.

In the baseline case, a detector is placed at some global angle, ϕ , of 20° off the incident beam. The total intensity on a detector placed at this angle ϕ with respect to the center of the cylinder is given by the intensity scattered in that particular angle by all the particles along the LED beam. Consider a region at a distance s' along the beam. The intensity incident on it can be found from equation 3.3.15. For a single particle, the power

scattered per solid angle Ω at local angle $\theta' \equiv \theta(s')$ is given by $I(s') \frac{d\sigma_{scat}}{d\Omega}$ where

$\frac{d\sigma_{scat}}{d\Omega}$ is evaluated at θ' . The power received by the detector at the fixed angle

$\phi \equiv \theta(s' = R)$ (as shown in figure 3.3.3) is given by $I(s') \frac{d\sigma_{scat}}{d\Omega} \left(\frac{A_{det} \cos(\phi - \theta')}{r(s')^2} \right)$.

Note that $\cos(\phi - \theta')$ is required to create the projected detector area when viewed from s' . Accounting for the polydispersity of the scattering particles, one gets the scattered power at the detector by particles at a spatial location s' and within the scattering volume $A_s ds'$ as:

$$dP(\phi) = I(s') k^4 a^6 F(m) \left(\frac{1 + \cos^2(\theta')}{2} \right) \left(\frac{A_{det} \cos(\phi - \theta')}{r(s')^2} \right) \int_0^\infty N(r_v)^2 S(qR_g(r_v)) n(r_v) dr_v A_s ds' \quad 3.3.16$$

The total power at angle ϕ is found by integrating over the contributions from all the particles along the beam path as:

$$P(\phi) = \int_{s'=0}^{2R} \left[I(s') k^4 a^6 F(m) \left(\frac{1 + \cos^2(\theta')}{2} \right) \left(\frac{A_{\text{det}} \cos(\phi - \theta')}{r(s')^2} \right) \int_0^\infty N(r_v)^2 S(qR_g(r_v)) n(r_v) dr_v \right] A_s ds' \quad 3.3.17$$

where the factor for absorption $F(m) = \left| \frac{m^2 - 1}{m^2 + 1} \right|^2$. To evaluate detector response characteristics, the criteria used for detector activation is taken to be the power at the detector per unit power of the LED given by

$$P'(\phi) = \frac{P(\phi)}{I_0 A_s} \quad 3.3.18$$

In deriving expression 3.3.16 I am assuming that there is no intercluster scattering and the scattered intensity travels to the detector without any attenuation. This is justified because the smoke volume fraction within the detector is usually sufficiently small given that the detector would sound before the concentration levels become high enough for intercluster multiple scattering. As described later, my choice of the critical power for detector activation gives an optical thickness less than 10^{-3} . The medium is certainly optically thin up to the moment at which the detector sounds. The evaluation of the scattered power received at the detector is as far as one can go in the prediction of the activation time from first principles. The alarm threshold is set by the electronics of the photodiode, which varies between different manufacturers.

3.3.4. Simulations and results.

Simulations of the smoke entry, accumulation and detection are carried out for a range of flow velocities and particle volume fractions. A plug flow velocity profile is used as the input boundary condition at the location $x = -0.1$ m (in figure 3.3.2). The flow is simulated using a commercial CFD package (Fluent 6.1). Taking the radius of the cavity as a characteristic length scale, the maximum Reynolds number is around 3000. The main flow is essentially an external flow past a flat plate. The velocities inside the cavity are even smaller. Therefore the flow is laminar for all the velocities considered. The boundary conditions used in the simulation are summarized in Table 3.3.1. For the particles, the inlet condition is a fixed lognormal distribution of fractal particles characterized by the volume equivalent radius. The geometric mean volume equivalent radius and the geometric standard deviation are taken to be 0.15 and $2\mu\text{m}$ respectively for a wide range of volume fractions. For fractal aggregates, the mean radius of $0.15 \mu\text{m}$ corresponds to $N = 400$ for a primary particle radius, $a = 20\text{nm}$. For this N and with $D_f = 1.8$, $R_g = 0.36\mu\text{m}$. These values are characteristic of soot produced from flaming hydrocarbon fuels and have been reported in Koylu and Faeth (1994). To predict the detector response I assume that a LED shines across the cavity diameter at the plane of symmetry ($y = 0$) and at the mid height ($z = 0.05\text{m}$). A detector is assumed to be placed at the circumference at an angle of 20° to the incident beam. The scattered field is calculated using a series of steps. First a steady state flow profile is obtained from the CFD calculation. Then the aerosol calculations are carried out in a time dependent manner in the presence of the steady velocity profile. The outputs of the calculation are

the temporally and spatially varying moments of the particle size distribution. The moments along the spatial direction of the incident LED beam are used in the scattering analysis to determine the scattered intensities at the light detector location.

Features of the flow field.

The flow is predominantly responsible for transport of smoke into the detector and hence I include a brief description of the flow field. Due to negligible inertial effects, all particles move at the same speed as the fluid. The flow field generated inside the cavity at the plane of symmetry due to the outside flow is shown in figure 3.3.4a. The x - and z - components of the velocity are shown as a detailed look at the flow field revealed the y -velocity component to be much smaller than the other two. The external flow field is entrained near the base of the cavity and is pushed upwards at the wall. This induces a counterclockwise recirculating flow inside the cavity. The same type of profile was observed at different vertical planes parallel to the one shown. Figure 3.3.4b shows the component of the velocity along the z -direction that is responsible for transporting the smoke into the sensing chamber. Almost all the particles enter at the right and are transported up. Figure 3.3.5 shows the x - y velocity vectors at four different horizontal planes inside the cavity. These velocity components are responsible for horizontally dispersing the particles that are transported inside by the vertical (z -) velocity. Near the base of the plane and slightly upward the flow is in the $+x$ direction. At a certain height the flow reverses due to the recirculation and flows in the $-x$ direction. This motion aids in filling up the cavity uniformly with particles. The same flow features are seen for a

wide range of values of the inlet velocity. At very low inlet velocities (~ 0.001 m/s), the smoke entry process differs. Smoke enters from the left and exits from the right.

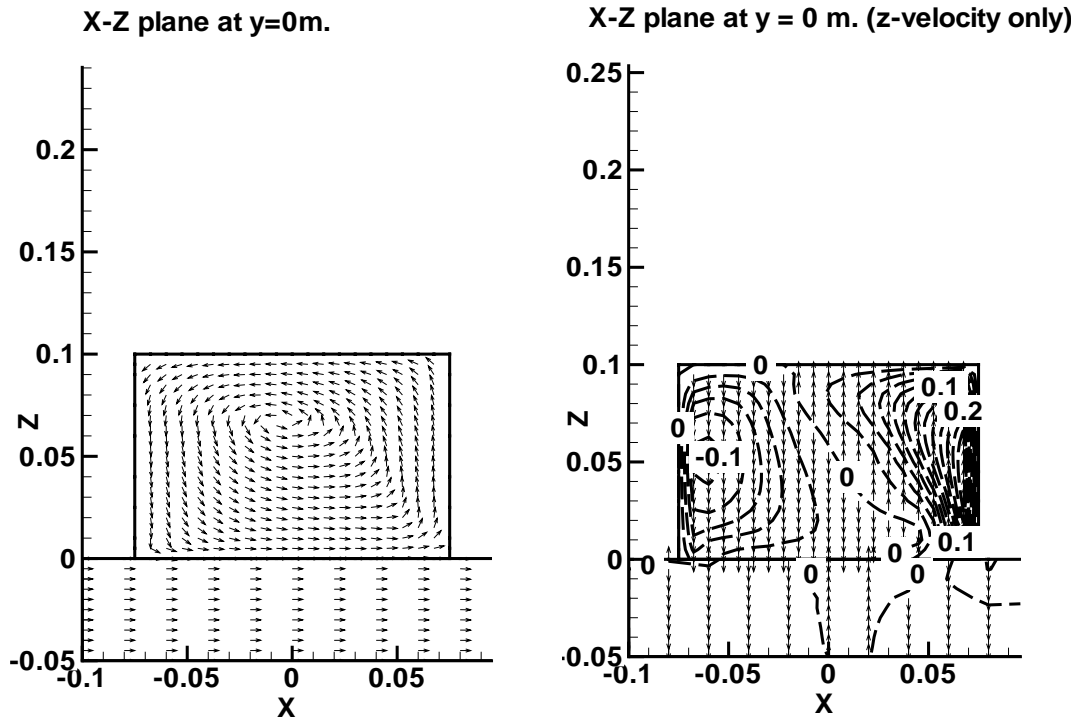


Figure 3.3.4 (a) X- and Z- velocity vector components at the plane of symmetry at $Y = 0.0$, (vector lengths are equal and do not show the magnitude). (b) Z-velocity component at the plane of symmetry at $Y = 0.0$.

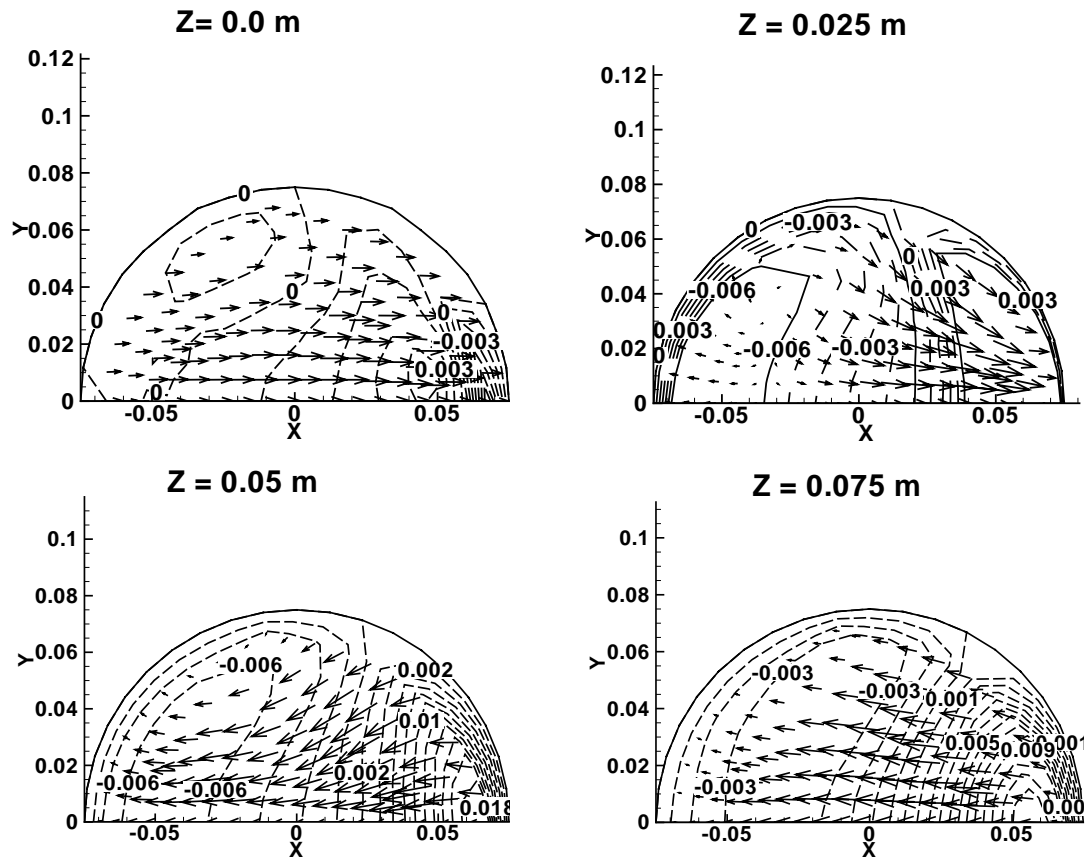


Figure 3.3.5. Plots of X-Y velocity vectors at the four different horizontal planes at $Z = 0.0\text{m}$, $Z = 0.025\text{m}$, $Z = 0.05\text{m}$ and $Z = 0.075\text{m}$. Z-velocity contours are also shown.

Smoke buildup within the detector.

I first examine the buildup of smoke at the scattering volume along the LED beam ($y = 0, z = 0.05\text{m}$). Figure 3.3.6 shows the volume fraction profiles at different times for free stream smoke volume fraction of 10^{-9} and inlet velocity of 0.1 m/s . It is seen that flow processes are largely responsible for the smoke distribution within the cavity. For instance the flow enters the cavity towards the right (close to $+7\text{ cm}$ in figure 3.3.2) and

that is where the smoke first begins to build up. Some of the smoke is then transported across the detector by the velocity in the $-x$ direction. After the flow loops around the cavity, smoke starts to appear at the opposite end and a second hump begins to grow.

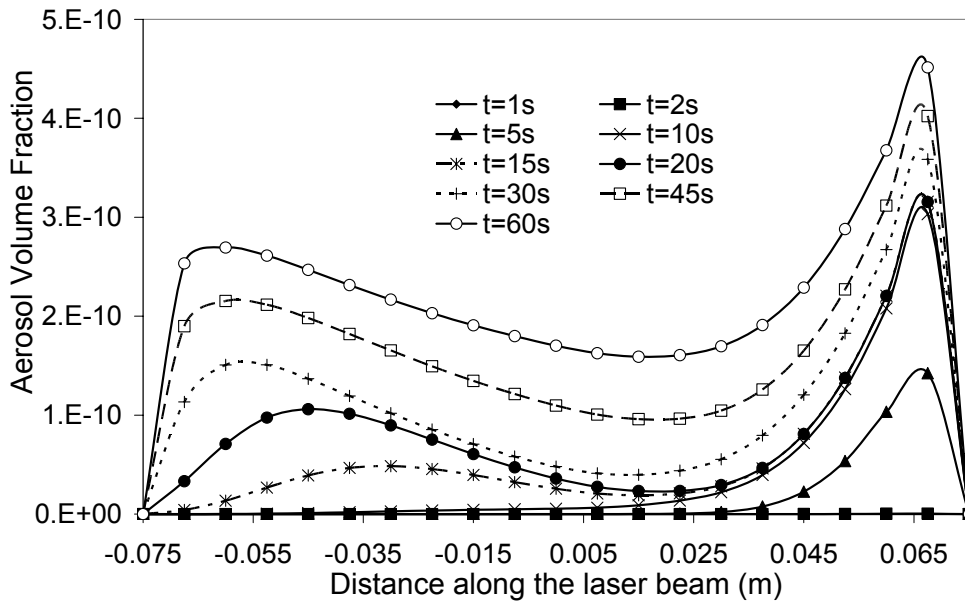


Figure 3.3.6. Variation of volume fraction with distance at the mid height of the cavity for various times. Volume fraction of the free stream is 10^{-9} .

Light scattering by smoke particles.

The angular distribution of the power due to scattering is computed using the methodology outlined in section 3.3.3. Figure 3.3.7 shows the attenuation of the incident intensity along the LED beam when the inlet volume fraction is 10^{-9} and the inlet velocity is 0.1 m/s. There is very little attenuation in this case. Figure 3.3.8 shows the variation in scattered power with angle along the circumference of the cavity for inlet volume fraction of 10^{-9} . There is a slight increase in the scattered power with time. The strong forward

scattering is due to the structure factor and it distinguishes the scattering from fractal aggregates from Rayleigh scattering. There have been numerous experimental measurements of the extinction coefficient of fractal shaped soot aggregates obtained from different hydrocarbon fuels. A check on the computations for the extinction coefficient can be made by comparison with the experimental results compiled in Widmann (2003). The mass specific extinction coefficient (σ_s) can be calculated from equation 3.3.14 as $\sigma_s = \bar{K}_{ext} / \rho, \rho \approx 1.8g/cc$. For the wavelength $\lambda = 632nm$ (and using typical values for the other parameters), $\sigma_s \lambda = 2.9 \times 10^{-6} m^3 g^{-1}$ while the empirical correlation given by Widmann (2003) is $\sigma_s \lambda = 4.808 \times 10^{-6} m^3 g^{-1}$. This discrepancy is mostly due to uncertainty in the refractive index of soot. For instance in the experimental study by Dobbins et al. (1994), at $\lambda = 630nm$ σ_s is reported as $7.8m^2g^{-1}$. They could get the same value from their theoretical computation only by setting the refractive index $m = 1.55 + 0.780i$. Using $m = 1.55 + 0.780i$ in (14), one gets $\sigma_s = 7.4m^2g^{-1}$. This small difference is possibly due to the simplified expression used by Dobbins et al. (1994) to compute the total scattering cross section. However, in this work the extinction is not significant and the slight error in its computation can be disregarded. My choice of the refractive index ($m = 1.54 + 0.48i$) probably leads to some error in the computation of the angular scattering as well. Due to uncertainty in the value for the refractive index for smoke, this error is not easy to quantify.

Since the scattered intensity is not exactly computed but is obtained from a quadrature approximation, it is necessary to test its accuracy. As mentioned earlier, due to

negligible effects of agglomeration, the distribution does not change (i.e. remains lognormal) and therefore higher moments can be calculated from any three moments. Results shown in figure 3.3.9 for the angular variation of scattered power show that there is a trivially small difference between two-point and higher point approximations. This is remarkable considering that the intensity has an M_6 dependence which is very accurately approximated using moments up to M_4 as in the 2-point scheme. In more realistic simulations of smoke detectors, where there may be more complex flow and diffusion effects and arbitrary size distribution of smoke, the accuracy of low order moment approximations would greatly simplify the simulations.

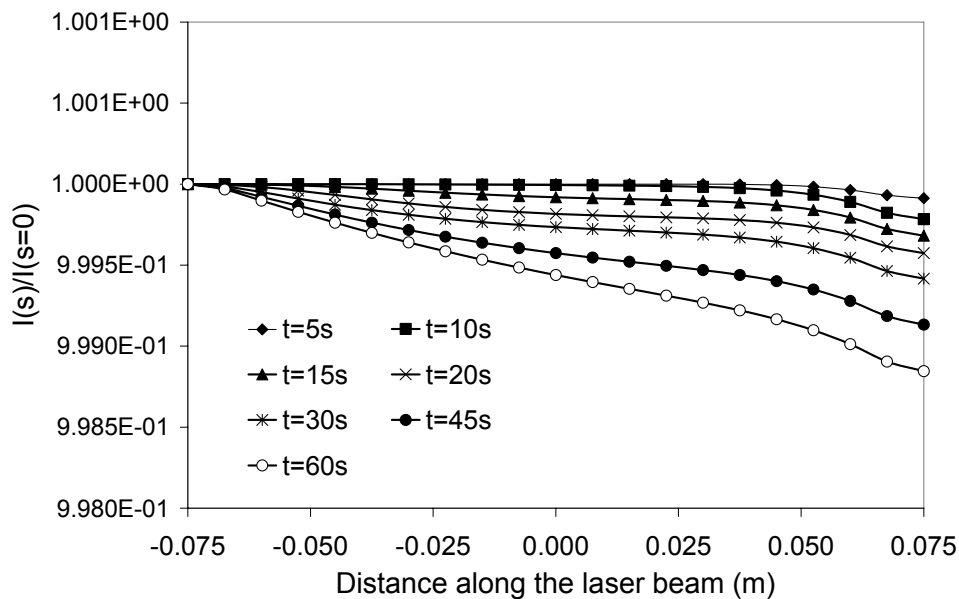


Figure 3.3.7. Variation of normalized intensity with distance at the mid height of the cavity for various times. Volume fraction of the free stream is 10^{-9} .

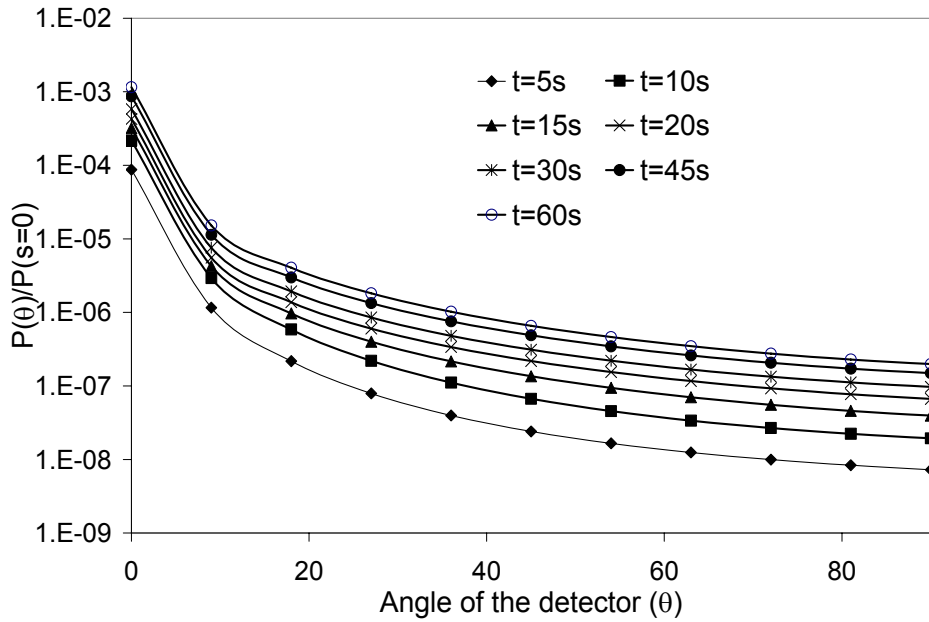


Figure 3.3.8. Variation of scattered power at the circumference of the cavity with angle at mid-height for different times. Volume fraction of the free stream is 10^{-9} .

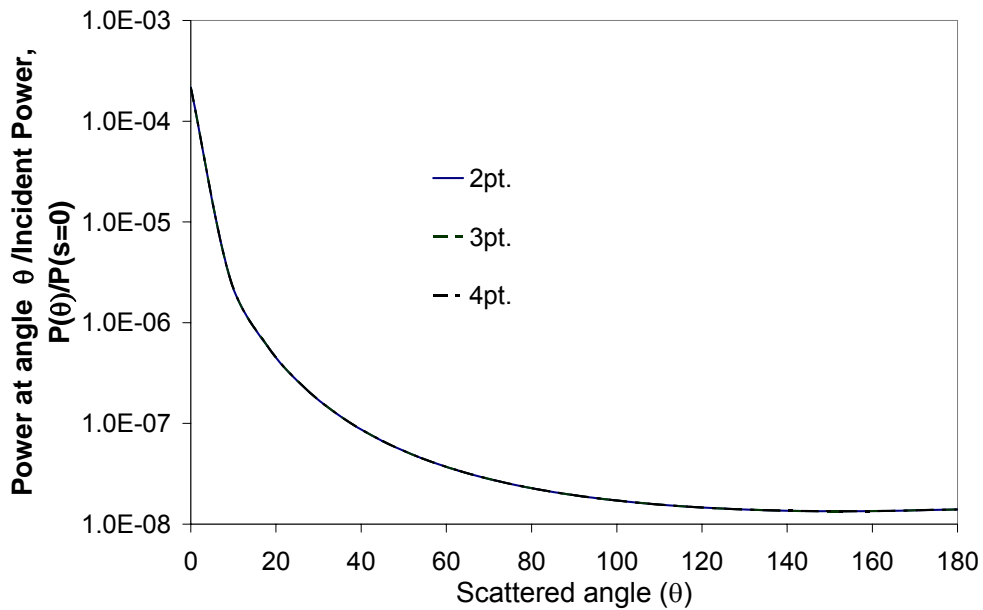


Figure 3.3.9. Comparison of the angular scattering computed using 2-point, 3-point and 4-point quadrature approximations. Differences are too small for the three profiles to be distinguishable.

3.3.5 Detector response study.

The objective of any analysis on smoke detectors or other similar geometries is to predict the detector response time. While the analysis presented above enables the computation of the scattered power falling on the photodiode, a translation of the incident power to a detector signal is required. In a typical operation, the photodiode converts the scattered LED power incident on it into an electric current that upon reaching a certain threshold value, causes the alarm to sound. The relation between the incident power and the output current is usually linear but the threshold current depends on the electronics and varies widely. Consequently, for a theoretical study, an arbitrary choice must be made. A fixed value for the incident power per unit power of the source (LED) (hereafter referred to as the critical power, P'_{cr}) is chosen as the threshold criterion. Then the time taken to reach this critical value is assumed to be the detector response time. Another empirically based method has been suggested by Mulholland (1995). It involves use of a detector response function, $R_{det}(d)$, which when integrated over the size distribution gives the detector output voltage. The parameter d represents the volume equivalent diameter of the fractal aggregate. To compare with the calculations based on the light scattering analysis, I use a correlation for $R_{det}(d)$ developed for a particular photoelectric smoke detector in Mulholland and Liu (1980). I evaluate the output voltage, p , by integrating over the smoke size distribution in the same scattering volume (i.e. along the LED beam).

$$p = \frac{1}{2R} \int_{s'=0}^{2R} \int_{\bar{d}=0}^{\infty} R_{det}(\bar{d})n(\bar{d})(s')d\bar{d}ds' \quad 3.3.19$$

$$R_{det}(\bar{d}) = 1312\bar{d}^{5.7} \quad 3.3.20$$

The integral for p in equation 3.3.19 is computed by a quadrature sum using the known quadrature points and weights. For this particular model, the detector sounds when $p \geq 2$ volts (Mulholland and Liu (1980)).

Figure 3.3.10 is the log-log plot showing the variation of the activation time with the velocity. Due to the arbitrary choice of the threshold signal only the comparison of the trends are meaningful. Calculations for t_{act} using the scattering computations closely match the calculations using the detector response function for $P'_{cr} \approx 10^{-6}$. As P'_{cr} increases to around 10^{-6} , there is a slight deviation from the power law behavior at around $U_e \sim 0.1$ m/s. For lower values of P'_{cr} , the light scattering calculations reveal a power law variation of the activation time, t_{act} , with velocity, U_e , given by $t_{act} \sim CU_e^{-1.12}$. The data for the entire range of velocities for different threshold criteria can be fit reasonably well with a power law given by $t_{act} \sim CU_e^{-m}$, $m \approx 1$, with a prefactor C that varies according to the threshold intensity criterion. These results indicate that at least for this particular geometry, a simple scaling for the mixing time as $t_{act} = \frac{L}{U_e}$ may be adequate.

Figure 3.3.11 shows the comparison of the detector response time with the smoke volume fraction at the inlet. The trends using the two different calculation procedures are again similar for $P'_{cr} \approx 10^{-6}$ for a wide range of inlet volume fractions. The two curves begin to deviate at very low volume fractions ($f_v \sim 10^{-10}$ onwards). At lower P'_{cr} , the light scattering computations show a power law for the activation time in terms of the volume fraction as $t_{act} \sim Cf_v^{-0.09}$. However as P'_{cr} is increased, the power law is only applicable at

higher volume fractions. For example figure 3.3.11 shows that with $P'_{cr} = 10^{-7}$, the power law scaling begins to break down at $f_v \sim 10^{-9}$ and for $P'_{cr} = 10^{-6}$, it breaks down at $f_v \sim 10^{-8}$. For these cases, the response time increases faster than a power law for decreasing volume fractions. It is interesting that I observe similar trends for the activation time variation with smoke volume fraction using two different computational methods: a CFD with scattering calculations and an empirical detector response function calculation. This can be explained by analyzing the activation criterion in more detail. The activation signal computed using equation 3.3.19 depends on the $M_{5.7}$ moment. The moment dependency for the light scattering is not so easy to evaluate. For the Guinier regime (small qR_g), equation 3.3.17 gives an $M_6 - \frac{q^2}{3} \cdot M_{6+\frac{12}{D_f}}$ dependence for the scattered intensity at a particular angle. However, for the power law regime (large qR_g) an M_6 dependence is expected. Using these scalings I can imagine that if the smoke sample contains only small particles or if q is small (i.e. small scattering angles), then the scattered intensity is proportional to M_6 . In this case it is reasonable to expect similar trends between the two types of calculations for the activation time. An interesting observation from figure 3.3.11 is that for the range of inlet velocity and volume fraction where a power law behavior is applicable, the value of the exponent is almost the same for all the curves.

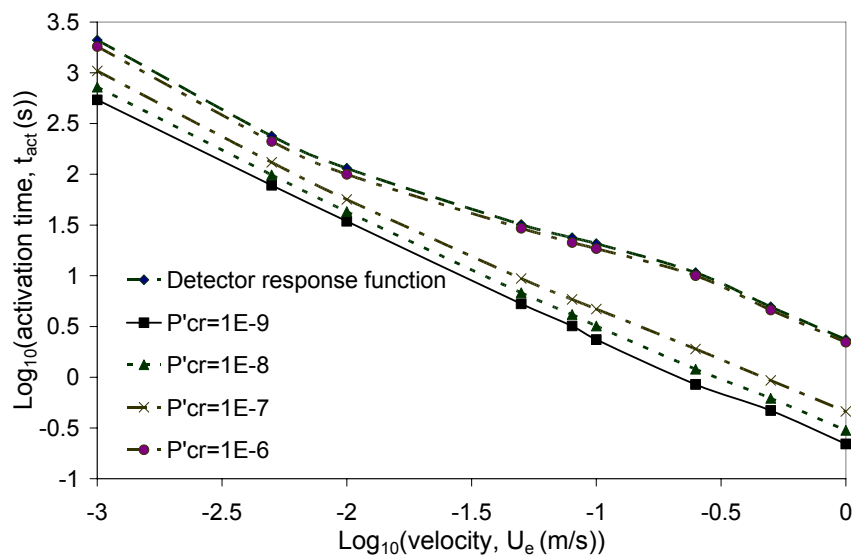


Figure 3.3.10. Log-log plot showing the variation of the detector activation time with velocity at the inlet. Comparison of the results obtained using the light scattering calculation (equation 3.3.18) and the detector response function (equation 3.3.19) for different choices of the threshold power, P'_{cr} .

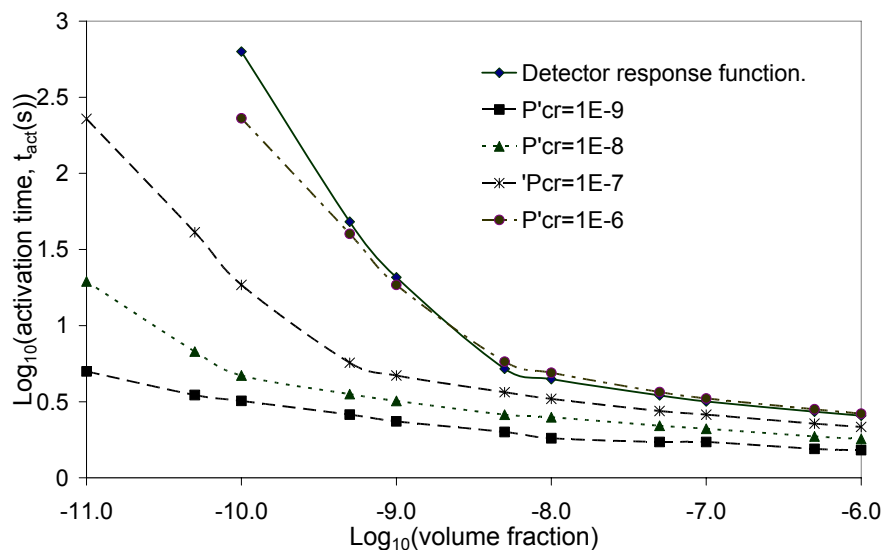


Figure 3.3.11. Log-log plot showing the variation of the detector activation time with smoke volume fraction at the inlet. Comparison of the results obtained using the light scattering calculation (equation 3.3.18) and the detector response function (equation 3.3.19) for different choices of the threshold power, P'_{cr} .

The CFD analysis and the light scattering computation allow a check on the validity of the assumptions leading to equation 3.3.3. This equation represents a model for a perfectly stirred mixing process. The volume fraction is proportional to the mass concentration and so equation 3.3.3 can be rearranged to give the following

$$\frac{t - t_e}{\tau_{mix}} = -\ln\left(1 - \frac{f_v(t)}{f_{v\infty}}\right) \quad 3.3.21$$

There are two unknowns t_e and τ_{mix} . The characteristic mixing time τ_{mix} can be determined by computing an average volume fraction \bar{f}_v obtained from CFD calculations

(given by $\bar{f}_v(t) = \frac{1}{V_{cav}} \int_{V_{cav}} f_v(\vec{x}, t) dV_{cav}$) for the entire cavity and fitting the variation of

$\frac{f_{v\infty} - \bar{f}_v(t)}{f_{v\infty}}$ with an exponential curve. The results shown in figure 3.3.12 show a very

good agreement with the basic model (equation 3.3.13) for the entire range of inlet velocities. The data from figure 3.3.12 shows that τ_{mix} scales as

$\tau_{mix} \sim 20.3U_e^{-0.97} \approx 20.3U_e^{-1}$. Comparison with equation 3.3.4 shows that $L_{mix} = 20.3m$

for this particular geometry. For a chosen fixed velocity, the mixing time τ_{mix} can then be

obtained. Supposing that there is a single critical volume fraction for detector activation

$f_v(t_{act})$, then t_{act} can be computed as a function of inlet volume fraction using equation

3.3.21. I fix $f_v(t_{act})$ for each case by assuming this relation holds for $f_{v0} = 10^{-10}$ and

using t_{act} computed from the CFD simulation. The other unknown parameter, t_e , is

obtained by a best fit of the data for t_{act} (obtained from direct simulations) to equation

3.3.21. Figure 3.3.13 shows a plot of activation time with external volume fraction calculated using equation 3.3.21 for free stream velocity of 0.1 m/s and 1m/s. It is seen that the detector activation times calculated using equation 3.3.21 are very similar to the activation times obtained using the full CFD and light scattering model. Further under the assumption that t_e is specified as in equation 3.3.2, values of L_e between 0.3m and 0.35m give the best fit for a wide range of inlet velocities. These values are of the order of the maximum size of the computational model (figure 3.3.2). However the most obvious choice of $L_e = L/2$ with L being the maximum size of the computational domain shown in figure 3.3.2 does not give a good fit.

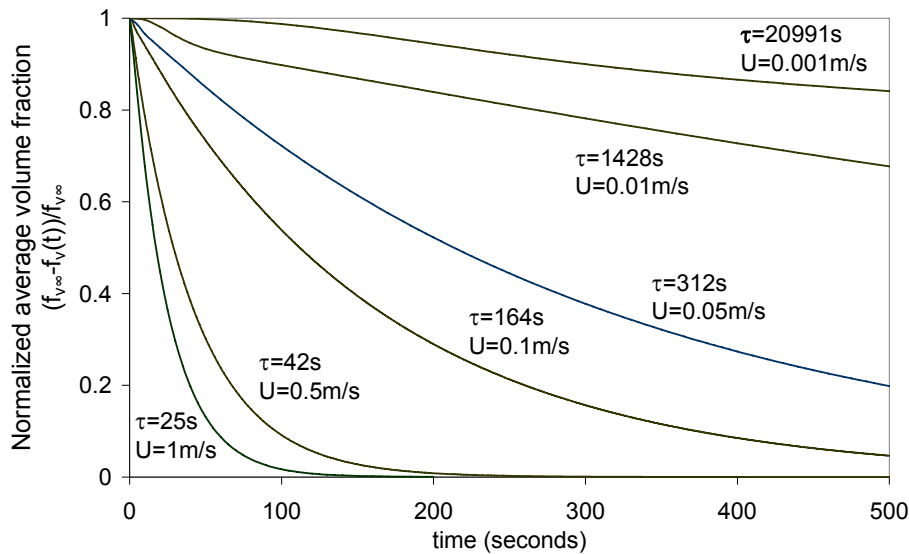


Figure 3.3.12. Plot of the averaged and normalized volume fraction with time for different velocities to evaluate the mixing time scale parameter τ .

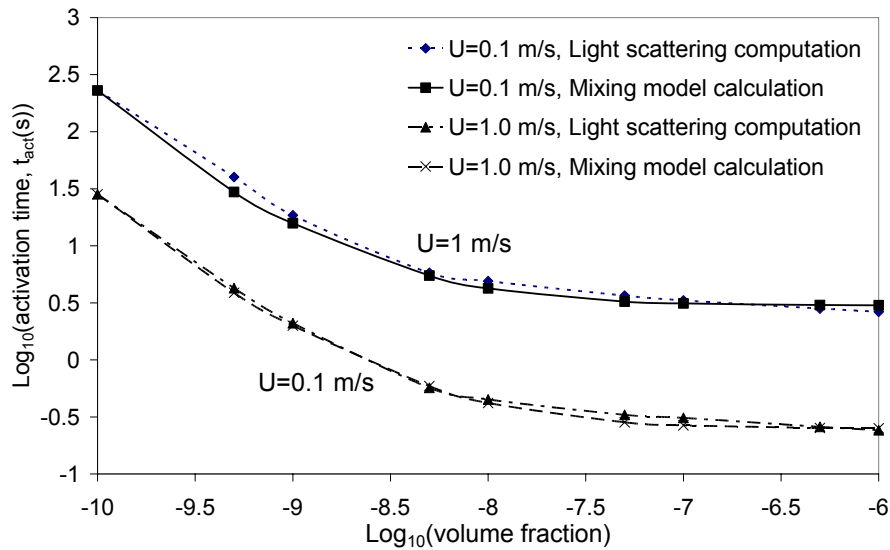


Figure 3.3.13. Log-log plot showing the variation of the detector activation time (calculated using equation 3.3.18) with smoke volume fraction at the inlet, free stream velocity is 0.1m/s and 1m/s. Also shown are the best fits of the data to equation 3.3.21 obtained from the simple model (equation 3.3.3).

Figure 3.3.6 shows that smoke volume fraction is not uniform inside the cavity, especially at short times when the detector activates. Even though the spatial and temporal distribution of smoke inside the cavity is not homogeneous, for this particular geometry, the two parameter first order model given by equation 3.3.2 and 3.3.3 is seen to work very well for the prediction of detector activation time.

The size distribution of the smoke that enters the detector can be quite different from the size distribution of the smoke at the location of the fire due to agglomeration during the transit from the fire to the detector. In figure 3.3.14, I plot the variation in activation time with volume fraction for different geometric mean radius and geometric standard deviation. For larger volume fractions there is no difference in the activation time while for smaller volume fractions $f_v \sim 10^{-10}$, some differences can be seen. I see

that the activation time is almost independent of the geometric mean radius, r_g , as the geometric standard deviation, σ_g , (polydispersity) becomes higher. For the monodisperse case and for lower values of σ_g , it is seen that detector activation time decreases with increasing r_g . The activation time decreases with increasing polydispersity due to the increased scattering from the larger sized particles. However, the differences are not substantial since the results are plotted on a linear scale. It is important to note that these results apply only for fractal aggregates and differences in aerosol morphology could affect the response time. Computations also showed that detector activation time does not vary significantly with primary particle size.

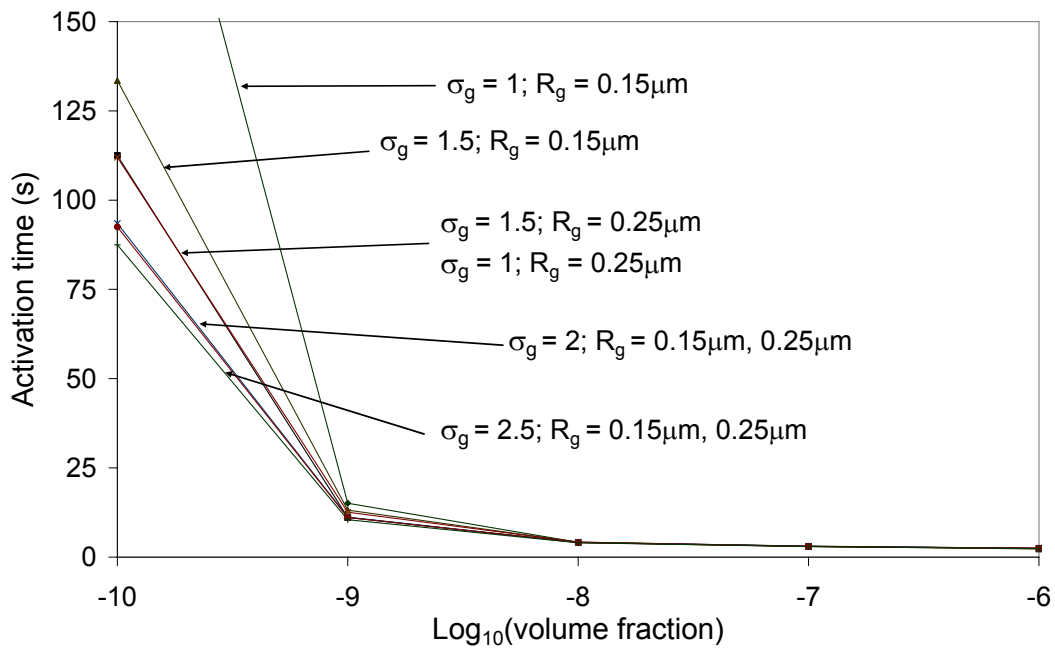


Figure 3.3.14. Plot of the activation time with logarithm of the volume fraction for different values of the geometric mean radius and the geometric standard deviation. The free stream velocity is 0.1 m/s.

3.3.6. Conclusions.

A coupled CFD and aerosol dynamics simulation of smoke entry and accumulation processes in a cylindrical cavity geometry was carried out. The geometry and the flow represented an idealized smoke detector. It was seen that for this configuration, flow processes determine the distribution of smoke inside the cavity. Flow enters the cavity by entrainment, it is pushed up at one side setting up a recirculating flow inside the cavity. The same type of flow was seen for a wide range of inlet velocities. Light scattering calculations were carried out using the RDGPFA model for fractal agglomerates. Attenuation is weak for inlet volume fractions around 10^{-9} and hence the light scattered is also weak. I found that for higher inlet volume fractions (around 10^{-6}), there is pronounced attenuation but the detector responds long before the attenuation effects become significant. Therefore, a simple model for the attenuation and scattering that ignores multiple scattering is applicable.

A detailed CFD study has been used to test the validity of the simple mixing model (equation 3.3.3) that is widely used in the empirical characterization of smoke detectors. My calculations indicate that this model is accurate to predict the average mass concentration or volume fraction inside the cavity as well as the detector response time for mass fractal aggregates. This is particularly useful as the detector response time appears to depend very weakly on the size distribution parameters. Even though the spatial distribution of smoke inside the cavity is not homogeneous, it may still be possible to define a single average volume fraction or smoke concentration as a threshold. However the parameters τ and t_e appearing in the simple model do not seem to be directly related to any geometric length scale of the problem. The manner of entry of the

smoke and its spatial variation within the sensing chamber may have to be considered only for the purposes of designing smoke detectors with faster response times. The results I have obtained are only for a very simple idealized model of a smoke detector. It is necessary to extend the type of analysis presented in this paper to more realistic smoke detector geometries and for different types of smoke to get a clearer understanding of how smoke entry and accumulation affects detector response time. The coupling of a general moment method like QMOM to a computational fluid dynamics package will allow more detailed evaluation of aerosol detector physics. Considering the importance of accurate prediction of smoke detector activation time, it is also desirable to check whether the simple model that is widely used in experimental characterization of smoke detectors is always applicable.

Chapter 4: Applications of QMOM and DQMOM to problems in uncertainty propagation and turbulent mixing and reaction.

One sees from the previous chapter that problems in aerosol science lead directly to the application of population balance modeling concepts. In this chapter I extend the field of application to problems in which there is no physical collection of particles to define a population. In the examples considered in this chapter, the population involves abstract entities such as events or conditional particles. These applications come under the broad category of stochastic modeling and simulation. Without getting into the rigorous definitions from probability theory and stochastic processes, I provide a brief and informal discussion.

The problems I am interested in are either deterministic processes with random initial conditions or stochastic processes. The first category of problems arises when one has a deterministic model that can be used to describe the time evolution of the dynamics of a system but one cannot specify the initial conditions in a precise manner. To describe the state of the system at a later time one needs to consider the evolution of the system starting from all the possible initial conditions. However with a particular initial condition, the dynamics is completely deterministic. In the second category of problems, the state of the system at a later time is not completely determined by its present state. This could be due to the dynamics itself being chaotic and unpredictable. The stochasticity could also arise because external influences, that have been neglected in constructing the model, do affect the evolution of the system and these effects cannot be ignored. This leads to a stochastic differential equation whose solution requires special

techniques. For these problems, even if the initial condition is exactly specified, the stochastic nature of the dynamics causes the solution at later times to be stochastic.

In this section I discuss some examples illustrating both types of problems. My objective will be to evaluate the applicability of quadrature based moment methods to tackle these problems. For the first type, I consider a design problem in fire safety engineering. The issue is to incorporate the uncertainty in the fire size into a model that is used for simulating a compartment fire. As a representative example for the second class of problems, I consider the problem of turbulent mixing and combustion. I will discuss the motivation for using PDF based methods for turbulence and the models that are currently used for closing the PDF transport equations. The main objective of this work is to apply the theory of multivariate direct quadrature method of moments by simulating the turbulent mixing and chemical reactions in a partially stirred reactor.

4.1 DESIGN FIRE EVALUATION USING THE QUADRATURE METHOD OF MOMENTS.

4.1.1. Introduction and Background.

Performance based fire design (Pbfd) stipulates that a building must satisfy some performance requirement. That is, the fire safety of the building must be evaluated before the building can be deemed fit for occupancy (e.g. Buchanan (1999)). This is normally done by simulating fire evolution in a structure and evaluating safety criteria, such as the height of the smoke layer at some critical time after the start of the fire. The fire model typically consists of a design fire, i.e. a typical fire with a typical rate of heat release. However, the use of a single design fire while simulating a fire scenario may be inadequate. The type of combustible materials in a room, their arrangement and the point

and source of ignition are unpredictable. To account for this variability, the use of a single representative fuel has been proposed in Yung and Benichou (2002). This is a single fuel source, located at a center of the room, having the same heat release rate characteristics as the actual distribution of combustible material in the room. The single representative fuel source may be considered to be an average of the actual distribution of fuel sources. Due to the extreme variability in the type of fire that can occur in any modern building compartment, a single average representative fuel source may not be sufficient to characterize all the possible fire scenarios, and therefore one may have to consider a distribution of fire sizes. Furthermore, there are many other uncertainties such as operation of safety devices such as smoke detectors and sprinklers, opening or closing of vents etc. An early discussion of the uncertainties inherent in fire safety design is given by Watts (1986). In recent years there have been systematic studies to incorporate the uncertainty inherent in the variables relevant to any given design fire. A thorough discussion of existing techniques is provided in Notarianni (2002). In this study, I investigate a very general mathematical technique that can be used to simulate the propagation of uncertainty of any variable that is used in a fire model. To this point my discussion of the use of probabilistic methods for performance based design analysis has been quite abstract. A more physically based example is provided to explore the use of the techniques and the value of the outputs.

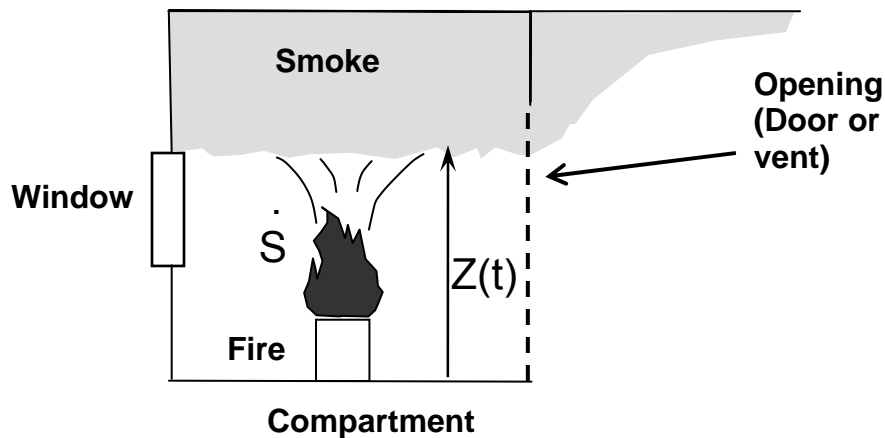


Figure 4.1.1. Schematic illustrating the fire heat release rate (\dot{S}) and the smoke layer height (Z) for a compartment fire.

Consider a design problem in which a designer requires an active fire protection system if a smoke layer descends below some critical height at a critical time as might be found from an egress model. A schematic illustrating the basic process is given in figure 4.1.1. Clearly, the layer height is strongly dependent on the fire size that would be assumed to take place in the compartment. As previously noted, the designer does not know a-priori the range of use of the compartment. One means of clarifying the likely hazard associated with a range of potential fires is through the use of probabilistic assumptions about the fire size and fire models used to propagate the uncertainty in the fire size into a layer height distribution. The problem is shown schematically in figure 4.1.2. One has a deterministic fire model that takes as input the heat release rate of the fire and provides as output the height of the smoke layer. Any uncertainty in the input variables is propagated in time by the fire model and gives rise to the uncertainty of the

output parameter. The uncertainty in input variable, the heat release rate, is represented using a probability distribution function (PDF). For the output variable, the smoke layer height, the cumulative distribution function (CDF) is desired. The CDF gives useful statistical information that can be used in risk assessment studies, such as the probability of the smoke layer height to be within some critical range at different instances after the occurrence of a fire. The two models that I have considered are the Available Safe Egress Time (ASET) Model (Janssens (2000)) and the Consolidated Fire and Smoke Transport (CFAST) model (Jones et al. (2005)). These are both deterministic fire models that require other input parameters such as the height and area of the enclosure, the location of the vents, windows etc. In this study, these parameters are assumed to be known to a high level of certainty. The only uncertain variable is the heat release rate that is usually sampled from a statistical distribution of known/historical data. Problems of this type in which one has uncertain inputs in a deterministic fire model have been discussed by Magnusson et al. (1996). In the same article, the authors discuss the use of Monte Carlo simulation as an attractive technique for solving these problems. Monte Carlo simulations although easy to use can be extremely costly in terms of computational requirements. These methods work by sampling from the PDF of the input variable and running the fire model for each sample. A large number of random samples may be needed for accurate representation of the PDF. If the fire model is sufficiently complex then each run of the fire model involves considerable computational cost and Monte Carlo simulations become prohibitively expensive. To address these issues, I look at an alternative approach involving the method of moments and reconstruction of the CDF using the moments of the PDF. The discussion of this method follows.

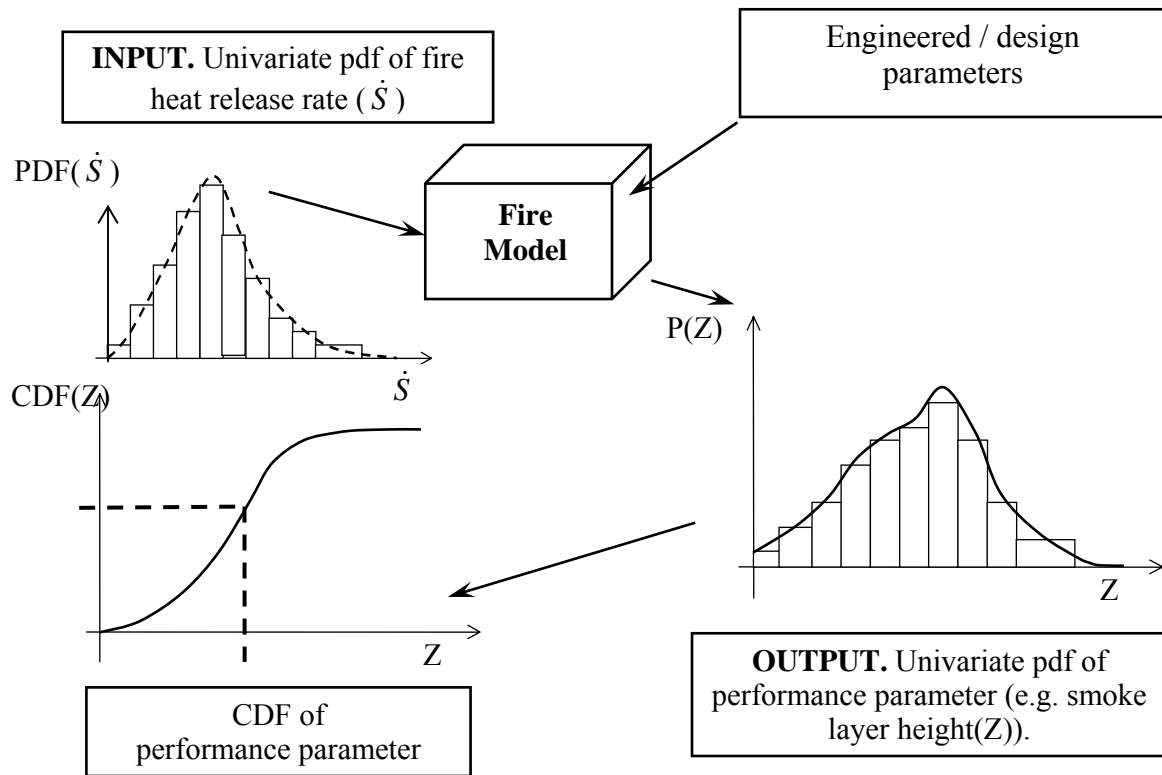


Figure 4.1.2. Schematic of the propagation of statistical uncertainty problem as applied to a design fire application.

4.1.2. Mathematical representation of the propagation of uncertainty and the quadrature method of moments.

One has a system where the dynamics depends on a random input variable such as the heat release rate. Let \dot{S} be the fire heat release rate, assumed to be stochastic, and let $m(\dot{S})$ be its PDF. The output of the model will be the PDF of the smoke layer height $n(Z)$ at some critical time, t_{cr} , where $Z(t_{cr})$ is the smoke layer height from the floor at the critical instant. The mathematical representation then consists of the transformation from $m(\dot{S}, t = t_0)$ to $n(Z, t = t_{cr})$ which is given by the change in variable rule for PDFs,

$$m(\dot{S})d\dot{S} = n(Z)dZ \quad 4.1.1$$

The actual mapping between $\dot{S}(t = t_0)$ and $Z(t = t_{cr})$ is given by

$$Z(\dot{S}, t_{cr}) = \int_{t_0}^{t_{cr}} f(\tau, \dot{S}(\tau)) d\tau \quad 4.1.2$$

where $\begin{cases} \frac{dZ}{dt} = f(t, \dot{S}(t)) \\ Z(t = t_0) = Z_0 \end{cases}$ is provided by the fire model discussed later.

A widely used technique for obtaining the statistical properties of the layer height is through Monte Carlo Simulations. In this technique, \dot{S} is randomly sampled from its known distribution and the fire model is integrated for each \dot{S} to build up an ensemble of Z . As discussed earlier, this can be a computationally intensive procedure since a large number of samples of \dot{S} need to be taken to obtain good statistics. If the fire model is sufficiently complex, each run of the fire model can be very expensive. In this study I attempt to solve the problem using the method of moments. I seek only the moments of the PDF of Z , $n(Z)$ and then attempt to reconstruct the CDF of Z using the moments. The moments of $n(Z)$ can be written in terms of the initial PDF of \dot{S} , $m(\dot{S})$ using 4.1.1 and 4.1.2.

$$M_k^{(Z)} = \int_{Z_{\min}}^{Z_{\max}} Z^k n(Z) dZ = \int_{\dot{S}_{\min}}^{\dot{S}_{\max}} Z(\dot{S})^k m(\dot{S}) d\dot{S} \quad 4.1.3$$

where $M_k^{(Z)}$ is the kth moment of $n(Z)$. Hence the problem reduces to the task of finding an accurate approximation of $M_k^{(Z)}$ given the moments of the initial distribution $m(\dot{S})$. The approximation is carried out using the Gaussian quadrature rule that is described in chapter 2.

$$M_k^{(Z)} = \int_{\dot{S}_{\min}}^{\dot{S}_{\max}} Z(\dot{S}, t_{cr})^k m(\dot{S}) d\dot{S} \approx \sum_{n=1}^{N_Q} Z(\dot{S}_n, t_{cr})^k W_n \quad 4.1.4$$

Here \dot{S}_n are the quadrature points and W_n are the quadrature weights that are obtained from the moments of $m(\dot{S})$. It is seen that this technique requires only N_Q samples of \dot{S}_n determined from $2N_Q$ moments of $m(\dot{S})$. The fire model is run for only the N_Q heat release rates (\dot{S}_n) to get $Z(\dot{S}_n, t_{cr})$. If N_Q is small, typically 3 or 4, then this technique enables a dramatic reduction in the computational effort required for these types of problems. There are two computational tasks involved in determining the feasibility of the QMOM approach. Firstly, one needs to determine the accuracy of the moments predicted using QMOM. This is necessary because the set of moments $M_k^{(Z)}$ is given by a quadrature approximation using a limited number of quadrature points, N_Q , and one needs to find the optimum N_Q that give accurate moments. Secondly, the moments do not give all the information that is contained in a CDF. Therefore, the CDF needs to be reconstructed from a finite number of known moments. This is carried out by matching the calculated moments to the moments of a four-parameter Generalized Lambda Distribution as discussed later. A schematic of the methodology is provided in Figure 4.1.3.

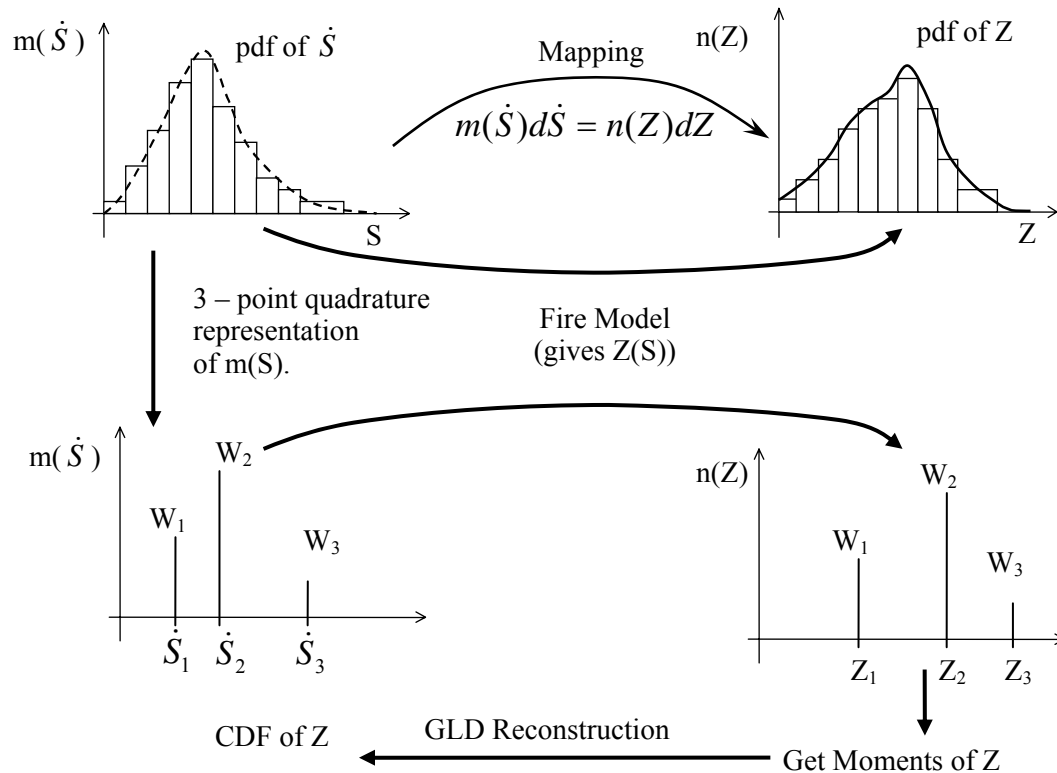


Figure 4.1.3. Schematic illustrating the sampling procedure used in the quadrature method of moments and the procedure for getting the CDF. Note that the schematic shows three quadrature points and three weights which would correspond to six known moments.

4.1.3. Details of input variable distributions and fire models used.

The methodology outlined in Figure 4.1.2 shows that the computational model requires an input PDF of heat release rates and a fire model for evaluating the output parameter for each heat release rate.

Input fire heat release rate distribution.

I use the generalized beta distribution for the input heat release rate PDF. In practice, the PDF needs to be determined from empirical or historical data. The generalized beta PDF is a four parameter distribution. It is very versatile because one can

create different shaped PDFs by varying the four parameters. Further the beta PDF has bounded support which means that one can specify the maximum and minimum fire sizes that can occur in a compartment. This feature prevents the possibility of unrealistically large fires in a room of finite size containing a finite amount of combustible material. The generalized beta distribution with parameters $\beta_1, \beta_2, \beta_3, \beta_4$ is given by Karian and Dudewicz (2000).

$$m(\dot{S}) = \begin{cases} \frac{(\dot{S} - \beta_1)^{\beta_3} (\beta_1 + \beta_2 - \dot{S})^{\beta_4}}{\beta(\beta_3 + 1, \beta_4 + 1) \beta_2^{(\beta_3 + \beta_4 + 1)}}; & \text{for } \beta_1 \leq \dot{S} \leq \beta_1 + \beta_2 \\ 0; & \text{otherwise} \end{cases} \quad 4.1.5$$

Here β_1, β_2 are the location and scale parameters. β is the beta function. I have taken $\beta_1 = 0$ and $\beta_2 = 200$ kW. This choice defines the range of fire sizes to be between 0 and 200 kW. β_3 and β_4 are the shape parameters. Different shaped beta PDFs can be obtained by changing β_3 and β_4 . The four different PDFs I use are parameterized by:

I. $\beta_3 = 1; \beta_4 = 4$

II. $\beta_3 = 0; \beta_4 = 2$

III. $\beta_3 = 2; \beta_4 = 0$

IV. $\beta_3 = 1; \beta_4 = 1$

For all these cases $\beta_1 = 0$ and $\beta_2 = 200$ kW. Figure 4.1.4 shows the different PDFs. PDFs II and III may respectively model situations where small and large sized fires are more likely to occur respectively. I and II model situations where mid-sized fires may be

more likely. Figure 4.1.5 shows the corresponding CDFs for these distributions. Next, I consider the fire models used.

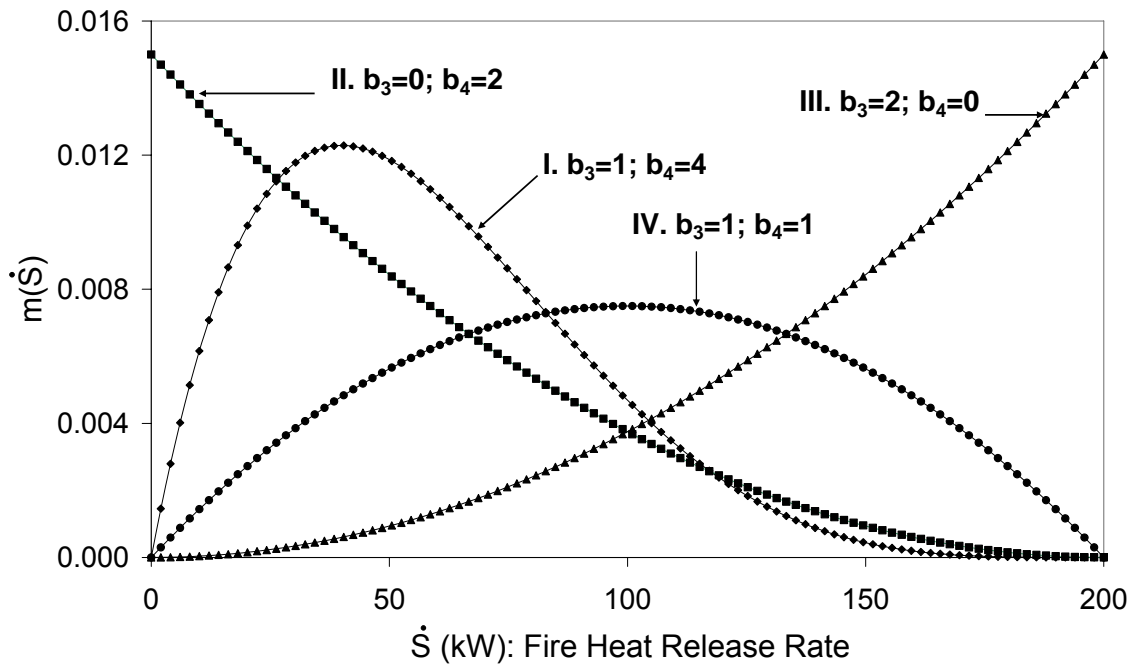


Figure 4.1.4. Generalized beta probability density functions (PDFs) used for the fire heat release rates.

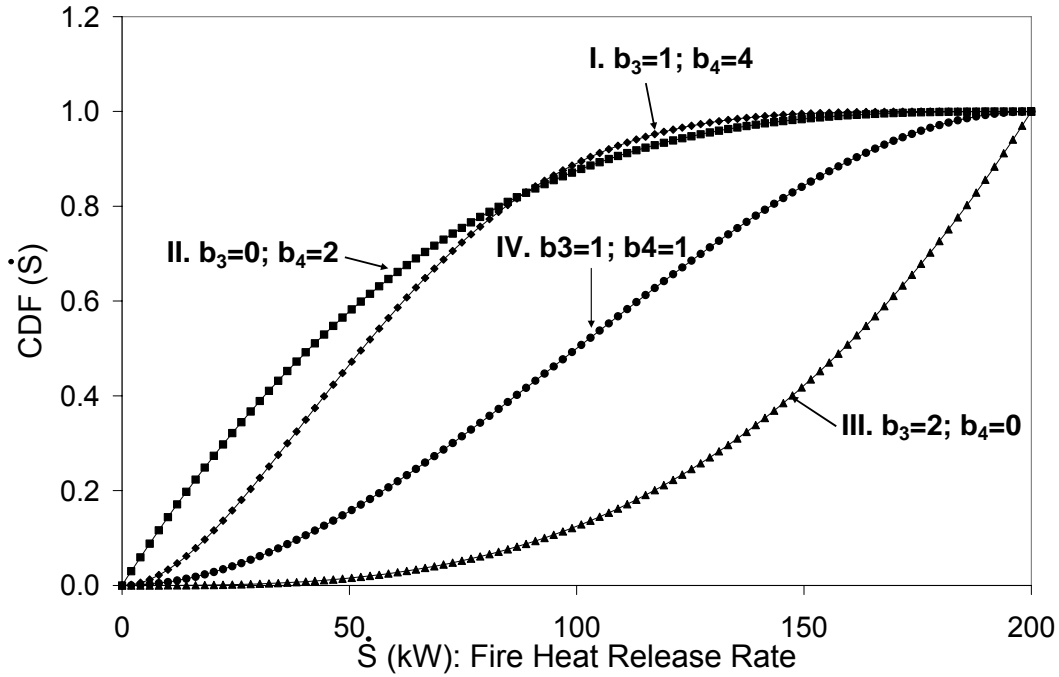


Figure 4.1.5. Cumulative distribution functions (CDFs) corresponding to the PDFs in Figure 4.1.4.

Available Safe Egress Time (ASET) Model.

I use two well characterized zone models for simulating compartment fires. The first model is the Available Safe Egress Time Model (ASET) that is described in detail in Janssens (2000). The governing equation for the smoke layer height is

$$\frac{dZ}{dt} = -\frac{\dot{m}_e}{\rho_a A} - \frac{(1-L_c)\dot{S}}{\rho_a c_p T_a A} \tag{4.1.6}$$

\dot{m}_e is the rate of entrainment of the air into the plume and is given by a correlation for plume flow.

$$\dot{m}_e = 0.21\rho_a (g\Delta Z)^{1/2} \Delta Z^2 \left[\frac{(1-L_r)\dot{S}}{\rho_a C_a T_a (g\Delta Z)^{1/2} \Delta Z^2} \right]^{1/3} \tag{4.1.7}$$

The properties of air are density ($\rho_a = 1 \text{ kg/m}^3$) and specific heat capacity ($c_a = 1.004 \text{ kJ/kgK}$). L_c and L_r are empirical constants taken to be 0.8 and 0.35 respectively. The ambient temperature is ($T_a = 300 \text{ K}$). $g = 9.8 \text{ m/s}^2$ is the acceleration due to gravity. The floor area A is 31.5 m^2 , $\Delta Z = Z - Z_f$ where $Z_f = 0.2 \text{ m}$ is the height of the base of the fire and the initial condition $Z(t = t_0)$ is the ceiling height which is taken as 6.15 m . \dot{S} is the heat release rate which is random and whose PDF is given by the generalized beta distribution. I assume that \dot{S} does not change with time. The range of fire heat release rates, room geometry, empirical constants and the assumption of steady heat release rate correspond to the conditions used in the experimental validation of the ASET model reported in Hurley (2003).

Consolidated Fire and Smoke Transport (CFAST) Model.

CFAST is a more sophisticated zone model than ASET that is widely used by architects, fire protection engineers, safety officials etc. (Jones et al. (2005)). It is a two zone model that models the evolution of smoke, combustion gases and temperature in a building compartment that is on fire (Jones et al. (2004)). The details of the software program can be found in Jones et al. (2004). One can take CFAST to be a fire model that provides, among other things, the smoke layer height for a particular fire heat release rate. CFAST simulations are performed for two cases. In one case I use exactly the same compartment geometry as in ASET. In the second case, I add a window of width 4 m , height 2 m located 2 m above the floor as shown in figure 4.1.6.

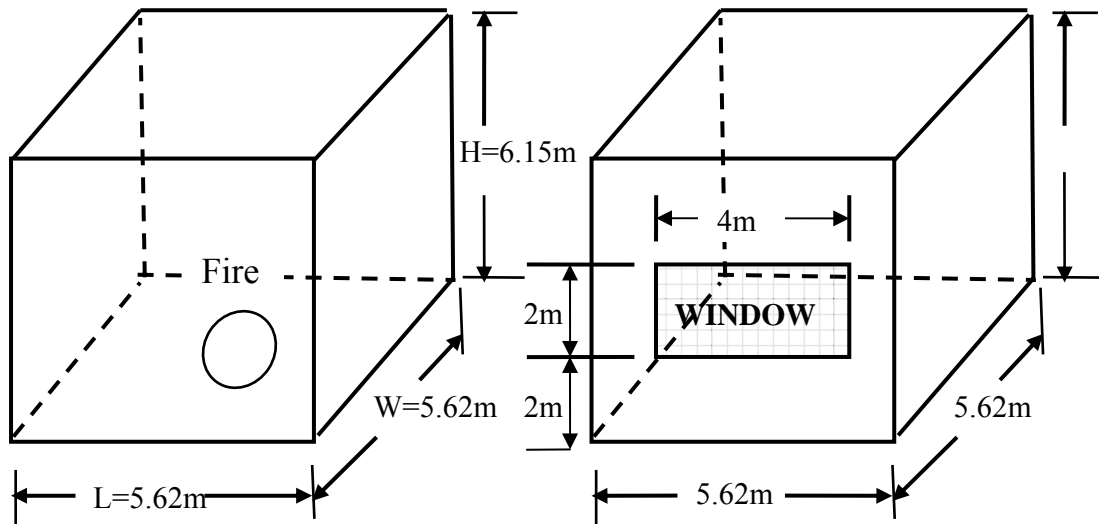


Figure 4.1.6. (Left) Compartment geometry for the ASET and CFAST (without window) models. (Right) Compartment geometry for the CFAST model with a window.

4.1.4. Computational methods.

Monte Carlo Simulations.

In the Monte Carlo simulations, the fire heat release rates, \dot{S} , are sampled from the generalized beta distribution (equation 4.1.5) using the rejection sampling method discussed in Cheng (1978). ASET and CFAST models are run for each sample of \dot{S} as an input. These models return the smoke layer height, Z , at the specified critical time of 120 seconds. The CDF of Z can then be directly obtained from the output of the multiple runs of the fire models. More efficient methods of sampling from a PDF have been developed (e.g. as discussed in Magnusson et al. (1996)). My objective in performing Monte Carlo simulations is to determine the accuracy of the results obtained using

moment methods and therefore I do not consider issues on the computational efficiency of My Monte Carlo simulations.

Quadrature Method of Moments (QMOM).

The quadrature method of moments is discussed in greater detail in Chapter 2. In this work I discuss its application to an uncertainty propagation problem discussed in section 4.1.2. In QMOM, one first computes the moments of the beta distribution. The moments of the beta distribution are given by

$$M_k = E(\dot{S}^k) = \frac{\beta(\beta_3 + k + 1, \beta_4 + 1)}{\beta(\beta_3 + 1, \beta_4 + 1)}; \quad 4.1.8$$

M_k is the k -th moment of $m(\dot{S})$, β is the beta function and β_3, β_4 are the shape parameters. Using a sequence of $2N_Q$ moments, one can find N_Q quadrature points and weights using the method discussed earlier. The N_Q quadrature points $\dot{S}_{n,BD}$ correspond to the beta PDF. The corresponding quadrature points for the generalized beta distribution (GBD), defined in equation 4.5, can be obtained using

$$\dot{S}_{n,GBD} = \dot{S}_{n,BD} \cdot \beta_2 + \beta_1, \quad 4.1.9$$

where $\dot{S}_{n,GBD}$ is the quadrature point for the GBD, β_1 is the location parameter, and β_2 the scale parameter defined earlier. In QMOM, one can choose either an integral moment sequence such as $\{M_0, M_1, M_2, \dots\}$ or any fractional moment sequence such as $\{M_{k/L}\} = \{M_0, M_{1/L}, M_{2/L}, \dots\}$. Upadhyay and Ezekoye (2006) have shown that the use of a fractional moment sequence can sometimes lead to better quadrature approximations.

The theoretical details and methods for using fractional moment sequences for QMOM applications are discussed in greater detail in chapter 3.

For the moment method, the N_Q quadrature points can be considered to be the samples of the heat release rate. The fire model is then run for each of these sampled heat release rates to get N_Q smoke layer heights at a specified instant. Therefore, the QMOM technique can be considered to be an efficient way of sampling from a known PDF. The moments of the layer height can be obtained using equation 4.1.4. The CDF is then reconstructed by matching the computed moments to the moments of the four-parameter GLD.

GLD reconstruction of the CDF.

Karian and Dudewicz (2000) detail the basis and development of the Generalized Lambda Distribution (GLD) for use in fitting statistical data. The four parameter GLD can be represented by $GLD(\lambda_1, \lambda_2, \lambda_3, \lambda_4)$. The GLD is most easily specified in terms of the percentile function

$$Q(y) = Q(y; \lambda_1, \lambda_2, \lambda_3, \lambda_4) = \lambda_1 + \frac{y^{\lambda_3} - (1-y)^{\lambda_4}}{\lambda_2} \quad 4.1.10$$

with $0 \leq y \leq 1$. The CDF is obtained as an inverse of 4.1.10, i.e. $CDF(Q(y)) = y$. The central task of the GLD method is to obtain the four parameters $\lambda_1, \lambda_2, \lambda_3, \lambda_4$ from the four moments $(M_k^{(Z)}; k = 1,2,3,4)$ of equation 4.1.4. One computes the skewness α_3 and kurtosis α_4 from the raw moments. One can also compute these terms for the GLD distribution using the (unknown) parameters λ_3 and λ_4 .

$$\alpha_3 = \frac{M_3 - 3M_1M_2 + 2M_1^3}{(M_2 - M_1^2)^{3/2}} = G_3(\lambda_3, \lambda_4)$$

$$\alpha_4 = \frac{M_4 - 4M_1M_3 + 6M_1^2M_2 - 3M_1^4}{(M_2 - M_1^2)^2} = G_4(\lambda_3, \lambda_4)$$
4.1.11

The G_i are irrational functions of λ_3 and λ_4 and contain beta functions in λ_3 and λ_4 . The difficulty lies in solving the coupled, nonlinear, bivariate equations in 4.1.11 to get an optimum λ_3, λ_4 . In this study I simply use the results for λ_3 and λ_4 presented in tabular form in Karian and Dudewicz (2000). The table provides λ_3 and λ_4 along with $\lambda_1(0,1), \lambda_2(0,1)$ for a wide range of allowable values of the skewness and kurtosis (α_3 and α_4). Linear interpolation is used for values in between. There are spaces of (α_3, α_4) that are not covered by the tables. In some of these cases a nonlinear optimization problem must be solved for equation 4.1.11, while for other cases either the generalized beta distribution (GBD) is a better fit or else the reconstruction of the CDF using GLD/GBD is impossible. In all My simulations, (α_3, α_4) fell in the range covered by the tables. λ_1 and λ_2 can be computed from the tabulated $\lambda_1(0,1), \lambda_2(0,1)$ using

$$\lambda_1 = \lambda_1(0,1)\sqrt{\alpha_2} + \alpha_1; \lambda_2 = \lambda_2(0,1)/\sqrt{\alpha_2}$$
4.1.12

where $\alpha_2 = M_2 - M_1^2$ is the variance and $\alpha_1 = M_1$ is the mean of the smoke layer height distribution obtained from the QMOM solutions. The four lambdas give us the percentile function, $Q(y)$, whose inverse gives the CDF.

4.1.5. Results and Discussions.

Comparison of ASET and CFAST results.

I first compare results obtained using CFAST and ASET results. The room geometry is the same as used by Hurley (2003) for comparison of the ASET predictions of the smoke layer height with full-scale test data. I take two particular cases with constant fire heat release rates of 195 kW and 33kW (test #1 and test#5 in Hurley (2003)). These cases correspond to some of the tests in which a constant heat release rate was maintained and these heat release rates also fall within the range that I consider in this study. Figure 4.1.7 shows the comparison of ASET and CFAST predictions of the smoke layer height for two different heat release rates. ASET results closely match the test data. These results agree with those presented by Hurley(2003). However, the CFAST results show smaller layer heights for both heat release rates.

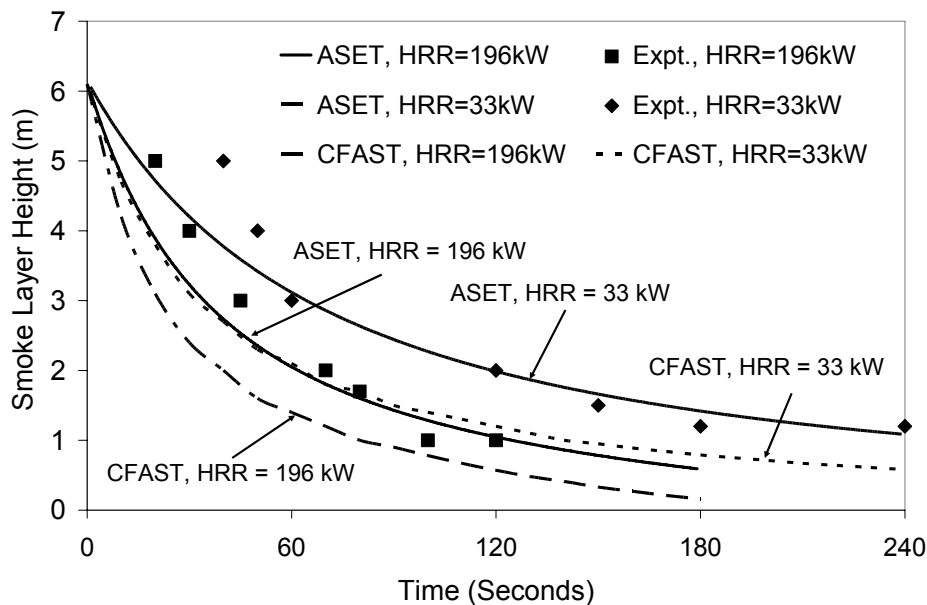


Figure 4.1.7. Comparison of the ASET and CFAST model results for the smoke layer height with experimental data reported in Hurley (2003).

Monte Carlo Simulation results for ASET and CFAST models.

Figure 4.1.8 shows the PDF of the smoke layer height obtained from Monte Carlo simulations using the ASET model. Four different PDFs of the smoke layer, $n(Z)$, are obtained for the four different input heat release rate PDFs, $m(\dot{S})$, defined in equation 4.1.5. 10,000 Monte Carlo samples of the heat release rates are taken to ensure converged results. All the PDFs show positive skewness and kurtosis (i.e. they are asymmetric, have a higher peak around the mean and fatter tails compared to a normal distribution). The mean smoke layer height depends on the $m(\dot{S})$. For instance, PDF III consists of a distribution of larger heat release rate fires and consequently the smoke layer heights are smaller. PDF II consists of a distribution of smaller heat release rate fires and the smoke layer heights are larger (farther from the ground). Figure 4.1.9 shows the corresponding CDFs. The CDFs are more useful for risk assessments since the probability of the layer being below any given value is immediately available from the CDF. Despite the variability in the shapes of the PDFs, the CDFs look almost the same, only the locations where they increase sharply are different. Figure 4.1.10 and Figure 4.1.11 show the PDF and corresponding CDF obtained using Monte Carlo simulations for the CFAST model where the compartment is exactly the same as for the ASET model. Figure 4.1.12 and Figure 4.1.13 show the PDFs and CDFs obtained using CFAST model for a compartment with a window (Figure 4.1.7 shows the compartment geometry for both cases). As discussed in the previous section, smoke layer heights predicted using CFAST are smaller than those predicted by ASET. Differences in the PDFs and CDFs due to the presence of a window are also apparent. Since the window allows smoke to escape, one sees that smoke layer height peaks between 2.5 and 3 m. Due to increased complexity of

the CFAST models, only 500 samples are used for the heat release rate. Furthermore, the smallest resolution of the smoke layer heights output by CFAST is 10cm. For these reasons, both the PDFs and CDFs obtained using CFAST are coarser compared to those obtained using ASET.

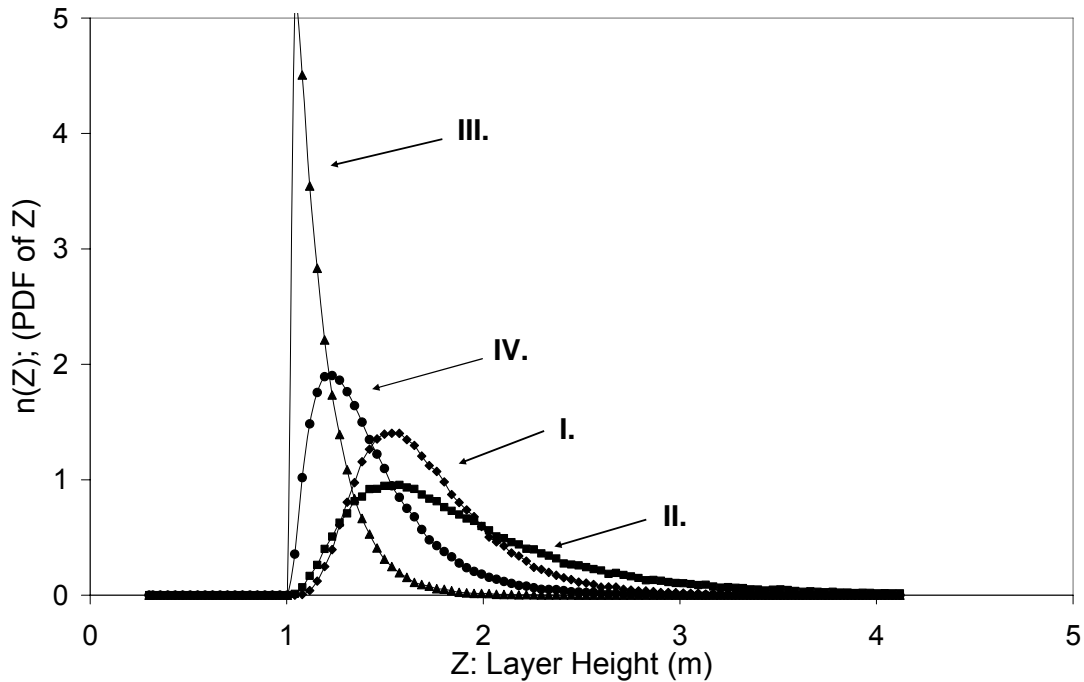


Figure 4.1.8. PDFs of the smoke layer height at a critical time $t_{cr} = 120s$ obtained from Monte Carlo Simulations using the ASET model. The labels I, II, III, IV correspond to the different heat release rate PDFs in figure 4.1.4.

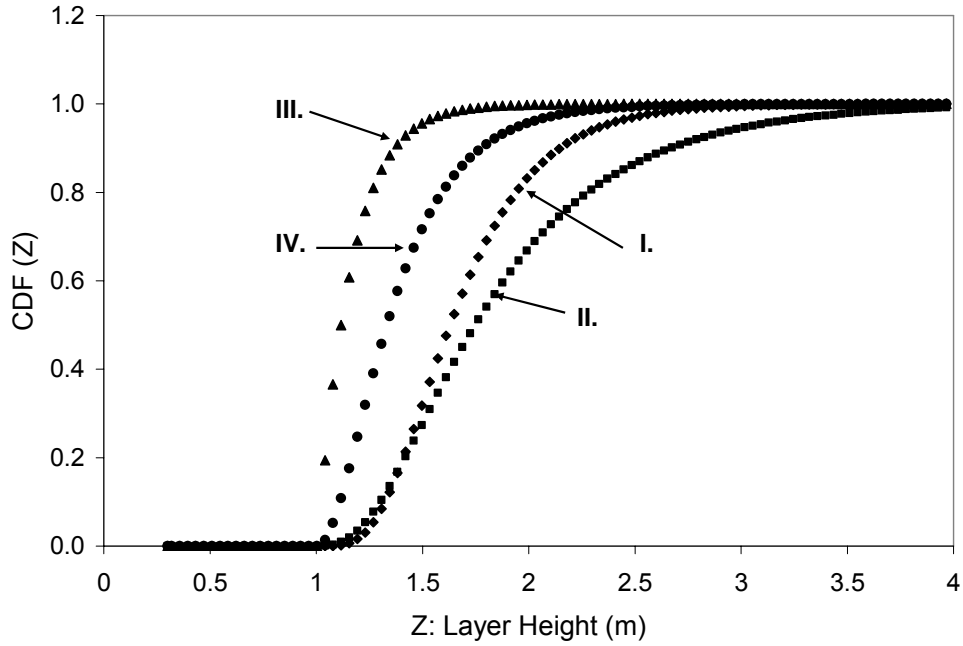


Figure 4.1.9. CDFs corresponding to the PDFs in figure 4.1.8.

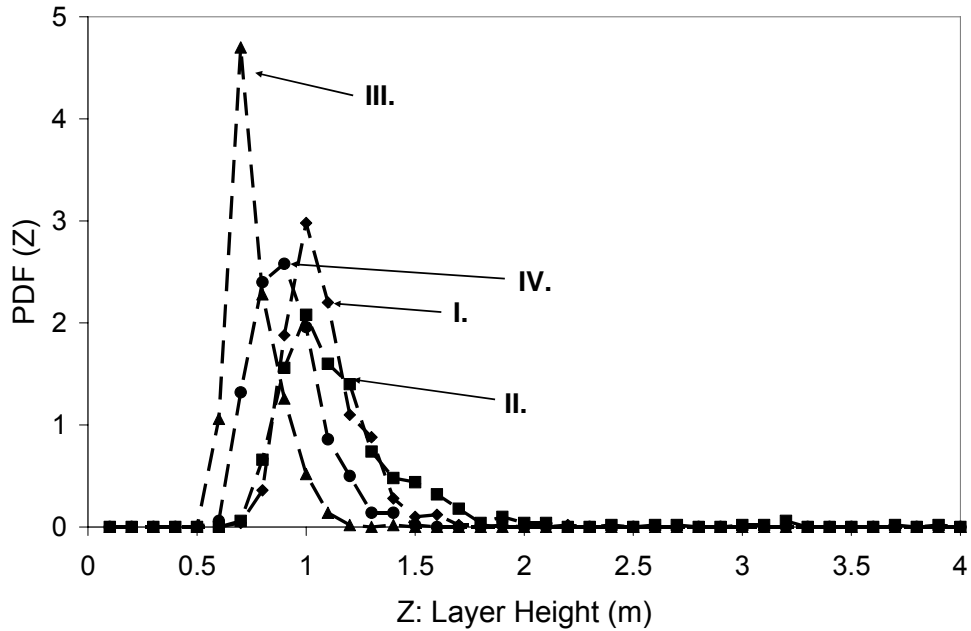


Figure 4.1.10. PDFs of the smoke layer height at a critical time $t_{cr} = 120s$ obtained from Monte Carlo Simulations using the CFAST model with the same geometry as for the ASET. I, II, III, IV correspond to the different heat release rate PDFs in figure 4.1.4.

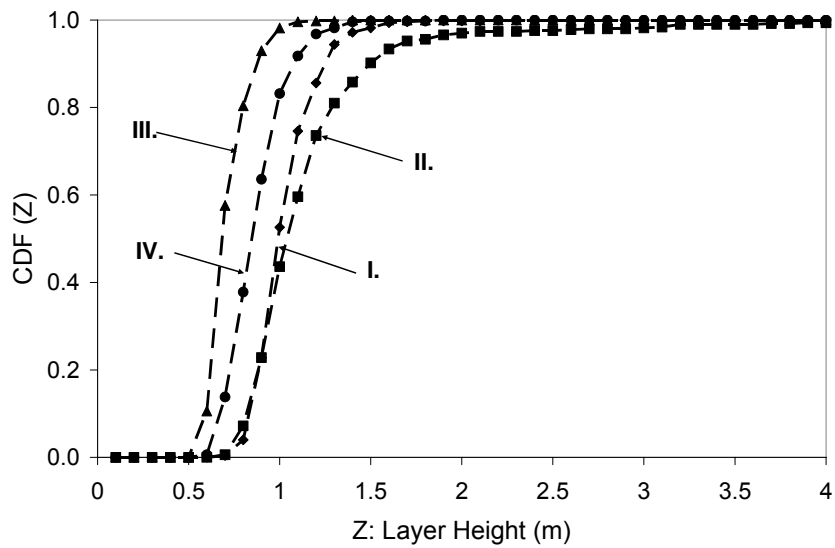


Figure 4.1.11. CDFs corresponding to the PDFs in figure 4.1.10.

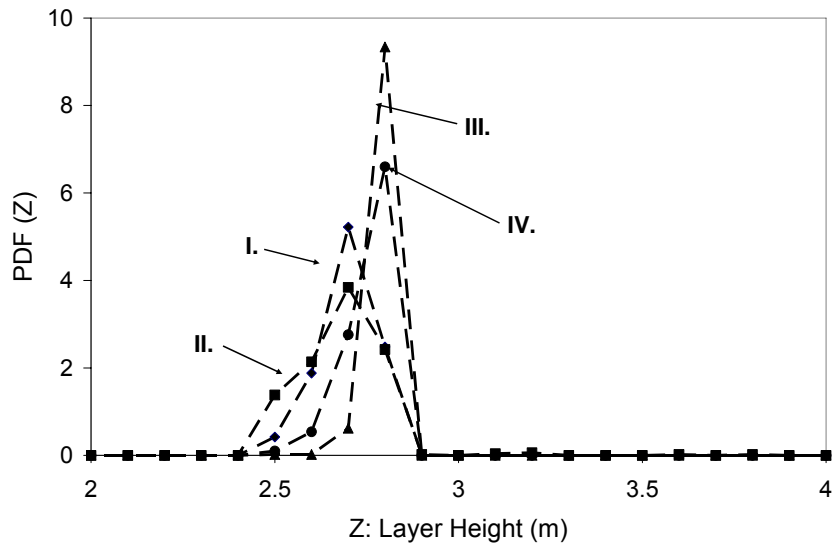


Figure 4.1.12. PDFs of the smoke layer height at a critical time $t_{cr} = 120s$ obtained from Monte Carlo Simulations using the CFAST model with a horizontal vent (window) shown in figure 4.1.7. I, II, III, IV correspond to the different heat release rate PDFs in figure 4.1.4.

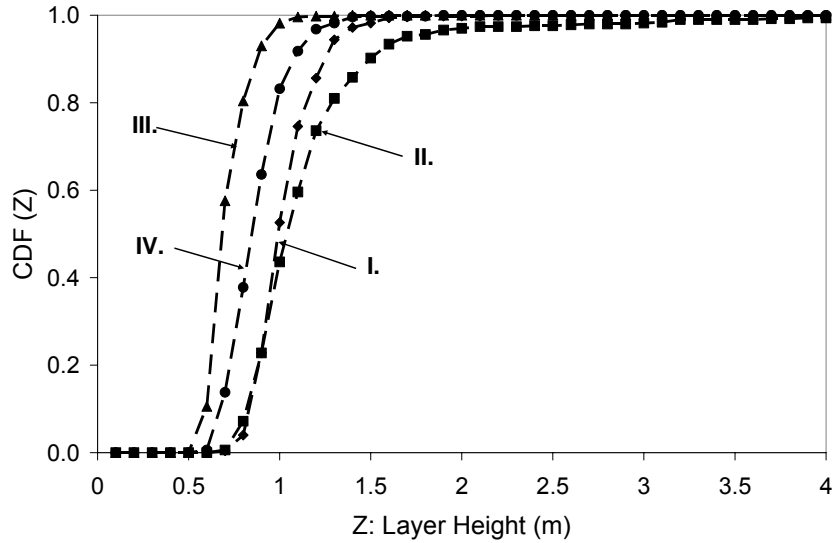


Figure 4.1.13. CDFs corresponding to the PDFs in figure 4.1.12.

QMOM results for ASET and CFAST models.

In the quadrature method of moments, one obtains the moments of the smoke layer height PDF, $n(Z)$. The moments required for matching with the GLD moments are the mean, variance, skewness and kurtosis. Since the moments of $n(Z)$, $M_k^{(Z)}$, are obtained from a quadrature approximation, it is essential to determine the accuracy in their prediction. As shown in equation 4.1.11, the skewness and kurtosis are functions of the moments $M_k^{(Z)}$. They are important quantities because the GLD parameters λ_3, λ_4 are found by matching the skewness and kurtosis (equation 4.1.11). In figure 4.1.14 and figure 4.1.15, I compare the skewness and kurtosis predicted using QMOM with those obtained from converged Monte Carlo simulations for the ASET model. One sees that both skewness and kurtosis fail to converge for the choice of an integral moment set (e.g. $\{M_0, M_1, M_2, \dots\}$). However the choice of fractional moment sets such as the $k/2, k/3$

and $k/4$ sets (i.e. the sets $\{M_0, M_{1/2}, M_1, M_{3/2}, \dots\}$, $\{M_0, M_{1/3}, M_{2/3}, M_1, \dots\}$, $\{M_0, M_{1/4}, M_{2/4}, M_{3/4}, \dots\}$), gives faster convergence and more accurate predictions. For instance, just three quadrature (or sampling) points determined from a set of 6 $k/4$ moments gives very accurate results for all cases considered. Similar trends are seen for the prediction of means and variances although their predictions are much more accurate.

Figure 4.1.16 shows the reconstructed CDFs using the Generalized Lambda Distribution (GLD) compared with CDFs obtained from Monte Carlo simulations. To get the moments, $M_k^{(Z)}$, four quadrature points, $\hat{S}_{n,GBD}$, obtained from eight $k/4$ moments of $m(\hat{S})$ are used in all cases. The GLD parameters are obtained from Appendix B in Karian and Dudewicz (2000). Figure 4.1.16 shows that the GLD reconstruction is very accurate for all four CDFs. Figure 4.1.17 shows the comparisons for the CFAST model, with and without a window. It is seen that the GLD reconstruction is accurate for the CFAST model as well. Only one input PDF (PDF I) is shown, but the same effect is seen for all four PDFs.

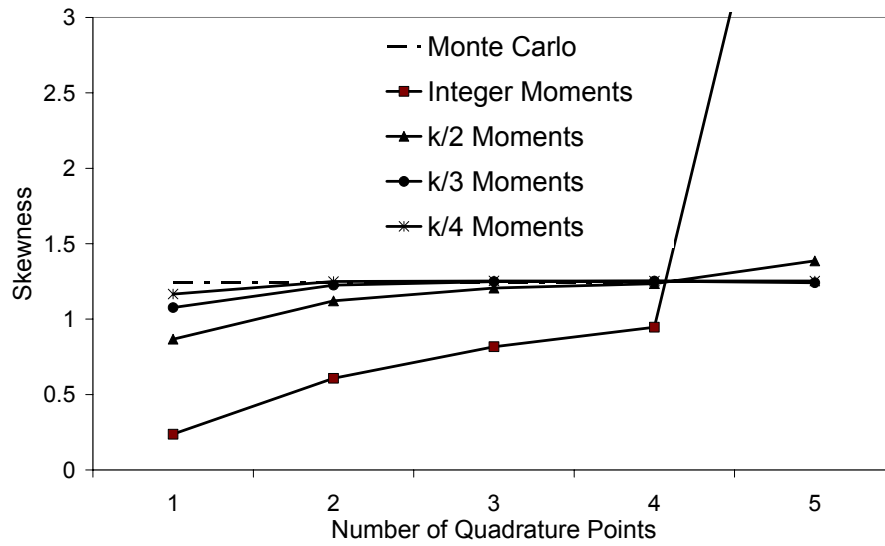


Figure 4.1.14. Study of the convergence of the skewness with increasing number of quadrature points. Results of using different moment sequences are shown.

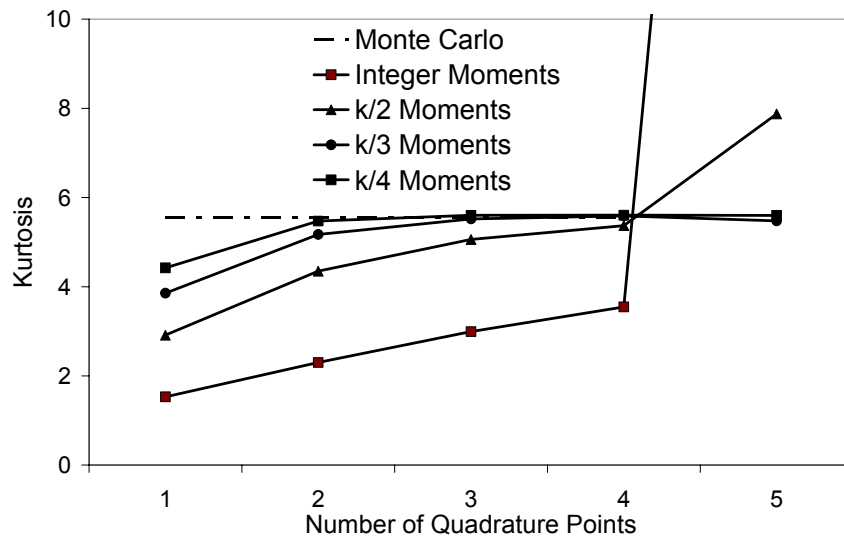


Figure 4.1.15. Study of the convergence of the kurtosis with increasing number of quadrature points. Results of using different moment sequences are shown.

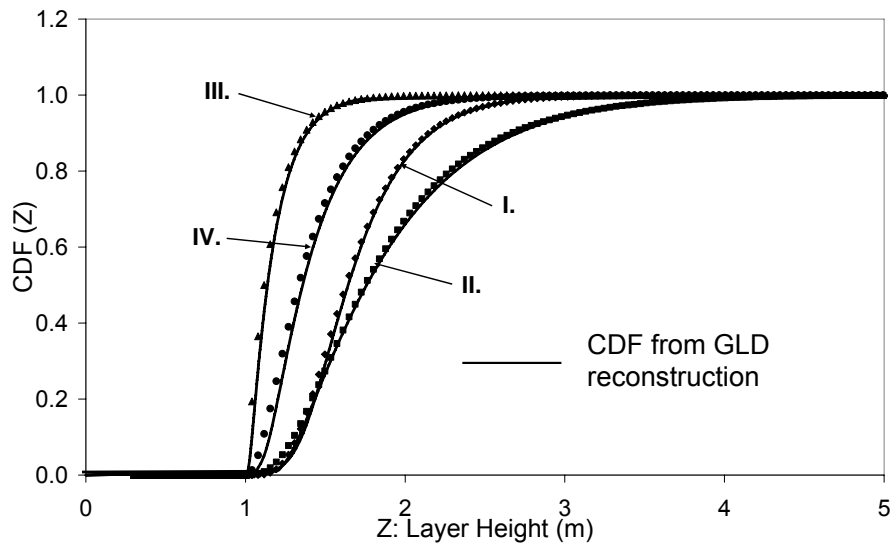


Figure 4.1.16. Reconstructed CDF using the Generalized Lambda Distribution (GLD) compared with CDF obtained from Monte Carlo simulations for the ASET model.

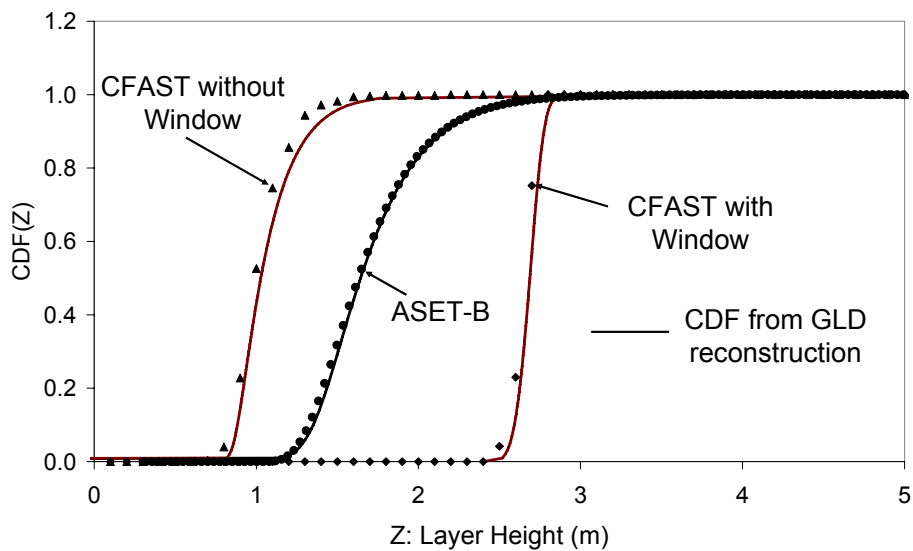


Figure 4.1.17. Reconstructed CDF using the GLD compared with the CDF obtained from Monte Carlo Simulations using the CFAST model, with and without a window. The CDFs obtained using the ASET model is also shown. PDF I is used for the heat release rate PDF.

4.1.6. Conclusions and further work.

As computational models become more widely used for fire safety designs, a methodology for incorporating the uncertainties in any fire scenario becomes extremely important. Due to the extreme complexity of the physical phenomena involved, the occurrence of fire in any building and the chain of events triggered by the fire are very uncertain. Designers and fire safety engineers need efficient computational techniques that provide statistical information for assessing the risk in any fire event. The quadrature method of moments proposed in this work is a general technique that has already been used in many other disciplines to solve for the time and space evolution of the moments of a PDF. In many cases, QMOM solutions are much more efficient and reasonably accurate when compared to results obtained using Monte Carlo simulations or other solution techniques as seen in the results presented in chapter 3.

In this work, I considered the evolution of the smoke layer height given the uncertainties in the fire heat release rate. For this problem, I saw that the moments of the smoke layer height PDF can be accurately predicted using very few quadrature points, especially if fractional moments are used to obtain quadrature points and weights. Since each quadrature point acts like a sample for the heat release rate, this method also has the potential to reduce the computational effort in Monte Carlo simulations. Furthermore, the CDF was reconstructed from the moments by matching the moments with those of a four parameter GLD. For all cases considered, I found that the reconstruction was accurate. The fire models used in this study were all reasonably simple and computational costs for running any given scenario were reasonable. If these zone fire models were replaced by computational fluid dynamics based models, it would be prohibitively expensive to

perform Monte Carlo type simulations in order to identify probabilistic estimates of risk. On the other hand, it would be feasible to run several (six to eight) CFD simulations in order to generate an accurate cumulative distribution function of the output variable.

While the results from the present study appear promising, this method remains to be tested for significantly more complex fire scenarios. As discussed earlier, there are a large number of uncertain variables in any fire event and one has to simulate the interactions among all these uncertain variables. While the QMOM is well suited for describing the dynamics of the moments of a univariate PDF (for a single uncertain variable), the extension to multivariate PDFs (for multiple uncertain variables) is not straightforward. The direct quadrature method of moments (DQMOM) detailed in chapter 2 can be used to simulate the dynamics of the moments of a multivariate PDF. For multivariate PDFs, there will be a question on the ability to generate meaningful CDFs for the system. While the QMOM approach appears to suitable for the type of problem considered in this work, both QMOM and DQMOM need to be tested on a number of relevant problems in fire science and engineering to investigate their computational efficiency and accuracy.

4.2. SIMULATION OF THE PDF TRANSPORT EQUATION FOR TURBULENT MIXING AND COMBUSTION USING THE DIRECT QUADRATURE METHOD OF MOMENTS.

4.2.1 Introduction and motivations.

The necessity of using stochastic methods for modeling deterministic systems has been discussed earlier. A typical example is the modeling of turbulence. In principle turbulent flow can modeled using the deterministic Navier Stokes Equations. It is well known that for higher Reynolds numbers these equations are chaotic and display sensitive

dependence on initial conditions. This leads to the impossibility of long term prediction and therefore the best that one can do is to predict some statistical properties of the turbulent flow. A brief discussion of the use of the PDF transport equation for modeling turbulent flows as well as turbulent reacting flows is provided in Chapter 2. More detailed discussions can be found in Pope (1985). My objective in this section is to investigate the applicability of multivariate DQMOM for simulation of the PDF transport equation.

Before discussing the computational aspects of the problem, I provide some motivation for using moment methods for turbulent reacting flows. The prediction of mixing and chemical reactions in the presence of a turbulent flow field is of great importance in the chemical process industries and is the subject of intense research. In a turbulent flow there are fluctuations at all length scales down to the Batchelor scales. However molecular mixing and combustion occur at the Batchelor scales that are generally of the same order or smaller than the Kolmogorov scales (Batchelor (1952)). Therefore the resolution of chemical processes requires resolution finer than the Kolmogorov scale. A computational simulation of an industrial scale chemical reactor that resolves the fluctuations of the velocity field and chemical species down to the smallest time and length scales is intractable with the currently available hardware and software, especially for large Reynolds numbers (Raman and Pitsch (2005)). Consequently different schemes for modeling turbulent reacting flow processes have been developed. A popular approach is called Large Eddy Simulation (LES) in which only the larger, energy containing velocity fluctuations are resolved while the smaller scales are assumed to be universal and are modeled using known statistics. However the

mixing and chemical reactions take place at the molecular scales and these processes are certainly not universal, i.e. they depend on the details of how the reactants are fed into the vessel, the rate of stirring, the large scale flow fields as well as the smaller scale velocity fluctuations that enhance mixing. In the chemical engineering literature various simplified approaches have been developed for treating turbulent reacting flows. In the fast mixing limit, the mixing process is much faster than the chemical reactions and therefore all fluctuations in the species mass fractions are negligible. In this simplified scenario, laminar reaction models that ignore fluctuations in species concentrations and temperatures are used. These cases are also amenable to the use of zone models which represent complex chemical reactors as a network of perfectly stirred reactors as discussed in the textbook by Hill (1977). Fox (2003) cautions that use of laminar reaction models in cases where the chemical reaction time scale is comparable to mixing time scales can lead to significant errors. In the fast chemistry-slow mixing limit, a mixture fraction approach has been widely used to describe the mixing, the conversion of reactants to products assumed to be instantaneous. Neglecting chemical reactions makes the problem more tractable but one still needs to model the mixing process which takes place at very small length scales over which there are unresolved turbulent velocity fluctuations. The interesting phenomena of extinction and reignition arise when the chemical reactions occur at time scales comparable to the mixing time scales and the residence time scales (determined by turbulent velocity fluctuations) as discussed in Peters (2000)). The computational modeling of these phenomena is another highly complex task.

Since mixing and chemical reactions take place at scales that are not resolved, one must resort to stochastic methods. A widely used stochastic modeling technique is the transport equation for the velocity-composition joint probability distribution function (Pope (1985)). This equation gives us the space and time variation of the PDF of the velocity and scalar concentrations from which one can determine the complete one point statistics of the state of the fluid. The PDF transport evolves in a higher dimensional space and therefore the solution requires alternative methods like Monte Carlo simulation or Moment methods. The computational requirements for using a statistical method such as Monte Carlo simulation in some grid based simulations are very large. As an example, in a simulation of a turbulent jet diffusion flame, Branley and Jones (2001) used 624,100 computational cells. To represent the subgrid scale processes around 20-100 notional particles are required to describe the PDF in each cell. Then stiff sets of ordinary differential equations need to be solved for each particle. Branley and Jones (2001) assumed fast chemistry and used a univariate PDF with a single mixture fraction variable. In the case of a reacting flow with finite rate chemistry, the number of equations to be solved increases linearly with the number of extra dimensions (species) needed to describe the PDF. In view of these requirements, it is useful to consider moment methods. The moment methods only track the moments of the PDF and therefore do not carry all the information that is present in the PDF. Thus I again encounter a closure problem for processes that cannot be described using a finite set of moments. The purpose in this section is to investigate the use of the Direct Quadrature Method of Moments (DQMOM) for solving the PDF transport equation describing turbulent mixing and combustion. For this purpose, I consider a partially stirred reactor (PaSR) model

(Ren and Pope (2004), Chen (1997)). As will be seen later, a PaSR model can be used to investigate most of the interesting features of a turbulent reacting flow problem. A PaSR can be considered to be a single computational cell in a more detailed CFD simulation or an element of zone models for industrial scale reactors. However, the purpose of the exercise is not to investigate the physics of the PaSR but to use it to validate the DQMOM simulations by comparison with the solutions obtained using Monte Carlo simulation.

4.2.2 Derivation of the pdf transport equation for simulating a Partially Stirred Reactor.

The joint scalar PDF transport equation has already been described in chapter 2. Using the IEM model (equation 2.10) in the joint scalar PDF transport equation (equation 2.9) gives us:

$$\frac{\partial f_\phi}{\partial t} + \langle U_i \rangle \frac{\partial f_\phi}{\partial x_i} = \frac{\partial}{\partial x_i} \left[\Gamma_T \frac{\partial}{\partial x_i} f_\phi \right] - \frac{\partial}{\partial \psi_i} \left[\left(\frac{\langle \phi_i \rangle - \psi_i}{\tau_{mix}} \right) f_\phi \right] - \frac{\partial}{\partial \psi_i} [S_i(\bar{\psi}) f_\phi]. \quad 4.2.1$$

The physical meaning of all terms in this equation is discussed in section 2.2.2. In a PaSR, one assumes the PDF to be homogeneous in space, i.e. f_ϕ is not a function of spatial variable \bar{x} . Thus one can integrate equation 4.2.1 over the reactor volume, shown in figure 4.2.1.

$$\frac{\partial \tilde{f}}{\partial t} = -\frac{\tilde{f}}{\tau_{res}} + \frac{1}{\tau_{res}} [P\tilde{f}^{(O)} + (1-P)\tilde{f}^{(F)}] - \frac{\partial}{\partial \psi_i} \left[\left(\frac{\psi_i - \langle \psi_i \rangle}{\tau_{mix}} \right) \tilde{f} \right] - \frac{\partial}{\partial \psi_i} [S_i(\bar{\psi}) \tilde{f}] \quad 4.2.2$$

For a variable density problem, I define the density weighted PDF by

$\tilde{f}(\bar{\psi}) = \frac{\rho(\bar{\psi})f(\bar{\psi})}{\langle \rho(\bar{\psi}) \rangle}$ as in Pope (1985). The first and second terms on the right hand side

represent the outflow and inflows at the boundaries of the reactor and hence model the large scale macromixing. The third term represents micromixing that is modeled using the IEM. I neglect the mesomixing term for simplicity. Inclusion of this term would require the turbulent diffusivity and the spatial gradient of \tilde{f} at the boundaries. This term is usually neglected in PaSR models and equation 4.2.2 is in the same form as given in Ren and Pope (2004). The residence time $\tau_{res} = \frac{m}{\dot{m}_{ox} + \dot{m}_{fu}}$ and $P = \frac{\dot{m}_{ox}}{\dot{m}_{ox} + \dot{m}_{fu}}$, where m is the mass of gas inside the reactor and $\dot{m}_{ox}, \dot{m}_{fu}$ are inlet mass flow rates of the oxidizer and fuel respectively. The equivalence ratio is then given by $\phi = \frac{(1-P)}{(1-P_{st})}$ where P_{st} is the value of P for which the inflow mixture gives stoichiometric proportions. $\tilde{f}^{(F)}$ and $\tilde{f}^{(O)}$ are the fuel and oxidizer PDFs at the inlet. In this example, I assume that there are no fluctuations in the fuel and oxidizer \tilde{f} concentrations at the inlet and hence $\tilde{f}^{(F)}$ and $\tilde{f}^{(O)}$ are given by Delta functions.

$$\begin{aligned}\tilde{f}^{(F)} &= \delta(\psi_{fu} - \psi_{fu}^{(F)})\delta(\psi_T - \psi_T^{(F)}) \prod_{\alpha \neq fu, T} \delta(\psi_\alpha - 0) \\ \tilde{f}^{(O)} &= \delta(\psi_{ox} - \psi_{ox}^{(O)})\delta(\psi_T - \psi_T^{(O)}) \prod_{\alpha \neq ox, T} \delta(\psi_\alpha - 0)\end{aligned}\tag{4.2.4}$$

$\psi_{fu}^{(F)}$ and $\psi_T^{(F)}$ are the concentration and temperature of fuel at the inlet fuel stream respectively. $\psi_{ox}^{(O)}$ and $\psi_T^{(O)}$ are the concentration and temperature of oxidizer at the inlet oxidizer stream.

By scaling the time by the residence time, $t^* = t / \tau_{res}$ I obtain equation 4.2.2 in a form that shows the effect of the chemical, mixing and residence time scales.

$$\frac{\partial \tilde{f}}{\partial t^*} = -\tilde{f} + [P\tilde{f}^{(O)} + (1-P)\tilde{f}^{(F)}] - \frac{\partial}{\partial \psi_i} \left[\frac{\tau_{res}}{\tau_{mix}} (\psi_i - \langle \psi_i \rangle) \tilde{f} \right] - \frac{\partial}{\partial \psi_i} [\tau_{res} S_i(\bar{\psi}) \tilde{f}] \quad 4.2.3$$

The mixing can be controlled by varying the mixing time scale τ_{mix} at fixed τ_{res} and the chemical time scale can be changed by changing the residence time τ_{res} .

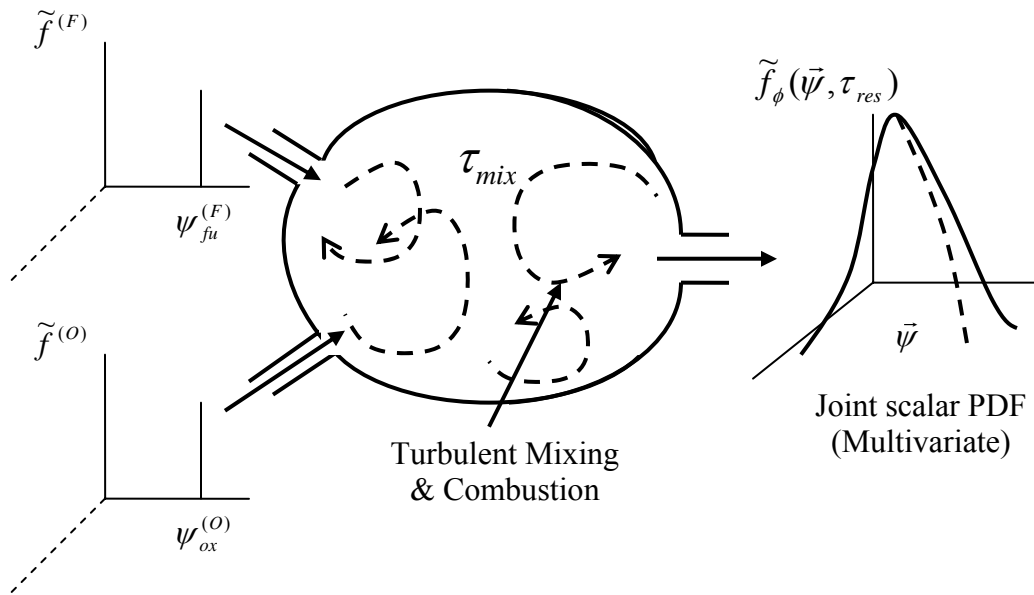


Figure 4.2.1. Schematic of a partially stirred reactor showing the fuel and oxidizer inlet and products outlet.

4.2.3 Application of the DQMOM.

As discussed in greater detail in chapter 2, the DQMOM uses a coarse grained representation of the underlying PDF (Fox (2003)).

$$\tilde{f}(\vec{\psi}; t) = \sum_{n=1}^{N_Q} W_n(t) \prod_{k=1}^d \delta(\psi_k - \hat{\psi}_{k,n}(t)) \quad 4.2.5$$

$W_n(t)$ is the quadrature weight, $\delta(\psi_k - \hat{\psi}_{k,n})$ is the Dirac delta function centered at the n^{th} quadrature point of the k^{th} variable, $\hat{\psi}_{k,n}$. N_Q is the total number of quadrature points, and d is the dimension of the space (i.e. the number of scalars defined in the pdf). As discussed in chapter 2, one can substitute 4.2.5 into equation 4.2.3 and obtain evolution equations for the densities $W_n(t)$ and $S_{k,n}(t) = W_n(t) \hat{\psi}_{k,n}(t)$.

$$\frac{dW_n}{dt} = a_n; n = 1, \dots, N_Q \quad 4.2.6$$

$$\frac{\partial S_{k,n}}{\partial t} = b_{k,n} - \left[\left(\frac{\tau_{res}}{\tau_{mix}} \right) (\hat{\psi}_{k,n} - \langle \psi_k \rangle) + \tau_{res} S_k(\vec{\psi}_n) \right] W_n; n = 1, \dots, N_Q; k = 1..d$$

The initial conditions are taken to be pure air inside the reactor.

To recapitulate, the $N_Q(d+1)$ source terms a_n and $b_{k,n}$ are obtained by forcing $N_Q(d+1)$ moments of the pdf to evolve correctly. This essentially involves solving a matrix equation of the form $A\alpha = \beta$ where A is an $N_Q(d+1) \times N_Q(d+1)$ matrix for which each row is of the form

$$A = \left[\underbrace{\left(1 - \sum_{\alpha=1}^d l_{\alpha} \right) \prod_{k=1}^d \hat{\psi}_{k,n}^{m_{\alpha}}; n = 1, \dots, N_Q}_{(N_Q)cols}; \underbrace{\frac{\partial}{\partial \hat{\psi}_{\alpha,n}} \left(\prod_{k=1}^d \hat{\psi}_{k,n}^{m_k} \right); n = 1, \dots, N_Q, \alpha = 1, \dots, d}_{(N_Q \times d)cols} \right] \quad 4.2.7$$

There are $N_Q(d+1)$ rows given by $N_Q(d+1)$ d -tuple (l_1, \dots, l_d) . This choice of A ensures that $N_Q(d+1)$ moments M_{m_1, \dots, m_d} moments evolve consistently. The vector

α contains the source terms ($a_n; n = 1, \dots, N_Q; b_{k,n}; n = 1, \dots, N_Q; k = 1, \dots, d$) and β consists of terms due to mixing, reactions, inlets and outlet. Each of the $N_Q(d+1)$ rows of β indexed by the d-tuple $\{l_\alpha\}$ is given by

$$\beta_{\{l_\alpha\}} = \left[P(\psi_{ox}^{(0)})^{l_{ox}} (\psi_T^{(0)})^{l_T} \prod_{\alpha \neq ox, T} 0^{l_\alpha} + (1-P)(\psi_{fu}^{(F)})^{l_{fu}} (\psi_T^{(F)})^{l_T} \prod_{\alpha \neq fu, T} 0^{l_\alpha} - \sum_{n=1}^{N_Q} \prod_{\alpha=1}^d \hat{\psi}_{\alpha,n}^{l_\alpha} W_n \right] 4.2.8$$

$\psi_{ox}^{(O)}, \psi_T^{(O)}$ denote the oxygen mass fraction and temperature at the oxidizer inlet.

$\psi_{ox}^{(F)}, \psi_T^{(F)}$ denote the fuel mass fraction and temperature at the fuel inlet. For simplified

chemistry schemes the scalars can be defined in terms of mixture fractions and progress variables and equation 4.2.8 must be redefined accordingly. Therefore the solution of the problem involves solving the system of ODEs (equation 4.2.6) with the source terms for each time step determined by the solution of a matrix equation.

From equation 4.2.3, one can see why the partially stirred reactor model is a suitable problem for investigating multivariate DQMOM. If one employs more sophisticated reaction mechanisms to evaluate the chemical source term S_i , then one needs to include the mass fraction information of a larger number of species. This immediately gives rise to a multivariate PDF. In the calculations that follow, I apply the theory for multivariate DQMOM outlined in Chapter 2 and compare the DQMOM predictions with Monte Carlo simulations.

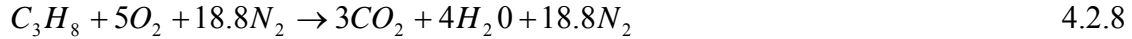
4.2.4 Chemistry Models.

To investigate the performance of DQMOM for low and high dimensional systems I consider chemical reaction mechanisms of increasing complexity. The

chemical reaction model is required to evaluate the chemical source terms $S_i(\bar{\psi})$ appearing in equation 4.2.6.

(a) One step chemistry mechanism.

This is the simplest possible mechanism. I use the global 1-step reaction for propane combustion from Westbrook and Dryer (1981).



The one step chemistry problem gives rise to a bivariate problem ($D = 2$). Here I use a mixture fraction and progress variable approach (Fox (2003)). The mixture fraction, Z , is defined to be zero for pure oxygen, i.e. $\psi = \psi_{ox}^{(O)}$ and 1 for pure fuel $\psi = \psi_{fu}^{(F)}$. The intermediate values represent the various degrees of mixing. The progress variable, Y , is a variable that is proportional to the mass fraction of carbon dioxide. For the one step mechanism, the mass fractions of all the species can be obtained from Z and Y using linear transformations. The concentration of nitrogen in the inlet air can be obtained from the concentration of the remaining species.

$$\begin{aligned} \psi_F &= \psi_{fu}^{(F)} (Z - Z_{st} Y) \\ \psi_O &= \psi_{ox}^{(O)} ((1 - Z) - (1 - Z_{st}) Y) \\ \psi_{CO_2} &= \psi_{fu}^{(F)} Z_{st} \left(\frac{3W_{CO_2}}{W_F} \right) Y \\ \psi_{H_2O} &= \psi_{fu}^{(F)} Z_{st} \left(\frac{4W_{H_2O}}{W_F} \right) Y \\ \psi_T &= \psi_T^{(O)} + (\psi_T^{(F)} - \psi_T^{(O)}) Z + \frac{\psi_{fu}^{(F)} Z_{st} Q_H Y}{C_p} \end{aligned} \quad 4.2.9$$

The stoichiometric mixture fraction, $Z_{st} = \frac{1}{1 + \left(\frac{5W_O}{W_F} \right) \left(\frac{\psi_{fu}^{(F)}}{\psi_{ox}^{(O)}} \right)}$ and the quantity $\frac{Q_H}{C_p}$ is

defined such that when $\psi_T^{(O)} = \psi_T^{(F)} = 298K$ and $Y = 1$, the temperature ψ_T equals the adiabatic flame temperature of propane (2250 K). Once the mass fractions of the species and the temperature are obtained using the above relations, the chemical source terms for Z and Y can be obtained as

$$S_Z = 0$$

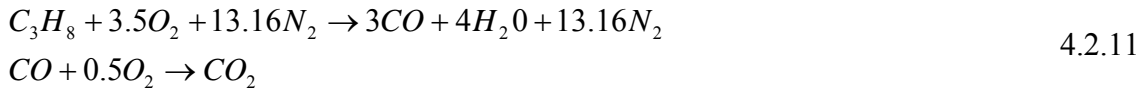
$$S_Y = \frac{1000 \cdot W_F}{\langle \rho \rangle Z_{st} \psi_{fu}^{(F)}} A [F]^a [O]^b \exp\left(\frac{-E_a}{R\psi_T}\right) \quad 4.2.10$$

where $[F] = \left(\frac{\rho \psi_F}{W_F} \right)$ is the molar concentration of the fuel in gmol/cc, $A = 8.6 \times 10^{11}$,

$E_a = 30.0 \text{ kcal/mol}$, $a = 0.1$ and $b = 1.65$.

(b) Two-step chemistry mechanism.

I use the 2-step mechanism for propane taken from Westbrook and Dryer (1981).



This is an example of a competitive-consecutive reaction (Fox (2003)) and gives rise to a trivariate ($D = 3$) problem. I again use the mixture fraction progress variable approach as in the one step reaction. Here one needs two progress variables, Y_1 and Y_2 that are proportional to the mass fractions of CO_2 and H_2O . The species mass fractions and temperature can again be written down in terms of Z , Y_1 and Y_2 as follows.

$$\begin{aligned}
\psi_F &= \psi_{fu}^{(F)} (Z - Z_{st} Y_1) \\
\psi_O &= \psi_{ox}^{(O)} [(1 - Z) - (1 - Z_{st})(0.7Y_1 + 0.3Y_2)] \\
\psi_{CO} &= \psi_{fu}^{(F)} Z_{st} \left(\frac{3W_{CO}}{W_F} \right) (Y_1 - Y_2) \\
\psi_{CO_2} &= \psi_{fu}^{(F)} Z_{st} \left(\frac{3W_{CO_2}}{W_F} \right) Y_2 \\
\psi_{H_2O} &= \psi_{fu}^{(F)} Z_{st} \left(\frac{4W_{H_2O}}{W_F} \right) Y_1 \\
\psi_T &= \psi_T^{(O)} + (\psi_T^{(F)} - \psi_T^{(O)})Z + \frac{\psi_{fu}^{(F)} Z_{st} (Q_{H_1} Y_1 + Q_{H_2} \left(\frac{W_{CO}}{W_F} \right) Y_2)}{C_p}
\end{aligned} \tag{4.2.12}$$

The stoichiometric mixture fraction, Z_{st} , is defined as in the previous section. In order to avoid issues arising due to the varying specific heats, I define C_p such that when $\psi_T^{(O)} = \psi_T^{(F)} = 298K$ and $Y_1 = Y_2 = 1$, ψ_T becomes the adiabatic flame temperature of propane.

The chemical source terms for the variables Z , Y_1 and Y_2 are

$$\begin{aligned}
S_Z &= 0.0 \\
S_{Y_1} &= \frac{1000 \cdot W_F}{\psi_{fu}^{(F)} Z_{st} \langle \rho \rangle} A_1 [F]^a [O]^b \exp\left(\frac{-E_{a1}}{R\psi_T}\right) \\
S_{Y_2} &= \frac{1000 \cdot W_F}{3\psi_{fu}^{(F)} Z_{st} \langle \rho \rangle} \{A_{2f} [CO]^c [H_2O]^d [O_2]^e - A_{2b} [CO_2]^f\} \exp\left(\frac{-E_{a2}}{R\psi_T}\right)
\end{aligned} \tag{4.2.13}$$

$[F] = \left(\frac{\rho \phi_F}{W_F} \right)$ denotes the molar concentration of fuel in gmol/cc etc.

$a = 0.1, b = 1.65, c = 1.0, d = 0.5, e = 0.25, f = 1.0$. Activation energies for the various

reactions are $E_{a1} = 30.0 \text{ kcal/mol}$, $E_{a2} = 40.0 \text{ kcal/mol}$. Pre-exponential factors are $A_1 = 1.0 \times 10^{12}$ and $A_{2f} = 10^{14.6}$, $A_{2b} = 5 \times 10^8$.

Problem	Dimension	Mixing Model	Chemistry	Chemical Source Terms
Mixing	1	IEM	N/A	N/A
1-step reaction	2	IEM	1 step global reaction for propane $\text{C}_3\text{H}_8 + 5\text{O}_2 + 18.8\text{N}_2 \rightarrow 3\text{CO}_2 + 4\text{H}_2\text{O} + 18.8\text{N}_2$	$R_1 = 0$ $R_2 \sim [\text{Y}_F]^a [\text{Y}_O]^b \exp(-E_a/RT)$
2-step reaction	3	IEM	2 step reaction for propane $\text{C}_3\text{H}_8 + 3\text{O}_2 + 13.3\text{N}_2 \rightarrow \text{CO} + 4\text{H}_2\text{O} + 13.2\text{N}_2$ $\text{CO} + \frac{1}{2} \text{O}_2 \rightarrow \text{CO}_2$	$R_1 = 0$ $R_2 \sim [\text{Y}_F]^a [\text{Y}_O]^b e^{(E_{a1}/RT)}$ $R_3 \sim \{[\text{Y}_{\text{CO}}]^c [\text{Y}_O]^d [\text{Y}_{\text{H}_2\text{O}}]^d - [\text{Y}_{\text{CO}_2}]^f\} e^{(-E_{a2}/RT)}$

Table 4.2.1. Summary of mixing and chemistry sub-models used in the computational problem for the partially stirred reactor.

4.2.5 Computations and Discussion of Results.

Having described the equations to be solved and the chemistry models used, I proceed to study the accuracy of the DQMOM solutions by comparing the means and variances of the species with the means and variances obtained using Monte Carlo

simulations. I present a summary of the problems studied in Table 4.2.1. To obtain the DQMOM solution I integrate equations 4.2.5 starting with conditions of pure air inside the reactor. As per Ren and Pope (2004), the time step is $\Delta t^* = 0.1 \min(\tau_{res}, \tau_{mix}) / \tau_{res}$ and fractional time stepping is used, that is first the inflow-outflow step is evaluated, then the mixing and finally the reaction step. For the Monte Carlo simulations I follow the exact procedure described in Ren and Pope (2004). Ren and Pope (2004) present only the stationary state results and start with an initial condition that is close to the expected stationary state. In this study, I use the initial condition of pure air in the reactor and simulate the transient phenomena as well. The mixture-fraction/ progress-variable PDF inside the reactor is represented using N_{tot} notional particles. At the beginning of each time step, $N_{replace} = NINT(\Delta t^* N_{tot})$ particles are chosen randomly with replacement from the ensemble of N_{tot} particles. (Here $NINT(x)$ is the function that returns the integer that is closest to x). The chosen $N_{replace}$ particles are replaced by

$$N_F = NINT\left(\Delta t^* N_{tot} \frac{\dot{m}_{fu}}{\dot{m}_{fu} + \dot{m}_{ox}}\right) \text{ fuel particles and } N_A = N_{replace} - N_F \text{ oxygen particles.}$$

Then all the particles are mixed according to the IEM model and finally the reaction step is evaluated by integrating the reaction rate term starting with the varying chemical compositions and temperature associated with each particle. The integration is performed using the stiff integrator DASSL (Petzold (1983)) that is available in the public domain.

(a) Two stream mixing problem.

The two stream mixing problem without chemistry can be described by the mixture fraction variable alone. The problem is then a univariate problem which presents fewer

difficulties. Further, for the simple, linear mixing model (IEM), one can obtain exact solutions for the time varying mean and variance of the mixture fraction in the reactor. Figures 4.2.2 and 4.2.3 show the mean and variances of Z for the case of slower mixing, $\frac{\tau_{mix}}{\tau_{res}} = 1.0$, and faster mixing, $\frac{\tau_{mix}}{\tau_{res}} = 0.1$. Also shown is the solution using Monte Carlo simulations with 10,000 and 100,000 particles. By comparing the two cases, one can see that the mean is unaffected by the mixing time scale while the variance goes down with faster mixing. A stationary state is attained at $\frac{t}{\tau_{res}} \sim 5$ when both the mean and variance do not change with time. The final steady state value for mean mixture fraction depends solely on the residence time and the rates of inflow of fuel and air. The steady state value for the variance depends on the mixing rate as well as the residence time and rates of fuel and air flow. In this case, the DQMOM solutions are also the exact, analytical solution and the Monte Carlo solutions converge to the same. Hence these results can be taken to be a validation of the Monte Carlo simulations.

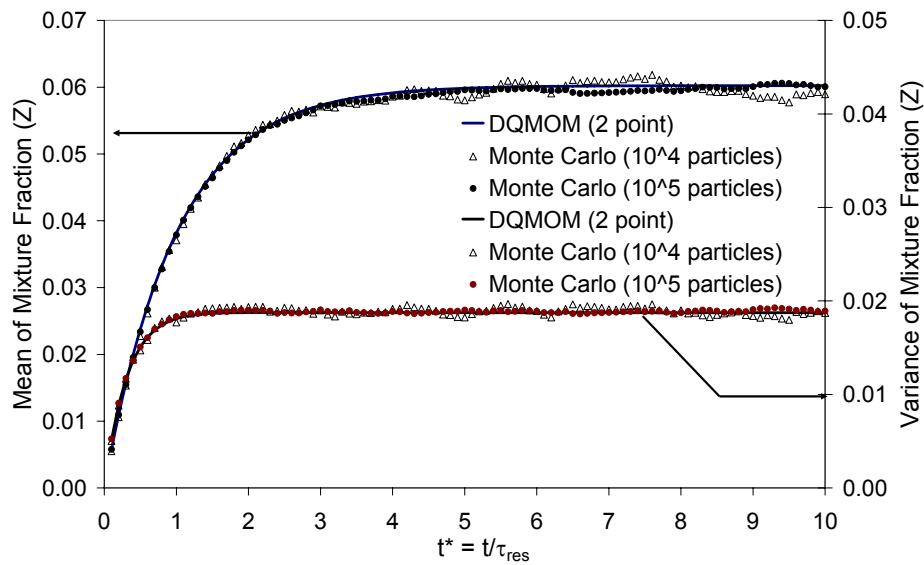


Figure 4.2.2. Plot showing the mean and variance of the mixture fraction for the case of slower mixing, $\frac{\tau_{mix}}{\tau_{res}} = 1$. Convergence of Monte Carlo solutions can be seen.

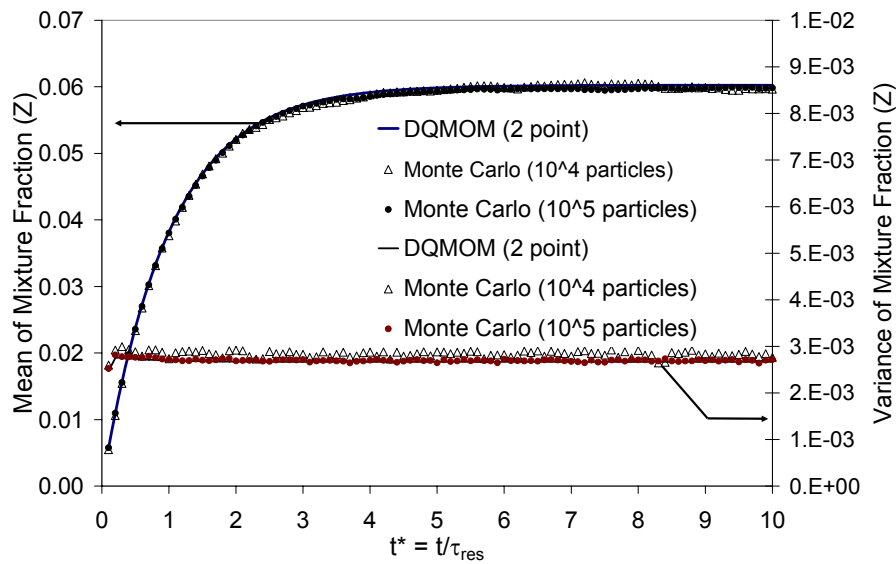


Figure 4.2.3. Plot showing the mean and variance of the mixture fraction for the case of faster mixing, $\frac{\tau_{mix}}{\tau_{res}} = 0.1$. Variances are lower due to faster mixing.

(b) One step chemistry problem.

The PaSR model with one step chemistry is a slightly more advanced model that allows the examination of finite rate chemistry effects such as ignition and extinction phenomena. Treatment of this problem using the transported PDF methods leads us to evaluate the time evolution of a bivariate PDF. This gives us an opportunity to test the theory for the multivariate DQMOM outlined in chapter 2. As stated earlier, the two variables will be the mixture fraction, Z , and a reaction progress variable, Y . Figure 4.2.4 shows the scatter plot for the final stationary distribution. One can see that all the Z, Y points lie on a manifold. This appears to be true for a deterministic mixing model such as the IEM but not for stochastic mixing models such as the coalescence-dispersion or the EMST models where there can be some scatter in the values of Z and Y as shown in Ren and Pope (2004). In addition one sees that the points lie on the equilibrium curve for the fast mixing case ($\tau_{res} = 0.1s; \tau_{mix} = 0.01s$) while for the slow mixing case ($\tau_{res} = 0.1s; \tau_{mix} = 0.1s$) there are some non-equilibrium effects for higher values of Z (fuel rich mixtures) even in the final stationary state.

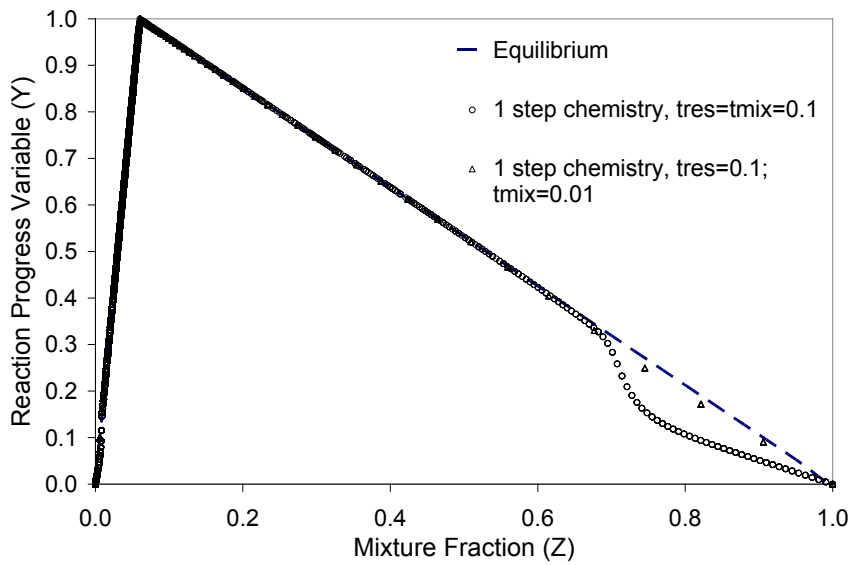


Figure 4.2.4 Scatter plot showing the distribution of mixture fraction (Z) and reaction progress variable (Y) at the stationary state. Dashed line shows the equilibrium state, circles slower mixing and triangles faster mixing.

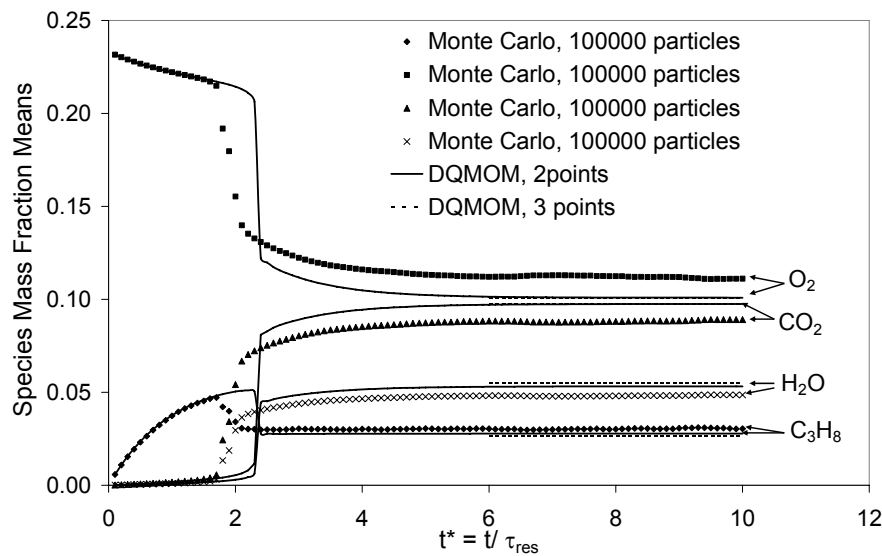


Figure 4.2.5 Species means for the slower mixing case of $\tau_{res} = 0.1, \tau_{mix} = 0.1$. Only stationary state values are shown for the 3 point quadrature results.

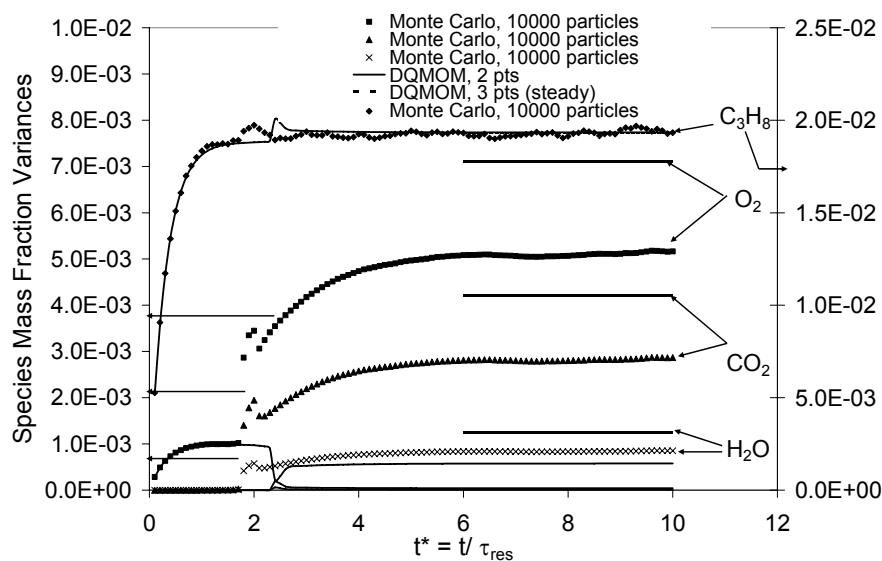


Figure 4.2.6 Species variances for the slower mixing case of $\tau_{res} = 0.1, \tau_{mix} = 0.1$. Only stationary state values are shown for the 3 point quadrature results.

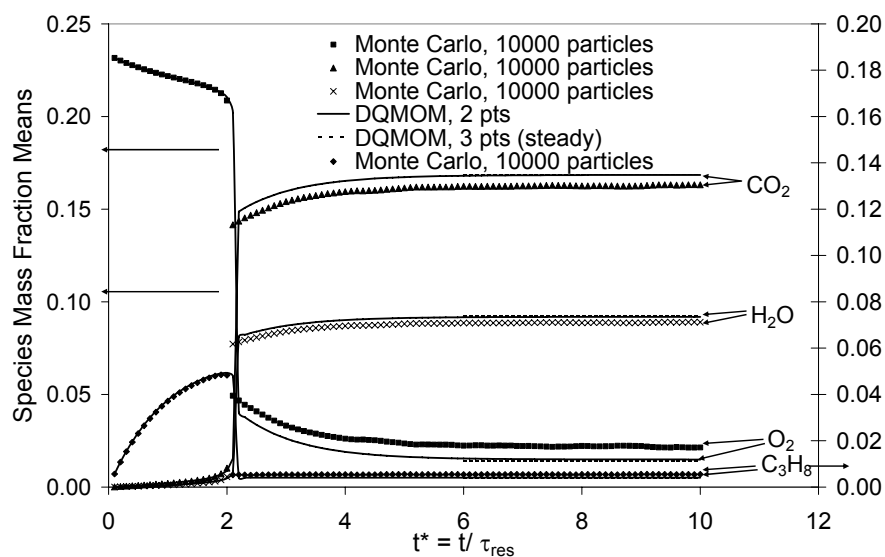


Figure 4.2.7 Species means for the faster mixing case of $\tau_{res} = 0.1, \tau_{mix} = 0.01$. Only stationary state values are shown for the 3 point quadrature results.

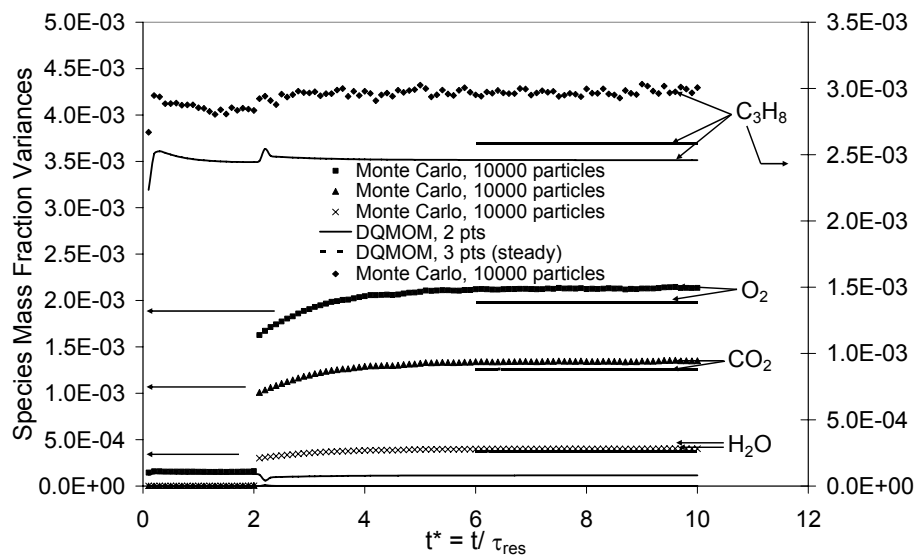


Figure 4.2.8 Species variances for the faster mixing case of $\tau_{res} = 0.1, \tau_{mix} = 0.01$. Only stationary state values are shown for the 3 point quadrature results.

Next I check the predictions for the species means and variances obtained using both the DQMOM as well as the Monte Carlo simulations. Since there are no closure issues in the Monte Carlo simulations one may assume that the converged Monte Carlo results are more accurate. For the DQMOM calculations I use both 2 and 3 point quadrature. For the 3 point calculations, due to difficulties encountered in starting with pure air in the reactor, the initial conditions are set from the results obtained from Monte Carlo simulations. Hence only the final stationary results are shown for the 3 point calculations. In figure 4.2.5 and 4.2.6, I plot the species means and variances for the slower mixing case. Looking at the species means in figure 4.2.5, one finds good agreement for the species means for both the transient phenomenon of ignition as well as the final stationary states. Further it is seen that the 3 point results coincide with the 2 point predictions. For the variances (shown in figure 4.2.6), one sees a lot of deviation

between the DQMOM results and the Monte Carlo simulations. The variances compare favorably only for the fuel while the 2 point DQMOM predictions for the other species show considerable error. Better agreement for the variances for all the species can be obtained with three point DQMOM. The same phenomena can also be seen for the faster mixing case. There is a very good agreement between 2 and 3 point DQMOM and Monte Carlo simulations for the species mass fraction means as shown in figure 4.2.7 while there is significant error in prediction of the variance (seen in figure 4.2.8) with the 2 point DQMOM. Again one finds much better agreement for the variances with three quadrature points . It should be noted that the variances are quite small in all cases. This appears to be true for air rich and stoichiometric combustion conditions as well as for fast mixing cases. However, even if the species variances are low, the variance in the temperature can be quite large and therefore it is important to predict the variances correctly.

As discussed in Chapter 2, there are two possible sources of error for the DQMOM solutions. One is the error due to the quadrature approximation of integrals for the chemical source term using a truncated set of moments. The other source of error is due to the selective elimination of some of the moments (Selective Graded Lexicographic Ordering) in order to get a non-singular matrix. For instance using the mixture fraction variable, Z , as the primary variable and using SGLO gives us the following valid moment set: $\{M_{i,j,k} : (i, j, k) = (0,0), (1,0), (0,1), (2,0), (1,1), (3,0)\}$. This set does not contain the second moment of the reaction progress variable $M_{0,2}$. From equation 4.2.9, one sees that the variance of CO_2 and H_2O will be proportional to the variance of the reaction

progress variable which in turn depends on $M_{0,2}$. Thus it is crucial to ascertain the magnitude of the error incurred in discarding some of the moments. To quantify the different sources of error, I define a total relative difference of species means and variances defined as:

$$ERR = \left[\sum_{species, i=1}^N \left(\frac{\delta E(\psi_i)}{E(\psi_i)} \right)^2 + \left(\frac{\delta Var(\psi_i)}{Var(\psi_i)} \right)^2 \right]^{1/2}. \quad 4.2.14$$

To isolate the error due to the incompleteness of the moment set, I first obtain the moment set used in the DQMOM simulations from the Monte Carlo simulations (e.g. the set $\{M_{i,j} : (i, j) = (0,0), (1,0), (0,1), (2,0), (1,1), (3,0)\}$) and reconstruct the quadrature points and weights directly from this set. This is done by solving the set of equations given by

$$M_{k,l} = \sum_{n=1}^{N_Q} W_n Z_n^k Y_n^l \text{ for the } 3N_Q \text{ variables } W_n, Z_n, Y_n. \text{ In this study, I used the}$$

multivariate Newton Raphson method (Press et al. (1992)) to solve these equations. It must be understood that the moments obtained in this manner are exact since they are obtained directly from the Monte Carlo simulations that do not contain closure errors. However, the species means and variances computed using these moments (or equivalently, using the quadrature points and weights W_n, Z_n, Y_n obtained from this moment set) are not exact. This is because the species means and variances also depend on other moments that are not contained in the DQMOM set. I compare the species means and variances using the “exact but incomplete” moment set with the species means and variances obtained using the “exact and complete” moment set. Let ERR_1 be the total relative difference between the two solutions. I also compare with the species means and

variances obtained using DQMOM with the “exact” values obtained from Monte Carlo simulations. Let ERR_2 be the total relative difference of the two solutions. ERR_2 quantifies the error due to the incomplete moment set as well as the error accumulated over time due to the quadrature approximation of integrals.

In figure 4.2.9, I plot the histogram summarizing the error for the slower mixing case. The first column is ERR_1 while the second column is ERR_2 . ERR_2 is only very slightly larger than ERR_1 which implies that most of the error is due to the incomplete moment set. The quadrature closure error accumulated during the DQMOM evolution is very small compared to the error in the selection of moments. For the first two columns, the moment sets are selected using the Selective Graded Lexicographic Ordering (SGLO) scheme with the mixture fraction variable Z as the principal dimension (variable) as discussed in section 2.7.2. The next two columns show the same comparison with the set of moments obtained by choosing the reaction progress variable Y as the principal dimension and applying SGLO. In this case a larger number of moments containing Y will be selected. Here the error in the reconstructed solution is lower probably because in the final stationary state, only the products are predominant and the reaction progress variable better describes the products. However the error in the DQMOM solution is much higher which indicates that proper resolution of the mixture fraction variable is essential to obtain accurate solutions while dealing with the transient phenomena. This could be due to the fact that the mixture fraction better describes the mixing of the incoming fuel and air streams. It is also noted that during the 2 point DQMOM simulations with Y as the principal variable, one of the quadrature points exceeds the bounds on the species mass fractions set by the constraint of element conservation.

Violation of element conservation bounds is not observed for cases in which Z is the principal dimension (variable). As a tentative conclusion, I propose that for problems of mixing and chemical reaction using the mixture fraction variable and two point quadrature, the mixture fraction Z as the principal dimension in SGLO. For three points, there is negligible error in the reconstructed solution because in this case one has all the relevant moments in the moment set. There is a smaller error in the 3 point DQMOM solution, most of which is due to errors in the variance. Figure 4.2.10 shows the same error histogram for the faster mixing case and one sees that similar conclusions can be drawn.

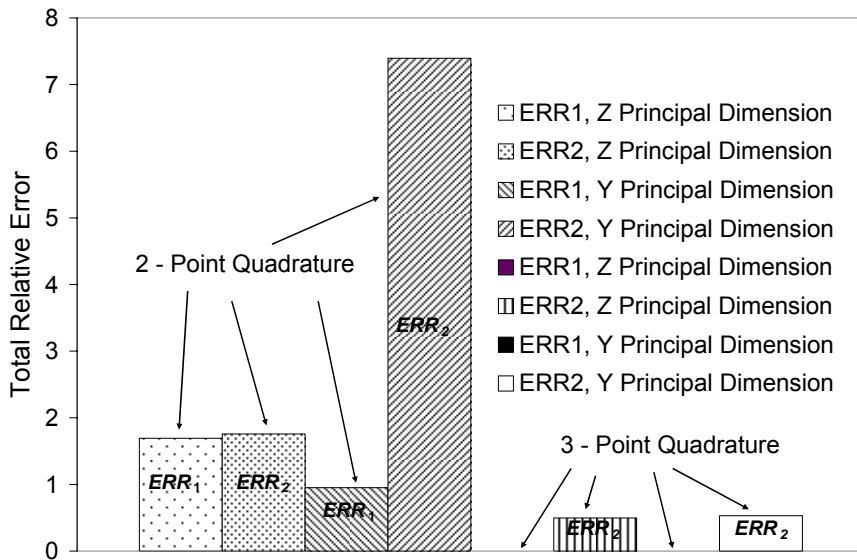


Figure 4.2.9. Histogram that summarizes the total relative errors in the species means and variances. (ERR_1 and ERR_2 are as defined in the text. Z , Y Principal Dimension indicates that the mixture fraction (Z), reaction progress variable (Y) respectively are used as the principal dimension in SGLO.) Case of slower mixing $\tau_{res} = 0.1, \tau_{mix} = 0.1$.

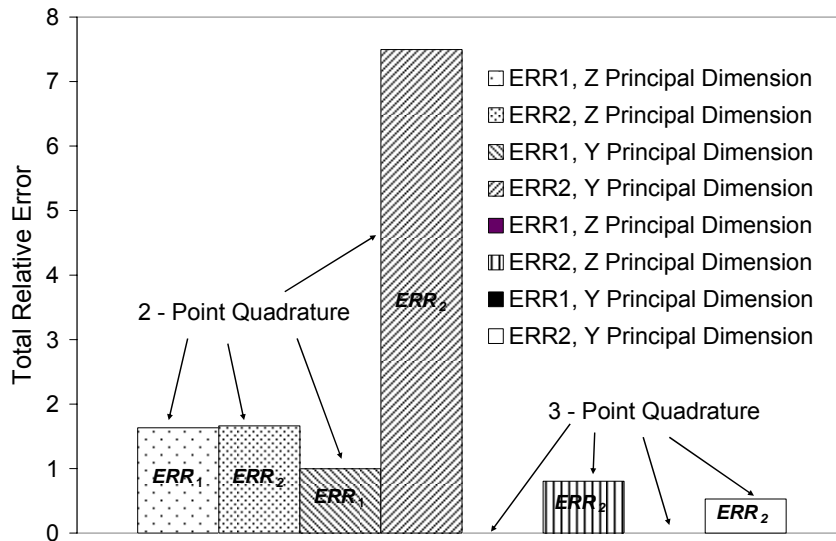


Figure 4.2.10. Same histogram as in figure 4.2.8 for the case of faster mixing ($\tau_{res} = 0.1, \tau_{mix} = 0.01$).

(b) Two step chemistry problem.

In the two step chemistry problem, I use a more sophisticated chemical reaction mechanism. There are now two reactions that compete with each other and also the dimension of the problem is increased by one so that one is dealing with a trivariate problem. The variables used in the PDF are the mixture fraction, Z and two reaction progress variables, Y_1 and Y_2 . One can get all the relevant species mass fractions from these two variables as shown in equation 4.2.12. Figure 4.2.11 shows the scatter plot for the stationary distribution. One again sees that the points lie on a (deterministic) manifold that is characteristic of a deterministic mixing model such as the IEM. Unlike the 1 step mechanism, one sees significant deviations from equilibrium and greater differences between the slow mixing and fast mixing cases. In figures 4.2.12 and 4.2.13, I compare the species means and variances for the faster mixing case. The species means show good

agreement both for the transient and final stationary states. In particular, the peak mean CO concentration as well as the steady mean concentration is in close agreement with the Monte Carlo results. The variances again show the same trend, large errors for the 2-point prediction that get a lot better with three points. In figures 4.2.14 and 4.2.15, I plot the means and variances for the slow mixing case. All species means are predicted correctly except the CO concentration which seems to show large and opposite deviations for the 2-point and 3-point calculations. I believe that this is due to the extreme sensitivity to the temperature of the second reaction that determines the CO concentration. It should be mentioned that in some cases I considered with a longer residence time $\tau_{res} = 1s$, I find the mean CO predictions to be reasonably accurate. In figure 4.2.16, I plot the error histogram. One sees that errors are larger in part because I consider more species. An interesting observation is that for the 3 point calculations, the error due to reconstruction of moments is slightly larger than the error due to DQMOM (i.e. the error ERR_1 defined earlier is larger than ERR_2). A closer examination reveals that the error in the reconstruction is due to a large error in the mean CO predictions. By ignoring the mean CO error in definition of the total error gives us the next two columns which follows the same trend as shown in the results obtained using the one-step chemistry model. The reason behind the error in mean CO prediction is puzzling. Apart from the extreme temperature sensitivity of the reaction, a possible reason is that for the trivariate case even the 3 point DQMOM calculations do not use all the moments that are required to reconstruct the species means and variances. In this higher dimensional setting, one may need to go to 4-point quadrature if one requires greater accuracy.

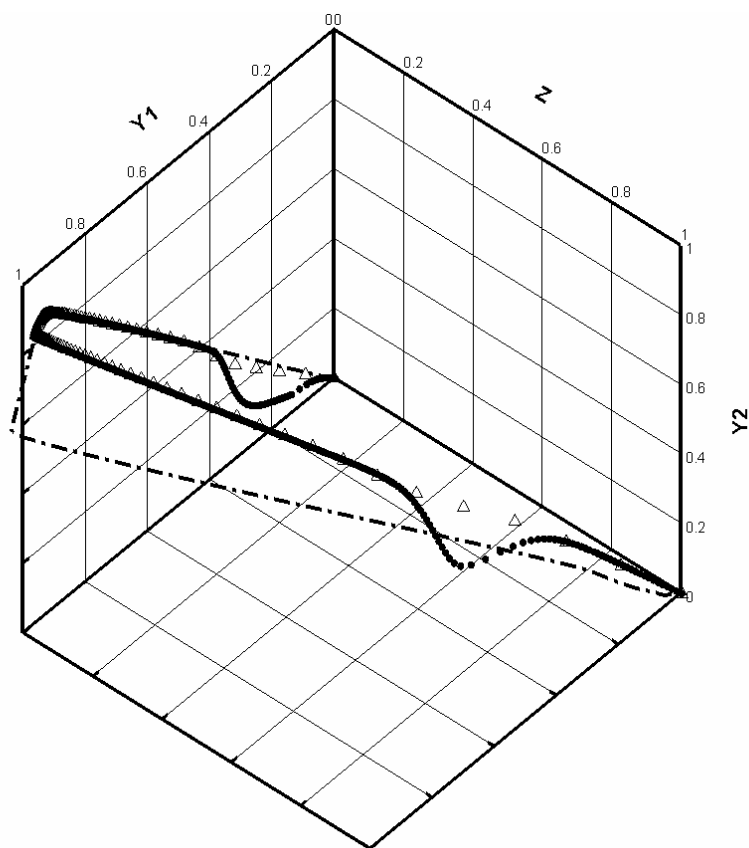


Figure 4.2.11. Scatter plot showing distribution of the mixture fraction and two reaction progress variables at the stationary state. Dash-dot lines correspond to equilibrium, unfilled triangles (Δ) the fast mixing case ($\tau_{res} = 0.1, \tau_{mix} = 0.01$) and filled circles the slow mixing case ($\tau_{res} = 0.1, \tau_{mix} = 0.1$).

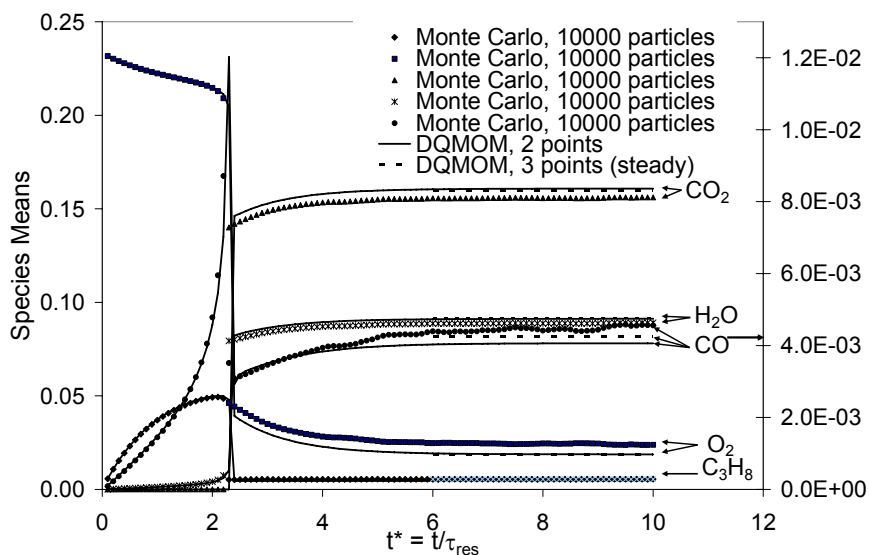


Figure 4.2.12. Species means for the faster mixing case of $\tau_{res} = 0.1, \tau_{mix} = 0.01$, 2 step chemistry model. Only stationary state values are shown for the 3 point quadrature results.

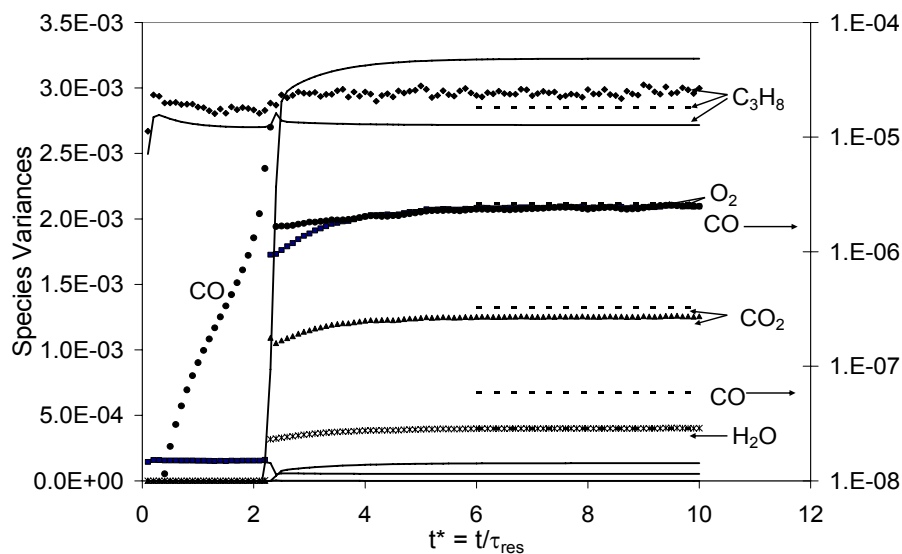


Figure 4.2.13. Species variances for the faster mixing case of $\tau_{res} = 0.1, \tau_{mix} = 0.01$, 2 step chemistry model. Only stationary state values are shown for the 3 point quadrature results.

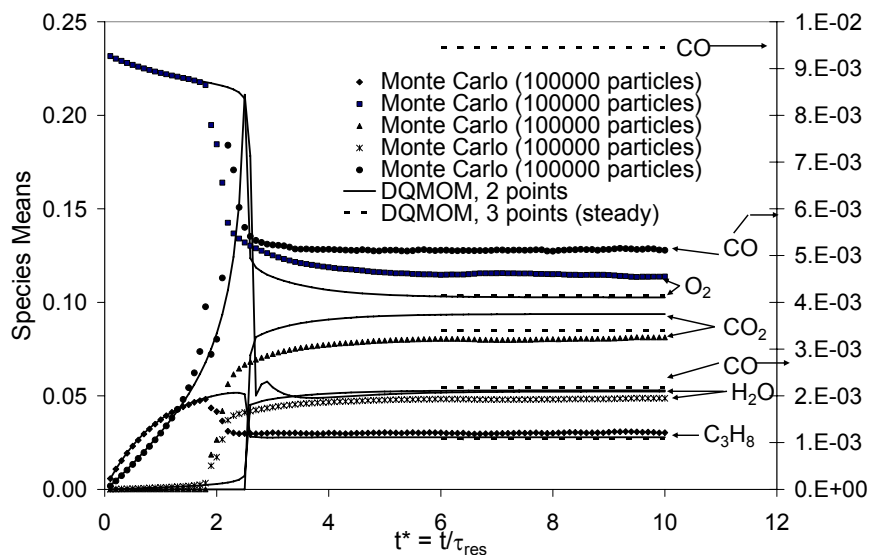


Figure 4.2.14. Species means for the slower mixing case of $\tau_{res} = 0.1, \tau_{mix} = 0.1$, 2 step chemistry model. Only stationary state values are shown for the 3 point quadrature results.

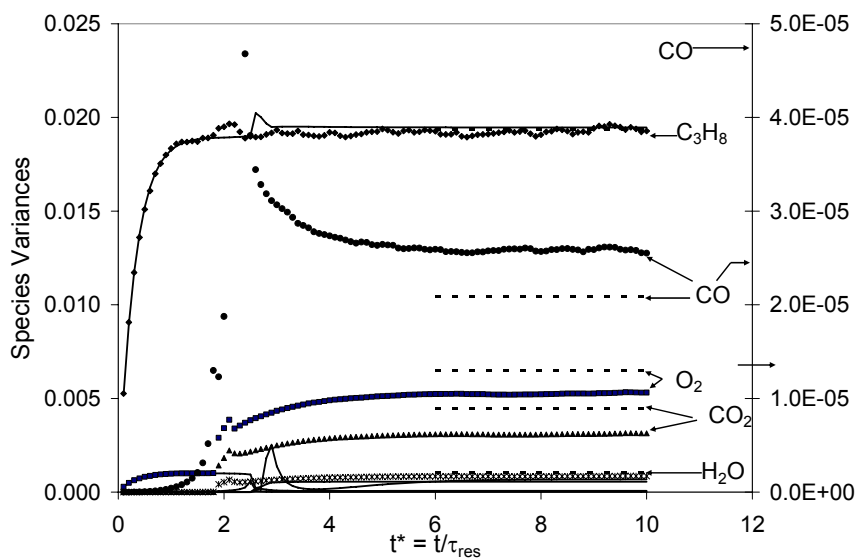


Figure 4.2.15. Species variances for the slower mixing case of $\tau_{res} = 0.1, \tau_{mix} = 0.1$, 2 step chemistry model. Only stationary state values are shown for the 3 point quadrature results.

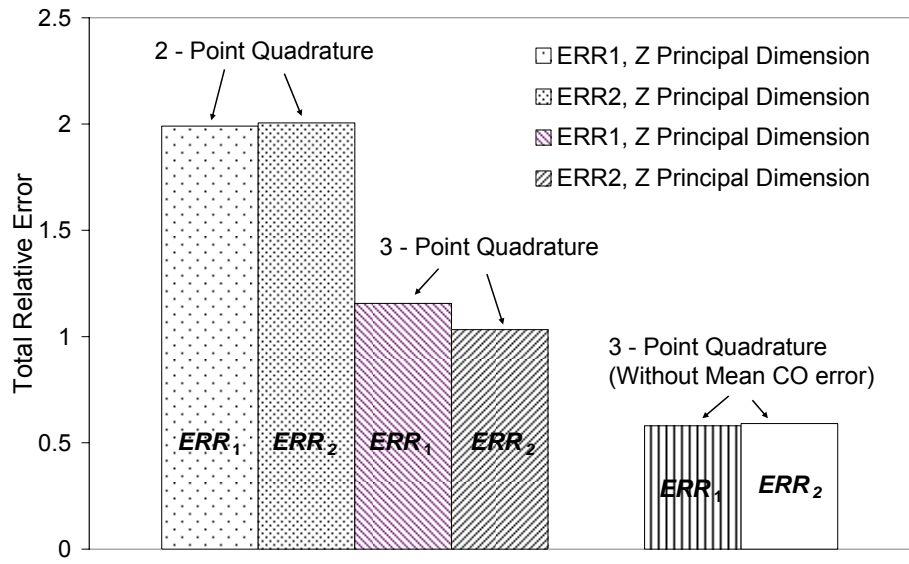


Figure 4.2.16. Histogram that summarizes the total relative errors in the species means and variances. (ERR_1 and ERR_2 are as defined in the text. Z , Y Principal Dimension indicates that the mixture fraction (Z), reaction progress variable (Y) respectively are used as the principal dimension in SGLO.) The two columns indicated as “Without Mean CO error” is the total relative error neglecting the mean CO mass fraction error. Case of slower mixing $\tau_{res} = 0.1, \tau_{mix} = 0.1$.

4.2.6 Conclusions.

In this section I discuss the implications of some of my findings in the previous section. The DQMOM method is really a systematic expansion of the PDF transport equation in terms of its moment equations. Hence its major advantage ought to be the reduced computational cost. Indeed in my simulations, I got results from DQMOM almost instantly while it took several hours to get the converged Monte Carlo results. As a caveat, I point out that I did not use some of the developments in accelerating the Monte Carlo results such as parallelization of the code, ISAT for the chemistry etc. While inclusions of these techniques would certainly speed up the Monte Carlo simulation, it

will be surprising if these computations become any faster than the DQMOM computations. The Monte Carlo simulations will eventually be more effective as the dimension of the problem becomes high enough. A detailed analysis of the algorithmic complexity of the DQMOM and asymptotic analyses on the dimensions and number of quadrature points is beyond the scope of this work. However, granted that DQMOM calculations are more efficient than the Monte Carlo simulations, one needs to evaluate the feasibility and accuracy of solutions. In terms of feasibility, I found that if the multivariate moments are chosen according to a scheme that avoids the formation of a singular or ill-conditioned Jacobian matrix, then the calculations can be carried out without any blowup. I found that this method even works for a 19 dimension problem (using the more detailed ARM2 chemical reaction mechanism described in the TNF website maintained by Sandia (<http://www.ca.sandia.gov/TNF/chemistry.html>)). However the act of creating a non-singular matrix forces me to discard moments that may be extremely important for the accuracy of my simulations. This appears to be a fundamental drawback of the DQMOM method for multivariate problems. This problem can only be avoided by choosing a larger number of quadrature points. My analysis of the error also revealed that the error due to the use of an incomplete moment set is higher than the error due to closure using the quadrature approximation.

In the univariate problem, one can evolve a full set of moments and therefore the QMOM/DQMOM method gives highly accurate results. This was observed in all the problems considered in chapter 3. In chapter 3, I made the observation that the accuracy of the solution can be increased by a proper choice of the moments. The proper choice of moments appears to be a more crucial in multivariate problems since in the multivariate

case there are further constraints in the choice of a valid set of moments. To avoid the constraints in the choice of moments, one needs to look at other methods that do not involve a Jacobian transformation between the space of moments and the space of quadrature points and weights. As a further extension of this work, one may apply the PCA-QMOM theory to this problem or investigate algorithms that provide the quadrature points and weights directly from the moments. As noted in chapter 2, this leads us to unsolved problems in Gaussian cubature.

After discussion of some of the limitations of the DQMOM method, it is important not to lose sight of key advantages. One is the ability to solve the PDF transport equation in an Eulerian setting and therefore being able to couple these problems to existing CFD codes that can handle complex geometries and large scale industrial reactors. DQMOM is like an asymptotic method where one can increase the number of quadrature points to get better and better accuracy. Further advances in key research areas in mathematics and numerical analysis such as multivariate cubature formulae, the theory of moments etc. has the potential to make a decisive impact on this method.

Chapter 5: Conclusions and further work.

5.1 SUMMARY OF MAIN RESULTS.

The objective of this work was to critically evaluate a promising technique for simulating population balance equations. The two solution techniques that I investigated were the Quadrature Method of Moments (QMOM) and the Direct Quadrature Method of Moments (DQMOM). The theory behind PBE, the method of moments along with the moment closure scheme that is used in QMOM/DQMOM was discussed in greater detail in chapter 2. There I mentioned that the closure scheme for QMOM involves Gaussian integration. Since an approximation was used to close moment equations, there was an accumulation of closure errors as the moment equations were evolved. A simple way of evaluating these errors is to use the QMOM to solve some well formulated problem in aerosol science for which exact solutions can be found. In my treatment of aerosol nucleation and growth in well stirred reactors and nozzles discussed in chapter 3 (section 3.1), I evaluated the possibility of using lower order quadrature schemes in QMOM. By comparison with exact solutions, I saw that results obtained using the lowest 1-point and 2-point quadrature schemes were remarkably accurate. In particular, even the one point approximation appeared to be superior to the lognormal method that is widely used. These results and conclusions are consistent with a growing number of results that have appeared in the literature dealing with the application of the QMOM to problems in aerosol science. QMOM has generated a great deal of excitement in the aerosol community due to its accuracy and computational simplicity.

The QMOM does have a few drawbacks. In chapter 3 (section 3.1) I studied a problem of size dependant transport of aerosols due to gravitational settling and diffusion between infinite parallel plates. The solution to this theoretical problem revealed an

interesting feature of moment equations. The solutions of the unclosed moment equations depended on the choice of moments that were evolved. Errors in the moment solutions provided in tables 3.2.1 to 3.2.3 indicated that the source of error due to incorrect choice of moment sets can be significant. In some cases, these errors were larger than the errors incurred in selecting smaller number of quadrature points. In much of the published work in QMOM, the convergence of the method is tested by increasing the number of quadrature points using integer moments. Convergence is typically not tested using different moment sequences. My findings indicate that solutions should also be checked for different moment sequences. The identification of the effect of choice of moment sequence on the accuracy of the solution is one of the key contributions of this study. In some cases, one may even converge to different solutions with different choices of moment sequences. The choice of optimal moment set for a problem appears to be a difficult problem. In this work, I have not been able to provide a systematic and rigorous procedure for developing an optimal moment set. An interesting problem in numerical analysis is to determine whether a globally optimal moment set exists for a particular PBE. In case of existence, one might find an algorithm for determining the optimal moment set.

An important technological objective is to couple population balance equations with CFD solvers for fluid flow. This enables the study of numerous interesting engineering problems involving particulate processes. An advantage of moment methods is that they are amenable to coupling with commercial CFD codes. I considered a problem of smoke entry and light scattering in a cylindrical cavity above a uniform flow. The solution to this problem demonstrated that it is possible to incorporate complex physical models along with the particle dynamics to make engineering level predictions. The methodology of calculating the electromagnetic scattering by fractal shaped

aggregates that is presented in section 3.3 can be implemented in more realistic models of smoke detectors. It is also possible to treat a host of engineering applications requiring a combination of population balance modeling and computational fluid dynamics at a much more detailed resolution than has been previously possible.

In chapter 4 (section 4.1), I examined the applicability of QMOM and DQMOM for applications in statistical uncertainty propagation. The study of statistical uncertainty propagation using moment methods is not very well known. The application of QMOM and DQMOM to this class of problems appears to be an original contribution of this work. I considered a design problem in which uncertainty in the size of a fire in the room leads to uncertainties in a critical design parameter, the height of the smoke layer from the ceiling. In these applications, one requires a cumulative distribution function for risk assessment studies. Moment methods provide only the moments of the uncertain variable. I used the QMOM and a CDF-reconstruction method that uses the Generalized Lambda Distribution. Solution to this problem revealed that predicted moments again depend on the choice of moments and that fractional moments provide greater accuracy. Furthermore, the CDF-reconstruction scheme was found to be very accurate when compared to exact results obtained from Monte Carlo simulations. The implications of this work suggest that QMOM may be a computationally efficient tool that can be used to simplify the uncertainty calculations in more complex design processes.

In section 4.2, I found that the simulation of turbulent mixing and chemical reaction using moment methods provided the greatest difficulties. In this work I used DQMOM to solve a bivariate and trivariate PBE that describes the turbulent mixing and reaction in a partially stirred reactor. Unlike earlier problems dealing with the univariate PBE, one requires special procedures for selecting a valid set of moments as discussed in section 2.7. In section 2.7.2 I presented a very general method that I call Selective Graded

Lexicographic Ordering (SGLO) for selection of valid moments in DQMOM. The development of the SGLO scheme is another original contribution of this dissertation. This scheme could be used for DQMOM solutions of multivariate population balance equations. Solutions using DQMOM-SGLO presented in chapter 4 (section 4.2.4) indicated that there can be large errors in the solutions obtained using some moment sequences. Furthermore, with some moment sequences, one may even obtain physically unrealistic solutions. Predictions for variances of species showed bigger errors than in the univariate examples discussed earlier. One must mention that solution of multivariate PBEs using moment methods is generally considered to be a difficult task and serious research on this subject has begun only very recently.

5.2 RECOMMENDATIONS FOR FUTURE WORK.

Further work on any of the applications of QMOM and DQMOM that is considered in this work is suggested in the conclusions at the end of each section. Here I outline some possible directions of work for the general QMOM and DQMOM. An open ended problem is to find efficient algorithms for obtaining cubature formulae in higher dimensions. A possible approach is suggested in section 2.6.1. Implementation of a cubature scheme for multivariate moment equations will lead to a better understanding of the limitations of the DQMOM method. More work is required on the use of DQMOM for solutions of multivariate PBEs. In particular, it is desirable to study the computational requirements for this method as the number of dimensions and/or the number of quadrature points is increased. It will be useful to see the comparison with Monte Carlo simulation techniques that are currently the only tools for studying very high dimensional systems. It is also important to demonstrate the stability of DQMOM for these calculations.

A difficult question is whether QMOM or DQMOM is a model or a rigorous numerical scheme for solving the moment equations of population balance equations. If it is a numerical scheme, then one needs to demonstrate that as the number of quadrature points are increased, one can exactly recover all the moments of the underlying density function (i.e. all moments converge). However this may not be possible in general because for a large class of density functions (for instance, those PDFs whose tails decay as a power law), the higher order moments may not even exist and therefore, indefinitely increasing the number of moments would not be feasible. Even if the convergence of the moment equations cannot be defined in the mathematical sense, one can still interpret the moment equations as models that accurately predict the evolution of physically relevant lower order moments of the density function. In this scenario, an analysis that shows how the closure error propagates in time would be very useful. Then one could independently test the accuracy of this method without having to run Monte Carlo simulations. For moment equations of a general population balance equation, the propagation of the error could depend on a number of factors such as the initial number density as well as the transition probability and other growth laws. Knowledge of how the moments of self-similar or other long time asymptotic density functions behave might give some clues about the stability and growth of error. Various schemes for numerical analysis of moment methods for linear kinetic equations exist in the literature as described in Schmeiser and Zwirchmayr (1998). The author is not aware of similar analyses for general nonlinear population balance equations. Alongside these theoretical considerations, one can develop QMOM or DQMOM based solution strategies for an ever wider range of important problems in engineering and the sciences.

Appendix A.

A.1. OBTAINING THE ABCISSAS AND WEIGHTS FOR THE QUADRATURE FORMULA.

A scheme for obtaining the quadrature points and weights for the Quadrature Method of Moments (QMOM) has been given by Gordon (1968). However his formulation involving continued fractions is more complicated and obscures the central mathematical concepts. An alternate formulation using orthogonal polynomials is provided here.

The problem is formulated as follows. Obtain the integral of any function with respect to an unknown size distribution, some of the lower order moments of the size distribution being known.

$$I = \int_0^{\infty} f(v)n(v)dv = \int_0^{\infty} f(v)dn(v) \quad \text{A.1}$$

The central idea is approximating the function using a set of orthonormal polynomials in a suitably defined normed inner product function space. The inner product is defined as

$$\langle f, g \rangle = \int_0^{\infty} f(v)g(v)n(v)dv \quad \text{A.2}$$

where f, g are any two functions in the space. The inner product is well defined even in an infinite interval because the weight $dn(v) \rightarrow 0$ as $v \rightarrow \infty$. In the calculations that follow, the exact form of the size distribution remains unknown. Its only role is in defining the weight so that integrals of the form A.2 do not diverge. Then the norm of any function f in this space is defined by

$$\|f\| = \left[\int_0^{\infty} |f(v)|^2 n(v) dv \right]^{1/2} \quad \text{A.3}$$

One seeks a sequence of orthonormal polynomials such that any function can be best approximated by a unique polynomial that belongs to the vector space spanned by that sequence. Then the problem is, given a linearly independent sequence $\{1, v, v^2, \dots, v^n, \dots\}$, generate an orthonormal sequence of polynomials $\{\hat{P}_0, \hat{P}_1, \hat{P}_2, \dots, \hat{P}_n, \dots\}$. One also knows a number of moments M_0, M_1, \dots, M_n that can be normalized so that $M_0 = 1$. Using the Gram-Schmidt orthogonalization process, one gets

$$\hat{P}_0 = 1 \quad \text{A.4}$$

$$P_1 = v - \langle v, \hat{P}_0 \rangle \hat{P}_0 = v - \int_0^{\infty} 1 \cdot v n(v) dv = v - M_1 \quad \text{A.5}$$

$$\hat{P}_1 = \frac{v - M_1}{\|P_1\|} = \frac{v - M_1}{(M_2 - M_1^2)^{1/2}} \quad \text{A.6}$$

$$P_2 = v^2 - \langle v^2, \hat{P}_0 \rangle \hat{P}_0 - \langle v^2, \hat{P}_1 \rangle \hat{P}_1 = v^2 - v \left(\frac{M_3 - M_1 M_2}{M_2 - M_1^2} \right) + \left(\frac{M_1 M_3 - M_2^2}{M_2 - M_1^2} \right) \quad \text{A.7}$$

$$\hat{P}_2 = \frac{P_2}{\|P_2\|} \quad \text{A.8}$$

In general one has,

$$\hat{P}_n = \frac{P_n}{\|P_n\|} = \frac{v^n - \langle v^n, \hat{P}_0 \rangle \hat{P}_0 - \langle v^n, \hat{P}_1 \rangle \hat{P}_1 - \dots - \langle v^n, \hat{P}_{n-1} \rangle \hat{P}_{n-1}}{\|P_n\|} \quad \text{A.9}$$

Formula A.9 gives a direct method of calculating the orthonormal polynomials from the moments. For 1-point and 2-point quadrature, the roots of the polynomials defined in A.5

and A.7 are required and these can be computed directly. For higher order quadrature schemes, the roots are not computed directly because ‘the numerical problem of finding roots of high-order polynomials is notoriously ill-conditioned’ (Gordon (1968)). The problem of finding the roots is reduced to the computation of eigenvalues of a tri-diagonal matrix for which efficient computational techniques exist. The first step in constructing a tri-diagonal matrix is to obtain a recurrence relationship among the polynomials using the orthogonality property (i.e. each \hat{P}_n is orthogonal to any polynomial up to the $(n-1)^{th}$ power. Taking the polynomial $\hat{P}_{n+1}(v)$ and eliminating the term v^{n+1} gives some polynomial up to the v^n power which can be written as a linear combination of $\{\hat{P}_0, \hat{P}_1, \hat{P}_2, \dots, \hat{P}_n\}$.

$$\hat{P}_{n+1}(v) - \frac{\|P_n\|}{\|P_{n+1}\|} v \hat{P}_n(v) = \gamma_0 \hat{P}_0(v) + \gamma_1 \hat{P}_1(v) + \dots + \gamma_n \hat{P}_n(v) \quad \text{A.10}$$

Taking the inner product of A.10 with $\hat{P}_0(v), \hat{P}_1(v), \dots, \hat{P}_n(v)$ and using the orthogonality property, one gets

$$\gamma_0 = \gamma_1 = \dots, \gamma_{n-2} = 0 \quad \text{A.11}$$

$$\gamma_{n-1} = \frac{-\|P_n\|}{\|P_{n+1}\|} \langle v \hat{P}_n, \hat{P}_n \rangle \quad \text{A.12}$$

$$\gamma_n = \frac{-\|P_n\|}{\|P_{n+1}\|} \langle v \hat{P}_n, \hat{P}_{n-1} \rangle \quad \text{A.13}$$

Using A.10, A.11, A.12 and A.13 one sees that there is a recurrence relationship involving three consecutive polynomials.

$$\hat{P}_{n+1} = \frac{\|P_n\|}{\|P_{n+1}\|} (v - \langle v\hat{P}_n, \hat{P}_n \rangle) \hat{P}_n - \frac{\|P_n\|}{\|P_{n+1}\|} \langle v\hat{P}_n, \hat{P}_{n-1} \rangle \hat{P}_{n-1} \quad \text{A.14}$$

$$\text{It can be shown that } \langle v\hat{P}_n, \hat{P}_{n-1} \rangle = \frac{\|P_n\|}{\|P_{n-1}\|} \quad \text{A.15}$$

Then A.9 can be rewritten as

$$\frac{\|P_{n+1}\|}{\|P_n\|} \hat{P}_{n+1}(v) = (v - \langle v\hat{P}_n, \hat{P}_n \rangle) \hat{P}_n(v) - \frac{\|P_n\|}{\|P_{n-1}\|} \hat{P}_{n-1}(v) \quad \text{A.16}$$

Hence

$$\beta_{n+1} \hat{P}_{n+1}(v) = (v - \alpha_n) \hat{P}_n(v) - \beta_n \hat{P}_{n-1}(v) \quad \text{A.17}$$

where

$$\beta_0 = 0 \text{ (arbitrary)} \quad \text{A.18}$$

$$\beta_n = \frac{\|P_n\|}{\|P_{n-1}\|}; n = 1, 2, 3, \dots \quad \text{A.19}$$

$$\alpha_n = \langle v\hat{P}_n, \hat{P}_n \rangle = \frac{\langle vP_n, P_n \rangle}{\|P_n\|^2}; n = 0, 1, 2, 3, \dots \quad \text{A.20}$$

The expressions for α_n and β_n look deceptively simple in the notation used. In practice it is easy to calculate a few of these terms by hand but for $n \geq 3$ the terms become very long and algebraically complicated. The product-difference algorithm can be used to compute these terms as given later. Equation A.17 can be written as the following system of linear equations

$$\begin{aligned} (\alpha_0 - v) \hat{P}_0(v) + \beta_1 \hat{P}_1(v) &= 0 \quad (n = 0) \\ \beta_0 \hat{P}_0(v) + (\alpha_1 - v) \hat{P}_1(v) + \beta_2 \hat{P}_2(v) &= 0 \quad (n = 1) \end{aligned} \quad \text{A.21}$$

$$\beta_2 \hat{P}_1(v) + (\alpha_2 - v) \hat{P}_2(v) + \beta_3 \hat{P}_3(v) = 0 \quad (n = 2)$$

and so on. Taking the example of the three point quadrature scheme, choose v such that

$P_3(v) = 0$. Then for a non trivial solution to A.21, one requires the determinant

$$\begin{vmatrix} \alpha_0 - \lambda & \beta_1 & 0 \\ \beta_1 & \alpha_1 - \lambda & \beta_2 \\ 0 & \beta_2 & \alpha_2 - \lambda \end{vmatrix} = 0 \quad \text{A.22}$$

That is the roots are the three eigenvalues of the matrix A such that $|A - \lambda I|$ is given by

A.17. The eigenvectors give the weights as shown below.

For each eigenvalue λ_k , the eigenvector is $\begin{pmatrix} \hat{P}_0(\lambda_k) \\ \hat{P}_1(\lambda_k) \\ \hat{P}_2(\lambda_k) \end{pmatrix}$ which can be normalized by

dividing with the length of the vector $[\hat{P}_0^2(\lambda_k) + \hat{P}_1^2(\lambda_k) + \hat{P}_2^2(\lambda_k)]^{1/2}$. Then the following orthonormality condition holds among the normalized eigenvectors.

$$\sum_{\alpha=1}^3 \hat{P}_i^*(\lambda_\alpha) \hat{P}_j^*(\lambda_\alpha) = \delta_{ij} \quad \text{A.23}$$

One is interested in approximating any function using the orthonormal polynomials

$\hat{P}_0(v), \hat{P}_1(v), \hat{P}_2(v)$ for the example of three-point quadrature.

$$f(v) \approx c'_0 \hat{P}_0(v) + c'_1 \hat{P}_1(v) + c'_2 \hat{P}_2(v) \quad \text{A.24}$$

Taking the points $v = \lambda_1, \lambda_2, \lambda_3$ which are the three eigenvalues, one gets

$$f(\lambda_1) = c'_0 \hat{P}_0(\lambda_1) + c'_1 \hat{P}_1(\lambda_1) + c'_2 \hat{P}_2(\lambda_1)$$

$$f(\lambda_2) = c'_0 \hat{P}_0(\lambda_2) + c'_1 \hat{P}_1(\lambda_2) + c'_2 \hat{P}_2(\lambda_2) \quad \text{A.25}$$

$$f(\lambda_3) = c'_0 \hat{P}_0(\lambda_3) + c'_1 \hat{P}_1(\lambda_3) + c'_2 \hat{P}_2(\lambda_3)$$

Using the orthonormality condition (A.13), the coefficients $c'_i, i = 1, 2, 3$. can be evaluated.

$$c'_i = \sum_{\alpha=1}^3 \rho_{\alpha}^2 f(\lambda_{\alpha}) \hat{P}_i(\lambda_{\alpha}) \quad \text{A.26}$$

$$\rho_{\alpha}^2 = \frac{1}{[\hat{P}_0^2(\lambda_{\alpha}) + \hat{P}_1^2(\lambda_{\alpha}) + \hat{P}_2^2(\lambda_{\alpha})]} \quad \text{A.27}$$

One needs to evaluate the integral

$$I = \int_0^{\infty} f(v)n(v)dv = \int_0^{\infty} [c'_0 \hat{P}_0(v) + c'_1 \hat{P}_1(v) + c'_2 \hat{P}_2(v) + \dots] \cdot [1]n(v)dv \quad \text{A.28}$$

But $\hat{P}_1(v), \hat{P}_2(v), \hat{P}_3(v), \dots$ etc. are all orthogonal to 1 and $\hat{P}_0(v) = 1$. So

$$I = \int_0^{\infty} c'_0 n(v)dv = c'_0 M_0 \quad \text{A.29}$$

$$\text{where } c'_0 = \sum_{\alpha=1}^3 \rho_{\alpha}^2 f(\lambda_{\alpha}) \quad \text{A.30}$$

$$\text{Therefore } I = M_0 \sum_{\alpha=1}^3 \rho_{\alpha}^2 f(\lambda_{\alpha}) = \sum_{\alpha=1}^3 w_{\alpha} f(\lambda_{\alpha}) \quad \text{A.31}$$

$w_{\alpha} = \rho_{\alpha}^2 M_0$ is the quadrature weight and λ_{α} is the quadrature point or abscissa.

A.2. THE PRODUCT DIFFERENCE ALGORITHM FOR GETTING ELEMENTS OF THE TRIDIAGONAL MATRIX.

The problem is given a set of moments M_0, M_1, M_2, \dots find the terms α_n and β_n that are defined in B.19 and B.20. This algorithm is outlined in McGraw (1997) and Gordon (1968). First an array $Q(i, j)$ is constructed from the moments as follows.

For the first column, $j = 1$, $Q(1,1) = 1, Q(i,1) = 0, i \neq 1$. A.32

In the second column, $j = 2$ the moments are written down with the signs changed:

$$Q(i,2) = (-1)^{i-1} M_{i-1}, i = 1,2,3,\dots \quad \text{A.33}$$

Then the remaining elements are obtained using the recursive formula for $j \geq 3$.

$$Q(i, j) = Q(1, j-1)Q(i+1, j-2) - Q(1, j-2)Q(i+1, j-1) \quad \text{A.34}$$

Once this array has been created, a vector is constructed with $A(1) = 0$ and

$$A(n) = \frac{P(1, n+1)}{P(1, n)P(1, n-1)} \quad \text{A.35}$$

Finally the matrix elements are calculated as

$$\begin{aligned} \alpha_{n-1} &= A(2n) + A(2n-1) \\ \beta_n^2 &= A(2n+1)A(2n) \end{aligned} \quad \text{A.36}$$

($n = 1,2,3,4,\dots$)

Appendix B.

B.1. DERIVATION OF DQMOM EQUATIONS FOR SIZE DEPENDENT DIFFUSION AND TRANSPORT.

Fox (2003) presents a detailed derivation of the DQMOM equations for general multivariate population balance equations. However, to the best of My knowledge, a derivation for the case where the diffusion coefficients depend on the internal variable does not exist in the literature. Equation 3.2.1 for the combined settling and diffusion of aerosols with size dependent diffusion coefficient and settling velocity is

$$\frac{\partial n(r; x, t)}{\partial t} = \frac{\partial}{\partial x} D(r) \frac{\partial n(r; x, t)}{\partial x} + \frac{\partial}{\partial x} C_s(r) n(r; x, t). \quad \text{B.1}$$

In DQMOM, the number density function is represented by Dirac Delta functions:

$$n(r; x, t) = \sum_{i=1}^{N_Q} \delta(r - \hat{r}_i(x, t)) W_i(x, t). \quad \text{B.2}$$

In the following I drop the x, t dependence of \hat{r}_i and W_i and also the limits of the summation.

Substituting B.2 in B.1 and using the properties of the delta function one gets,

$$\begin{aligned} & \sum_i \delta(r - \hat{r}_i) \left[\frac{\partial W_i}{\partial t} - \frac{\partial C_s(r) W_i}{\partial x} - \frac{\partial}{\partial x} D(r) \frac{\partial W_i}{\partial x} \right] \\ & - \sum_i \delta^{(1)}(r - \hat{r}_i) \left\{ \left[\frac{\partial S_i}{\partial t} - \frac{\partial C_s(r) S_i}{\partial x} - \frac{\partial}{\partial x} D(r) \frac{\partial S_i}{\partial x} \right] \right. \\ & \left. - \hat{r}_i \left[\frac{\partial W_i}{\partial t} - \frac{\partial C_s(r) W_i}{\partial x} - \frac{\partial}{\partial x} D(r) \frac{\partial W_i}{\partial x} \right] \right\}, \quad \text{B.3} \\ & = \sum_i \delta^{(2)}(r - \hat{r}_i) D(r) \left(\frac{\partial \hat{r}_i}{\partial x} \right)^2 \end{aligned}$$

where $\delta^{(1)}$ and $\delta^{(2)}$ are distributional derivatives of the delta function given by

$$\int_{-\infty}^{\infty} \delta^{(m)}(r - \hat{r}_i) g(r) dr = (-1)^m g^{(m)}(\hat{r}_i). \quad \text{B.4}$$

Equation B.3 is exact. Now by multiplying both sides by $g(r) = r^m$, $m = 0, 1, 2, 3, \dots, 2N_Q - 1$, one can force the $2N_Q$ moments to be exact and one gets the following relation:

$$\begin{aligned}
& \sum_i (1-m)(\hat{r}_i)^m \left[\frac{\partial W_i}{\partial t} - C_s(\hat{r}_i) \frac{\partial W_i}{\partial x} - D(\hat{r}_i) \frac{\partial^2 W_i}{\partial x^2} \right] \\
& + \sum_i m(\hat{r}_i)^{m-1} \left\{ \left[\frac{\partial S_i}{\partial t} - C_s(\hat{r}_i) \frac{\partial S_i}{\partial x} - D(\hat{r}_i) \frac{\partial^2 S_i}{\partial x^2} \right] \right. \\
& + \sum_i \left\{ -(\hat{r}_i)^m \frac{dC_s(r)}{dr} \Big|_{\hat{r}_i} \left(\frac{\partial S_i}{\partial x} \right) - (\hat{r}_i)^m \frac{dD(r)}{dr} \Big|_{\hat{r}_i} \left(\frac{\partial^2 S_i}{\partial x^2} \right) \right. \\
& + (\hat{r}_i)^{m+1} \frac{dC_s(r)}{dr} \Big|_{\hat{r}_i} \left(\frac{\partial W_i}{\partial x} \right) + (\hat{r}_i)^{m+1} \frac{dD(r)}{dr} \Big|_{\hat{r}_i} \left(\frac{\partial^2 W_i}{\partial x^2} \right) \\
& = \sum_i \frac{d^2 r^m D(r)}{dr^2} \Big|_{\hat{r}_i} W_i \left(\frac{\partial \hat{r}_i}{\partial x} \right)^2
\end{aligned} \tag{B.5}$$

It is not necessary to choose only integer moment sequences; m can also be a fraction or any arbitrary sequence of real numbers.

In deriving B.5, I have used the property of the derivatives of the delta function B.4. The derivation so far follows from Fox (2003). In this derivation additional terms appear because of the r dependence of $C_s(r)$ and $D(r)$. After some manipulation I obtain transport equations for W_i and S_i :

$$\begin{aligned}
\frac{\partial W_i}{\partial t} - \frac{\partial C_s(\hat{r}_i) W_i}{\partial x} - \frac{\partial}{\partial x} D(\hat{r}_i) \frac{\partial W_i}{\partial x} &= a_i, \\
\frac{\partial S_i}{\partial t} - \frac{\partial C_s(\hat{r}_i) S_i}{\partial x} - \frac{\partial}{\partial x} D(\hat{r}_i) \frac{\partial S_i}{\partial x} &= b_i.
\end{aligned} \tag{B.6}$$

Now substituting B.6 into B.5, one gets

$$\begin{aligned}
& \sum_i (1-m)(\hat{r}_i)^m a_i + \sum_i m(\hat{r}_i)^{m-1} b_i \\
& = \sum_i (\hat{r}_i)^m \frac{dD(r)}{dr} \Big|_{\hat{r}_i} \frac{\partial}{\partial x} W_i \frac{\partial \hat{r}_i}{\partial x} + \left[\frac{d^2 r^m D(r)}{dr^2} \Big|_{\hat{r}_i} - m(\hat{r}_i)^{m-1} \frac{dD(r)}{dr} \Big|_{\hat{r}_i} \right] W_i \left(\frac{\partial \hat{r}_i}{\partial x} \right)^2.
\end{aligned} \tag{B.7}$$

For the general aerosol problem involving coagulation, breakage etc., there will be additional source terms in addition to the source terms for the diffusion. The source terms a_i, b_i for the transport equations B.6 are obtained by the solution of the set of simultaneous linear equations B.7. This can be written in matrix form as shown in Fox (2003). The purpose of this appendix is to illustrate that additional terms appear due to the radius dependence of the diffusivity. For constant diffusivity one recovers the expression given in Fox (2003).

Bibliography

- Adler, R.J. 1981. The geometry of random fields. Chichester (UK); New York: J. Wiley.
- Baldyga, J. & Bourne, J.R. 1999. Turbulent mixing and chemical reactions. Chichester: J. Wiley.
- Batchelor, G.K. 1952. The effect of homogeneous turbulence on material lines and surfaces. *Proceedings of the Royal Society London A*, 213, 349-366.
- Benjamin, I., Heskestad G., Bright R. & Hayes T. 1979. An analysis of environments of fire detectors. Fire Detection Institute, USA, (pp.37).
- Bjorkman, J., Baroudi, D., Latva, R., Tuomisaari, M. & Kokkala, M. (2002). Determination of dynamic model parameters of smoke detectors. *Fire Safety Journal*, 37, 395-407.
- Branley, N. & Jones, W.P. 2001. Large Eddy Simulation of a turbulent non-premixed flame. *Combustion and Flame*, 127, 1914-1934.
- Buchanan, A.H. 1999. Implementation of performance based fire codes. *Fire Safety Journal*, 32, 377-383.
- Bukowski, R.W. & Averill, J.D. 1998. Methods for predicting smoke detector activation. Fire Suppression and Detection Research Application Symposium. Research and Practice: Bridging the Gap. Proceedings. National Fire Protection Research Foundation. Orlando, FL, (pp.64-72), (available on the World Wide Web at URL: <http://fire.nist.gov/bfrlpubs/fire98/art185.html>).
- Carmona, R.A. & Rozovskii, B. 1998. Stochastic partial differential equations : six perspectives. In R.A. Carmona & B. Rozovskii, Eds. Mathematical surveys and monographs no. 64. Providence, R.I.: American Mathematical Society.
- Cercignani, C. 1990. Mathematical methods in kinetic theory. 2nd ed. New York: Plenum Press.
- Chen, J.Y. 1997. Stochastic modeling of partially stirred reactors. *Combustion Science and Technology*, 122, 63-94.
- Cheng, R.C.H. 1978. Generating beta variates with nonintegral shape parameters. *Communications of the ACM*, 21(4), 317-322.
- Cleary, T., Chernovsky, A., Grosshandler, W. & Anderson, M. 1999. Particulate entry lag in spot-type smoke detectors. Fire Safety Science. Proceedings. Sixth International Symposium. International Association for Fire Safety Science

- (IAFSS). July 5-9,1999, Poitiers, France, International Association for Fire Safety Science, Boston, MA, Curtat, M., Editor, (pp.779-790), (available on the World Wide Web at URL: <http://fire.nist.gov/bfrlpubs/fire00/art075.html>).
- Curl, R.L. 1963. Dispersed phase mixing: 1. Theory and effects in simple reactors. *AIChE Journal*, 9, 175-181.
- Davies, C.N. 1949. The sedimentation and diffusion of small particles. *Proceedings of the Royal Society of London. Series A, Mathematical and Physical Sciences*, 200(1060), 110-113.
- Diemer, R.B., & Olson, J.H., 2002a. A moment methodology for coagulation and breakage problems: Part 1-analytical solution of the steady-state population balance. *Chemical Engineering Science*, 57, 2193-2209.
- Diemer, R.B., & Olson, J.H., 2002b. A moment methodology for coagulation and breakage problems: Part 2-moment models and distribution reconstruction. *Chemical Engineering Science*, 57, 2211-2228.
- Dobbins, R.A. & Megaridis, C.M. 1991. Absorption and scattering of light by polydisperse aggregates. *Applied Optics*, 30(33), 4747-4754.
- Dobbins, R.A., Mulholland, G.W. & Bryner, N.P. 1994. Comparison of a fractal smoke optics model with light extinction measurements. *Atmospheric Environment*, 28(5), 889-897.
- Dopazo, C. 1975. Probability density function approach for a turbulent axisymmetric heated jet. Centerline evolution. *Physics of Fluids*, 18, 397-404.
- Dunkl, C.F. & Xu, Y. 2001. Orthogonal polynomials of several variables. In *Encyclopedia of mathematics and its applications*, v. 81. Cambridge; New York: Cambridge University Press.
- Einstein, A. 1905. On the motion of small particles suspended in a liquid at rest as required by the molecular kinetic theory of heat. *Annalen der Physik*, 17, 549-560.
- Fan, R., Marchisio, D.L. & Fox, R.O. 2004. Application of the direct quadrature method of moments to polydisperse, gas-solid fluidized beds. *Powder Technology*, 139, 7-20.
- Farias, T.L., Koylu, U.O. & Carvalho, M.G. 1996. Range of validity of the Rayleigh-Debye-Gans theory for optics of fractal aggregates. *Applied Optics*, 35, 6560-6567.

- Feller, W. 1967. An introduction to probability theory and its applications. 3rd ed. New York: Wiley.
- Fox, R.O. 2003. Computational models for turbulent reacting flows. Cambridge: Cambridge University Press.
- Fox, R.O. & Raman, V.R. 2004. A multienvironment conditional probability density function model for turbulent reacting flows. *Physics of Fluids*, 16(12), 4551-4565.
- Frenklach, M. 2002. Method of moments with interpolative closure. *Chemical Engineering Science*, 57, 2229-2239.
- Frenklach, M., & Harris, S.J. 1987. Aerosol dynamics modeling using the method of moments. *Journal of Colloid and Interface Science*, 118, 252-261.
- Friedlander, S.K. 1983 Dynamics of aerosol formation by chemical reaction. *Annals of the New York Academy of Sciences*, 404, 354-363.
- Friedlander, S.K. 2000. Smoke, Dust and Haze, Fundamentals of Aerosol Dynamics. 2nd ed. New York: Oxford University Press.
- Frisch, U. 1995. Turbulence: the legacy of A.N. Kolmogorov. Cambridge; New York: Cambridge University Press.
- Fuchs, N.A. 1964. The mechanics of aerosols. Oxford, New York: Pergamon Press.
- Gelbard, F. & Seinfeld, J.H. 1980. Simulation of multicomponent aerosol dynamics. *Journal of Colloid and Interface Science*, 78, 485-501.
- Gelbard, F., Tambour, Y. & Seinfeld, J.H. 1980. Sectional representations for simulating aerosol dynamics. *Journal of Colloid and Interface Science*, 76, 541-556.
- Goldberg, I.S., Lam, K.Y., Bernstein, B., & Hutchens, J.O. 1978. Solutions to the Fokker-Planck equations governing simultaneous diffusion and gravitational settling of aerosol particles from a stationary gas in a horizontal circular tube. *Journal of Aerosol Science*, 9, 209-218.
- Gordon, R.G. 1968. Error bounds in equilibrium statistical mechanics. *Journal of Mathematical Physics*, 9, 655-663.
- Heskestad, G. 1975. Generalized characterization of smoke entry and response for products of combustion detectors, International Conference on Automatic Fire Detection, 7th. Probleme der Automatischen Brandentdeckung. March 5-6, 1975, (pp. 267-310).

- Heskestad, G. & Delichatsios, M.A. 1977a. Environments of fire detectors – Phase I: Effect of Fire Size, Ceiling Height and Material, Volume 1 – Measurements. Factory Manual Research Corporation Technical Report 22427, Norwood, MA..
- Heskestad, G. & Delichatsios, M.A. 1977b. Environments of fire detectors – Phase I: Effect of Fire Size, Ceiling Height, and Material, Volume 2 – Analysis. NBSGCR-77-95.
- Hidy, G.M. & Brock, J.R. 1970. The dynamics of aerocolloidal systems. 1st ed. Oxford; New York: Pergamon Press.
- Hill, C.G. 1977. An Introduction to Chemical Engineering Kinetics and Reactor Design. New York: John Wiley and Sons.
- Hulburt, H.M., & Katz, S. 1964. Some problems in particle technology: A statistical mechanical formulation. *Chemical Engineering Science*, 19, 555-574.
- Hurley, M.J. 2003. ASET-B: Comparison of model predictions with full scale test data. *Journal of Fire Protection Engineering*, 13, 37-63.
- Janssens, M.L. 2000. An introduction to mathematical fire modeling. 2nd ed. Lancaster: Technomic publishing company inc.
- Jones, W.W., Peacock, R.D., Forney, G.P. & Reneke, P.A. 2005. CFAST- Consolidated Model of Fire Growth and Smoke Transport (Version 6). Technical reference guide. NIST Special Publication 1026, US Department of Commerce, NIST-BFRL, Gaithersburg, MD.
- Jones, W.W., Peacock, R.D., Forney, G. P. & Reneke, P.A. 2004. CFAST, Consolidated Model of Fire Growth and Smoke Transport (Version 5). Technical Reference Guide. NIST SP 1030; 153 p.
- Ierardi, J.A. & Barnett J.R. 2003. CFD modelling of aerosol entry in simplified smoke detector geometries. Fire Safety Science. Proceedings. Seventh (7th) International Symposium. International Association for Fire Safety Science (IAFSS), (pp.1170-1170), (available on the World Wide Web at URL: <http://fire.nist.gov/bfrlpubs/fire03/art043.html>).
- Karian, Z.A. & Dudewicz, E.J. 2000. Fitting statistical distributions: the generalized lambda distribution and generalized bootstrap methods. Boca Raton: CRC Press.
- Klimenko, A.Y. & Bilger, R.W. 1999. Conditional moment closure for turbulent combustion. *Progress in Energy and Combustion Science*, 25, 595-687.
- Kloeden, P.E. & Platen, P.E. 1992. Numerical solution of stochastic differential equations. Berlin; New York: Springer-Verlag.

- Koylu, U.O. & Faeth, G.M. 1994. Optical properties of overfire soot in buoyant turbulent diffusion flames at long residence times. *Journal of Heat Transfer*, 116, 152-159.
- Koylu, U.O. & Faeth, G.M. 1996. Spectral extinction coefficients of soot aggregates from turbulent diffusion flames. *Journal of Heat Transfer*, 118, 415-421.
- Lanczos, C. 1956. Applied Analysis. Englewood Cliffs, N.J.: Prentice-Hill Inc. pp 396-414.
- Langford, J. A. & Moser, R.D. 1999. Optimal LES Formulations for Isotropic Turbulence, *Journal of Fluid Mechanics*, 398, 321-346.
- Loepfe, M., Ryser, P., Tompkin, C. & Wieser, D. 1997. Optical properties of fire and non-fire aerosols. *Fire Safety Journal*, 29, 185-194.
- Magnusson, S.E., Frantzich, H. & Harada, K. 1996. Fire safety designs based on calculations: uncertainty analysis and safety verification. *Fire Safety Journal*, 27, 305-334.
- Marchisio, D.L., Piktorna, J., Fox, R.O., Vigil, R.D. & Barresi, A.A. 2003. Quadrature method of moments for population balances. *AIChE Journal*, 49, 1266-1276.
- Marchisio, D.L., Vigil, R.D. & Fox, R.O. 2003a. Quadrature method of moments for aggregation breakage processes. *Journal of Colloid and Interface Science*, 258, 322-334.
- Marchisio, D.L., Vigil, R.D. & Fox, R.O. 2003b. Implementation of the quadrature method of moments in CFD codes for aggregation-breakage problems. *Chemical Engineering Science*, 58, 3337-3351.
- Marchisio, D.L. & Fox, R.O. 2005. Solution of population balance equations using the direct quadrature method of moments. *Journal of Aerosol Science*, 36, 43-73.
- McGraw, R. 1997. Description of aerosol dynamics by the quadrature method of moments. *Aerosol Science and Technology*, 27, 255-265.
- McGraw, R. & Wright, D.L. 2003. Chemically resolved aerosol dynamics for internal mixtures by the quadrature method of moments. *Journal of Aerosol Science*, 34, 189-209.
- Mulholland, G.W. 1995. Smoke production and properties. In SFPE Handbook of Fire Protection Engineering, 2nd ed. (pp. 2-217-27). Quincy, MA: NFPA.
- Mulholland, G.W. & Liu, B.Y.H. 1980. Response of smoke detectors to monodisperse aerosols. *Journal of Research of the National Bureau of Standards*, 85(3), 223-238.

- Nelson, J. 1989. Test of a mean field theory for the optics of fractal clusters. *Journal of Modern Optics*, 36, 1031-1057.
- Newman, J.S. 1997. Prediction of fire detector response. *Fire Safety Journal*, 29, 99-112.
- Notarianni, K.A. Uncertainty. In: DiNenno, P.J., Drysdale, D., Beyler, C.L. & Walton, W.D., editors. NFPA HFPE-02; SFPE Handbook of Fire Protection Engineering. 3rd ed., Chapter 4, Section 5. Quincy, MA, pp. 5-40:5-64.
- Panton, R. 2005. Incompressible flow. 3rd ed. Hoboken, N.J.: J. Wiley.
- Patankar, S.V. 1980. Numerical heat transfer and fluid flow. New York: McGraw-Hill.
- Peters, N. 2000. Turbulent Combustion. Cambridge: Cambridge University Press.
- Petzold, L.R. 1983. A description of DASSL: A differential algebraic equation solver. In R.S. Stepleman, editor, Scientific Computing, pp. 65-68. Amsterdam: North-Holland.
- Piskunov, V.N. & Golubev, A.I. 2002. The generalized approximation method for modeling coagulation kineticsw-Part I: Justification and implementation of the method. *Journal of Aerosol Science*, 33, 51-63.
- Piskunov, V.N., Golubev, A.I., Barrett, J.C. & Ismailova, N.A. 2002. The generalized approximation method for modeling coagulation kineticsw-Part II: Comparison with other methods. *Journal of Aerosol Science*, 33, 65-75.
- Pope, S.B. 1985. PDF Methods for Turbulent Reacting Flows. *Progress in Energy and Combustion Science*, 11, 119-192.
- Pratsinis, S.E. 1988. Simultaneous nucleation, condensation and coagulation in aerosol reactors. *Journal of Colloid and Interface Science*, 2, 416-427.
- Press, W.H., Teukolsky, S.A., Vetterling, W.T. & Flannery, B.P. 1992. Numerical recipes in FORTRAN 77, the art of scientific computing. 2nd ed. Cambridge: Cambridge University Press.
- Raman, V. & Pitsch. H. 2005. LES / Filtered-Density Function simulation of turbulent combustion with detailed chemistry. *Center for Turbulence Research, Annual Research Briefs*, 297-309.
- Ramkrishna, D. 2000. Population balances: theory and applications to particulate systems in engineering. San Diego: Academic Press.
- Randolph, A.D. & Larson, M.A. 1988. Theory of particulate processes: analysis and techniques of continuous crystallization. 2nd ed. Orlando: Academic Press.

- Ren, Z. & Pope, S.B. 2004. An investigation of the performance of turbulent mixing models. *Combustion and Flame*, 136, 208-216.
- Rosner, D.E. & Pykkonen, J.J. (2002). Bivariate moment simulation of coagulating and sintering nanoparticles in flames. *AIChE Journal*, 48, 476-491.
- Rosner, D.E., McGraw, R. & Tandon, P. 2003. Multivariate population balances via moment and Monte Carlo simulation methods: An important sol reaction engineering bivariate example and “mixed” moments for the estimation of deposition, scavenging and optical properties for populations of nonspherical suspended particles. *Industrial & Engineering Chemistry Research*, 42, 2699-2711.
- Settumba, N. & Garrick, S.C. 2004. A comparison of diffusive transport in a moment method for nanoparticle coagulation. *Journal of Aerosol Science*, 35, 93-101.
- Snegirev, A.Yu., Makhviladze, G.M. & Roberts, J.P. 2001. The effect of particle coagulation and fractal structure on the optical properties and detection of smoke. *Fire Safety Journal*, 36, 73-95.
- Sorensen, C.M., Cai, J. & Lu, N. 1992. Light-scattering measurements of monomer size, monomers per aggregate and fractal dimension for soot aggregates in flames. *Applied Optics*, 31, 6547-6557.
- Sorensen, C.M. 1997. Scattering and absorption of light by particles and aggregates. In Birdi, K.S. (Editor), *Handbook of Surface and Colloid Chemistry* (pp.533-558), CRC Press.
- Sorensen, C.M. & Fischbach, D.J. 2000. Patterns in Mie scattering. *Optics Communications*, 173, 145-153.
- Sorensen, C.M. 2001. Light scattering by fractal aggregates: a review. *Aerosol Science and Technology*, 35, 648-687.
- Schmeiser, C. & Zwirchmayr, A. 1998. Convergence of moment methods for linear kinetic equations. *SIAM Journal of Numerical Analysis*, 36(1), 74-88.
- Terry, D.A., McGraw, R. & Rangel, R.H. 2001. Method of moments solutions for a laminar flow aerosol reactor model. *Aerosol Science and Technology*, 34, 353-362.
- Turner, J.R., Kodas, T.T. & Friedlander, S.K. 1988 Monodisperse particle production by vapor condensation in nozzles. *Journal of Chemical Physics*, 1, 457-465.

- Upadhyay, R.R. & Ezekoye, O.A. 2003. Evaluation of the 1-point quadrature approximation in QMOM for combined aerosol growth laws. *Journal of Aerosol Science*, 34, 1665-1683.
- Upadhyay, R.R. & Ezekoye, O.A. 2005a. Smoke buildup and light scattering in a cylindrical cavity above a uniform flow. *Journal of Aerosol Science*, 36, 471-493.
- Upadhyay, R.R. & Ezekoye, O.A. 2005b. Treatment of size-dependent aerosol transport processes using quadrature based moment methods. *Journal of Aerosol Science*, 37, 799-819.
- Van Kampen, N.G. 1992. Stochastic Processes in Physics and Chemistry. Amsterdam; New York: North-Holland.
- Villani, C. 2002. A review of Mathematical topics in collisional kinetic theory. In S. Friedlander & D. Serre, Eds. Handbook of Mathematical Fluid Dynamics, Volume 1. North-Holland.
- Wall, H.S. 1948. Analytical theory of continued fractions. New York: D. Van Nostrand Company Inc.
- Wang, C.S., Altshuler, B. & Palmes, E.D. (1968). The distribution and deposition of particles suspended between parallel plane surfaces. *Journal of Colloid and Interface Science*, 26, 41-44.
- Watts, J.M. 1986. Dealing with uncertainty: some applications in fire protection engineering. *Fire Safety Journal*, 11(1-2), 127-134.
- Weinert, D.W., Cleary, T.G., Mulholland, G.W. & Beever, P.F. 2003. Light scattering characteristics and size distribution of smoke and nuisance aerosols. Fire Safety Science. Proceedings. Seventh (7th) International Symposium. International Association for Fire Safety Science (IAFSS). June 16-21, 2003, Worcester, MA, International Association for Fire Safety Science, Boston, MA, Evans, D. D., Editor(s), (pp. 209-220), (available on the World Wide Web at URL: <http://fire.nist.gov/bfrlpubs/fire03/art058.html>).
- Weisstein, E.W. 1999. "Log Normal Distribution." From MathWorld--A Wolfram Web Resource. <http://mathworld.wolfram.com/LogNormalDistribution.html>.
- Westbrook, C.K. & Dryer, F.L. 1981. Simplified Reaction Mechanisms for the Oxidation of Hydrocarbon Fuels in Flames. *Combustion Science and Technology*, 27, 31-43.
- Widmann, J.F. 2003. Evaluation of the Planck mean absorption coefficients for radiation transport through smoke. *Combustion science and Technology*, 175, 2299-2308.

- Wilck, M. 2001. A general approximation method for solving integrals containing a lognormal weighting function. *Journal of Aerosol Science*, 32, 1111-1116.
- Williams, M.M.R. & Loyalka, S.K. 1991. *Aerosol Science. Theory and Practice*. Oxford: Pergamon Press.
- Wright, D.L., McGraw, R. & Rosner, D.E. 2001. Bivariate extension of the quadrature method of moments for modeling simultaneous coagulation and sintering of particle populations. *Journal of Colloid and Interface Science*, 236, 242-251.
- Xu, Y. 1994. Common zeros of polynomials in several variables and higher dimensional quadrature. In *Pitman research notes in mathematics series*. New York: J. Wiley and Sons.
- Yoon, C. & McGraw, R. 2004a. Representation of generally mixed multivariate aerosols by the quadrature method of moments: I. Statistical foundation. *Journal of Aerosol Science*, 35, 561-576.
- Yoon, C. & McGraw, R. 2004b. Representation of generally mixed multivariate aerosols by the quadrature method of moments: II. Aerosol Dynamics. *Journal of Aerosol Science*, 35, 561-576.
- Yung, D.T. & Benichou, N. 2002. How design fires can be used in fire hazard analysis. *Fire Technology*, 38, 231-242.

Vita

Rochan Raj Upadhyay was born in 19th of June 1976 in Bangkok, Thailand of Nepalese parents. He attended St. Xavier's High School in Kathmandu, Nepal. After that he joined the Indian Institute of Technology in Delhi graduating in August 2001 with a Bachelor of Technology degree in Mechanical Engineering. Since then he has been enrolled in the University of Texas at Austin where he has already obtained a master's degree in August 2003 and is expecting a PhD in December 2006. He has had two semesters of teaching experience in the University of Texas at Austin. Some of his publications that have already been printed in peer-reviewed journals are listed in the bibliography.

Permanent address: Cha 2/40, Jorpipal, Gairidhara, Kathmandu, Nepal.

This dissertation was typed by the author.